VOLUME 122 NUMBER 3

THE ASTROPHYSICAL JOURNAL

AN INTERNATIONAL REVIEW OF SPECTROSCOPY AND ASTRONOMICAL PHYSICS

NOVEMBER 1955

ABSORPTION OF 21-CM RADIATION BY INTERSTELLAR HYDROGEN
J. P. Hagen, A. E. Lilley, and E. F. McClain 361

AN APPROXIMATE DISTANCE DETERMINATION FOR RADIO SOURCE SAGITTARIUS A
Edward F. McClain 376

THE RADII OF δ CEPHEI AND η AQUILAE. II
Charles Whitney 385

SPECTROSCOPIC OBSERVATIONS OF THE CLUSTER-TYPE VARIABLE VZ CANCRI
Helmut A. Abt 390

RELATIVE ABUNDANCES AND ATMOSPHERIC CONDITIONS IN THE MAGNETIC STAR HD 133029
E. Margaret Burbidge and G. R. Burbidge 396

THE SPECTRUM OF NU ERIDANI
O. Struve and K. D. Abhyankar 409

THE SPECTRUM OF THE SLOW NOVA V 356 AQUILAE (1936)
Dean B. McLaughlin 417

PHOTOMETRIC AND SPECTROSCOPIC OBSERVATIONS OF THE DOUBLE CLUSTER IN PERSEUS
H. L. Johnson and W. W. Morgan 429

THE M-TYPE SUPERGIANTS IN h AND χ PERSEI
Victor M. Blanco 434

PRELIMINARY NOTE ON MEASURES OF CORONAL EMISSION LINES OBSERVED AT THE TOTAL SOLAR ECLIPSE, FEBRUARY 25, 1952, BY B. LYOT AND M. K. ALY
M. K. Aly 438

A PHOTOMETRIC STUDY OF THE SOLAR CORONA
Nannielou Hepburn 445

A SEARCH FOR SOLAR VARIATION
R. H. Hardie and H. L. Giclas 460

ON THE SOLAR GRANULES
Mahinder S. Uberoi 466

EXPANDING *H* II REGION
Malcolm P. Savedoff and John Greene 477

ON THE SOLUTION OF EQUATIONS OF TRANSFER. I
Max Krook 488

NEAR THERMODYNAMIC EQUILIBRIUM. II
L. G. Henyey and William Grasberger 498

THE EQUILIBRIUM OF MAGNETIC STARS
P. H. Roberts 508

RADIO DETERMINATION OF THE ORBIT OF THE ETA AQUARID METEORS
D. W. R. McKinley 513

RECORDINGS OF THE ZODIACAL LIGHT
Victor H. Regener 520

THE HEIGHT OF THE NIGHTGLOW BY THE VAN RHIJN METHOD
F. E. Roach and A. B. Meinel 530

NIGHTGLOW HEIGHTS: A REINTERPRETATION OF OLD DATA
F. E. Roach and A. B. Meinel 554

ABLATION FROM ALUMINUM ULTRASPEED PELLETS
William C. White 559

NOTES

DOPPLER SHIFTS IN SOLAR GRANULES
Robert R. McMath, Orren C. Mohler, and A. Keith Pierce 565

SHORT-PERIOD FLUCTUATIONS IN THE INTENSITY OF SS CYGNI
Gordon Grant 566

ABSTRACTS OF ASTROPHYSICAL JOURNAL SUPPLEMENT SERIES

TOROIDAL OSCILLATIONS OF AN INCOMPRESSIBLE CONDUCTIVE FLUID SPHERE IN A DECAY FIELD
Eberhart Jensen 569

INDEXES 571

THE UNIVERSITY OF CHICAGO PRESS
CHICAGO, ILLINOIS, U.S.A.

November 1955 Vol. 122, No. 3

THE ASTROPHYSICAL JOURNAL

AN INTERNATIONAL REVIEW OF SPECTROSCOPY AND ASTRONOMICAL PHYSICS

Founded in 1895 by George E. Hale and James E. Keeler

Published in Collaboration with the American Astronomical Society

S. CHANDRASEKHAR
Managing Editor

GERARD P. KUIPER
Associate Editor

Yerkes Observatory of the University of Chicago

EDITORIAL BOARD

LEO GOLDBERG (1955-59)
The Observatory of the University of Michigan

H. W. BABCOCK (1953-57)
Mount Wilson Observatory of the Carnegie Institution of Washington

MARTIN SCHWARZSCHILD (1954-58)
Princeton University Observatory

G. HERZBERG (1952-56)
National Research Council, Ottawa

C. D. SHANE (1952-55)
Lick Observatory, University of California

The Astrophysical Journal is published bimonthly by the University of Chicago at the University of Chicago Press, 5750 Ellis Avenue, Chicago 37, Illinois, during January, March, May, July, September, and November. ¶Two volumes are published per year, one beginning with the January issue and the other beginning with the July issue. On all orders from the United States and its possessions the subscription price is $7.50 per volume or $15.00 per year; the price of single copies is $3.50. ¶On all orders from Canada the subscription price is $8.00 per volume or $16.00 per year; the price of single copies is $3.65. On all orders from all other countries the subscription price is $8.25 per volume or $16.50 per year; the price of single copies is $3.75. (Orders for service of less than a volume will be charged at the single-copy rate.) ¶Subscriptions are payable in advance. Please make all remittances payable to The University of Chicago Press, in United States currency or its equivalent by postal or express money orders or bank drafts. (Exception: members of The American Astronomical Society must send their subscriptions and remittances to the Treasurer of the Society.)

The following is an authorized agent:

For the British Commonwealth, except North America and Australasia: The Cambridge University Press, Bentley House, 200 Euston Road, London, N.W. 1, England. Prices of yearly subscriptions and of single copies may be had on application.

Claims for missing numbers should be made within the month following the regular month of publication. The publishers expect to supply missing numbers free only when losses have been sustained in transit, and when the reserve stock will permit.

Business correspondence should be addressed to The University of Chicago Press, Chicago 37, Illinois.

Communications for the editors and manuscripts should be addressed to: S. Chandrasekhar, Editor of THE ASTROPHYSICAL JOURNAL, Yerkes Observatory, Williams Bay, Wisconsin.

Line drawings and photographs should be made by the author, and all marginal notes such as co-ordinates, wave lengths, etc., should be included in the cuts. It will not be possible to set up such material in type.

One copy of the corrected galley proof should be returned as soon as possible to the editor, Yerkes Observatory, Williams Bay, Wisconsin. Authors should take notice that the manuscript will not be sent to them with the proof.

The cable address is "Observatory, Williamsbay, Wisconsin."

The articles in this journal are indexed in the *International Index to Periodicals*, New York, N.Y.

Applications for permission to quote from this journal should be addressed to The University of Chicago Press, and will be freely granted.

Microfilms of complete journal volumes are available to regular subscribers only and may be obtained at the end of the year. Orders and inquiries should be addressed to University Microfilms, 313 North First Street, Ann Arbor, Michigan.

Notice to subscribers: If you change your address, please notify us and your local postmaster immediately.

Entered as second-class matter, July 31, 1940, at the Post-Office at Chicago, Ill., under the Act of March 3, 1879.
Acceptance for mailing at special rate of postage provided for in United States Postal Act of October 3, 1917, Section 1103, amended February 28, 1925.
Copyright 1955 by the University of Chicago.

[PRINTED IN U.S.A.]

THE ASTROPHYSICAL JOURNAL

AN INTERNATIONAL REVIEW OF SPECTROSCOPY AND ASTRONOMICAL PHYSICS

VOLUME 122 NOVEMBER 1955 NUMBER 3

ABSORPTION OF 21-CM RADIATION BY INTERSTELLAR HYDROGEN

J. P. HAGEN, A. E. LILLEY, AND E. F. MCCLAIN
Naval Research Laboratory, Washington 25, D.C.
Received June 27, 1955; revised July 20, 1955

ABSTRACT

Absorption effects have been observed in the continuous microwave noise spectra of certain radio stars. The absorption is produced by the $F = 0$ to $F = 1$ hyperfine transition in interstellar hydrogen and occurs at a wave length of approximately 21 cm. For radio stars and interstellar *H* I, the effect is similar to the presence of optical interstellar absorption lines in stellar spectra. Three absorption-line components due to interstellar *H* I are found in the microwave spectrum of the Cassiopeia source. The absorption lines are characterized by their narrow breadth and do not necessarily coincide with the gross 21-cm emission maxima of the same region. The physical interpretation of the absorption profiles is sensitive to the manner in which the *H* I is distributed in the interstellar medium. The analysis strongly supports the distribution of *H* I in clouds or in condensations in a less dense medium. Distances to the absorbing clouds and minimum distances to the discrete sources may be determined from a galactic-rotation analysis of the absorption profiles. A minimum distance to the Cassiopeia A discrete source of 3 kpc is found.

EQUIPMENT

The equipment used in obtaining the observations reported here is the Naval Research Laboratory 50-foot, alt-azimuth mounted, parabolic antenna. This radio telescope is driven in equatorial co-ordinates by means of a computer. The main lobe, half-power-point separation is 55′ of arc at 1420 Mc. Figures 1, 2, and 3 display the equipment components.

The receiver (Fig. 3) performs a dual role. It acts as a d.c. comparison radiometer for hydrogen measurements and as a straight (nonchopped) radiometer for continuum measurements. Hydrogen-line detection in emission or absorption, respectively, above or below the background radiation field of a celestial position is achieved by the comparison radiometer function. The quantity displayed by the comparison radiometer is the average d.c. noise-power difference per unit band width between the signal and comparison bands. A detailed discussion of the performance of this type of radiometer has been published by W. Selove (1954).

A determination of the "figure of merit" of the radiometer, the noise figure, permits the output to be calibrated in terms of temperature. One first determines the effective temperature of the receiver itself with no signal in the antenna; the percentage deflection of the output level when the antenna is directed toward a celestial source then corresponds to the apparent antenna temperature of the source. The gaseous discharge-tube method was used to determine the noise figure of the receiver (Mumford 1949).

A block diagram of the receiver is shown in Figure 3. The signal and comparison bands are moved through the spectrum automatically by the tuning action of the local oscillator. This action displays $\Delta T(\nu)$, the temperature difference between signal and comparison bands, at recorder No. 1, which is the "21-cm hydrogen-line profile" for the direction toward which the antenna is pointed. The width of the signal band is 5 kc, corresponding to a radial-velocity width of 1 km/sec at $\lambda = 21$ cm.

The No. 2 recorder in Figure 3 receives the noise from the 2-Mc-wide comparison band which is displaced 3.25 Mc from the hydrogen band. This recorder has been used to measure the temperatures of the discrete sources given in Table 1.

TABLE 1

SOURCES OBSERVED AT 21-CM WAVE LENGTH*

No.	Source	Right Ascension	Declination	T_A (° K)	Flux (Watts/M²)/(C/S)	Remarks
1...	05N2A	5^h31^m	+22° 00′	46	106×10^{-25}	Crab Nebula
2...	05S0A	5 32	− 5 20	18	42	Orion Nebula, M 42
3...	Orion B	5 39	− 1 30	2	5	*H* II region, near Horsehead Nebula
4...	06N2A	6 13	+22 40	7	16	High-velocity emission nebula IC 443
5...	12N1A	12 27	+12 20	13	30	M 87 (galaxy with jet)
6...	13S4A	13 22	−42 40	17	40	NGC 5128 (colliding galaxies)
7...	17S2A	17 43	−28 45	73†	.....	Sagittarius A (perhaps galactic center)
8...	NRL No. 9	17 43	−28 45	6–30‡	.....	Extended source around 17S2A Sagittarius A
9...	M20	17 57	−23 03	18	42	*H* II region, Trifid Nebula
10...	NGC 6604	18 16	−12 10	4	9	*H* II region
11...	M16	18 17	−13 40	9	21	*H* II region
12...	18S1A	18 17	−16 00	35	82	*H* II region, Omega Nebula, M17
13...	Unidentified	18 24	−12 20	11	26	Unidentified in a complex region
14...	Unidentified	18 59	+ 5 00	4	9	Possibly Mills (19+07)
15...	19N4A	19 58	+40 30	63	146	Cygnus A, colliding galaxies
16...	S78	20 22	+40 20	15	34	*H* II region
17...	S79	20 30	+43 45	3	7	*H* II region
18...	20N4A	20 40	+40 40	16	.....	Cygnus X, extended source
19...	NGC 7000	20 53	+44 30	4	.....	*H* II region, North American Nebula
20...	23N5A	23 21	+58 32	116	270	Cassiopeia A, high-velocity emission nebula

* J. P. Hagen, E. F. McClain, and N. Hepburn, *Proc. I.R.E.*, **42**, 1811, 1954.

† Total temperature at this position.

‡ Difficult to separate from 17S2A.

ABSORPTION EFFECTS IN A HOMOGENEOUS GAS

Interstellar hydrogen atoms in the ground state act as emitters and absorbers between the hyperfine levels. Van de Hulst, Muller, and Oort (1954) have extensively employed the emission in a determination of the spatial distribution of hydrogen which outlines the spiral-arm structure of our Galaxy.

The absorption was first observed for discrete sources at the Naval Research Laboratory by Hagen and McClain (1954*a*, *b*). At a joint meeting of the International Scientific Radio Union, Institute of Radio Engineers, and the American Geophysical Union in Washington, D.C., May 5, 1954, it was pointed out that this absorption technique made possible a determination of the distance of the source with respect to the hydrogen clouds: "Clearly this technique makes it possible in some cases to determine whether the radio

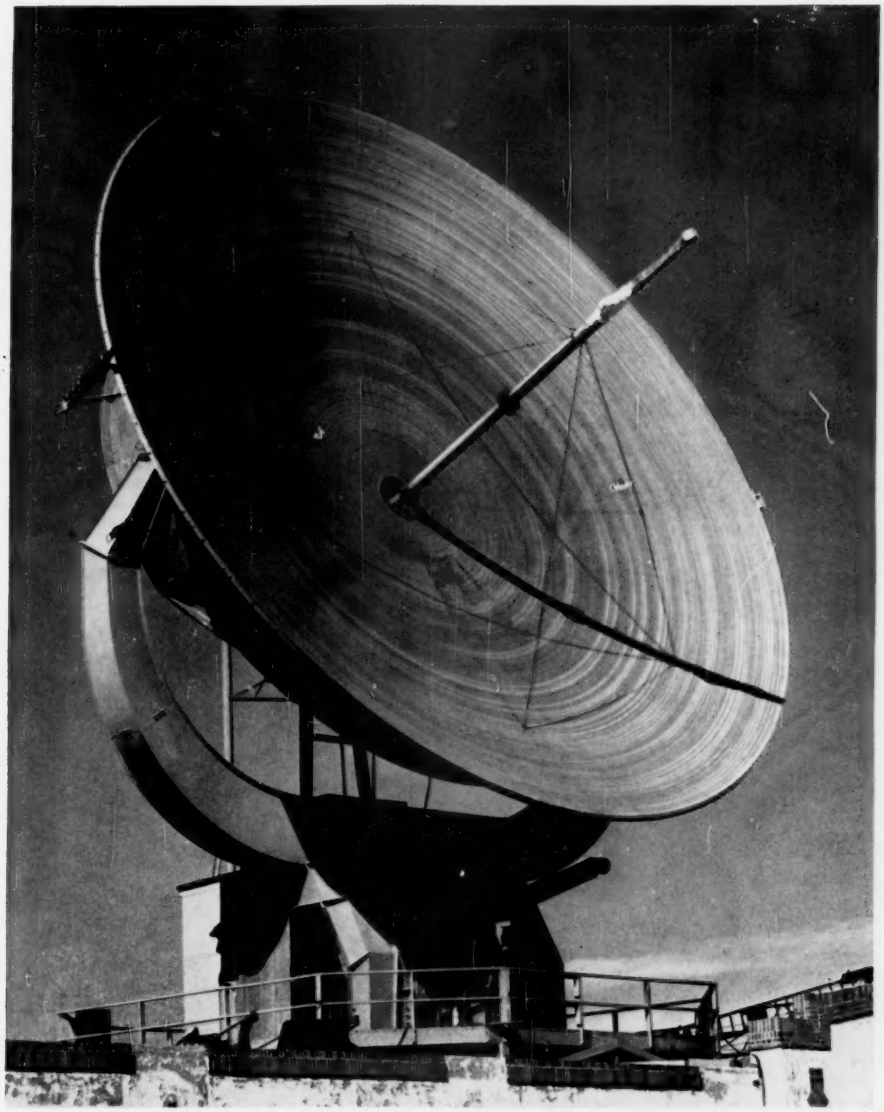

FIG. 1.—The 50-foot radio telescope at the Naval Research Laboratory, Washington, D.C. The antenna is alt-azimuth mounted and is driven in equatorial co-ordinates by means of a computer.

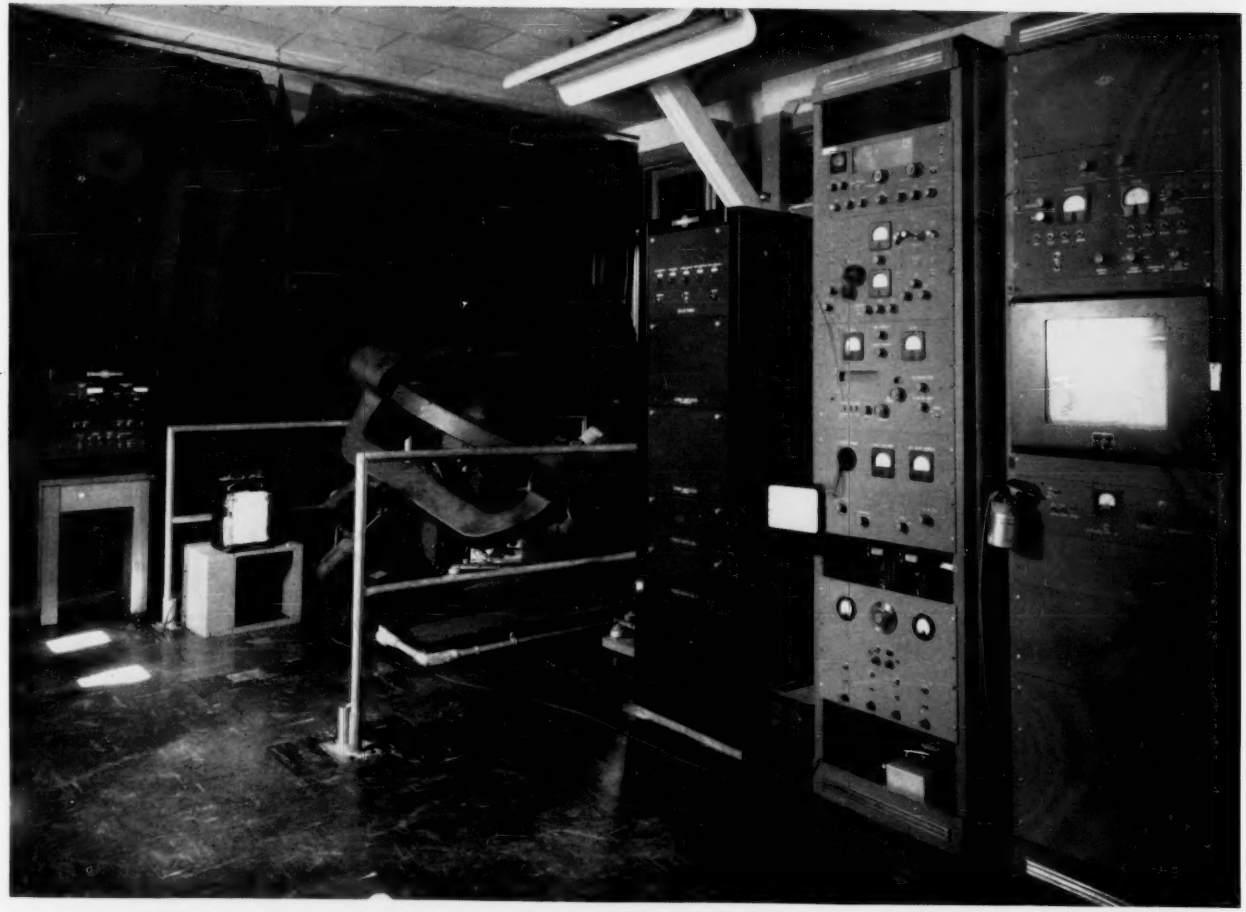

FIG. 2.—The antenna control system and 21-cm receiver equipment. *Left to right:* antenna position control console, 21-cm continuum recorder, co-ordinate computer, computer-power supplies, local oscillator, and the hydrogen-line radiometer.

source is between us and the hydrogen cloud or beyond the cloud." The first notes by Hagen and McClain (1954*a*, *b*) neglected the mechanisms discussed in the present paper. Observations reported in this paper were obtained by using a band width of 5 kc, whereas those reported in the first notes were obtained with a 55-kc band width. Williams and Davies (1954) have applied the absorption effect as an indication of the distance to the discrete sources in Cassiopeia and Cygnus. The Australian 21-cm group has also secured observations of the absorption effect.

In the Naval Research Laboratory experiments, absorption observations for discrete sources have been obtained in two ways. The first method consists of pointing the antenna to a position adjacent to a discrete source and tuning the hydrogen radiometer for maximum signal or other distinctive feature of the emission profile. The main lobe of the antenna is then moved "across" the discrete source. For the sources discussed here, an apparent reduction of the hydrogen signal strength is coincident with the transit of the source. The second method involves obtaining 21-cm hydrogen profiles for positions im-

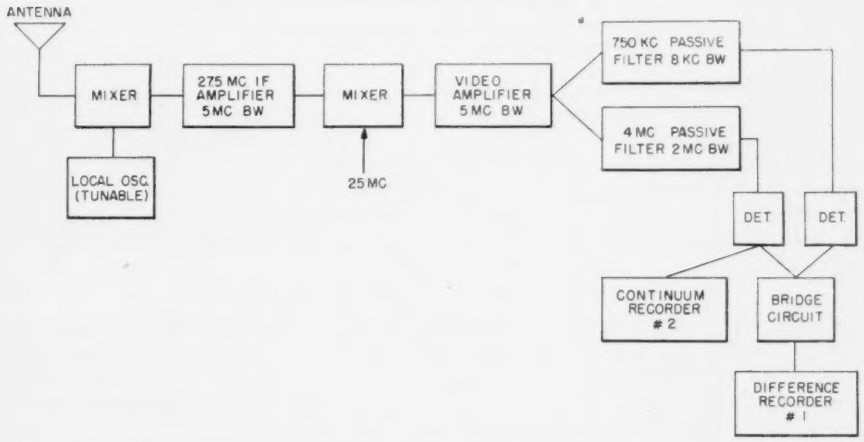

FIG. 3.—Block diagram of the hydrogen radiometer. Recorder No. 2 is used to measure the continuous radiation from discrete sources at a wave length near the hydrogen line (21 cm). The hydrogen-line spectrum is displayed at recorder No. 1.

mediately adjacent to the discrete radio source and a profile for the exact direction which contains the source. The observations show that the 21-cm profile obtained "on" the source is markedly different from the profiles obtained just "off" the source.

We will now derive the equation for a special case which accounts for the modification of a 21-cm profile produced by the presence of a discrete source in the antenna beam, assuming that no hydrogen gas exists beyond the radio source and that the kinetic temperature and optical depth of the hydrogen gas are constant across the beam width. Interstellar hydrogen will absorb energy from the microwave continuum of a radio star. If T_A is the apparent antenna temperature of a discrete source in the vicinity of $\lambda = 21$ cm and if $\tau(\nu)$ is the optical depth of a column of interstellar hydrogen which exists between the antenna and the discrete source, then, over a small range of frequencies dominated by the interstellar hydrogen, the modified apparent antenna temperature of the discrete source becomes $T_A e^{-\tau(\nu)}$. Over the range of frequencies where the hyperfine transitions of H I may occur, the apparent antenna temperature is reduced.

The function of a hydrogen radiometer under these conditions must be determined.

The comparison band in the radiometer, being separated approximately 3.25 Mc from the signal band, never encounters the hydrogen range of frequencies. Therefore, the temperature which excites the comparison band, due to the discrete source, may be regarded as constant and equal to T_A. In a detailed consideration of the radiometer, the contribution of signal- and comparison-band images must be evaluated. This is done in the appendix, where it is shown to be essential that the noise figures of the signal and comparison bands be made equal, to remove instrumental distortion of the profile. If the noise figures of the signal and comparison bands are made equal, the output currents of the radiometer may be considered in terms of apparent antenna temperatures. In our equipment, the noise figures have been made identical within the limit imposed by measurement.[1] The second detector is linear in voltage, and this has been accounted for in the calibrations.

When the antenna is directed toward a discrete source, the contributions to signal and comparison bands, expressed in terms of temperature, are

$$T \text{ signal} = T_A\, e^{-\tau(\nu)} + T_K\,[1 - e^{-\tau(\nu)}]\,, \tag{1}$$

$$T \text{ comparison} = T_A\,. \tag{2}$$

The signal band includes both the modified continuum emission of the discrete source and the interstellar hydrogen emission. T_K is the temperature which characterizes the population distribution over the $F = 1$ and $F = 0$ hyperfine levels. Dicke, Purcell, and Wittke (1954) have shown that this temperature should be equal to the kinetic temperature of the interstellar hydrogen. The quantity displayed by the radiometer (recorder No. 1) is the difference between the signal and comparison bands.[2] Subtracting equation (2) from equation (1), the profile obtained with the antenna pointed at a discrete source is

$$\Delta T'(\nu) = (T_K - T_A)\,[1 - e^{-\tau(\nu)}]\,. \tag{3}$$

The shape of the profile is controlled by $\tau(\nu)$. If T_K is larger than, equal to, or smaller than T_A, there results, with respect to the effective radiometer zero level, an emission line, no line, or an absorption line. Conditions equivalent to these were first discussed by Ewen and Purcell (1951). Van de Hulst *et al.* (1954) corrected profiles obtained toward the galactic center by similar considerations.

To clarify the action of the 21-cm radiometer, a graphical representation of the action of the signal and comparison bands is given. Figure 4 is a schematic representation of the development of the hydrogen profile by the equipment. In Figure 4, four cases are shown, *A* through *D*. In each case, three quantities are displayed. These are, left to right respectively, the temperature contribution in the signal band, the temperature contribution in the comparison band, and their difference, which is the hydrogen profile displayed by the radiometer.

When no hydrogen is present (*A*, Fig. 4) and the antenna is pointed toward a radio source, the output of the signal and comparison bands will each be the apparent antenna temperature of the discrete source. The equipment is so adjusted that the difference between the signal- and comparison-band outputs is zero. This is referred to as the "radiometer zero."

If the antenna is directed toward *H* I gas and if there is no discrete source present in the field of the antenna (*B*, Fig. 4), the signal band will record the hydrogen profile, whereas there will be no temperature contribution to the comparison band. Thus in *B*,

[1] An operational test for identical noise figures in both bands consists of varying the input noise to both bands in an identical fashion and requiring that no radiometer (recorder No. 1) deflection result. Tests demonstrated that if such a deflection exists, it is below the noise level of the output.

[2] The frequency separation between signal and comparison bands is relatively quite small, and T_A may be safely regarded as the apparent antenna temperature for both bands.

the hydrogen profile, $\Delta T(\nu)$, will be the same as the temperature contribution to the signal band, T_S.

In *C*, consider the result of hydrogen gas which lies behind the discrete source. If the angular size of the source is small compared to the antenna beam width, no radiation interaction between the *H* I cloud and the discrete source will be detected. The signal band will record the apparent antenna temperature of the discrete source and also the

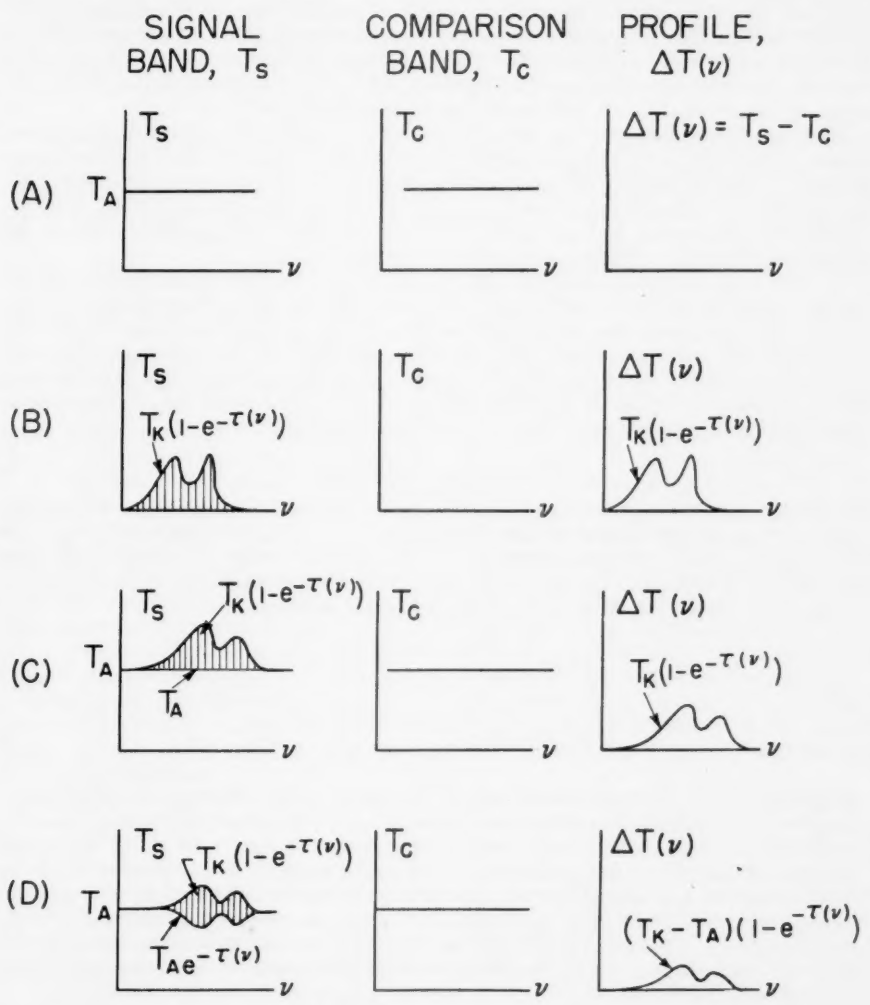

FIG. 4.—Action of the hydrogen radiometer in four cases. In each case the signal band reception, T_s, the comparison band reception, T_c, and $T_s - T_c$, the quantity displayed by the radiometer, which is called $\Delta T(\nu)$, are shown. The four cases display the effect of the antenna pointed toward: *A*, discrete source and no hydrogen; *B*, hydrogen and no discrete source; *C*, hydrogen behind the discrete source; and *D*, hydrogen between the antenna and the discrete source.

H I emission. The comparison band will record the apparent antenna temperature of the discrete source, and the hydrogen profile displayed by the radiometer will appear unreduced in amplitude. Then $\Delta T(\nu)$ will be the same as T_S for the *H* I cloud behind the source.

If an extensive *H* I cloud lies between the observer and the discrete source (*D*, Fig. 4), the signal band records the apparent antenna temperature of the discrete source modified by the optical depth of the hydrogen cloud (*lower curve*) and the superposed hydrogen emission. The comparison band again records the apparent antenna temperature of the discrete source. The difference between the signal and comparison bands now yields a hydrogen profile which is apparently reduced in amplitude. From the construction it is clear that the reduction of the profile amplitude, $\Delta T(\nu)$, is actually due to the attenuated temperature of the discrete source which appears in the signal band.

Equation (3) pertains only to the case for which the source lies behind the gas. If the source is immersed in the gas, two terms must be added to equation (3). The added terms include the contribution of the gas column behind the discrete source and possibly attenuated by it and the "spill-over" contribution from gas existing behind, but not shielded by, the source. For extragalactic sources, we may readily assume that all the effective hydrogen lies between the observer and the source.

Published 21-cm profiles indicate that in most regions the gross characteristics of the profiles change slowly with position. The major features of the profiles occasionally persist for several degrees. As a first approximation, assume that this allows us to take $\tau(\nu)$ as the same for positions separated by a small angle. The degree of separation required will be determined in each case by the angular resolution of the antenna. For the work described here, this angle is approximately 1°. Under this assumption, the hydrogen-emission profile for a position near the discrete source will be given by

$$\Delta T(\nu) = T_K [1 - e^{-\tau(\nu)}] . \tag{4}$$

In writing equation (4), the background continuous radiation temperature of the adjacent position has been neglected in comparison to T_A and T_K. With the assumption that the two gas columns of small angular separation have essentially the same distributions of $\tau(\nu)$ and T_K, equations (3) and (4) become simultaneous equations, which yield values of T_K and $\tau(\nu)$. On the basis of this assumption, the solutions are

$$T_K = \frac{\Delta T(\nu) \cdot T_A}{\Delta T(\nu) - \Delta T'(\nu)} \tag{5}$$

and

$$\tau(\nu) = -\ln\left[1 - \frac{\Delta T(\nu) - \Delta T'(\nu)}{T_A}\right] . \tag{6}$$

All the quantities in the right-hand members of equations (5) and (6) are observed values, and, on the basis of the foregoing assumptions, T_K and $\tau(\nu)$ may be determined directly.

The quantity T_K, which is of considerable interest in the study of the interstellar medium, has previously been estimated in radio astronomy by means of equation (4) for directions where the optical depth is assumed to be large and the background radiation field is negligible. Under these conditions the largest ΔT observed is assumed to be approximately T_K. This provides no information about the variation of T_K from point to point in space. Equation (5), however, for directions which contain discrete sources, yields a value of T_K.

The quantity T_A is a function of the antenna size if the angular size of the source is small compared to the antenna beam width. The relation which governs T_A and the antenna size is

$$T_A = \frac{G}{4\pi} T_B \Omega_S = \frac{A_e T_B \Omega_S}{\lambda^2} , \tag{7}$$

where

G = Antenna gain,
A_e = Acceptance area of antenna,
T_B = Source brightness temperature,
λ = Wave length.
Ω_S = Angular size of the source,

It is interesting to note that the proper choice of antenna size could produce $T_A = T_K$. A measurement of T_A with an antenna of varying dimensions would yield the value of T_K when the emission line "disappeared."

OBSERVATIONAL RESULTS

Peak-intensity sweeps and profiles have been obtained in these absorption investigations. Displayed (Fig. 5) are the variations of the continuum and hydrogen radiations, observed with a 55-kc band width. The maximum of the continuum radiation (*solid curve*) occurs at approximately $l = 327°.8$ and $b = -1°.4$ (Lund pole). A sharp reduction of the 21-cm hydrogen peak brightness (*dotted line*) is coincident with the strong continuum source. Note that the continuum radiation has a broad base as well as a pronounced maximum and includes the area of the sky which contains the galactic center. It is interesting to speculate that the pronounced maximum may be the continuum contribution of the galactic center. At present, however, the only support for this is the agreement of the maximum with the approximate center of the isophotic convergence at longer wave lengths. Additional support is found in the recent detailed survey of this region at 400 Mc by McGee and Bolton (1954). They found a maximum of radiation at 400 Mc in the same direction as the pronounced maximum shown in Figure 5. The positions agree within the observational uncertainties.

An example of the profile measurement of absorption is shown in Figure 6 for the Cassiopeia source. The absorption profile is shown in relation to an emission profile for an adjacent position. Figure 7 is an example of an unreduced scan which shows the raw data obtained by the radio telescope when the Cassiopeia source is kept on the axis of the beam and the hydrogen radiometer scans in frequency. The amplitude of the three sharp absorption lines exceeds the root-mean-square fluctuation of the receiver by better than an order of magnitude. The amplitude of the fluctuations is inversely proportional to the square root of the band width; a band width of 5 kc, used here, causes a receiver output fluctuation greater than that normally encountered in 21-cm research when broader bands have been used. The emission and absorption profiles shown in Figure 5 have been reduced to the local standard of rest by correcting for the earth's motion and a solar motion of 20 km/sec directed toward galactic longitude 23°.5 and galactic latitude +21°.6 (Lund pole).

Van de Hulst *et al.* (1954) have identified the emission maxima (Fig. 6) with the spiral-arm structure in our Galaxy. Both spiral arms are found here to exhibit the absorption effect. Accordingly, we may take the minimum distance to the Cassiopeia source as that of the second spiral arm, or approximately 3.2 kpc on the basis of a galactic-rotation analysis. If we accept this measure of the distance and consider the angular dimension of about 6'.3 of arc stated by Baade and Minkowski (1954), then the emitting filaments of the source must be spread over a region at least 6 pc in diameter.

The importance of the absorption profile is its shape. From the development leading to equation (3), we expect the profile obtained for the direction containing the Cassiopeia source to resemble in shape the profile obtained from adjacent positions. However, the observed profile bears little relation to the shape of the emission profile for the adjacent position. In addition, a second difficulty is encountered. In equation (3) the maximum depression below the radiometer zero in an absorption profile is given by $T_K - T_A$. One cannot safely assume that T_K is the same throughout the Galaxy, but the

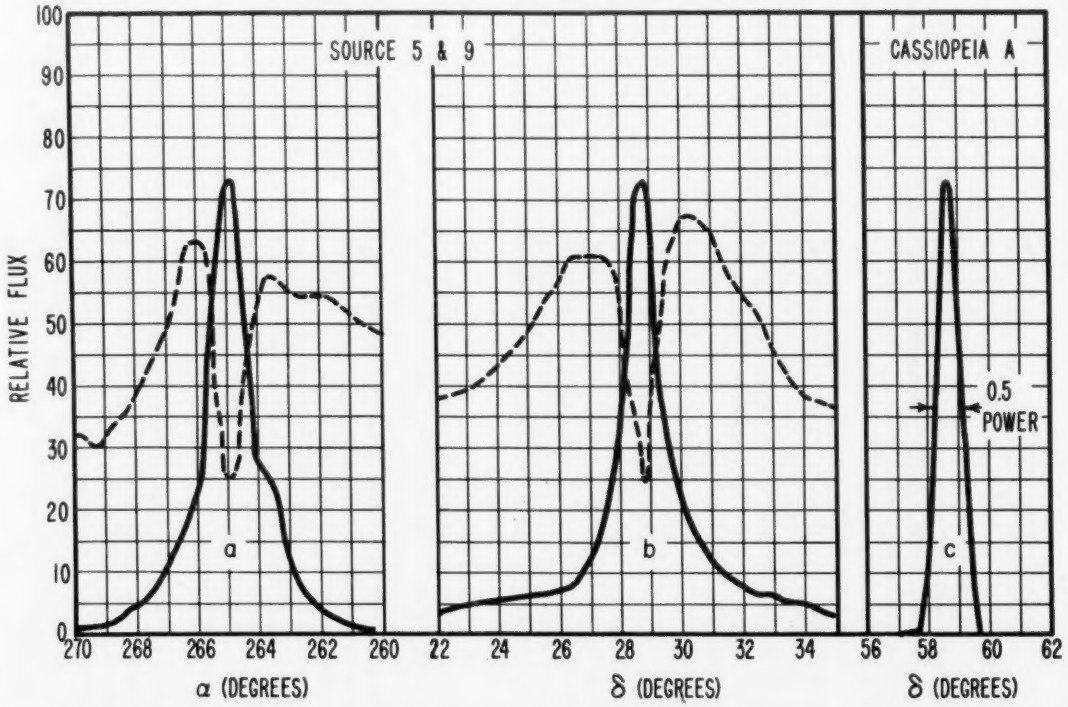

FIG. 5.—Absorption measurement obtained by movement of the antenna in right ascension and declination. The solid and dotted lines represent, respectively, 21-cm continuum and 21-cm hydrogen-line radiations. The curves may be regarded as drift-curve peak intensities. The pronounced maximum of the continuum emission (*solid curve*) is located at galactic longitude 327°.8 and galactic latitude −1°.4 (Lund Pole). This source is called NRL No. 5 and Sagittarius A. The broad continuum radiation below the peak is called source No. 9. The approximate antenna pattern of the 50-foot antenna at 21 cm is shown on the right and was obtained by drift-curves of the continuous radiation of the source Cassiopeia A.

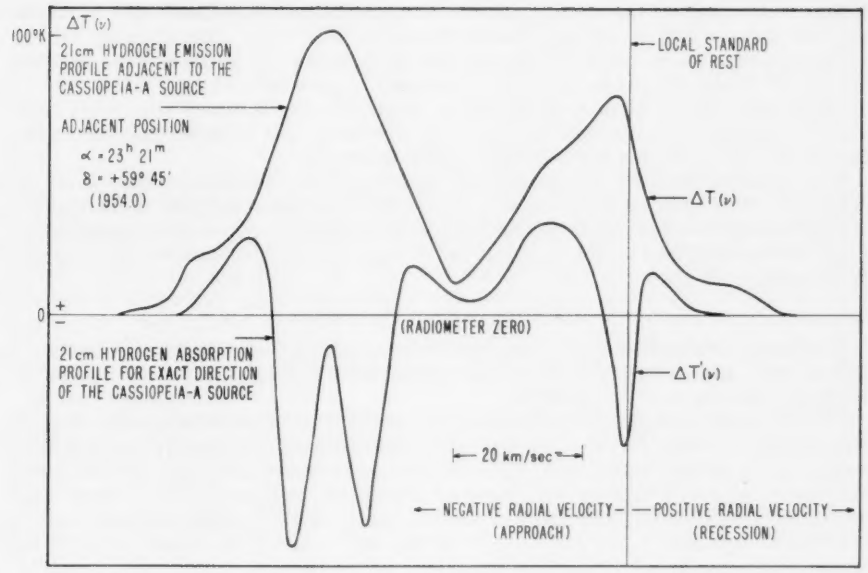

FIG. 6.—Profile type of absorption measurement. Two 21-cm hydrogen-line profiles are shown, one for the direction of the Cassiopeia A source and one for a comparison position approximately 1° away.

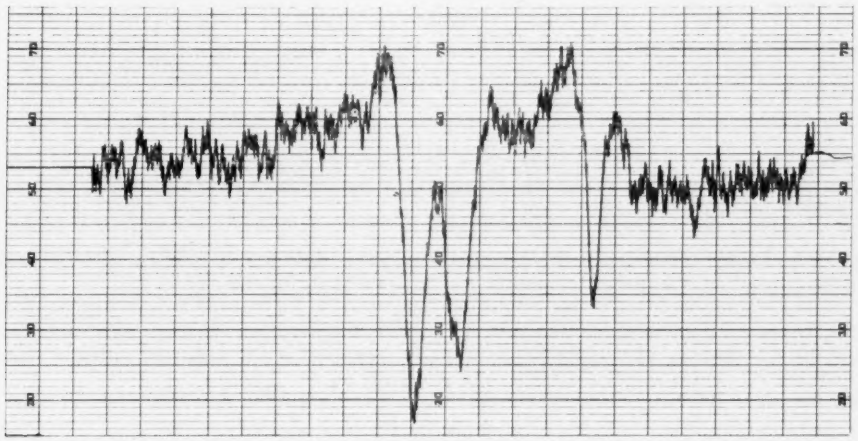

FIG. 7.—Example of an unreduced 21-cm profile for the direction of the Cassiopeia A source. Frequency is the abscissa, and $\Delta T(\nu)$ is the ordinate. The "radiometer zero" changes approximately linearly from a reading of 53 on the left to 51 on the right.

regions which produce the major emission are apparently characterized by a T_K somewhat in excess of 100° K. For the Cassiopeia source, with T_A of approximately 115° K, the depression allowed below radiometer zero by equation (3) would then be approximately 15° or less. However, the observed absorption goes 80° and more below the "radiometer zero." Thus, both in shape and in amplitude, the observed absorption-curve deviates sharply from the expected behavior. However, this behavior may be readily explained if the hydrogen is considered to exist in clouds.

It is apparent that if the distribution of hydrogen is in individual clouds or in condensations in a more tenuous medium, equation (3) is not applicable. This equation applies strictly to a continuous gas and should be considered only as an approximation. Also, the development leading to equation (6) must be reconsidered for the case of a nonhomogeneous gas.

THE CLOUD MODEL ABSORPTION

If, instead of continuous gas, the interstellar medium is composed of a system of clouds, or perhaps condensation in a fluctuating density field of H I gas, then the absorption equation must be modified.

We shall take a simple case to illustrate the modification of the development. Suppose that a single H I cloud, i, lies along the line of sight between the observer and a discrete source, and a second cloud, j, lies within the antenna reception beam but not in line with the discrete source. This situation is shown schematically in Figure 8. The antenna has a reception beam of solid angle Ω_B. The discrete source and H I clouds are considered to subtend solid angles Ω_S, Ω_i, and Ω_j. The optical depths of the H I clouds are $\tau_i(\nu)$ and

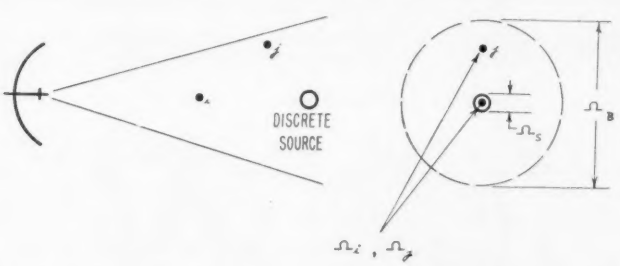

FIG. 8.—Schematic representation of the antenna beam directed toward a discrete source. Two ideal H I clouds, i and j, are present. The projected view, seen by the observer located at the antenna, is given at the right.

$\tau_j(\nu)$, and these quantities include a gross frequency shift due to galactic rotation and random motion. A uniform temperature, T_K, is assumed for the clouds.

The discrete source has a true brightness temperature, T_B, but the radio telescope does not measure T_B unless the antenna beam angle is smaller than the angle subtended by the discrete source. The temperature actually measured is the apparent antenna temperature T_A, which may be written approximately as

$$T_A = T_B \frac{\Omega_S}{\Omega_B}. \tag{8}$$

For the conditions shown in Figure 8, we shall write down the temperature contributions to the signal and comparison bands and take their difference. To simplify the development, we take $\Omega_i < \Omega_S$, but in the general case this is not a limitation. The temperature contribution to the comparison band is

$$T_C = T_A = T_B \frac{\Omega_S}{\Omega_B}, \tag{9}$$

and the signal-band contribution is

$$T_S = T_B \frac{\Omega_S - \Omega_i}{\Omega_B} + T_B \frac{\Omega_i}{\Omega_B} e^{-\tau_i(\nu)} + T_K [1 - e^{-\tau_i(\nu)}] \frac{\Omega_i}{\Omega_B} + T_K [1 - e^{-\tau_j(\nu)}] \frac{\Omega_j}{\Omega_B} G_j(\theta) . \quad (10)$$

The first term in equation (10) is effectively the contribution to the apparent antenna temperature due to that part of the discrete source which is not shielded by the i cloud. The contribution to the apparent antenna temperature due to the discrete source, which includes the opacity of the i cloud, is contained in the second term of equation (10). Note that, in the absence of the H I cloud, the first two terms reduce to T_A, which is simply the apparent antenna temperature due to the discrete source. The third and fourth terms are, respectively, the observed emissions of the i and j clouds. The antenna gain function, $G(\theta)$, is normalized to unity on the main axis of the antenna reception beam and therefore has been omitted for the i cloud. Anywhere except on the main axis of the antenna beam, $G(\theta) < 1$.

The difference between the signal- and comparison-band temperature contributions is the quantity displaced by the output of the radiometer. Subtracting the comparison-band contribution, T_C, from that of the signal band, T_S, we find:

$$\Delta T'(\nu) = \left(T_K \frac{\Omega_i}{\Omega_B} - T_A \frac{\Omega_i}{\Omega_S}\right) [1 - e^{-\tau_i(\nu)}] + T_K [1 - e^{-\tau_j(\nu)}] \frac{\Omega_j}{\Omega_B} G_j(\theta) . \quad (11)$$

We may now write down an approximate expression for the 21-cm hydrogen-line profile on the basis of a cloud model and include the effect of the discrete source. If we place the discrete source beyond the H I clouds, then the profile may be written as

$$\Delta T'(\nu) = \sum_j T_K [1 - e^{-\tau_j(\nu)}] \frac{\Omega_j}{\Omega_B} G_j(\theta) + \sum_i \left(T_K \frac{\Omega_i}{\Omega_B} - T_A \frac{\Omega_i}{\Omega_S}\right) [1 - e^{-\tau_i(\nu)}] . \quad (12)$$

In the last equation, j refers to clouds which do not fall within the cone subtended by the discrete source, and i refers to clouds which do. Equation (12) is written with the understanding that if two or more clouds coincide in apparent position and if they also have identical optical-depth distributions for the observer, then the effective optical depth of the two or more clouds must be used in computing the emission rather than the sum of the individual emissions. There is, of course, the possibility that the individual cloud temperatures are different and that cloud-to-cloud interactions may occur. However, equation (12) is written with the assumption that all the clouds have the same kinetic temperature.

In equation (12) we find the absorption effect in the second term dominated in shape by $\tau_i(\nu)$, which may differ sharply from the shape of 21-cm emission profiles from near-by regions. In addition to the shape of the absorption profile, a second point concerning the amplitude is evident in equation (12). The beam width of the 50-foot NRL antenna at $\lambda = 21$ cm is approximately 1°. If we consider the Cassiopeia source to be approximately 6′ of arc in diameter, then

$$\frac{\Omega_i}{\Omega_B} \ll \frac{\Omega_i}{\Omega_S} . \quad (13)$$

Under these conditions, the observed emission term for the H I clouds which "cover" the discrete source is only 1 per cent as effective as the observed absorption.

We may rewrite equation (12) as follows:

$$\Delta T'(\nu) = \sum_{i,j} T_K [1 - e^{-\tau_{i,j}(\nu)}] \frac{\Omega_{i,j}}{\Omega_B} G_{i,j}(\theta) - \sum_i T_A [1 - e^{-\tau_i(\nu)}] \frac{\Omega_i}{\Omega_S} , \quad (14)$$

where in the first term the summation is taken over all clouds i and j. The first term represents the total hydrogen emission in the entire antenna beam in the direction which contains the discrete source and may be taken as a properly determined mean of 21-cm profiles obtained in near-by comparison regions. The second term gives the absorption of the radio star continuum produced by the H I clouds which lie between the observer and the discrete source. In the data analysis the first term of equation (14) is replaced by the equivalent mean profile, which is determined from the comparison-field profiles, and the quantity is called $\overline{\Delta T(\nu)}$. Also we replace the second term by

$$-T_A\,[1 - e^{-\tau_s(\nu)}]\,,$$

where $\tau_s(\nu)$ is the H I optical depth between the observer and the discrete source and is contained within the solid angle Ω_S. Equation (14) now becomes

$$\Delta T'(\nu) = \overline{\Delta T(\nu)} - T_A\,[1 - e^{-\tau_s(\nu)}]\,. \tag{15}$$

We may solve equation (15) for $\tau_s(\nu)$, since all other quantities are available from our observational data,

$$\tau_s(\nu) = -\ln\left[1 - \frac{\overline{\Delta T(\nu)} - \Delta T'(\nu)}{T_A}\right]. \tag{16}$$

In equation (15), gas which lies "behind" the discrete source has been neglected. However, Lilley (1955) has shown that when the H I gas behind the discrete source is included, the resulting expression is equivalent to equation (15), provided that $\Omega_S \ll \Omega_B$ or that the discrete source is thin.

TABLE 2

THE OBSERVATIONAL AND DERIVED DATA

Radial Velocity of Absorption Component (Km/Sec)	$\overline{\Delta T(\nu)} - \Delta T'(\nu)$	Maximum Optical Depth of Component $\tau_s(\nu)_{max}$	R.m.s. Random Velocity, η (Km/Sec)
− 1.0	71.5	0.96	1.7
−38.5	89.4	1.47	2.3
−48.6	100	2.04	1.8

While the development has shown that the gas along the cone, Ω_S, of optical depth $\tau_s(\nu)$, is fully effective in absorbing the observed continuum radiation from the discrete source, note that the H I emission contribution from this same cone is only a small part of $\overline{\Delta T(\nu)}$.

The absorption profile obtained for the Cassiopeia source shows three deep minima, which are produced by three small condensations of H I along a line to the discrete source. The solution of equation (16) for these three clouds is of interest, since these features are the most narrow yet encountered in 21-cm radio astronomy. Table 2 gives the observed and derived data for the three absorption components in the Cassiopeia spectrum. In Table 2 the first column gives the radial velocity of the absorption component reduced to the local standard of rest. The second column gives the maximum observed total absorption in the three components, expressed in terms of the difference between the expected profile and the observed profile for the Cassiopeia A source. The third column gives the maximum optical depth $\tau_s(\nu)_{max}$ in the center of the absorption peak computed with the aid of equation (16), and the fourth column gives the r.m.s.

random velocity, η, based on an assumed Gaussian distribution. Here η is taken as half the total width of $\tau_s(v)$ at 0.606 $\tau_s(v)_{max}$. This quantity is given in kilometers per second and has been corrected for the effects of a 5-kc band width.

The absorption results in Table 2 and the sizes of the *H* I clouds needed to "cover" the discrete source permit a rough determination of the densities of the clouds. The distance to the absorbing clouds may be taken as the distance to the spiral arm whose emission profile covers the radial-velocity range of the absorption component. It is possible that all three clouds are actually near by and that two happen to have peculiar large negative radial velocities which are the same as the galactic-rotation shift of the Perseus arm. However, this requires a special explanation to maintain the Cassiopeia radio source in the near arm. Neglecting the effects of possible peculiar velocities and using the distance criterion mentioned earlier, we place one of the absorbing clouds in the Orion arm and the other two in the Perseus arm. If the Cassiopeia A source lies beyond the absorbing clouds, it must be at a distance of at least 3000 parsecs and have a diameter of 5 or 6 pc. The size of the absorbing *H* I cloud must at least "cover" the discrete source in projection. They can, of course, be larger.

We have used an angular diameter for the Cassiopeia source of approximately 6′ of arc, following the optical results of Baade and Minkowski (1954) and the radio results of Smith (1952) and Hanbury-Brown (1954). An *H* I cloud which just "covers" the Cassiopeia source at a distance of the second spiral arm would have to be at least 5–6 pc in diameter. When one has the optical-depth distribution for the *H* I, an estimate of the total number of atoms along a column of 1 cm^2 cross-section may be obtained (see, e.g., van de Hulst *et al.* 1954). We find 2–4 $\times$ 10^{21} atoms through the cloud along a 1-cm^2 column, leading to number densities in the clouds of 100–200 *H* atoms/cm^3. If the clouds are larger than assumed, the number densities would be correspondingly reduced.

Finally, it is interesting to note that the absorption measures depend upon the angular diameter of the Cassiopeia source, approximately 5′–6′ of arc. An antenna 500 feet in diameter would be required to observe *H* I cloud emission alone with comparable resolution. If such an antenna existed, we might expect to see 21-cm emission profiles with very sharp maxima similar to those now seen only in absorption.

APPENDIX

Absorption of 21-Cm Radiation by Interstellar Hydrogen

In order to interpret properly the simultaneous effect of continuum radiation and line radiation on the radiometer, it is necessary to develop the expressions which relate the output indications to the received radiation. The radiometer employed (Fig. 3) is of the d.c. comparison type first described by Selove (1954). In the development here, expressions will be derived for the two outputs of the receiver, ΔI_C and I_H. The quantity ΔI_C is the increment in the output current of the comparison channel caused by radiation from a discrete source in the antenna beam. The quantity I_H is the difference between the output currents of the comparison and signal bands and is shown to be a function of both the intensity of the hydrogen radiation and the temperature of the discrete source.

No image rejection is employed, so that there are actually four acceptance bands—two broad and two narrow—present at the antenna terminals. A diagrammatic representation of the acceptance bands is shown in Figure 9; bands c_1, s_1, s_2, and c_2 receive radiation from any continuous source present in the antenna beam. Band s_2 receives, in addition, any hydrogen radiation present. Noise-power output is proportional to the second detector current in a receiver with a square-law characteristic. The results of the following derivation made on the assumption that the receiver has a square-law response hold equally well for a receiver with any other known detector characteristic.

The expressions for the second detector currents in the comparison and signal bands when the receiver is pointed at the cold sky are (Friis 1944)

$$I_C = I_{c1} + I_{c2} = G_{c1}B_{c1}\,(F'_{c1} - 1)\,T_0 + G_{c2}B_{c2}\,(F'_{c2} - 1)\,T_0\,, \tag{A1}$$

$$I_S = I_{s1} + I_{s2} = G_{s1}B_{s1}\,(F'_{s1} - 1)\,T_0 + G_{s2}B_{s2}\,(F'_{s2} - 1)\,T_0\,, \tag{A2}$$

where I_{c1}, I_{c2}, I_{s1}, and I_{s2} are the current contributions of the respective bands; B_{c1}, B_{c2}, B_{s1}, and B_{s2} are the band widths of the respective bands; G_{c1}, G_{c2}, G_{s1}, and G_{s2} are the gain factors of the respective bands (these terms may be considered to include K, Boltzmann's constant); and F'_{c1}, F'_{c2}, F'_{s1}, and F'_{s2} are the noise figures of each band defined as half the usual noise figure (Friis 1944), since all open bands receive radiation. The term $(F' - 1)T_0$ gives the effective receiver input temperature referred to the antenna when the antenna is pointed at the cold sky. Under actual operating conditions great care is taken to insure that $B_{c1} = B_{c2}$, $G_{c1} = G_{c2}$, $B_{s1} = B_{s2}$, $G_{s1} = G_{s2}$, and $F'_{c1} = F'_{c2} = F'_{s1} = F'_{s2} = F'$.

If it is stipulated that I_C equals I_S (balanced condition), a gain band-width factor A may be defined so that $A = G_cB_c = G_sB_s$. Equations (A1) and (A2) now become

$$I_C = A\,(F'_{c1} - 1)\,T_0 + A\,(F'_{c2} - 1)\,T_0\,, \tag{A3}$$

$$I_S = A\,(F'_{s1} - 1)\,T_0 + A\,(F'_{s2} - 1)\,T_0\,. \tag{A4}$$

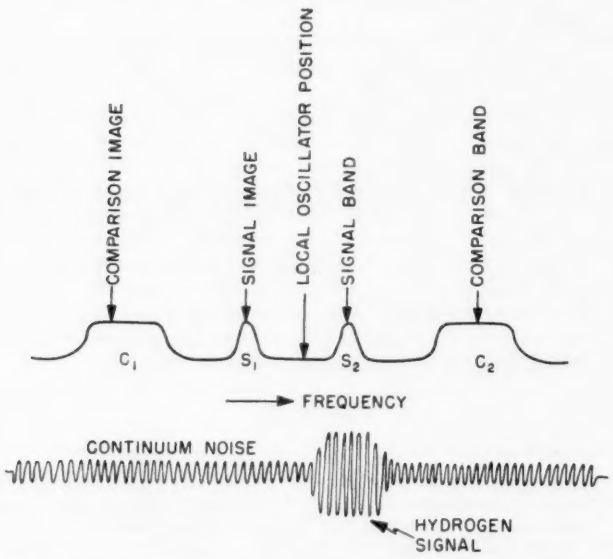

FIG. 9.—The pass bands of the 21-cm hydrogen radiometer are shown schematically and not to scale; the signal and comparison bands have images symmetrically positioned in frequency below the local oscillator frequency. The "noise" shown below the pass bands represents that which results when both a radio star and hydrogen gas are in the antenna beam.

Assume that each band receives energy from a source at some temperature over and above $(F' - 1)T_0$ and further replace $(F' - 1)T_0$ by T_R, then

$$I_C = A\,(T_R + T_{c1}) + A\,(T_R + T_{c2})\,, \tag{A5}$$

$$I_S = A\,(T_R + T_{s1}) + A\,(T_R + T_{s2})\,, \tag{A6}$$

where T_{c1}, T_{c2}, T_{s1}, and T_{s2} are the apparent antenna temperatures of the received energy at the frequencies of the respective bands. Because of the nature of the sources and because the frequencies of c_1 and c_2 are relatively close together, T_{c1} and T_{c2} are, in general, very nearly equal,

so that $I_C = 2A(T_R + T_C)$. In operation, the quantity which is recorded or displayed is not I_C but rather ΔI_C, the change or increase in I_C over the cold-sky value:

$$\begin{aligned} \Delta I_C &= 2A(T_R + T_C) - 2AT_R \\ &= 2AT_C . \end{aligned} \tag{A7}$$

Considering equation (A6) in connection with Figure 9, it is seen that continuum radiation (T_A) enters all bands, so that T_{s1} may be replaced by T_c. Band s_2, however, receives energy from both the continuum and the hydrogen radiation and must be retained as a separate term. Equation (A6) may then be written

$$I_S = A(2T_R + T_C + T_{s2}) . \tag{A8}$$

In hydrogen measurements, the quantity displayed is $I_H = I_s - I_c$, or

$$I_H = A(T_{s2} - T_C) . \tag{A9}$$

Writing the proper expression for T_{s2} for the case where there is a uniform hydrogen column of optical depth τ and hydrogen temperature T_K between the continuum source and the receiver, we have

$$T_{s2} = T_C e^{-\tau} + T_K(1 - e^{-\tau}) . \tag{A10}$$

Substituting equation (A10) in equation (A9), we obtain

$$I_H = A(T_K - T_C)(1 - e^{-\tau}) . \tag{A11}$$

The quantity T_C used here is equivalent to T_A, which was employed earlier in the text.

Comparing equation (A7) with equation (A11), it is seen that a given change in continuum temperature, T_C, causes twice the change in ΔI_C that the same change in hydrogen temperature causes in I_H. This requires the introduction of a factor of 2 in calibrating the continuum recorder but does not alter the development leading to equation (A11).

REFERENCES

Baade, W., and Minkowski, R. 1954, *Ap. J.*, **119**, 206.
Dicke, R. H., Purcell, E. M., and Wittke, J. 1954, *J. Geophys. Res.*, **59**, 191.
Friis, H. T. 1944, *Proc. I.R.E.*, **32**, 419.
Hagen, J. P., and McClain, E. F. 1954*a*, *Ap. J.*, **120**, 368.
———. 1954*b*, paper read at joint meeting of U.R.S.I., I.R.E., and A.G.U. (abstr.) (Washington, D.C.: U.R.S.I, May, 1954).
Hanbury-Brown, R. 1954, *J. Geophys. Res.*, **59**, 150.
Hulst, H. C. van de, Oort, J. H., and Muller, C. A. 1954, *B.A.N.*, **12**, No. 452, 117.
Lilley, A. E. 1955, *A.J.*, **60**, 167.
McGee, R. X., and Bolton, J. G. 1954, *Nature*, **173**, 985.
Mumford, W. W. 1949, *Bell System Tech. J.*, **28**, 608.
Purcell, E. M., and Ewen, H. I. 1951, *Nature*, **168**, 356.
Selove, W. 1954, *Rev. Sci. Inst.*, **25**, 120.
Smith, F. G. 1952, *Nature*, **170**, 1065.
Williams, D. R. W., and Davies, R. D. 1954, *Nature*, **173**, 1182.

AN APPROXIMATE DISTANCE DETERMINATION FOR RADIO SOURCE SAGITTARIUS A

EDWARD F. MCCLAIN
Radio Astronomy Branch, Naval Research Laboratory, Washington, D.C.
Received July 6, 1955

ABSTRACT

Radio source Sagittarius A (IAU 17S2A) lies very close to the predicted center of the Galaxy. Hydrogen absorption measurements at a wave length of 21 cm reveal that hydrogen gas is present between the sun and the source as well as beyond the source. An independent distance scale has been obtained by assuming a constant thickness for the hydrogen gas and by relating the angular extent of the gas to its radial velocity. Using a thickness of 240 pc for the Galaxy, the radio source is found to have a probable distance of 3 or 4 kpc. Source 17S2A is therefore thought to be complex and to consist of a rather intense discrete source superimposed on the broad central galactic background.

The 21-cm radiation from interstellar neutral hydrogen has been extensively employed to measure the gross characteristics of the Galaxy. More recently the absorbing property of hydrogen in conjunction with the continuum radiation of discrete radio sources has revealed previously undetected fine structure in the hydrogen itself. The absorption was first observed at the Naval Research Laboratory by Hagen and McClain (1954). Williams and Davis (1954) used the absorption effect in an attempt to measure the distance to the discrete sources Cassiopeia and Cygnus. More recently, Hagen, Lilley, and McClain (1954), using equipment of high resolution, have detected very sharp absorption peaks in the radiation from Cassiopeia. In this paper the absorption technique is applied to that portion of the sky containing the galactic center.

EQUIPMENT

The equipment used was the Naval Research Laboratory 50-foot parabolic antenna. The beam width is 55′ of arc at 1420 Mc. The receiver is of the d.c. comparison type, with a comparison band width of 2 Mc and a signal band width of 5 kc. The signal band width of 5 kc corresponds to a radial-velocity half-width of 1 km/sec. With such narrow band widths, the uncertainty in any one measurement is of the order of $\pm 3°$ K, ± 5 per cent of the indicated temperature. In order to insure stability for periods up to 1 hour, all power supplies are referenced to batteries, and all parts of the radiometer are temperature-controlled. The output of the comparison band is displayed as the temperature of the discrete radio source, while the difference between the comparison and signal bands is displayed as the hydrogen profile.

Figure 1 is a photograph of a scan before reduction. The base line and mean curve have been drawn in. The position of the base line was determined by cold-sky checks before and after the scan. A small amount of radar interference is present in the left-hand wing, giving rise to a wider trace. The continuum recorder is operated at all times as a check on interference. The flutter is seen to be about $\pm 5°$ peak to peak in the absence of interference, and it is felt that the mean curve as drawn has a probable error of approximately 3° K.

Figure 2 is a photograph of a work sheet showing the reduced data from two scans at the same position. The maximum deviation of either curve from the mean is 3° K.

A second factor affecting the accuracy of the data is the noise factor of the receiver. Variations in noise factor and gain are checked periodically by means of continuum measurements on convenient radio sources. Such variations are found to represent errors no greater than 5 per cent of the indicated temperature. A total of forty-five frequency and angular scans was used in obtaining the data for this report.

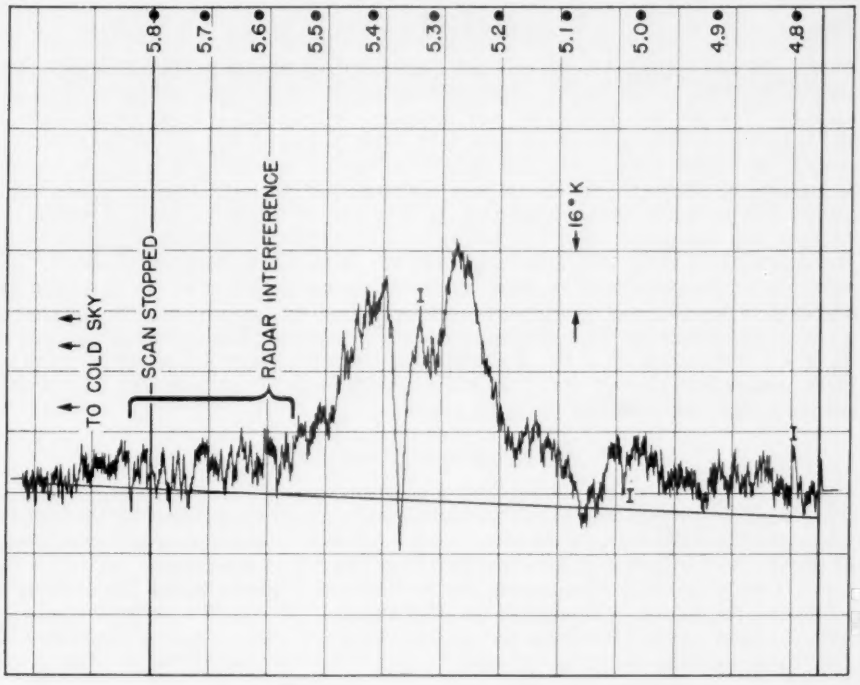

FIG. 1.—An example of an unreduced scan taken at the position of the Sagittarius A source. The zero line has been drawn in. The 100-kc frequency markers may be seen along the top of the chart. A cold-sky zero check is shown at the extreme left. The entire scan requires about 65 minutes. The zero line changes approximately 8° from left to right as a function of receiver tuning.

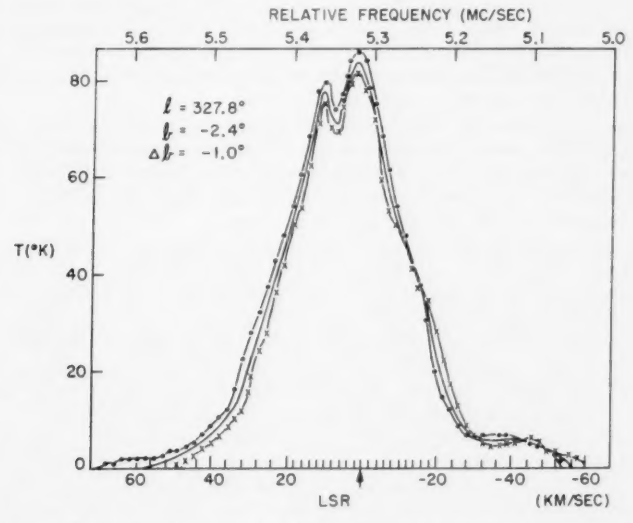

FIG. 2.—A copy of a work sheet showing the reduced data taken from two scans at the same position. In computing the local standard of rest, the solar vector is assumed to be 20 km/sec directed toward $l = 23°.5$, $b = +21°.6$. The two curves have a maximum deviation from the mean of 3° K.

If a properly adjusted receiver of the type described here is pointed at a radio star with no hydrogen in the reception beam, no indication will be registered on the hydrogen recorder. The continuum recorder will, however, indicate the antenna temperature of the radio source. If a smooth hydrogen cloud, large compared with the antenna beam, is present behind the radio source and the optical depth of the source is negligible, the antenna may be alternately moved to positions on and off the radio source with no effect on the indicated hydrogen temperature. If, however, hydrogen is present between the antenna and the radio source, that hydrogen lying within the solid angle subtended by the source will be effective in absorbing continuum radiation emitted by the source. This reduction of the continuum radiation at the resonance frequency of the hydrogen gas will cause a depression of the signal-band temperature and, in turn, will be indicated as a lower temperature by the hydrogen recorder. The amount of this reduction is equal to $T_A(1 - e^{-\tau_1(\nu)})$, where T_A is the temperature of the radio source as indicated by the receiver comparison channel and $\tau_1(\nu)$ is the optical depth of the hydrogen lying within the solid angle subtended by the radio source.

THE ABSORPTION MEASUREMENTS

Lilley (1954) has introduced the concept of "expected profile" and "observed profile." The "expected profile," $\overline{\Delta T(\nu)}$, is that profile which would be obtained for the position containing the radio source if the source were not present and may be taken as the mean of profiles from adjacent comparison positions. The "observed profile," $\Delta T'(\nu)$, is the actual profile obtained by scanning the receiver in frequency when the antenna is pointed at the source. By assuming the solid angle of the source to be small compared with the solid angle of the beam and by neglecting the optical depth of the source, he derives an equation for $\tau_1(\nu)$, the optical depth of the hydrogen lying in front of the source:

$$\tau_1(\nu) = -\ln\left(1 - \frac{\overline{\Delta T(\nu)} - \Delta T'(\nu)}{T_A}\right). \tag{1}$$

As previously stated, T_A is the indicated temperature of the radio source. It will be noted that if $\overline{\Delta T(\nu)}$ and $\Delta T'(\nu)$ are equal, $\tau_1(\nu)$ will be zero, and the gas responsible for $\Delta T'(\nu)$ must lie beyond the radio source. If, within the uncertainty of the measurements, $\overline{\Delta T(\nu)}$ and $\Delta T'(\nu)$ are equal for a part of a profile and unequal for the remainder, one is permitted to associate radial velocities and relative distance positions with the gas beyond the source and the gas between source and observer.

The foregoing technique has been applied to radio source IAU 17S2A (NRL No. 5, Sagittarius A, BSS68), which has been suggested as being associated with the galactic center (McGee and Bolton 1954). For the present it is assumed that this source is a single source, and the optical depths are derived on that basis. In addition, it is assumed that T_K, the temperature of the hydrogen, is constant.

Two methods were employed in the determination of the expected profile. The first method consisted of making a number of comparison profiles at positions around the source but separated from the source by from 2° to 4°. These profiles were then averaged, and a mean profile obtained which was characteristic of the region. In view of the rapid changes in hydrogen distribution with position which are present in the region surrounding the galactic center, a second method of evaluating the expected profile was employed. This method is illustrated in Figure 3. Shown at the top of the figure is the observed profile, and at the bottom representative declination sweeps made with the receiver tuned to different radial velocities (frequencies). Declination sweeps made in this way actually represent common radial-velocity points on an infinite number of profiles and are believed to be a more accurate and convenient way of estimating the expected profile. Two of the illustrated declination sweeps show marked reductions in temperature at the po-

sition of IAU 17S2A, and one shows no reduction. In the case of all declination sweeps an attempt was made to estimate (*dashed line*) what the temperature would have been if the radio source had not been present. These values were then used to correct the mean profile obtained from the comparison positions. Declination sweeps were made at maxima, minima, and points of inflection of the observed profile. The resulting expected profile and the observed profile are shown in Figure 4. It is seen that absorption occurs over a radial-velocity range extending from +30 to −16 km/sec.

An interesting feature of the expected profile is the reduction in temperature at +5.5

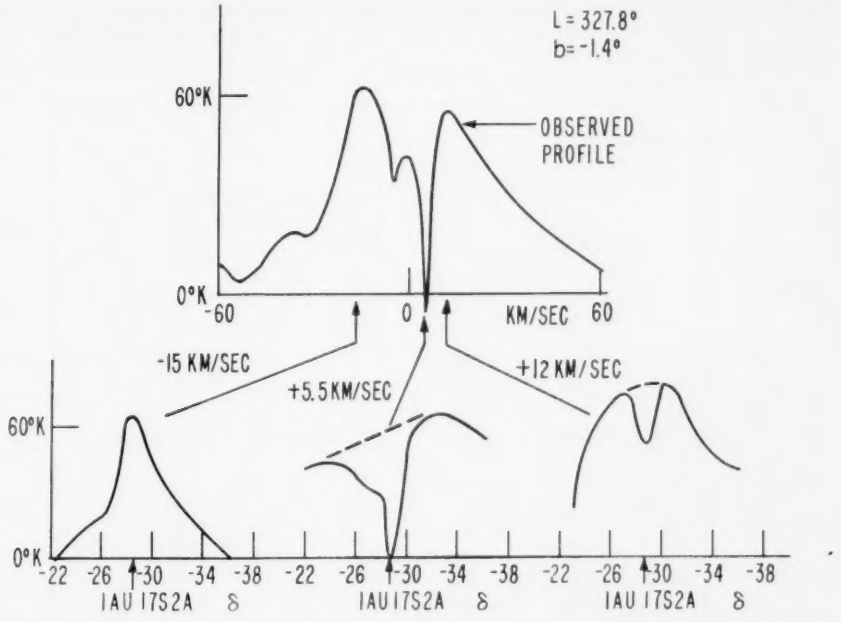

FIG. 3.—At the top is shown the profile obtained at the position of Sagittarius A. At the bottom are shown representative declination sweeps made with the receiver tuned to different radial velocities. Two of the declination sweeps show marked reductions at the position of the source, and one shows no reduction. An attempt was made to estimate (*dashed line*) what the temperature would have been in the absence of the source.

km/sec. Heeschen (1954) noted this feature in all profiles of this region and suggested the possibility that mass motions or, alternately, near-by cool gas may be responsible for the lower emission at this velocity. A third possibility, that the intervening gas absorbs the continuum background, has been investigated. It has been found that notch depths as great as 40° K in the surrounding profiles correspond to only 12° or 15° K of continuum. It would therefore appear that absorption of continuum background radiation by the gas could not account for the total depth of the notch. The present measurements reveal that the observed profile goes 6°–8° below radiometer zero at +5.5 km/sec, with an estimated value of η for the absorbing gas of about 1 km/sec. This is believed to be the sharpest hydrogen feature noted to date. The fact that the profile goes below radiometer zero is absolute proof that an absorption mechanism is operating at +5.5 km/sec. In addition, the magnitude of the absorption and the small width of the line

imply low temperatures. An attempt is being made to arrive at a more precise shape for the observed profile in the range -5 to $+15$ km/sec. It is not expected that this will change the velocity range over which the absorption occurs.

Figure 5 illustrates the velocity dependence of the computed optical depth $\tau_1(\nu)$. The value of $\tau_1(\nu)$ is seen to be zero for velocities greater than -16 and $+30$ km/sec, indicating that gas responsible for emission in this range is probably beyond the radio source. Optical depths derived from the absorption occur over the range from -16 to $+30$ km/sec, indicating that the gas with velocities in this range is present between the observer and the source. Optical depths for the gas in front of the source computed by means of equation (1) reach peak values as high as 2.0 at a radial velocity of $+5.5$ km/sec It should be noted that the effect of self-absorption on $\tau_1(\nu)$ has been accounted for by the manner in which $\overline{\Delta T}(\nu)$ has been derived. The value of $\tau_1(\nu)$ as computed is the

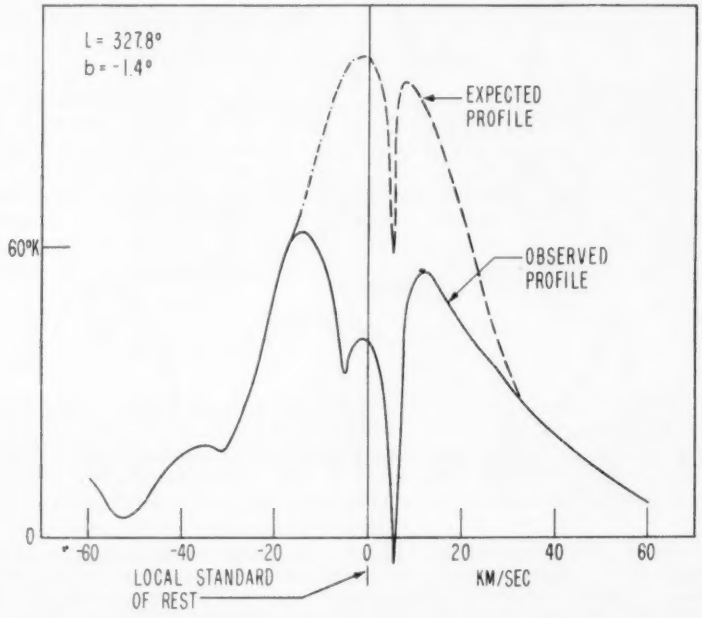

FIG. 4.—The observed profile (*solid curve*) and the expected profile (*dashed curve*). The absorption is seen to occur over the velocity range -16 to $+30$ km/sec.

total value between the observer and the radio source. An inspection of the equation used for determining optical depths will also reveal that small measurement uncertainties will result in rather large uncertainties in the computed optical depth when the optical depth is large. For the case of IAU 17S2A, with an indicated temperature of 73° K, optical depths higher than 2 must be regarded as tentative.

The secondary maximum at -40 km/sec in the expected and observed profiles corresponds to a ridge of high negative velocities noted by Kwee, Muller, and Westerhout (1954). This ridge extends in longitude from approximately $l = 321°$ to $l = 330°$ and is confined to a narrow band about 1°.5 below the galactic plane. The present measurement would indicate that at $l = 327°.8$ the gas in this ridge is beyond the radio source.

An alternative interpretation, that the nonabsorbing gas lies in the side of the antenna

beam when the beam is centered on the source and hence has an indeterminate relative distance, is improbable for two reasons. First, angular sweeps made with the receiver tuned to nonabsorbing frequencies indicate that, while the gas is of limited angular extent, the angular size is several beam widths centered very close to the source. For example, the −15-km/sec declination sweep shown at the bottom of Figure 1 reveals a half-temperature angular width for the gas of 4°36′, while the antenna beam half-power width is only 55′ of arc. The peak of the emission occurs within 15′ of arc of the position of the radio source. Thus the gas undoubtedly does fill the antenna beam. Second, if only a portion of the beam were filled with a small gas cloud, the emission intensity would suffer by the radio of the solid angle of the beam to the solid angle of the gas cloud. The

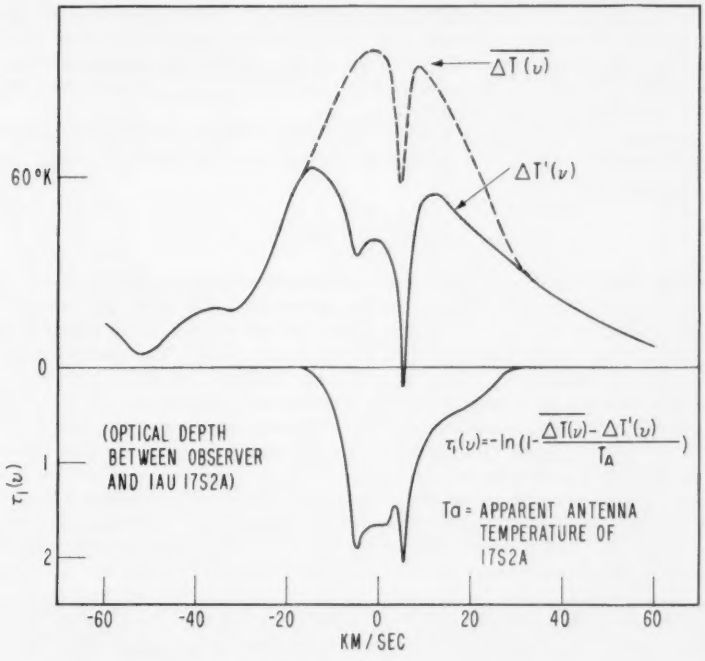

FIG. 5.—The expected profile $\overline{\Delta T(\nu)}$ and the observed profile $\Delta T'(\nu)$ are shown at the top, with the computed value of the optical depth illustrated at the bottom on a common velocity scale.

emission temperature of the observed profile in the range of −15 to −20 km/sec, where absorption is known to be absent, is of the order of 50° K. This temperature is characteristic of the region at this velocity and would seem to preclude a partially filled beam.

It is therefore justifiable at this point to make the following four statements: First there is a discrete radio source at an unknown distance whose apparent position is very close to the expected position of the galactic center. Second, the absorption measurements reveal that there is hydrogen gas, having an approximate radial-velocity range from −16 to +30 km/sec, between the sun and the radio source. Third, from the measurement with a 5-kc band width it appears that the magnitude and sharpness of the absorption at +5.5 km/sec can best be accounted for by assuming the existence of near-

by cool gas. Fourth, hydrogen gas with velocities in excess of -16 and $+30$ km/sec is present on the far side of the radio source.

THE DISTANCE SCALE

The absorption effect does not of itself yield an absolute distance scale. The ability of the absorption technique to reveal structure in distance is based on the assumption that the radial velocity along the line of sight is a function of distance. This is generally conceded to be true for all galactic longitudes, with the exception of the galactic center and anticenter, where the classical assumption of pure circular motion would preclude the existence of a radial velocity other than zero. In previous work on discrete radio sources the distance scale has been supplied by the work of van de Hulst, Muller, and Oort on spiral structure.

If one could obtain an independent relation between radial velocity and distance in the direction of the center, it would then be possible to assign distances to the radio source and various structural features noted in the absorption measurements. An approximate distance scale has been derived from a study of the angular extent of the hydrogen as a function of radial velocity.

If one assumes that the Galaxy is a flat disk of thickness t, an observer inside the disk can relate the angular width ϕ of the disk to the distance d at which the angle was measured by the relation

$$\tan \frac{\phi}{2} = \frac{t}{2d}. \tag{2}$$

The assumption that the Galaxy is of uniform thickness is obviously not rigorous, but a more complicated model would hardly be justified. The angular extent of the gas was measured by two different methods. First, several profiles were taken at positions along a line normal to the plane at $l = 327.^{\circ}8$ (Lund pole). The positions were symmetrically spaced about $b = -1.^{\circ}4$. The central position $l = 327.^{\circ}8$ and $b = -1.^{\circ}4$ is the measured position of 17S2A at 21 cm. Profiles were taken at $\pm 0.^{\circ}5$, $\pm 1.^{\circ}0$, $\pm 1.^{\circ}5$, $\pm 2.^{\circ}5$, and $\pm 4^{\circ}$ with respect to $b = -1.^{\circ}4$. Temperatures at corresponding radical velocities on the profiles were then plotted as a function of angle. Profiles taken in this manner do not yield a satisfactory measure of angular extent at velocities lower than ± 10 km/sec. This is a result of the large Ophiuchus dark complex (Heeschen and Lilley 1954), which makes an angle of about 20° with the galactic plane. For this reason declination sweeps (which miss most of the complex), corrected to equivalent widths normal to the plane, were used as the measure of angular extent at the lower radial velocities. The angular extent of the gas was taken as the measured half-intensity point in the case of the declination sweeps. Very little structure was found in the wings of the declination sweeps, but absorption made it necessary to estimate what the intensity would have been at the position of the radio source (see Fig. 3).

The probable error in determining the angular extent of the gas is somewhat different at the different radial velocities. In general, the pointing accuracy of the 50-foot antenna is about $\pm 3'$ of arc for small incremental position changes about a given point and may be neglected. In the case of the declination sweeps employed at low radial velocities, the data were replotted on cross-section paper and the half-intensity points noted. The measured angle was then converted to an equivalent width normal to the plane. Angular widths obtained in this way are considered somewhat tentative, with a probable error of the order of 20 per cent.

In the velocity range ± 10 to ± 30 km/sec the distribution of the gas was found to be of the form $T = ke^{-a\phi}$, where T is the indicated temperature and k and a are constants. In this range ln T was plotted as a function of ϕ on semilog paper, and the best straight line was passed through the points. The half-intensity point was then deter-

mined for the line. The scatter was rather small, and the probable error is thought to be less than 15 per cent.

At velocities greater than ± 30 km/sec the scatter increased because of the lower emission temperatures and the smaller angles involved. An actual increase in structure at the greater distances may have been partly responsible. In this range the data were plotted on cross-section paper, and an estimate was made of the half-intensity points. The values in this range are considered tentative, with a probable error of the order of 30 per cent.

The data obtained in these measurements is illustrated in Figure 6. The left-hand ordinate is the dimensionless quantity $(t/d)^{-1}$ (arctan of the full half-intensity width). The right-hand ordinate is the distance scale obtained by assuming a thickness of 240 pc. The abscissa is the radial velocity with respect to the local standard of rest. The crosses are the values taken from the hydrogen profiles, and the dots are those obtained by

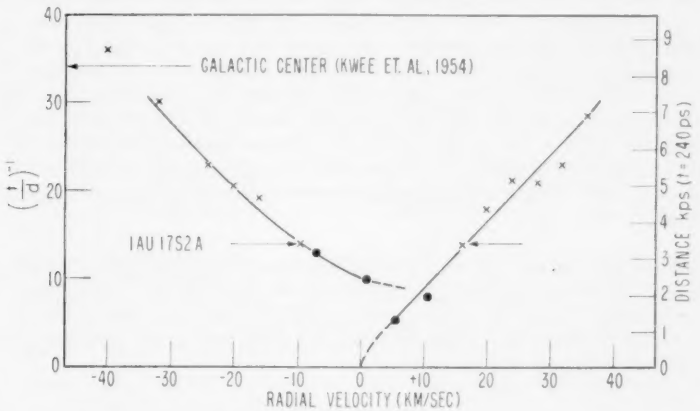

FIG. 6.—Diagram showing the relation between distance and radial velocity obtained from the measurements reported herein. The left-hand ordinate is the dimensionless quantity $(t/d)^{-1}$. This quantity is the arctan of the full half-intensity width. The right-hand ordinate is a distance scale derived by assuming a uniform thickness of 240 pc for the Galaxy.

means of angular sweeps. Both the positive and the negative wing are seen to reach values commensurate with the value of 1°.7 at 8.2 kpc given by Kwee *et al.* (1954) for the galactic center. Of primary interest, however, is the region within 4 kpc of the sun. It will be noted that there is an indication of a double-valued distance at about +5 km/sec. This is a necessary condition if one invokes the self-absorption hypothesis of Heeschen. An attempt at a direct measurement of the angular extent of the more distant gas at +5 km/sec leads to ambiguities, and its existence can be inferred only by the notch in the profiles surrounding the center.

INTERPRETATION OF THE OBSERVATIONS

In applying the distance scale to radio source 17S2A, one is forced to consider the random motions present at the distance of the source. These random motions make it difficult to associate a particular value of radial velocity with the onset of absorption. In Figure 5 it is seen that $\tau_1(\nu)$ and hence absorption occur from -16 to $+32$ km/sec. If one assumes that the correct value of $\tau_1(\nu)$ lies between 0.1 and 0.5 of the maximum value, the limits placed on the associated radial velocities are -7 to -12 km/sec for the

negative wing and +10 to +24 km/sec for the positive wing. These velocities place the distance of the source between 3 and 4 kpc for the negative branch of Figure 6 and between 2 and 5 kpc for the positive branch. Since the positive and negative branches have different slopes, it is of interest to determine at what value of $\tau_1(\nu)$ and hence at what velocity the positive and negative branches yield the same distance. The value of $\tau_1(\nu)$ at which this occurs is 0.5 (25 per cent of the maximum value), and the distance indicated by both branches of the distance scale is 3.4 kpc. This value is indicated by arrows in Figure 6.

CONCLUSIONS

A consideration of the measurements reported herein leads to the conclusion that the radio source responsible for the intense emission peak at $l = 327\overset{\circ}{.}8$ and $b = -1\overset{\circ}{.}4$ is probably not associated with the galactic center but rather is superimposed on the broad central galactic background. A consideration of the uncertainties of the measurement places it between extreme limits of 2 and 6 kpc, with a probable distance of between 3 and 4 kpc. It is interesting to note that Haddock and McCullough (1955) have suggested that this source is thermal and possibly associated with an *H* II region in the group of OB stars studied by Hiltner (1954). The mean distance given by Hiltner for this group is 3 kpc. It should be noted that the apparent position of a complex source might vary with the wave length at which the observation is made and with the antenna-beam size if the sources are not exactly concentric. Such variation has been noted for this source. Positive identification will probably be the result of high-resolution radio studies in the vicinity of 3-cm wave length and a possible optical identification made feasible by the radio position.

In conclusion the author wishes to acknowledge many interesting discussions with his colleagues F. T. Haddock and A. E. Lilley during the preparation of this paper. Finally, the author wishes to thank the various members of the Radio Astronomy Branch, in particular Joseph H. Nichols, and John A. Waak for their assistance in making the measurements and in reducing the data.

REFERENCES

Haddock, F. T., and McCullough, T. P. 1955, *A.J.*, **60**, 161.
Hagen, J. P., Lilley, A. E., and McClain, E. F. 1954, *NRL Rept.*, No. 4448, October 18, 1954; *Ap. J.*, **122**, 361, 1955.
Hagen, J. P., and McClain, E. F. 1954, *Ap. J.*, **120**, 364.
Heeschen, D. S. 1955, *Ap. J.*, **121**, 569.
Heeschen, D. S., and Lilley, A. E. 1954, *Proc. Nat. Acad. Sci.*, **40**, 1095.
Hiltner, W. A. 1954, *Ap. J.*, **120**, 41.
Kwee, K. K., Muller, C. A., and Westerhout, G. 1954, *B.A.N.*, **458**, 211.
Lilley, A. E. 1955, *A.J.*, **60**, 167.
McGee, R. X., and Bolton, J. G. 1954, *Nature*, **173**, 985.
Williams, D. R. W., and Davies, R. D. 1954, *Nature*, **173**, 1182.

THE RADII OF δ CEPHEI AND η AQUILAE. II

CHARLES WHITNEY*
Harvard College Observatory
Received June 27, 1955

ABSTRACT

Discrepancies between the results of several methods for determining the radii of cepheids are discussed. The discrepancy is considerably reduced, for δ Cephei, by proper allowance for the distortion of the continuum by line absorption. A revision of the zero point of the period-luminosity relation is derived.

I. INTRODUCTION

Attempts to show that the observed luminosity variations of cepheids are compatible with inferred variations of surface brightness and area have achieved only moderate success. These investigations have postulated radial symmetry and the validity of integrating the radial-velocity-curve to derive surface displacements.

Menzel has proposed (1931) that radial symmetry be abandoned and replaced by a model that incorporates "hot spots" on the stellar photosphere. Whipple suggested (1932) that the existence of such hot spots might account for the discrepancies. A quantitative test (Whitney 1955*a*) shows that such a model can reconcile the observed and theoretical variations of luminosity.

Since no *direct* evidence exists that the simplifying postulates are incorrect, we should consider other possible reasons for the discrepancies, before adopting this complex model. This note presents evidence that the discrepancy has arisen through the improper analysis of observed luminosities. The present analysis differs from preceding analyses in that it accounts for the variations of weak-line absorption with phase. The data do not suffice for a definitive solution, but they indicate that the discrepancy will be reduced and that the simplifying postulates may be retained.

II. QUANTITATIVE STATEMENT OF THE PROBLEM

Rather than treat luminosities per se, this discussion will treat stellar radii as derived by different methods. In an earlier paper (Whitney 1955*b*), referred to as "Paper I," the radial variations of δ Cephei and η Aquilae were derived from six-color observations (Stebbins 1945; Stebbins, Kron, and Smith 1952). That analysis was based on (1) monochromatic fluxes computed from model atmospheres assumed to be in radiative equilibrium and (2) calibration of the photometry through reference to the solar continuum. Table 3 of Paper I gives theoretical colors on the six-color system as functions of effective temperature and surface gravity. In the analysis, observed colors were corrected for line absorption by assuming that measures of the "blanketing effect" in the spectrum of α Persei were directly applicable to the cepheids. Variations of line absorption with phase were not considered.

By interpolating the observed colors (corrected for line absorption) into Table 3, Paper I, and using equation (5), the radii of these two stars were determined as functions of phase. The derived radii differed markedly from radii determined by the "Wesselink method," which utilizes surface displacements and phase pairs of equal color. The results of the two methods differed in the values of mean radius and the amplitude and phase of radius variations.

This disparity had appeared in earlier investigations. For example, Becker (1940*a*, *b*),

* Predoctoral fellow of the National Science Foundation, 1954–1955.

adopting a different attack, had forced agreement between the Wesselink and photometric radii and derived an empirical relation between brightness temperature and color temperature. However, present knowledge concerning the absorption coefficient in stellar atmospheres does not confirm this relation (Whitney 1955*a*).

Miss Canavaggia and Pecker (1954) discussed the difficulty by considering the numerical coefficient a, defined by the relation

$$\Delta m_i = a\,(\Delta m_j - \Delta m_i)\,, \tag{1}$$

where the subscripts refer to wave length ($\lambda_j < \lambda_i$) and the Δ's denote changes with effective temperature. These authors noted that such a linear relation nicely fits the magnitude changes computed from model atmospheres and that the value of a corresponding to the atmospheres nearly equals the value corresponding to a black-body radiator. Miss Canavaggia and Pecker concluded that the radius discrepancy for δ Cephei would be removed if a were about 0.58 times the black-body value. They did not suggest a possible cause for this low value of a. It has been shown (Whitney 1955*a*) that, assuming a plane-parallel atmosphere, the value of a for δ Cephei is insensitive to expected deviations from radiative equilibrium. Such deviations arise from (1) convective transport of energy and (2) the time dependence at atmospheric flux.

In the present paper, I shall again adopt the theoretical colors of Table 3, Paper I, but shall attempt a more explicit evaluation of the "blanketing effect."

III. EFFECTS OF LINE ABSORPTION ON OBSERVED COLORS

The theoretical colors of Table 3, Paper I, refer to continua undistorted by absorption lines. In the present section I shall estimate the corrections for line absorption in the spectrum of δ Cephei at two phases. The data to be utilized are (1) Milford's (1950) measures of the percentage of depression of the continuum of α Persei within 25 a.u. intervals from λ 4000 to λ 4600 and 50 a.u. intervals from λ4600 to λ 6650, and (2) Walraven's (1948) measures of the equivalent widths of all lines in the spectrum of δ Cephei between λ 4050 and λ 4800.

Datum 1 led to the values of δm^i of Paper I, Table 2. Here $\delta\, m^i$ is the depression, in magnitudes, of the stellar continuum as observed through the ith filter of the six-color photometer. The value of δm^i for the infrared filter was based on extrapolation, and I shall not use it in the present analysis. For the blue, green, and red filters, Table 2, Paper I, gives $\delta \mathrm{m}^i = 0.20$, 0.12, and 0.05 mag., respectively.

Walraven's values of equivalent widths represent the means of data obtained from four plates exposed near maximum brightness and three plates exposed near minimum brightness. I designate the phases corresponding to the means of these two sets of data by X and N, respectively.

The equivalent widths tabulated by Walraven do not encompass a wave-length interval sufficient to allow direct determination of the $\delta \mathrm{m}^i$'s. Therefore, I derive the ratios $\delta \mathrm{m}_X / \delta m_{\alpha\ \mathrm{Per}}$ and $\delta m_N / \delta m_{\alpha\ \mathrm{Per}}$ for the wave-length interval over which Milford's and Walraven's data overlap, and I assume the same ratios to hold throughout the spectrum at the corresponding phases. That is,

$$\delta\, m_X^i = \delta\, m_{\alpha\ \mathrm{Per}}^i \frac{\delta\, m_X}{\delta\, m_{\alpha\ \mathrm{Per}}}, \tag{2}$$

$$\delta\, m_N^i = \delta\, m_{\alpha\ \mathrm{Per}}^i \frac{\delta\, m_N}{\delta\, m_{\alpha\ \mathrm{Per}}}. \tag{3}$$

The use of the simple proportionality expressed by equations (2) and (3) is suggested by the excellent linear correlation between the δm_X and δm_N for 25 a.u. intervals within the spectrum of δ Cephei. The regression line passes through the origin.

Summation of the equivalent widths measured by Walraven gives $\delta m_X = 0.30$ mag. and $\delta m_N = 0.45$ mag. for the wave-length interval λλ 4050–4800, omitting the intervals λλ 4075–4125 and λλ 4300–4375. Similarly, for α Persei, Milford's data give $\delta m_{\alpha\ \mathrm{Per}} = 0.276$ mag. Therefore, the ratios appearing in equations (2) and (3) are 1.09 and 1.63, respectively. Table 1 lists the δm^i's obtained from Table 2, Paper I, and equations (2) and (3) above.

IV. EFFECTIVE TEMPERATURES AND RADII

The data of group X were obtained from plates exposed at phases 0^{p}90, 0^{p}06, 0^{p}10, and 0^{p}14, and the data of group N were obtained from exposures at phases 0^{p}38, 0^{p}46, and 0^{p}56. The characteristic phase of each group was obtained by deriving the mean of the colors at each observation and taking the phase corresponding to this mean. The

TABLE 1

CORRECTIONS FOR LINE ABSORPTION (MAG.)

Filter	B	G	R
α Persei	0.20	0.12	0.05
δ Cephei X	.22	.13	.055
δ Cephei N	0.325	0.195	0.08

TABLE 2

DETERMINATION OF EFFECTIVE TEMPERATURE
(Phase $X = 0.12$)

	B	G	R
Mean colors	−0.06	−0.015	+0.08
δm^i_X	+ .22	+ .13	+ .055
$\delta m^i_X\ (\overline{B\text{-}G\text{-}R})$	+ .08	− .005	− .08
Corrected colors	− .14	− .01	+ .16
$\vartheta_e = 0.816$	−0.14	−0.015	+0.16

results are $X = 0^p12$ and $N = 0^p46$. In the remaining discussion, I treat the data as though they were all obtained at precisely these two phases.

Applying the corrections of Table 1 to the colors of δ Cephei observed at phases X and N and interpolating in Table 3, Paper I, the effective temperatures are determined for the corresponding phases. I have assumed $\log g = 1.8$ for the present discussion, noting that the results are insensitive to the choice of effective gravity. Interpolating the effective temperatures in Table III of Miss Canavaggia and Pecker (1953), I derive the flux integrals required for the solution of equation (5), Paper I. From this equation and the observed monochromatic light-curves, the ratio of radii at phases X and N follow.

Tables 2 and 3 present the steps in the determination of effective temperature at X and N. The third entries in each column are the values of δm^i minus the mean of the values at the B, G, and R wave lengths. This subtraction reduces the δm^i to the six-color system. The last entries in each column give the theoretical colors which best fit the observed colors, as corrected for line absorption.

Table 4 presents the process of determining the ratio of the radii of δ Cephei at phases 0^{p}12 and 0^{p}46 from the effective temperatures derived in Tables 2 and 3.

The present mean value of Δm_A between phases X and N is 0.11. Table 4, Paper I,

lists the radii resulting from an analysis similar to the foregoing but does not consider the variation of line absorption. From those data, $\Delta m_A = 0.18$.

These values of Δm_A are to be compared with the value resulting from the Wesselink analysis. Applying the surface-displacement-curve of δ Cephei derived by Schwarzschild (1938) from radial velocities to the mean radius given in Table 1, Paper I, I find $\Delta m_A = 0.08$. The uncertainties of these values for Δm_A are about ± 0.03 mag. Therefore, I conclude that the present analysis appreciably reduces the discrepancy discussed in Paper I.

Phrasing the discussion in the terms which Miss Canavaggia and Pecker employed, I

TABLE 3

DETERMINATION OF EFFECTIVE TEMPERATURE
(Phase $N = 0.46$)

	B	G	R
Mean colors	+0.07	−0.01	−0.06
δm_N^i	+ .325	+ .195	+ .08
$\delta m_N^i\,(B\text{-}G\text{-}R)$	+ .125	− .005	− .12
Corrected colors	− .055	− .005	+ .06
$\vartheta_e = 0.895$	−0.05	−0.01	+0.065

TABLE 4

DETERMINATION OF RATIO OF RADII
(δ Cephei)

Phase			B	G	R
0.12	$2.51 \log \int F_\lambda S_\lambda^i d\lambda$	(1)	23.24	23.07	23.17
	δm_X^i	(2)	0.22	0.13	0.05
0.46	$2.51 \log \int F_\lambda S_\lambda^i d\lambda$	(3)	22.66	22.56	22.77
	δm_N^i	(4)	0.33	0.19	0.08
	(1)−(3),	(5)	0.58	0.51	0.40
	(4)−(2),	(6)	0.11	0.06	0.03
	Theoretical, area-free brightness change (5)+(6)		0.69	0.57	0.43
	Observed brightness change		0.59	0.45	0.32
	$\Delta m_A = 5.02 \log (R_{0.46}/R_{0.12})$		0.10	0.12	0.11

compute the value of a corresponding to the B and G filters. From data utilized in the analysis of Paper I, I find $a = 6.8 \pm 0.5$, where

$$\Delta m_G = a\,(\Delta m_B - \Delta m_G)\,,$$

and the Δm's are surface-brightness changes between phases 0^p12 and 0^p46. From the data utilized in the present analysis, I find $a = 4.5 \pm 0.5$. The ratio of these values of a is 0.66 ± 0.15. This ratio is satisfactorily close to the value (0.58) which Miss Canavaggia and Pecker state will lead to agreement between the photometric and Wesselink methods.

Thus it appears that the photometric analysis agrees closely with the Wesselink analysis, if one allows for the variation in line absorption. However, the Wesselink method assumes that (*a*) equal color means equal surface brightness and (*b*) surface displacements may be derived from the radial-velocity-curve. The present agreement between the photometric and Wesselink analyses substantiates, but *does not prove*, the validity of these assumptions.

For future programs designed to provide adequate data for evaluating line absorption, one point deserves emphasis. The mean equivalent width of the lines measured in the spectrum of δ Cephei by Walraven is 0.12 a.u. Therefore, equipment of fairly high dispersion is required to evaluate the distortion of the continuum by absorption lines. This fact contributed to the failure of previous spectrophotometric investigations to eliminate the distortion.

V. ZERO-POINT CORRECTION TO THE PERIOD-LUMINOSITY RELATION

The present derivation of what appears to be a consistent set of effective temperatures and radii allows a determination of the absolute magnitude of δ Cephei. This magnitude is subject to uncertainties in the absolute calibration of the six-color photometry, and these uncertainties are about 0.05 mag. in the values of ϵ^i in Paper I. I assume that δ Cephei lies on the mean period-luminosity relation, and I directly derive a zero-point correction to this relation.

The spectrum of α Persei closely resembles that of δ Cephei at phase 0^p05. The important differences, notably hydrogen-line strengths, will have minor influence on corrections for total line absorption. Therefore, I assume that the photometric analysis in Paper I is correct at this phase to within a numerical factor in the radius, i.e., that the effective temperature is correct.

I further assume, following the results of the present paper, that the Wesselink method is valid. At phase 0^p05, the Wesselink method gives, for the stellar radius, $R = 36 \pm 3 \times 10^6$ km, while the photometric analysis in Paper I gave $R = 32.2 \pm 2 \times 10^6$ km. Thus the revision to the zero-point correction is

$$\delta M_v = 5 \log (32.2 \pm \tfrac{2}{36} \pm 3)$$

$$= -0.25 \pm 0.3 ,$$

and the revised zero-point correction is

$$\Delta M_v = -1.65 \pm 0.3 .$$

REFERENCES

Becker, W. 1940*a*, *Zs. f. Ap.*, **19**, 269.
———. 1940*b*, *ibid.*, p. 289.
Canavaggia, R., and Pecker, J.-C. 1953, *Ann. d'ap.*, **16**, 47.
———. 1954, *C.R.*, **239**, 225.
Menzel, D. H. 1931, *Pop. Astr.*, **39**, 16.
Milford, N. 1950, *Ann. d'ap.*, **13**, 243.
Schwarzschild, M. 1938, *Harvard Circ.*, No. 431.
Stebbins, J. 1945, *Ap. J.*, **101**, 47.
Stebbins, J., Kron, G., and Smith, J. L. 1952, *Ap. J.*, **115**, 292.
Walraven, T. 1948, *Pub. Astr. Inst., U. Amsterdam*, No. 8.
Whipple, F. L. 1932, *Lick Obs. Bull.*, **16**, 1.
Whitney, C. 1955*a*, thesis, Harvard University.
———. 1955*b*, *Ap. J.*, **121**, 682.

SPECTROSCOPIC OBSERVATIONS OF THE CLUSTER-TYPE VARIABLE VZ CANCRI*

HELMUT A. ABT
McDonald Observatory
Received May 9, 1955

ABSTRACT

The radial velocities obtained from ninety-two spectrograms of VZ Cancri show variations with both periods (4^h17^m and 17^h12^m) found by Fitch from light-observations. The phase shift of mid-rising light with the long-period variation is reflected by a similar phase shift in the radial velocities. Mid-decreasing velocity occurs at mid-rising light. Maximum velocity range occurs at the same phase of the long-period variation as does maximum light-range. The range of 39.6 km/sec in the mean velocity-curve is consistent with expectations from three other short-period variables. The spectrum is of luminosity class III and varies between A7–A9 at light-maxima and F1–F2 at light-minima.

The light-variability of VZ Cancri[1] was announced by B. S. Whitney (1950), who identified it as a cluster-type variable with a period of 4^h17^m. A few spectroscopic observations by A. H. Joy and R. E. Wilson (1950) indicated a range in velocity of about 50 km/sec and in spectral type of A7–F2. Recently, W. S. Fitch (1955) has made an extensive photoelectric study and has found a secondary variation in light with a period of 17^h12^m. The purpose of the present study is to investigate the spectroscopic changes during the short- and long-period variations.

A series of ninety-two spectrograms of VZ Cancri were obtained with the shortest-focus camera (dispersion of 36 A/mm) of the McDonald 82-inch coudé spectrograph. Well-exposed spectrograms with a width of 0.26 mm and a resolution of 0.7 A (50 km/sec) were obtained with exposure times of 9–20 minutes (0^p04–0^p08). Since the ranges in velocity for individual cycles are only 26–51 km/sec, the resolution is insufficient for the detection of double lines, if they exist. The spectrograms were obtained during ten short-period cycles and are well distributed over the long-period variation.

The following ephemeris, due to Fitch (1955), gives the short-period (ϕ) and long-period (ψ) phases:

$$\phi = \frac{T - \text{JD}2433631.84615}{0.17836376}, \tag{1}$$

$$\psi = \frac{T - \text{JD}2433631.8421}{0.716292}, \tag{2}$$

where T is the heliocentric Julian Date. Fitch found that the time of mid-rising visual light varies slightly with the phase in the long-period variation in the following manner:

$$T(\bar{m}) = \text{JD } 2433631.84615 + 0^d.17836376E + 0^d.00418 \sin 2\pi [\psi(\bar{m}) + 0.825]. \tag{3}$$

To compare velocity-curves obtained at different times of the long-period variation, it would be preferable to count our phases ϕ from these predicted times of mid-rising light rather than the epoch given in equation (1).

The measured velocities are plotted in Figure 1. These were obtained from the follow-

* *Contributions from the McDonald Observatory, University of Texas*, No. 259.

[1] VZ Cancri = HD 73857; $\alpha = 8^h35^m4$; $\delta = +10°11'$ (1900); $m_{pg} = 7.7$–8.2.

TABLE 1

SPECTROSCOPIC OBSERVATIONS OF VZ CANCRI

Plate No. Cg	Heliocentric JD 2435000+	ϕ	ψ	ρ (Km/Sec)	Spectral Type
1016	51.8907	7961.4879	1982.4996	+22.1	F0: III
1017	.9032	.5590	.5171	+25.4	F0:
1018	.9185	.6467	.5384	+38.0	F0:
1019	.9338	.7347	.5598	+42.8	F1:
1020	.9490	.8225	.5810	+49.9	F0:
1021	.9622	.8988	.5994	+57.4	F0:
1022	.9747	.9712	.6169	+42.1	A9
1023	.9865	7962.0397	.6333	+ 8.4	A7
1024	.9983	.1082	.6498	− 0.1	A7
1025	52.0101	.1768	.6663	+ 3.5	A7
1037	.8998	7967.1893	1983.9084	+ 0.6	A8
1038	.9116	.2555	.9249	+ 6.5	F0:
1039	.9234	.3216	.9413	+ 8.5	F0
1040	.9353	.3879	.9579	+22.9	F0:
1041	.9471	.4535	.9744	+21.7	F0
1042	.9588	.5182	.9908	+30.5	F0
1043	.9706	.5832	1984.0072	+41.0	A9:
1044	.9844	.6590	.0265	+36.8	F0:
1045	.9998	.7432	.0480	+42.6	F1
1046	53.0158	.8305	.0703	+41.9	F0
1056	.9048	7972.7826	1985.3114	+37.5	F2
1057	.9263	.9007	.3415	+41.2	F0
1058	.9416	.9851	.3628	+26.2	F0
1059	.9569	7973.0699	.3842	+15.0	A8
1060	.9700	.1428	.4045	− 3.9	A9
1061	.9818	.2088	.4189	+ 4.9	A9
1062	.9936	.2750	.4354	+ 9.4	A9
1063	54.0055	.3421	.4520	+12.4	F0
1064	.0173	.4088	.4685	+18.8	F0
1078	.9000	7978.3843	1986.7008	+ 7.9	F0.
1079	.9160	.4771	.7232	+15.7	F0
1080	.9313	.5657	.7445	+26.6	F0
1081	.9542	.6981	.7765	+38.6	F0
1082	.9694	.7857	.7977	+45.2	F1
1083	.9846	.8731	.8189	+44.5	F0
1084	55.0000	.9612	.8404	+38.9	A9
1085	.0153	7979.0483	.8618	+10.7	A7
1086	.0306	.1351	.8832	+ 8.4	A7
1144	148.7431	8504.5190	2117.7132	+23.7	F0
1145	.7591	.6118	.7355	+35.4	F1
1146	.7757	.7079	.7587	+40.6	F1
1147	.7917	.8003	.7810	.....	F1
1148	.8098	.9046	.8063	+45.3	F0
1149	.8237	.9843	.8257	+29.1	F0:
1150	.8369	8505.0597	.8441	+ 5.3	A7
1331	155.7025	8543.5078	2127.4289	+17.3	F0
1332	.7159	.5832	.4476	+30.2	F0
1333	.7281	.6521	.4646	+35.5	F1
1334	.7406	.7230	.4821	+37.7	F1
1335	.7534	.7958	.5000	+45.9	F1
1336	.7659	.8673	.5174	+46.2	F2
1337	.7784	.9389	.5349	+49.7	F1
1338	.7881	.9945	.5484	+30.0	F0
1339	.7969	8544.0453	.5607	+15.5	A8:
1340	.8052	.0931	.5723	− 5.1	A8:
1341	.8136	.1415	.5840	− 2.4	A9:

TABLE 1—*Continued*

Plate No. Cg	Heliocentric JD 2435000+	ϕ	ψ	ρ (Km/Sec)	Spectral Type
1392	157.7089	8554.7720	2130.2300	+35.9	F0
1393	.7220	.8430	.2483	+43.0	F1
1394	.7349	.9130	.2663	+43.9	F0
1395	.7467	.9772	.2828	+36.5	F0
1396	.7572	8555.0343	.2974	+22.9	F0:
1397	.7676	.0913	.3119	+13.0	A9
1398	.7773	.1445	.3255	+19.1	F0:
1399	.7857	.1906	.3372	+12.5	F0:
1400	.7940	.2364	.3489	+13.6	F0:
1401	.8024	.2828	.3605	+ 8.8	F0
1402	.8103	.3266	.3715	+15.7	F0
1403	.8172	.3647	.3812	+15.7	F1
1449	159.7606	8566.2942	2133.0945	+20.0	F1
1450	.7742	.3680	.1135	+21.3	F0
1451	.7870	.4373	.1313	+29.6	F0
1452	.8002	.5080	.1498	+32.5	F0
1453	.8138	.5820	.1687	+32.4	F1
1454	.8277	.6571	.6882	+34.9	F2
1455	.8422	.7354	.2084	+43.2	F1
1477	160.7082	8571.5724	2134.4174	+34.4	F0:
1478	.7196	.6363	.4333	+45.3	F0
1479	.7311	.7011	.4494	+49.3	F0
1480	.7436	.7717	.4668	+46.8	F0
1481	.7561	.8426	.4843	+47.3	F1
1482	.7679	.9098	.5007	+41.7	F0
1483	.7786	.9709	.5157	+21.8	A9
1484	.7881	8572.0253	.5289	+ 3.8	A7
1485	.7971	.0769	.5415	+ 2.0	A7
1486	.8054	.1249	.5531	+ 2.9	A9:
1534	163.7396	8588.5876	2138.6495	+44.5	F1
1535	.7538	.6702	.6693	+55.1	F1
1536	.7667	.7451	.6873	+53.4	F1
1537	.7792	.8177	.7048	+54.9	F1
1538	.7918	.8909	.7223	+47.9	F0
1539	.8032	.9570	.7383	+24.1	A9:
1540	.8133	8589.0155	.7524	+11.6	A7

ing lines: K, λ 4045, λ 4077, $H\delta$, λ 4215, λ 4233, and $H\gamma$. No systematic differences with phase were found between the velocities of hydrogen and metallic lines. It will be shown below that the mean velocity is +26.0 km/sec. Eight of the observed velocity-curves reach this velocity on their descending branches at a mean phase of 0.993 ± 0.015. We conclude that mid-decreasing velocity occurs at mid-rising light, and the velocity-curves confirm the phase shift, which may be as large as $\pm 0^{p}023$, in light as found by Fitch.

The variations in shape of the velocity-curves are apparent in Figure 1. At any phase ϕ the observed velocities are a function of ψ, which can be expressed sufficiently well by a sine-curve. For example, by a least-squares solution the radial velocity, $\rho(\phi, \psi)$, at $\phi = 0.8$ is

$$\rho\,(0.8, \psi) = +44.26 + 4.77 \sin 2\pi\,(\psi + 0.583) \qquad (4)$$
$$\pm\ 0.23 \pm 0.31 \qquad \pm 0.106\ .$$

At $\phi = 0.1$ we obtain

$$\rho\,(0.1, \psi) = +8.37 - 9.78 \sin 2\pi\,(\psi + 0.612) \qquad (5)$$
$$\pm 0.31 \pm 0.42 \qquad \pm 0.203\ .$$

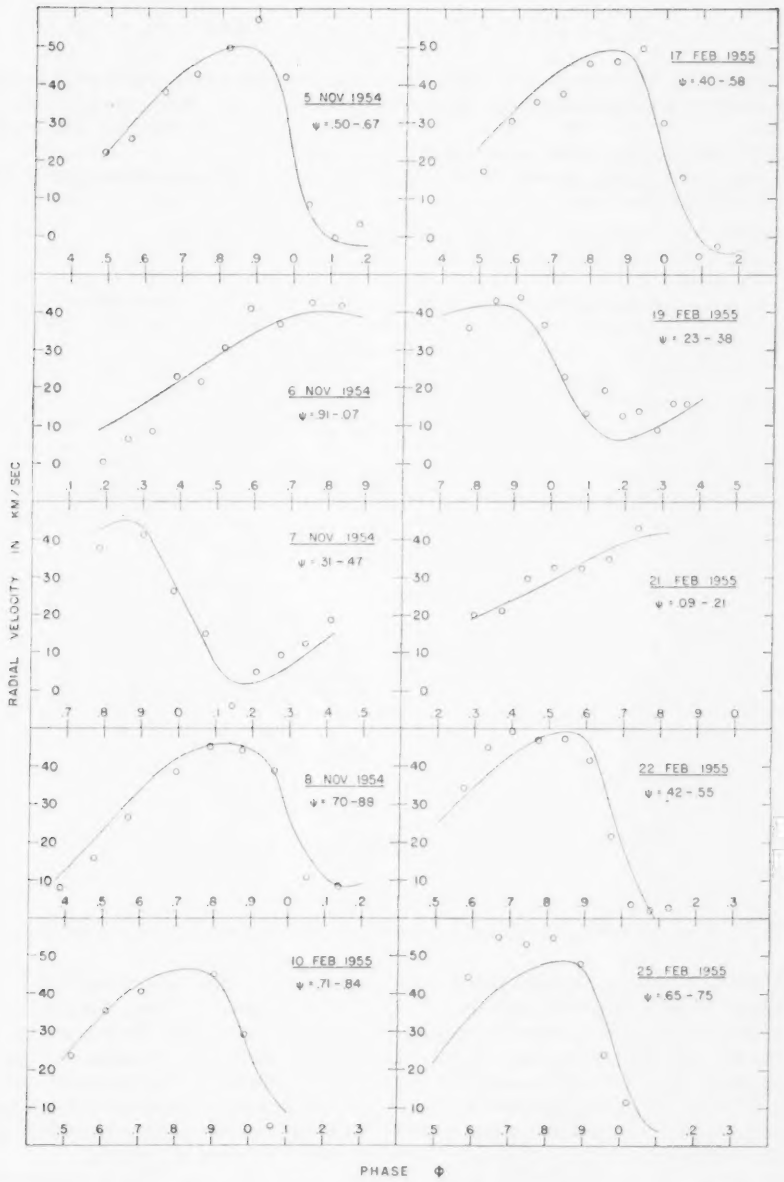

FIG. 1.—The measured radial velocities of VZ Cancri (*circles*) and the corresponding computed velocity-curves (*lines*). The long-period phases, ψ, are given under each date.

Fitch finds that the visual light-range varies as

$$A = 0^{m}.521 + 0^{m}.147 \sin 2\pi (\psi + 0.654) . \quad (6)$$

A comparison of the phase shifts in these three equations shows that, within our probable errors, the maximum velocity range, given approximately by $\rho(0.8, \psi)-\rho(0.1, \psi)$, and the maximum light-range occur at the same phase of the long-period variation. This time is $0^{p}.17$ after maximum retardation of phase.

At each of ten equally spaced phases ϕ the velocities were fitted by least-squares solutions to a variation of the form

$$\rho (\phi, \psi) = \bar{\rho} (\phi) + K (\phi) \sin 2\pi (\psi + 0.654) , \quad (7)$$

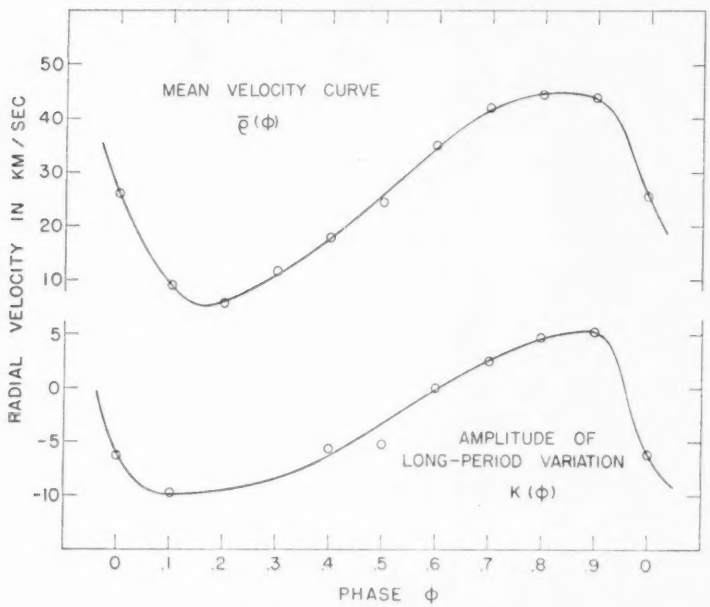

FIG. 2.—The mean velocity-curve (*top*) and the amplitude of the long-period variation (*bottom*)

where the first term on the right side represents the mean velocity-curve and $K(\phi)$ is the amplitude of the long-period variation. Figure 2 shows these functions. No solution for K was obtained at $\phi = 0.2$ and 0.3 because of a lack of observations. From equation (8) and the smoothed curves in Figure 2 we computed the velocity-curves drawn in Figure 1. The internal consistency of the velocity measures indicates a probable error per spectrogram of 1.9 km/sec. Since the mean scatter of the observed velocities about the computed curves is 3.3 km/sec and is sometimes systematic during parts of cycles, we probably have not been completely successful in describing the radial motions of the star.

The mean velocity-curve (Fig. 2) has a range of 39.6 km/sec. This is intermediate between the smaller range for AI Velorum (Gratton 1953), whose period is shorter, and the larger ranges for XZ Cygni (Struve and Van Hoof 1949) and RR Lyrae (Struve and Blaauw 1948), whose periods are longer. The large velocity range of 45 km/sec reported

for DY Pegasi (Bidelman 1947), whose period is 1^h45^m, places that star outside the foregoing apparent sequence.

The mean velocity of VZ Cancri, derived from an integration of the mean velocity-curve, is +26.0 km/sec. Measures on six spectrograms, taken in a similar manner as those of VZ Cancri, of three standard-velocity stars suggest a correction of $+4.0 \pm 1.1$ km/sec to bring our velocities to the system of the *Publications of the Lick Observatory*, Volume **18**.

It is possible that the long period is actually a beat period between the primary period (4^h17^m) and a second short period (3^h26^m). However, no simplification in the velocity analysis resulted from this consideration.

The spectra, although rather narrow for the purpose, were classified by a comparison with standards (Johnson and Morgan 1953) taken with the same equipment. VZ Cancri is apparently of luminosity class III and is not very different from the standards most of the time. Particularly at light-maxima, however, a discrepancy occurs between types derived from different line ratios. This is usually in the direction that the relative strength of K to $H + H\epsilon$ yields an earlier type than the metallic lines. At times λ 4067 *Fe* I and λ 4077 *Sr* II are unusually strong. Uncertain or averaged types are followed by a colon in Table 1. The latest type occurs at $\phi = 0.8$ and is F1 or F2, the latter predominating at high-velocity maxima. The earliest type is A7–A9 and occurs at $\phi = 0.1$.

I am grateful to Dr. W. S. Fitch for supplying his results in advance of publication and to Drs. B. Strömgren and A. Blaauw for the observing time used to obtain the spectrograms.

REFERENCES

Bidelman, W. P. 1947, *Ap. J.*, **106**, 135.
Fitch, W. S. 1955, *Ap. J.*, **121**, 690–710.
Gratton, L. 1953, *B.A.N.*, **12**, No. 444, 31.
Johnson, H. L., and Morgan, W. W. 1953, *Ap. J.*, **117**, 313.
Joy, A. H., and Wilson, R. E. 1950, *Pub. A.S.P.*, **62**, 58.
Struve, O., and Blaauw, A. 1948, *Ap. J.*, **108**, 60.
Struve, O., and Van Hoof, A. 1949, *Ap. J.*, **109**, 215.
Whitney, B. S. 1950, *Pub. A.S.P.*, **62**, 56.

RELATIVE ABUNDANCES AND ATMOSPHERIC CONDITIONS IN THE MAGNETIC STAR HD 133029*

E. MARGARET BURBIDGE AND G. R. BURBIDGE
Cambridge, England
Received June 15, 1955

ABSTRACT

A spectrophotometric study of HD 133029 has been made, based on nine medium-dispersion coudé spectrograms obtained at the McDonald Observatory. A table of equivalent widths of about 350 lines is given. No evidence of line-intensity variations through the period of observations has been found. There are no detectable radial-velocity differences between the different elements and no significant variations during the period of the observations; if there is any variation with a period of $\sim 1\frac{1}{2}$ days (corresponding to a possible magnetic period suggested by Babcock), its total amplitude does not exceed 5 km/sec. From curves of growth it is found, by comparison with the magnetic variable α^2 C Vn, that $T_{\text{ion}} = 8000°$, $T_{\text{exc}} = 8000°$, and the mean total apparent velocity is 4.9 km/sec; it is possible that about 1 km/sec of this is really due to the magnetic intensification effect.

Si, *Cr*, *Sr*, and *Zr* are overabundant by factors of 25, 10, 16, and 38, respectively; *Ca* is underabundant by a factor of 20; *La* and the rare earths are overabundant by a mean factor of 390. These results confirm those in α^2 C Vn, although in some cases the differences between the two stars are significant. It is suggested that the majority of the anomalies are due to surface nuclear reactions, although the small overabundance of *Fe*, if real, requires a different explanation, possibly connected with the early condensation history of the star. The possible effect of a hydromagnetic turbulent zone into which we are looking is discussed.

I. INTRODUCTION

This paper is the third in a series dealing with the spectrophotometry of magnetic stars and is based on observations made by the authors with the 82-inch telescope and coudé grating spectrograph of the McDonald Observatory during April and May, 1953. The method of analysis follows closely that used for the magnetic star α^2 C Vn (Burbidge and Burbidge 1955*a*), which will be referred to as "Paper I."

HD 133029[1] is listed in the *Henry Draper Catalogue* as having the spectral type A0p, the peculiarity being the strength of the *Si* II lines. The star has been found to have a strong variable magnetic field (Babcock and Burd 1951); a maximum field of +10,500 gauss has been observed in it (Babcock and Cowling 1953), and this is the largest stellar field so far published. The field has not been observed to change in polarity; the minimum field observed is +4300 gauss, and H. W. Babcock has reported that there appears to be a secular variation and a short-period fluctuation ($\sim 1\frac{1}{2}$ days), with an amplitude of several hundred gauss.

II. OBSERVATIONS AND RESULTS

Nine spectrograms were obtained with the C camera (linear dispersion 18 A/mm). The calibrations, microphotometer tracings, and reductions were made as described in Paper I. Because of the lower dispersion in this study, blending presents more of a problem, and fewer lines were measured for equivalent widths. A total of about 1650 measures was made. In addition, five of the spectra were measured for radial velocities.

In order to see whether there was any cyclic variation in line strengths through the period of the observations (2 weeks), a period of 36 hours was assumed, and the phases were determined, that of the first plate being arbitrarily set at zero. The phases and dates (U.T.) are given in Table 1. If the equivalent-width measures are plotted against

* *Contributions from the McDonald Observatory, University of Texas*, No. 260.

[1] $\alpha_{1950} = 14^h58^m56^s$; $\delta_{1950} = +47°28'$; $m = 6.16$.

phase, no real variations are apparent. There also seems to be no evidence for a secular variation in equivalent width over the period of the observations. This confirms the statement of Babcock and Burd that this star is not a spectrum variable like α^2 C Vn and HD 125248.

In Table 1 we give the mean velocities (reduced to the sun) from (*a*) about 25 lines of the rare-earth elements and (*b*) about 30 lines of *Si* II, *Mg* II, *Ca* II, *Ti* II, *Cr* I, *Cr* II, *Fe* I, *Fe* II, and *Sr* II. It can be seen that there is no significant difference between the rare earths and the other elements. Nor is there any variation between elements within each group. On the other hand, the measures are not inconsistent with a small variation, within the 36-hour period, whose total amplitude does not exceed 5 km/sec. Further, the mean radial velocity differs from the value of −14.0 km/sec given in the *Catalogue of Radial Velocities* (Wilson 1953), so that a small secular change is possible. However, our plates were not obtained primarily for radial-velocity measurement and no standard radial-velocity stars were observed as a check. We conclude, however, that no velocity variations of the magnitude observed in α^2 C Vn are present in HD 133029, and no differences between different elements are observed. Both these results are consistent with the absence of line-intensity variations. According to Provin (1953), the star does not show measurable light-variations.

In view of the absence of line-intensity variations, we have taken straight means of all the measures of equivalent width for each line, and these results are given in Table 2.

TABLE 1

PHASES OF PLATES AND RADIAL VELOCITIES

Phase	Date (U.T.) 1953	Radial Velocity (Km/Sec)		Phase	Date (U.T.) 1953	Radial Velocity (Km/Sec)	
		a	*b*			*a*	*b*
0.000.....	Apr. 26, 8^h38^m	.....	.....	0.594.....	Apr. 30, 6^h2^m	−10.9	− 8.1
.009	Apr. 26, 8 57	− 6.1	− 5.6	.657.....	May 6, 8 17	.....	.....
.046.....	May 2, 10 18	.....	.....	0.708.....	May 3, 10 8	− 6.4	− 7.0
.285.....	May 7, 6 54	− 7.5	− 9.8				
.313.....	Apr. 28, 7 54	.....	.....	Mean velocities	.....	− 8.1	− 8.1
0.570.....	May 9, 5 10	− 9.4	−10.2				

The number of measures on which the mean is based is given in the last column, and $-\log W/\lambda$ is given in the third column. The lines are arranged according to element for easy comparison with Table 1 of Paper I. When the wave length is given to one decimal only, the measured line is a blend of two lines of the same element; if these were resolved in α^2 C Vn, the corresponding value of log η_0, if used here, has been found from the sum of the two equivalent widths in that star. The symbol "b" following the value of *W* indicates that the line is affected by blending, which may sometimes be different from the blending suffered in α^2 C Vn. As in α^2 C Vn, the *Dy* III identifications should still be regarded as provisional. The wave lengths given for *Dy* III are the means from the measures in HD 133029. The strongest unidentified lines are given at the end of Table 2. Here, when an element in parentheses follows the value of *W*, it means that the line was listed erroneously under that element in α^2 C Vn. The line λ 4509.40, listed as unidentified, is near a sensitive line of *Am* II. The possibility that this element might be present in peculiar A stars has been discussed elsewhere (Burbidge and Burbidge 1955*b*).

Comparison of the spectra of α^2 C Vn and HD 133029 shows that they are very similar. Qualitatively, the main differences are: (1) lines of *Si* II are stronger in HD 133029; (2) lines of *Cr* and, to a lesser extent, *Fe* tend generally to be stronger in HD 133029

TABLE 2

EQUIVALENT WIDTHS

λ	W (mA)	−log W/λ	No.
	Mg II		
4428.00	59 b	4.88	7
4481.23	474	3.97	8
	Al II		
3995.86	65 b	4.79	1
4026.50	33	5.08	7
4226.83	25	5.23	1
4227.5	75	4.76	3
4585.82	28	5.21	2
	Si II		
3856.02	477	3.91	8
3862.59	365	4.03	8
4075.45	197 b	4.32	8
4076.78	162 b	4.40	8
4128.05	472	3.95	8
4130.88	466	3.95	8
4198.17	146	4.46	8
	Si III		
4552.61	58	4.90	2
4567.83	54	4.93	2
	P II		
4288.53	44 b	4.98	4
	Ca II		
3933.66	307	4.10	8
	Ti I		
4474.85	24	5.26	1
4518.02	46	5.00	1
	Ti II		
3913.46	88 b	4.65	8
4028.33	71	4.76	7
4163.64	81	4.71	7
4287.89	58	4.86	4
4294.10	69	4.79	7
4300.05	154	4.44	8
4301.93	50	4.93	5
4312.86	120	4.55	8
4314.98	121	4.55	6
4316.81	47	4.97	6
4367.66	56	4.89	5
4374.82	116 b	4.58	1
4386.86	82	4.72	6
4394.06	27	5.20	1
4395.03	115	4.58	4
4395.85	72 b	4.79	3
4399.77	70	4.79	5
4411.94	28	5.19	2
4417.72	64	4.84	3
4423.22	30	5.18	1
4450.49	61	4.87	6
4468.49	76	4.83	2
4470.86	30	5.17	1
4488.32	39	5.06	1
4501.27	113	4.60	7
4529.46	110 b	4.62	2
4545.14	68 b	4.83	2
4563.76	86	4.72	3
4568.31	19	5.38	1
4571.97	123	4.57	8
	V II		
4183.44	60	4.84	6
4600.19	63 b	4.86	1
	Cr I		
4254.35	182	4.37	8
4274.80	77	4.75	5
4545.96	36	5.10	1
	Cr II		
3856.93	52	4.88	4
3859.38	44	4.95	1
3865.59	209	4.27	8
3866.54	92	4.63	4
3868.32	47	4.92	5
3869.62	24	5.20	3
3909.17	53	4.86	1
3911.4	119	4.52	8
3914.13	96 b	4.61	7
3936.95	32	5.10	5

TABLE 2—*Continued*

λ	W (mA)	−log W/λ	No.
	Cr II—*Continued*		
4003.33	128	4.49	8
4006.75	50	4.90	3
4007.56	31	5.10	2
4012.50	237	4.23	8
4017.96	83	4.68	6
4022.36	110	4.56	6
4038.03	148	4.44	8
4051.97	133	4.49	8
4054.11	146	4.44	1
4056.07	62	4.81	2
4070.90	114	4.55	8
4072.56	168	4.38	8
4082.30	107	4.58	8
4145.77	209	4.30	8
4151.00	98	4.63	6
4161.05	119 b	4.54	1
4170.86	119	4.54	3
4172.60	77	4.73	2
4179.43	130	4.51	8
4185.50	31	5.13	3
4195.41	138	4.48	7
4207.35	108	4.58	3
4209.02	70	4.77	4
4224.85	109	4.59	5
4242.38	195	4.34	8
4250.51	135 b	4.50	8
4252.62	189	4.35	5
4256.16	83	4.71	7
4261.92	173	4.39	8
4269.1	212	4.30	8
4275.57	139	4.49	5
4284.21	156	4.44	8
4302.58	35	5.09	1
4306.95	118	4.56	8
4309.75	55	4.89	5
4382.53	85	4.71	3
4465.78	77	4.76	3
4539.62	178 b	4.41	8
4555.02	183	4.40	7
4558.66	333	4.14	8
4564.27	67	4.83	3
4565.78	114	4.60	8
4587.30	78	4.77	4
4588.22	235	4.29	7
4589.89	149 b	4.49	7
4591.39	32	5.15	1
4592.09	171	4.43	7
4616.64	227	4.30	7
4618.83	204	4.35	7
4634.11	145	4.51	6
4697.62	100	4.67	4
	Mn I		
4041.36	52 b	4.90	2
4235.29	64 b	4.82	3
4502.22	33 b	5.14	1

λ	W (mA)	−log W/λ	No.
	Mn II		
4010.84	13	5.49	1
4125.86	34	5.07	1
4136.91	77	4.74	1
4206.38	43	4.99	1
4259.20	62 b	4.83	8
4510.21	23	5.29	1
	Fe I		
3859.91	100	4.59	8
3927.92	66 b	4.77	1
4005.25	102 b	4.59	8
4045.82	125	4.51	8
4063.60	127	4.51	8
4071.74	51	4.90	7
4143.6	104	4.60	1
4202.03	92 b	4.66	4
4235.94	46	4.96	2
4260.48	56	4.88	6
4271.5	127	4.53	3
4282.41	65 b	4.82	5
4299.24	47	4.96	4
4307.91	136 b	4.50	7
4383.55	98	4.65	5
4404.75	145	4.48	8
4415.12	79	4.74	1
4459.12	28	5.21	1
4466.55	35 b	5.11	1
4476.02	56	4.91	3
4547.85	36 b	5.10	1
	Fe II		
3863.95	105	4.57	4
3935.94	114	4.54	8
3938.29	101 b	4.59	7
3938.97	95	4.62	7
4024.55	117	4.54	7
4031.46	70	4.76	7
4032.95	124 b	4.51	8
4044.01	59	4.84	7
4048.83	200 b	4.31	8
4057.46	117	4.54	7
4061.79	69	4.77	4
4069.88	59	4.84	1
4122.64	201	4.31	8
4124.79	54	4.89	6
4138.21	64	4.81	2
4173.45	188	4.35	8
4178.86	130	4.51	8
4233.17	348	4.08	8
4258.16	181	4.37	8
4263.90	83	4.71	5
4273.32	150	4.46	7
4278.13	123 b	4.54	7

TABLE 2—*Continued*

λ	W (mA)	−log W/λ	No.
	Fe II—Continued		
4286.31	64	4.83	6
4296.57	172	4.40	7
4303.17	240	4.26	8
4314.29	107	4.60	6
4319.72	79	4.74	6
4361.25	96	4.66	8
4369.40	122 b	4.55	8
4385.38	181	4.38	8
4389.40	27	5.21	2
4402.88	100	4.64	8
4413.60	94	4.67	2
4416.82	186	4.38	8
4431.63	78	4.76	2
4446.25	54	4.91	8
4449.66	56	4.90	3
4451.54	100	4.65	8
4455.26	101	4.65	8
4472.92	173	4.41	7
4474.19	67	4.83	4
4489.18	162	4.44	8
4491.40	89	4.70	5
4493.58	114	4.60	3
4499.71	109	4.62	6
4508.28	142	4.50	8
4515.34	294	4.19	8
4520.24	158	4.46	8
4522.63	187	4.38	7
4534.17	247 b	4.26	7
4541.52	147	4.49	8
4549.4	364	4.10	8
4555.90	188	4.38	7
4576.33	140	4.51	8
4579.52	106	4.63	1
4580.05	58	4.90	1
4582.84	135	4.53	8
4583.83	220	4.32	8
4598.53	91	4.70	5
4620.51	133	4.54	5
4625.90	132	4.54	5
4629.34	164	4.45	6
4631.90	48	4.99	2
4635.33	134	4.54	8
4656.97	155 b	4.48	7
4663.70	87	4.73	3
4666.75	128	4.56	4
4731.44	132	4.55	3
	Ni II		
4015.50	30	5.13	3
4067.05	46	4.95	1
	Sr II		
4077.71	175	4.37	8
4215.52	124	4.54	8
4305.45	36	5.08	1
3915.94	41	4.98	1
4149.22	41	5.01	1
4379.78	66	4.82	2
	La II		
3929.22	24	5.20	3
4286.97	18	5.38	3
4662.51	19	5.38	1
	Ce II		
3921.73	53 b	4.86	3
3993.82	34	5.07	5
4040.76	42	4.99	3
4042.58	51	4.90	6
4054.99	24	5.23	1
4123.7	40	5.01	5
4133.80	66	4.80	8
4137.65	58	4.86	1
4214.04	18	5.37	1
4222.60	71	4.78	1
4248.68	40	5.03	2
4285.37	24	5.25	1
4289.94	140	4.49	8
4388.01	18	5.39	1
4391.66	79	4.74	6
4418.78	70 b	4.79	2
4449.34	45	4.99	1
4460.21	37	5.08	1
4491.10	23	5.29	1
4527.35	68 b	4.83	1
4593.93	63	4.86	6
4628.16	50	4.97	1
4654.29	82	4.76	7
	Pr II		
3908.43	49	4.90	1
3924.14	46	4.93	1
4025.55	85 b	4.67	6
4293.58	12	5.54	2
4294.70	28	5.19	3
4371.2	78 b	4.75	3
4419.67	99 b	4.65	2
4628.75	74 b	4.80	1
	Nd II		
3869.04	23	5.22	2
3995.24	64	4.79	3
4020.87	36	5.04	4
4059.96	24	5.23	1

TABLE 2—*Continued*

λ	W (mA)	−log W/λ	No.
	Nd II—*Continued*		
4061.08	36	5.06	2
4135.32	44	4.98	3
4157.58	46 b	4.96	3
4175.61	64	4.81	7
4228.4	22	5.29	3
4290.96	34	5.10	2
4513.33	32	5.15	1
4594.46	25	5.27	1
	Sm II		
4229.70	51	4.92	5
4262.68	23	5.27	2
4292.18	37	5.06	2
4433.88	34	5.12	1
4434.32	103	4.64	7
4511.83	106 b	4.62	5
4537.95	31	5.17	3
	Eu II		
3907.10	41	4.98	3
3930.50	160	4.39	8
4062.15	22	5.28	1
4129.73	77	4.73	6
4141.72	48 b	4.94	1
4148.40	31	5.13	1
4213.48	48 b	4.94	2
4236.22	43	5.00	1
4270.50	38	5.06	1
4313.85	27	5.20	1
4399.32	41	5.03	1
4414.64	39	5.05	1
4435.58	37	5.08	2
4485.15	30	5.17	1
4504.8	94 b	4.68	1
	Gd II		
3916.51	36	5.03	1
3934.82	22	5.25	6
4046.84	33	5.09	1
4047.81	36	5.05	4
4053.29	86 b	4.68	1
4132.28	119 b	4.54	8
4184.25	114	4.56	8
4208.37	29	5.15	2
4212.00	24	5.24	3
4223.02	42	5.00	4
4238.78	74 b	4.76	3
4241.28	22	5.29	2
4243.84	27	5.20	1
4251.73	57	4.87	2
4253.37	54	4.90	1
4280.49	67	4.80	1
4292.75	16	5.42	1
4296.08	36	5.07	1
4304.5	52	4.91	1
4380.64	44	5.00	2
4406.67	120 b	4.56	5
4427.03	40	5.05	1
4436.22	17	5.41	1
4453.93	21	5.33	1
4471.29	62	4.85	5
4478.80	32	5.14	1
4483.33	56	4.90	3
4498.28	16	5.44	1
4517.10	23	5.29	1
4551.46	40	5.06	1
4581.09	48 b	4.98	1
4596.98	27	5.23	1
4619.63	35	5.11	1
4693.00	33	5.15	1
	Tb II		
3935.25	34	5.06	1
4276.75	8	5.70	1
4531.83	66 b	4.84	2
4584.62	48 b	4.98	1
	Dy II		
4010.08	27	5.17	1
4011.30	24	5.21	2
4027.79	32	5.11	1
4060.58	40	5.01	1
4143.10	83	4.70	3
4294.94	28	5.19	3
4409.38	102 b	4.63	6
4448.23	47 b	4.98	6
	Dy III		
4164.72	24	5.23	2
4199.26	46	4.96	7
4393.4	40	5.03	3
4514.33	88	4.71	5
4573.17	50	4.96	4
	Yb II		
4180.83	40	5.01	1
	Pb II		
4386.4	24	5.26	2

TABLE 2—*Continued*

λ	W (mA)	$-\log W/\lambda$	No.	λ	W (mA)	$-\log W/\lambda$	No.
	Some Well-defined Unidentified Lines				Some Well-defined Unidentified Lines—*Continued*		
3908.10	64	4.79	4	4430.24	105	4.63	2
3918.61	147	4.42	7	4447.56	53	4.92	7
3920.48	157	4.39	8	4461.61	155 (*Fe* I)	4.46	7
4167.04	99	4.62	7	4509.40	14	5.50	6
4177.64	135	4.49	8	4546.54	75	4.78	5
4196.46	58 (*Fe* I)	4.86	6	4595.92	130	4.54	7
4200.79	288	4.16	8	4621.60	253	4.26	7
4224.18	49	4.94	3	4637.92	90 (*Fe* I)	4.72	6
4377.00	248 (*Dy* III)	4.25	7	4673.35	210	4.35	4
4384.27	202 (*Pr* II)	4.33	8				

(this is more noticeable in the neutral elements); (3) lines of the rare earths are generally weaker in HD 133029; and (4) certain unidentified lines, present in α^2 C Vn, are stronger in HD 133029.

III. RESULTS FROM THE CURVE OF GROWTH

The conditions in the atmosphere of HD 133029 have been determined relative to those in α^2 C Vn by means of the curve of growth. Mean equivalent widths, W, have been converted to $\log W/b'$, where, as in Paper I, the thermal velocities v' corresponding to $T = 10{,}000°$ have been taken. By using values of $\log \eta_0$ taken from Table 1 of Paper I for all the elements, curves of growth have been plotted and are shown in Figures 1 and 2. The theoretical curves, as before, are those computed by Wrubel (1949) for a Milne-Eddington model with $B_0/B_1 = \frac{1}{3}$.

a) DAMPING

In Figure 1 the theoretical curves are drawn for three values of the damping parameter, $\log a = -3.0$, -1.8, and -1.4. The greater intensity of the strongest lines of *Fe* II and *Cr* II leads to distinctly better agreement with the curve for $\log a = -1.8$, corresponding approximately to classical damping. Although the curve for $\log a = -3.0$ was used in Paper I for all elements except *Si* II, *Mg* II, and *Ca* II and was also used by Buscombe (1951) for γ Gem, it appears artificial to force the points for HD 133029 onto this curve. Accordingly, we have taken the curve for $\log a = -1.8$ for all elements except *Si* II and *Mg* II, for which $\log a = -1.4$ has been used (this was the value used for these elements in Paper I).

b) EXCITATION TEMPERATURE

From a comparison between the plotted points for lines of high and low excitation potential of *Fe* I and *Fe* II, $\Delta\theta_{\text{exc}}$ between HD 133029 and α^2 C Vn is found to be negligible ($\Delta\theta_{\text{exc}}$ [HD 133029 − α^2 C Vn] < 0.04). Thus $T_{\text{exc}} \approx 8000°$ in Hd 133029, and no correction need be applied to $\log \eta_0$ taken from α^2 C Vn. This value is in agreement with that obtained from preliminary plots of *Fe* I lines, using laboratory gf-values.

c) IONIZATION TEMPERATURE AND ELECTRON PRESSURE

The hydrogen-line profiles in HD 133029 and α^2 C Vn are very similar, and the quantum number of the upper level of the last resolved line ($n = 19$) is the same in both

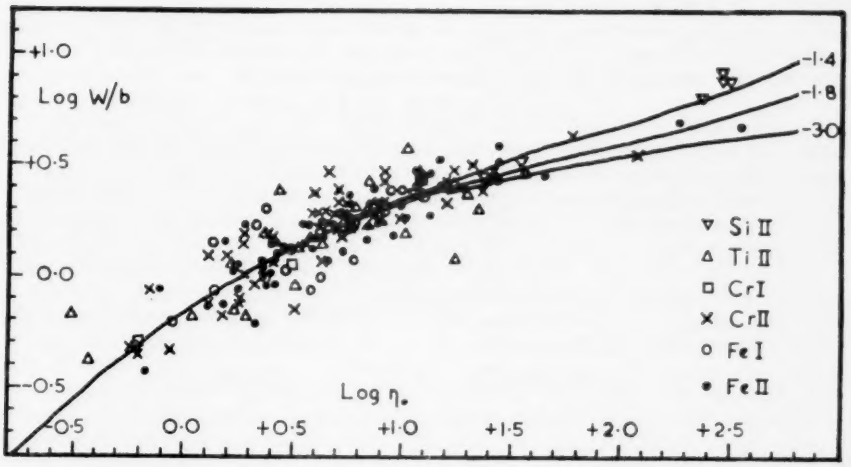

FIG. 1.—Curve of growth for *Si* II, *Ti* II, *Cr* I, *Cr* II, *Fe* I, and *Fe* II. The theoretical curves for $B_0/B_1 = \frac{1}{3}$ and $\log a = -1.4$, -1.8, and -3.0 are plotted.

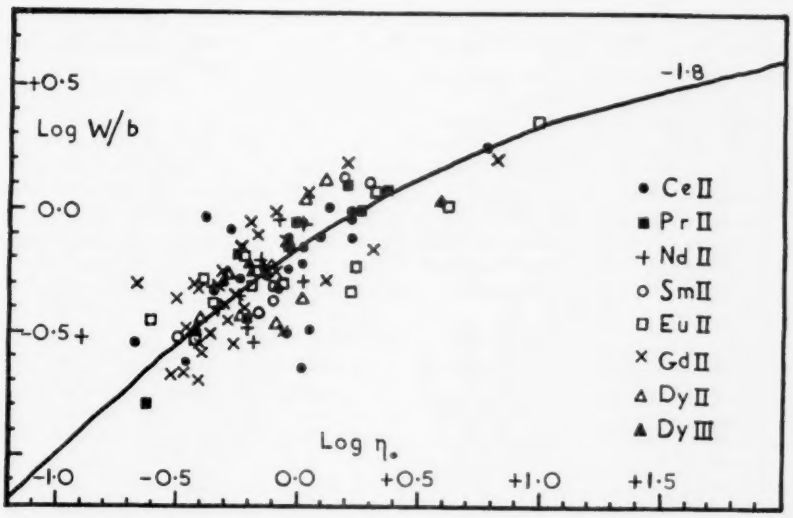

FIG. 2.—Curve of growth for *Ce* II, *Pr* II, *Nd* II, *Sm* II, *Eu* II, *Gd* II, *Dy* II, and *Dy* III. The theoretical curve for $B_0/B_1 = \frac{1}{3}$ and $\log a = -1.8$ is plotted.

stars. We conclude, therefore, that κ_λ and P_r have approximately the same values; thus for HD 133029 we take $\log P_r = 2.0$.

The ratios of the numbers of various ions of different elements in HD 133029 relative to those in α^2 C Vn have been determined, from the horizontal shift necessary to fit the points to the curve, by means of the relation (Paper I, eq. [3])

$$\Delta \log N_r = \Delta \log \eta_0 + \Delta \log v \,, \tag{1}$$

since $\Delta \log \kappa_\lambda$ and $\Delta\theta$ are effectively zero. Values of $\Delta \log N_r$ are tabulated in Table 3, third column. In the second column the number of lines used for each element is given. Several elements appear in two stages of ionization in both stars, and values of $\Delta \log N_r$ for these cases have been used to estimate $\Delta T_{\rm ion}$ by means of the Saha equation. From the ratios *Fe* II/*Fe* I, *Cr* II/*Cr* I, *Ti* II/*Ti* I, *Mn* II/*Mn* I, and *Dy* III/*Dy* II, $\Delta T_{\rm ion}$ (α^2 C Vn − HD 133029) = +300°, 600°, 500°, 300°, and 300°, respectively; *Fe* and *Cr* give the best-determined values. The mean is +400°. As was shown in Paper I, the absolute value of $T_{\rm ion}$ is uncertain in α^2 C Vn. We shall adopt 8400°, as before, so that $T_{\rm ion}$ = 8000° in HD 133029.

d) TOTAL EFFECTIVE VELOCITIES AND MAGNETIC INTENSIFICATION

The total effective velocities, v, obtained from the curve of growth, are given in the fourth column of Table 3. Ions with only a few lines do not give determinate values for

TABLE 3

RELATIVE ABUNDANCES OF THE ELEMENTS IN HD 133029

Element	No. of Lines	Δ log N_r (133029 − α^2 C Vn)	v (Km/Sec)	Abundance Ratios		
				133029/ α^2 C Vn	133029/ Standard	133029/Standard (Direct)
Mg	2	+0.55	.....	3.5	1.3	1.5 (1)
Al	4	+ .31	.....	2.0	2.2	.....
Si	7	+ .39	4.3	2.5	25	30 (1)
Ca	1	+ .58	.....	2.6	0.05	0.05 (1)
Ti I	2	+ .36	.....	1.0	2.6	2 (21)
Ti II	29	+ .04	2.9			
V	2	+ .39	.....	2.3	3.2	.....
Cr I	3	+ .74	4.7	1.8	9.6	11 (16)
Cr II	54	+ .26	5.2			
Mn I	3	+ .17	.....	1.0	15:	15: (1)
Mn II	5	− .02	.....			
Fe I	19	+ .36	3.7	1.5	4.3	4 (34)
Fe II	64	+ .17	4.9			
Ni	1	− .12	.....	0.8	2.4	1.5 (1)
Sr	2	+ .29	.....	1.1	16	7 (1)
Zr	3	+ .12	.....	1.3	38	42 (1)
La	3	− .5:	.....	0.2:	200:	.....
Ce	23	+ .02	5.3	0.6	230	150 (7)
Pr	7	+ .12	5.3	0.6	630	.....
Nd	11	+ .01	.....	0.6	140	260 (1)
Sm	7	+ .06	.....	0.6	260	.....
Eu	13	− .06	5.3	0.5	890	380 (3)
Gd	31	− .16	5.3	0.4	320	360 (5)
Tb	4	+ .10	6.6	0.8	.....	.....
Dy II	8	− .01	.....	0.6	460	.....
Dy III	5	− .20	.....			
Yb	1	− .06	.....	0.6	.....	.....
Pb	1	+0.02	.....	1.0	1500:	.....

both horizontal and vertical shifts. The vertical shift for *Ti* I was set equal to that for *Ti* II. The mean value of v for the metals is 4.3 km/sec; so the undetermined vertical shift for the elements up to and including *Zr* II, with the exception of *Ti* I, have been arbitrarily set equal to the value corresponding to this velocity. For those rare earths for which velocities were not determined and for *Pb*, the shift was set equal to that given by the best-determined elements, *Ce* II, *Eu* II, and *Gd* II.

The velocities v in HD 133029 show a general tendency to be slightly larger than those in α^2 C Vn (which were approximately equal to those found by Buscombe for γ Gem). We have used $\Delta \log v$ in equation (1) for deriving $\Delta \log N_r$ from $\Delta \log \eta_0$. The velocities in HD 133029, especially those given by the rare earths, tend to be rather large for a main-sequence star, and the question again arises as to what proportion, if any, can be attributed to magnetic intensification. The maximum observed field in HD 133029 is about twice that in α^2 C Vn.

The available *Fe* II lines range in Zeeman pattern from triplets with less than the normal triplet separation (e.g., λ 4491.40 with the pattern [0.00], 0.40) to lines with about twenty components and a total spread of about three times the normal triplet separation. When the points on the curve of growth are divided into groups according to number of components and total spread, the difference in ordinates for the different groups is found to be small. The maximum possible shift in ordinate between groups having the largest and smallest Zeeman patterns is 0.08, corresponding to a factor of 1.2 in W, between the two stars. In view of the scatter of the points, this is barely significant. The plotted points for *Ce* II, which also has a wide range of Zeeman patterns, have been examined in the same way, but no effect of different magnetic intensification in the two stars is detectable. The data and range of Zeeman patterns for the other rare earths are insufficient for any analysis to be made. The *Fe* II points have also been plotted with $\log \eta_0$ taken from the nonmagnetic star γ Gem. Here the maximum shift between lines with large and small Zeeman patterns is 0.06.

For a star with a magnetic field of 10,000 gauss, *Fe* II lines with the widest Zeeman patterns will have a total pattern width of about ten times the thermal Doppler half-width (Babcock 1949). The reason why this leads to so small an observed effect can only be that it is largely masked by true velocities due to the smallest eddies of hydromagnetic turbulence, so that magnetic intensification contributes only a small additional apparent velocity to the parameter v. Further work on stars with a range of magnetic fields is still needed to determine the relative contributions precisely, but we estimate that, in case of *Fe* II in HD 133029, magnetic intensification may contribute not more than 1 km/sec to the parameter v. As was previously emphasized, the effect on the derived abundances can only be small. It is clear that it cannot contribute appreciably to the differences in abundance of the rare earths and other elements described in the following sections.

IV. RELATIVE ABUNDANCES

From the values of $\Delta \log N_r$ in the third column of Table 3, abundances relative to α^2 C Vn have been derived by means of the Saha equation and are given in the fifth column. In the sixth column the abundances in α^2 C Vn relative to γ Gem and the sun (Paper I, Table 5) have been used to derive abundances in HD 133029 relative to these standard stars.

To estimate the errors which arise through fitting sets of scattered points onto the theoretical curve, we have used the values of $\log \eta_0$ for γ Gem to plot curves of growth and derive abundances directly relative to γ Gem, for the elements up to and including *Sr*. The results are given in the last column, together with the number of lines used, in parentheses. Since there are fewer lines common to γ Gem and HD 133029, this method is more uncertain. However, the results are seen to be in fairly good general agreement.

In order to check the results for the elements *Zr*, *Ce*, *Nd*, *Eu*, and *Gd*, a similar direct comparison has been made with the sun, using the method described in Paper I. The preliminary comparison of *Fe* I lines, in order to derive the zero-point error due to $\Delta \log \kappa_\lambda$

and $\Delta \log v$, gave a larger scatter than that quoted in Paper I; the mean error in the logarithm is ± 0.41. However, the abundances of these elements given in the last column of Table 3 are also seen to be in reasonable agreement with those in the sixth column. The factor 1.5 between the abundance of *Fe* in the two magnetic stars has been taken into account in deriving these abundances.

Before considering the results of the abundance determinations, we shall discuss various possible sources of error.

1. Systematic differences in equivalent-width measures, due to the different dispersions used in the two studies, are possible. The error involved would be less than 30 per cent (cf. Deutsch 1954) and would not account for the factor of 2 between the equivalent widths of the strong lines of *Si* II in the two stars. Also, such an error could not explain an effect which is proportionately larger for strong than for weak lines. Further, it could not explain the systematic weakening of the rare-earth lines in HD 133029.

2. A small increase in T_{exc} would increase the strength of the high-excitation-potential lines of *Si* II and *Mg* II. However, if there is any difference in T_{exc} between the two stars, amounting to a few hundred degrees, one would expect it to be a *decrease*, since T_{ion} is lower in HD 133029.

3. An error in T_{ion} is unlikely to have much effect, even for the rare earths (cf. the agreement in ΔT_{ion} derived from *Dy* and from the other elements, in Sec. III*c*).

4. The effect of using a larger damping constant for the metals in HD 133029 is to *minimize* the derived abundance increase. For *Mg* II, *Si* II, and *Ca* II the same damping constants, respectively, were used in both stars.

5. The uncertainty due to magnetic intensification has already been discussed. In the extreme cases we estimate that the slightly different magnetic intensification effects in the two stars would, at maximum, cause the abundances in HD 133029 to have been estimated too large by a factor of 1.2 for the rare earths and between 1.2 and 1.5 for the other elements.

V. DISCUSSION

This study has shown that HD 133029 is similar to α^2 C Vn as far as the abundance anomalies are concerned. The discussion of Table 3, given in the previous section, shows, however, that the abundance differences averaged over our periods of observation of the two stars are real, and it also enables us to place greater weight on some of the apparent anomalies which were not emphasized in Paper I. The metals, especially *Cr* and *Mn*, are more abundant in both stars than in normal A stars. *Fe* also is overabundant, but by a smaller factor. The mean factors for the group *Ti* to *Ni* are 6.2 (HD 133029) and 5.2 (α^2 C Vn), while the means for the best-determined of the group, *Ti*, *Cr*, and *Fe*, are 5.5 and 3.6, respectively. The mean overabundance ratio for *La* and the rare earths in this star is 390, whereas in α^2 C Vn it was 830; this reduction by a factor of about $\frac{1}{2}$ is significant. Though we were not able to make a quantitative estimate of the abundance of *Ba* in HD 133029, it does appear fairly certain that, in comparison with the elements of the rare-earth group, this element is greatly underabundant, as it was in α^2 C Vn, and any detailed theory of the abundance anomalies must account for this feature. Table 3 also shows that *Si* is more overabundant, and *Ca* slightly less underabundant in HD 133029 than in α^2 C Vn. HD 133029 is not among the stars examined in the infrared by Slettebak (1951), and we cannot say whether *O* is underabundant or not. The *Pb* abundance in Table 3 depends on one line, which was tentatively attributed to *Pb* II in Paper I, and is consequently uncertain.

We suggested in Paper I that these anomalies are due to surface nuclear reactions, and we described in a qualitative way how certain features may be explained. A more detailed study (Fowler, Burbidge, and Burbidge 1955) has shown that such a model is indeed very plausible, although it cannot as yet account for all the results. In particular, the overabundance of the metals is a difficult feature, since only a quasi-equilibrium

theory (Hoyle 1954) is apparently capable of building the normal metal peak in the cosmical abundance-curve. It is tempting to associate this anomaly with the intrinsic magnetism of this group of stars, so that it would be connected with the early condensation history of stars of this type. The occurrence of peculiar A stars in galactic clusters would, however, then imply differential concentrations of grains to gas in condensations. Further, the distribution of abundance anomalies within the metallic group does suggest that further nuclear processes on the stellar surface have produced them. Arguments based on initial condensation peculiarities would suggest that the metals are overabundant through the whole volume of the star and are not merely a skin effect, as we suppose is the case for the other elements. Since *Fe* is the main contributor to the metallic group in the "cosmical" abundance-curve, it is therefore most important to establish the reality or otherwise of the small overabundances which we have determined for this element in the two stars so far studied. The question will, it is hoped, be checked in a future paper by a comparison of other normal A stars with γ Gem. If this overabundance is real and has a different origin from the heavy-element anomalies, it becomes easier to explain these latter, since more metals are available to capture neutrons.

It has been shown in the previous section that the total velocities obtained from the curve of growth are, in general, greater in HD 133029 than in α^2 C Vn. But HD 133029 is not a magnetic variable in the same way that α^2 C Vn and HD 125248 are, and this difference is reflected in its small (possibly zero) radial-velocity variations and negligible equivalent-width variations. Thus, while the radial velocities measured in α^2 C Vn are probably representative of large-scale atmospheric motions through the magnetic cycle, superposed on a state of hydromagnetic turbulence (or to stellar rotation, depending upon which theory is assumed), the velocities measured from the curve-of-growth analysis are indicative of hydromagnetic turbulent motions alone. Dr. Strömgren[2] has pointed out to us that in normal A stars there is probably a very thin hydrogen convection zone, setting in at an optical depth $\tau = 0.25$ and extending only about 1000 km (there is some uncertainty concerning the possibility of a helium convection zone). If the extent of this convection zone remains unaltered in the presence of a magnetic field, it seems probable that we are looking into this zone. The small depth of the zone suggests that the hydromagnetic turbulence is highly anisotropic. That the pattern of motions is very complex is seen from the work of Chandrasekhar (1954), who has considered a convective layer in the presence of a uniform magnetic field when the field direction and that of gravity do not coincide. According to the theory of Cowling (1952), the magnetic variations of stars are due to nonradial mechanical oscillations. This theory might be applied to account for the small magnetic oscillation of a few hundred gauss in a period of $\sim 1\frac{1}{2}$ days, which Babcock has suggested may be present in HD 133029, but it could not easily account for the slow secular variation. On the other hand, it has been shown by Cowling and Sweet (1954) that an oscillator model of this sort cannot explain the reversing magnetic fields observed in many magnetic stars, if one assumes either a dipole or a quadrupole field. It does appear, however, that if the observations in all the peculiar A magnetic stars are being made of a layer which is in a state of anisotropic hydromagnetic turbulence, a new analysis must be made of the original observations, since, in obtaining the field strengths which are always used, Babcock has assumed that the field has a uniform dipole character. An analysis of this sort, in which the magnetic field is assumed to have a form dictated by the magnetoturbulence spectrum (which can be expanded in multipole form), is currently being attempted.

Finally, the bearing of Deutsch's oblique rotator theory (Deutsch 1952, 1955) on the abundance differences between α^2 C Vn and HD 133029 must be mentioned. If this theory is assumed, the observed differences in abundances between the two stars may not extend over the whole of the stellar surfaces. Since in a magnetic variable star like α^2 C Vn there are apparent abundance differences between positive and negative mag-

[2] Private communication.

netic-field phases (Paper I), a phase in α^2 C Vn could probably be found for which the apparent abundance determinations would agree with those found over the whole of the period of observations in HD 133029. If this star were being observed more nearly along the axis of rotation and the two spot regions, with their different element concentrations, were also near the poles of rotation, we might be able to explain qualitatively the constant sign of the magnetic polarity and lack of line-intensity variations and the abundance ratios relative to α^2 C Vn. This theory may provide an alternative to that of Cowling in explaining the possible $1\frac{1}{2}$-day period variation, but both theories meet with difficulties in explaining the possible secular variation.

This study was begun while the authors were working at the Yerkes and McDonald Observatories.

REFERENCES

Babcock, H. W. 1949, *Ap. J.*, **110**, 126.
Babcock, H. W., and Burd, S. 1951, *Pub. A.S.P.*, **63**, 81.
Babcock, H. W., and Cowling, T. G. 1953, *M.N.*, **113**, 357.
Burbidge, G. R., and Burbidge, E. M. 1955*a*, *Ap. J. Suppl.*, **1**, 431.
———. 1955*b*, *Observatory*, **75**, 116.
Buscombe, W. 1951, *Ap. J.*, **114**, 73.
Chandrasekhar, S. 1954, *Phil. Mag.*, **45**, 1177.
Cowling, T. G. 1952, *M.N.*, **112**, 527.
Deutsch, A. J. 1952, *Trans. I.A.U.*, **8**, 801.
———. 1954, *J. Opt. Soc. Amer.*, **44**, 492.
———. 1955, *Ann. d'ap.*, **18**, 1.
Fowler, W. A., Burbidge, G. R., and Burbidge, E. M. 1955, in preparation.
Hoyle, F. 1954, *Ap. J. Suppl.*, **1**, 121.
Provin, S. S. 1953, *Ap. J.*, **118**, 489.
Slettebak, A. 1951, *Ap. J.*, **113**, 437.
Sweet, P. A. 1954, *M.N.*, **114**, 549.
Wilson, R. E. 1953, *Catalogue of Radial Velocities*. ("Carnegie Institution of Washington Publications," No. 601 [Washington: Carnegie Institution.])
Wrubel, M. 1949, *Ap. J.*, **109**, 66.

THE SPECTRUM OF NU ERIDANI*

O. Struve and K. D. Abhyankar
Berkeley Astronomical Department, University of California
Received June 7, 1955

ABSTRACT

Observations in 1953–1954 confirm de Jager's and our own interpretation of our previous velocity-curves. The new results show that the absorption lines tend to be sharpest on the ascending branch near minimum and broadest on the descending branch near maximum. Three cycles show pronounced departures from the velocity-curves predicted on the basis of two interfering harmonic oscillations. There are some indications that, in addition to $P_1 = 0.1779$ day and $P_2 = 0.1735$ day, there is a third period, $P_3 = 0.064$ day and $K_3 = 5$ km/sec.

In a previous paper Struve *et al.* (1952) discussed the radial-velocity observations of ν Eridani over a period of about fifty years. A beat phenomenon was detected, and a beat period of 6.9808 days was found to represent the observations fairly well. However, it was difficult to ascertain the exact beat period because of irregular variations in the smaller amplitude, K_1. The following periods and amplitudes were obtained:

$$P_1 = 0.1779 \text{ day}, \qquad K_1 = < 8\text{–}15 \text{ km/sec},$$

$$P_2 = 0.1735089 \text{ day}, \qquad K_2 = 24.5 \text{ km/sec}.$$

C. de Jager (1953) tried to separate the dominant variation by constructing a mean curve for the period $P_2 = 0.1735089$ day. The residuals could then be combined to form a mean curve with period $P_1 = 0.1779$ day. These two periods represented the variation of radial velocity as well as of magnitude. They confirmed the previous value of the beat period, viz., 6.9808 days. The mean values of K_1 and K_2 were 10.6 and 20.2 km/sec, respectively.

The present observations confirm these results. But the radial velocity-curves show more complicated shapes, perhaps because of the greater dispersion used in the current work. It seems that the observations cannot be interpreted as a combination of two pure sine-curves.

All the measured spectrograms were obtained during 1953–1954 by Struve (on five nights) with the 100-inch coudé spectrograph of the Mount Wilson Observatory (designated "Cd") and by McNamara (on two nights) with the Mills three-prism spectrograph and the three-prism combination spectrograph with the 12-inch camera of the Lick Observatory (designated "LS"). The coudé plates taken on October 24, 1953, September 19, 1954, and November 18, 1954, have a dispersion of 4.5 A/mm, and the Lick plates taken on October 14, 1954, have a dispersion of 25 A/mm. The rest of the plates have a dispersion of 10 A/mm. The lines which were measured are listed in Table 1.

The observed radial velocities and phases, calculated from maximum radial velocity, are given in Table 2 and are plotted in Figure 1. The observed and calculated minima and maxima, and the differences (O − C) are given in Table 3. They were obtained from:

$$\text{Minimum} = 2423709.816 + 0.1735089E;$$

$$\text{Maximum} = 2433965.857 + 0.1735089E.$$

The differences (O − C) for the minima are small (except for October 14, 1954) and show that the period $P_2 = 0.1735089$ is correct. The differences (O − C) for the maxima

* The observational material used in this paper was obtained at Mount Wilson and Lick Observatories by O. Struve and D. H. McNamara, respectively.

are systematically negative except for October 21, 1954. In order to see whether this was due to the beat phenomenon, theoretical differences (O − C) were calculated for the three pairs of values of K_1 and K_2, already given, by means of the formula (Struve 1950):

$$\phi = \tan^{-1}\left\{\frac{K_1 \sin \phi}{K_2 + K_1 \cos \phi}\right\}.$$

Upon fitting these curves with the differences (O − C) for the present observations, as well as the observations of 1951–1952, it seems that the epoch of the maximum can be changed by 8×10^{-3} days to 2433965.849 (Fig. 2). But even after making this change, many of the points lie considerably off any of the curves.

In order to verify the beat period, the observed values $2K$, given in Table 4, were plotted against the phases of the beat period. Figure 3, which contains these points, as well as three theoretical curves, shows that the estimated period of 6.9808 days is fairly accurate. But it appears that K_1 and to some extent K_2 are irregularly variable. This and the scatter of points in Figure 2 indicate that the oscillations involved are not simple

TABLE 1

LIST OF MEASURED LINES

Wave Length	Identification	Plate*	Wave Length	Identification	Plate*
3964.73	*He* I	Cd	4349.43	*O* II	Cd, LS_2
3973.26	*O* II	Cd	4387.93	*He* I	Cd, LS_2
4026.19	*He* I	Cd	4414.91	*O* II	Cd, LS_2
4072.16	*O* II	Cd	4416.98	*O* II	Cd, LS_2
4075.87	*O* II	Cd	4471.48	*He* I	Cd, LS_2, LS_1
4101.74	*Hδ*	Cd	4481.23	*Mg* II	Cd, LS_2, LS_1
4119.22	*O* II	Cd	4552.65	*Si* III	Cd, LS_2, LS_1
4120.81	*He* I	Cd	4567.87	*Si* III	Cd, LS_2, LS_1
4143.76	*He* I	Cd	4574.78	*Si* III	Cd, LS_2, LS_1
4340.47	*Hγ*	Cd, LS_2	4590.97	*O* II	Cd, LS_1
4345.56	*O* II	Cd, LS_2	4596.17	*O* II	Cd, LS_1
4347.42	*O* II	Cd, LS_2			

* Cd = Mount Wilson coudé; LS_1 = Lick 10 A/mm; LS_2 = Lick 25 A/mm.

harmonic. Also the radial velocity-curves are complicated, particularly when $2K$ is small.

Unlike DD Lacertae, BW Vulpeculae, and σ Scorpii, no doubling of spectral lines was observed on any of the plates. But the lines showed broadening near the maximum, on the descending branch of the velocity-curve. The plates on which the lines were sharpest are marked by *s*, and those on which the lines were broadest are marked by *b* in Figure 1. We note that on all curves the sharpest lines occur on the ascending branch near the minimum and the broadest lines are found on the descending branch near the maximum. This agrees with the previous result that the line broadening is associated with period P_2.

In the curve for December 8, 1954, we find two distinct maxima. In this case the lines are sharpest on the main ascending branch at the point marked *ss*. They become broad on the descending portion after the first maximum. The lines become sharp again on the ascending portion of the second maximum, but they are not so sharp as in the first case. Hence this point is marked by a single *s*. Finally, the lines again become broad on the main descending branch of the curve. It is interesting to note that a similar sharpening and broadening of the lines has been observed in the case of BW Vulpeculae (McNamara *et al.* 1955).

At first sight it is tempting to interpret the flat portion of the velocity-curve on December 8, 1954, between 0.790 and 0.825 as a "stillstand" of the kind observed pre-

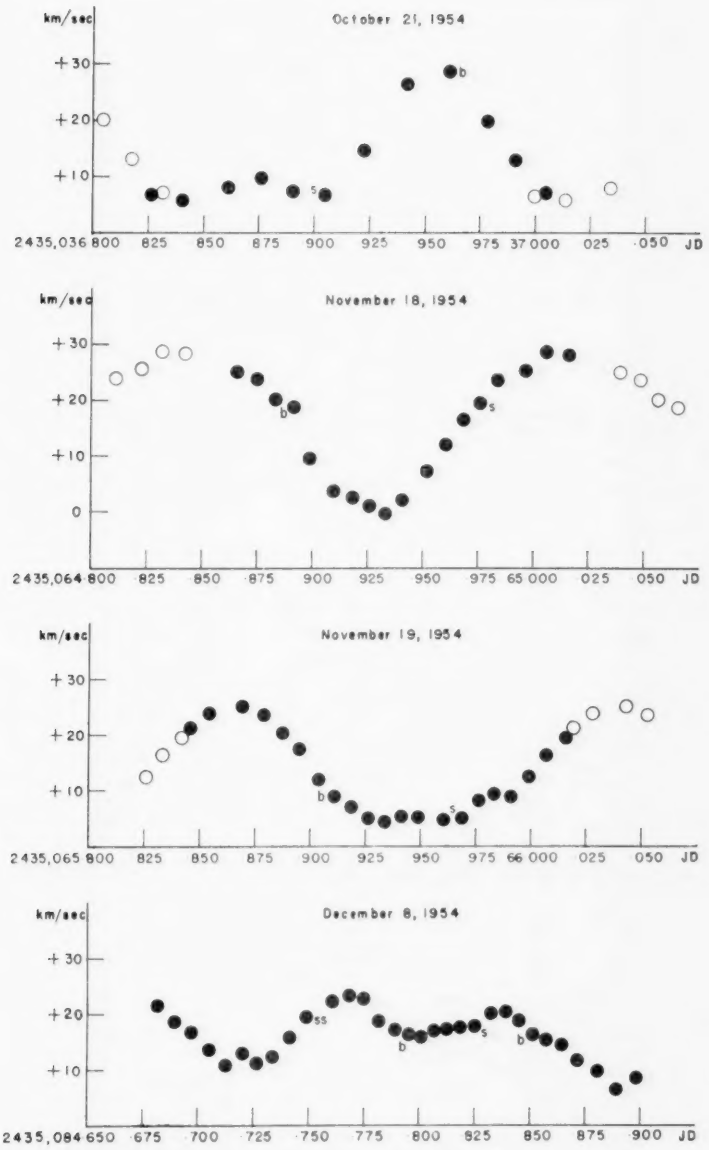

FIG. 1*a*—Individual radial velocities of ν Eridani

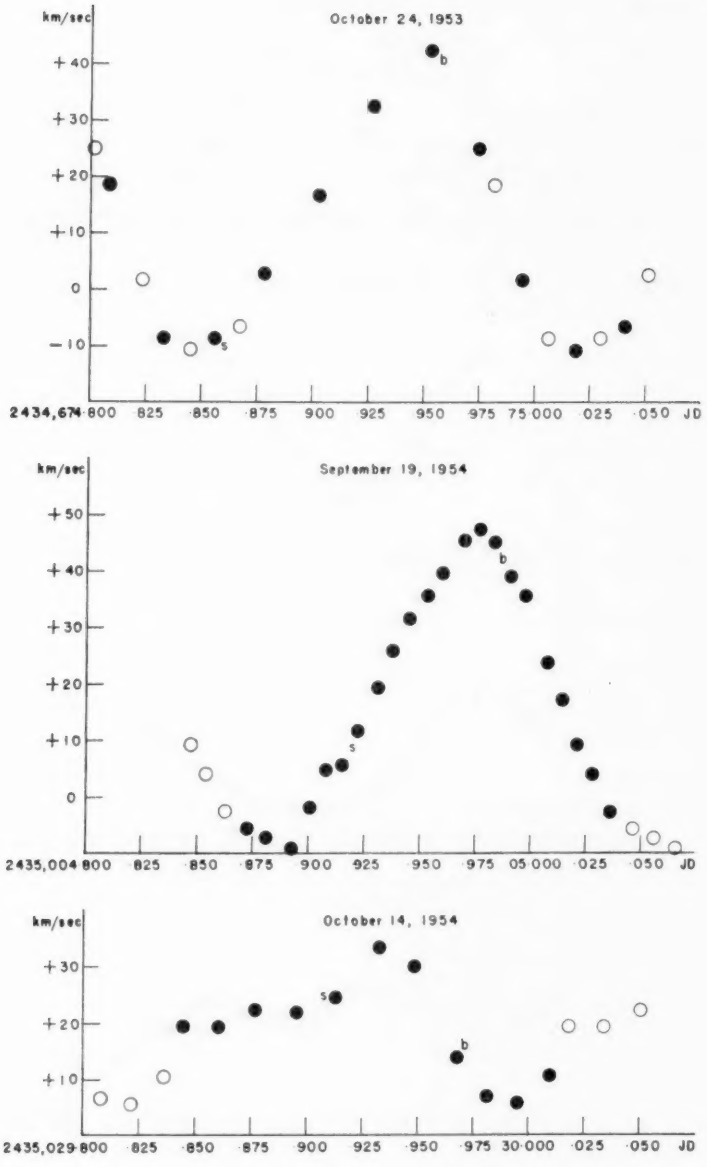

FIG. 1*b*.—Individual radial velocities of ν Eridani

TABLE 2

OBSERVED RADIAL VELOCITIES

Plate	JD 243+	Phase (Days)	Velocity (Km/Sec)	Plate	JD 243+	Phase (Days)	Velocity (Km/Sec)
Cd.....	4674.808	0.035	+18.5	Cd.....	5064.926	0.083	+ 1.0
	.833	.060	− 8.7		.933	.090	− 0.4
	.856	.083	− 8.7		.941	.098	+ 2.1
	.878	.106	+ 2.7		.952	.109	+ 7.2
	.903	.130	+16.7		.960	.117	+12.1
	.927	.154	+32.3		.968	.125	+16.6
	.953	.006	+42.4		.976	.133	+19.6
	.975	.028	+25.0		.984	.141	+23.7
	.997	.050	+ 1.6		.996	.154	+25.3
	4675.019	.072	−10.8		5065.006	.163	+28.7
	.041	.094	− 6.5		.016	.173	+28.2
	5004.873	.069	− 5.6		.846	.156	+21.2
	.882	.078	− 7.2		.854	.164	+23.8
	.892	.089	− 9.1		.869	.005	+25.0
	.901	.097	− 2.0		.879	.015	+23.5
	.908	.105	+ 4.6		.888	.024	+20.2
	.915	.112	+ 5.5		.895	.031	+17.4
	.922	.119	+11.6		.904	.040	+11.9
	.931	.128	+19.3		.911	.047	+ 8.9
	.938	.134	+25.7		.919	.055	+ 6.9
	.945	.141	+31.5		.926	.062	+ 5.1
	.953	.149	+35.6		.934	.070	+ 4.4
	.960	.156	+39.7		.942	.078	+ 5.2
	.969	.166	+45.3		.949	.085	+ 5.2
	.976	.173	+47.4		.960	.096	+ 4.7
	.983	.006	+45.2		.969	.105	+ 5.0
	.990	.013	+39.1		.976	.112	+ 8.2
	.997	.020	+35.6		.983	.119	+ 9.3
	5005.008	.031	+23.8		.991	.127	+ 8.9
	.015	.038	+17.1		.999	.135	+12.5
	.021	.044	+ 9.2		5066.007	.143	+16.2
	.028	.051	+ 3.9		.015	.151	+19.5
	.036	.059	− 2.8		5084.682	.088	+21.4
LS_2.....	5029.845	.082	+19.3		.690	.096	+18.6
	.860	.097	+19.2		.697	.103	+16.8
	.877	.114	+22.2		.705	.111	+13.5
	.896	.133	+21.8		.712	.118	+10.8
	.913	.150	+24.5		.720	.126	+12.9
	.933	.170	+33.2		.727	.133	+11.1
	.949	.012	+29.9		.734	.140	+12.2
	.967	.030	+13.8		.742	.148	+15.8
	.981	.044	+ 6.8		.749	.155	+19.4
	.995	.058	+ 5.7		.760	.166	+22.2
	5030.010	.073	+10.3		.768	.000	+23.2
LS_1.....	5036.826	.046	+ 6.7		.775	.007	+22.7
	.840	.060	+ 5.8		.782	.014	+18.6
	.861	.081	+ 8.0		.789	.021	+17.0
	.876	.096	+ 9.7		.795	.027	+16.2
	.890	.110	+ 7.3		.801	.033	+15.8
	.905	.125	+ 6.8		.807	.039	+17.0
	.922	.142	+14.7		.812	.044	+17.2
	.942	.162	+26.4		.818	.050	+17.5
	.960	.006	+28.7		.825	.057	+17.8
	.978	.024	+20.0		.833	.065	+20.1
	.991	.037	+13.0		.839	.071	+20.3
	5037.005	.051	+ 7.1		.845	.077	+18.8
Cd.....	5064.866	.023	+25.0		.851	.083	+16.3
	.875	.032	+23.6		.858	.090	+15.2
	.883	.040	+20.1		.865	.097	+14.4
	.892	.049	+18.7		.872	.103	+11.7
	.899	.056	+ 9.6		.881	.113	+ 9.6
	.910	.067	+ 3.7		.890	.122	+ 6.2
	.918	0.075	+ 2.5		.899	0.131	+ 8.4

TABLE 3

THE OBSERVED AND CALCULATED MAXIMA AND MINIMA
(Minimum = 2423709.816 + 0.1735089E; Maximum = 2433965.857 + 0.1735089E)

DATE	E	OBSERVED JD	CALCULATED JD	DIF.
	Minimum			
Oct. 24, 1953	63196	2434674.846	2434674.884	-38×10^{-3}
	63197	2434675.020	2434675.058	−38
Sept. 19, 1954	65098	2435004.888	2435004.898	−10
	65099	2435005.061	2435005.072	−11
Oct. 14, 1954	65242	2435029.815	2435029.884	−69
	65243	2435029.991	2435030.057	−66
Oct. 21, 1954	65282	2435036.840	2435036.824	+16
	65283	2435037.015	2435036.998	+17
Nov. 18, 1954	65444	2435064.929	2435064.932	− 3
Nov. 19, 1954	65450	2435065.949	2435065.974	−25
Dec. 8, 1954	65558	2435084.720	2435084.712	+ 8
	65559	2435084.893	2435084.886	+ 7
	Maximum			
Oct. 24, 1953	4087	2434674.947	2434674.988	−41
Sept. 19, 1954	5989	2435004.977	2435005.002	−25
Oct. 14, 1954	6133	2435029.937	2435029.987	−50
Oct. 21, 1954	6173	2435036.954	2435036.927	+27
Nov. 18, 1954	6334	2435064.843	2435064.862	−19
	6335	2435065.015	2435065.036	−21
Nov. 19, 1954	6340	2435065.864	2435065.903	−39
	6341	2435066.040	2435066.077	−37
Dec. 8, 1954	6449	2435084.768	2435084.816	−48

TABLE 4

OBSERVED $2K$

Date	Observed $2K$ (Km/Sec)	(O−C) (Maximum) (Days)	Phase (Days)	Date	Observed $2K$ (Km/Sec)	(O−C) (Maximum) (Days)	Phase (Days)
Oct. 24, 1953	54.5	-41×10^{-3}	4.7	Nov. 18, 1954	29.7	-20×10^{-3}	3.7
Sept. 19, 1954	57.0	−25	6.6	Nov. 19, 1954	21.4	−38	4.8
Oct. 14, 1954	29.2	−50	3.7	Dec. 8, 1954	14.6	−48	2.6
Oct. 21, 1954	24.0	+27	3.7				

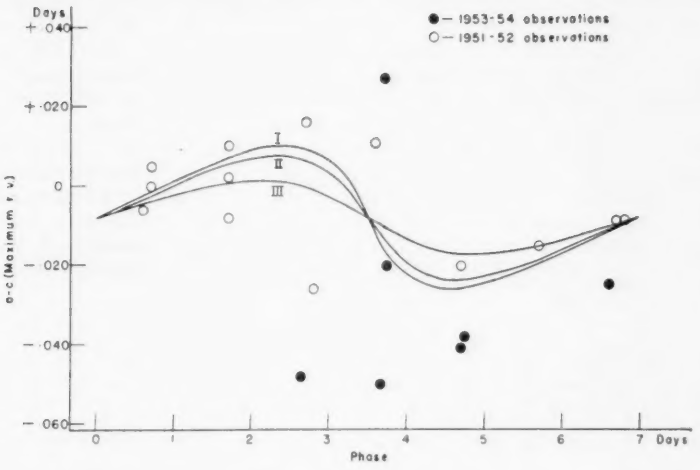

FIG. 2.—Differences (O−C) for maximum radial velocity. *I*, $K_1 = 15.0$ km/sec, $K_2 = 24.5$ km/sec; *II*, $K_1 = 10.6$ km/sec, $K_2 = 20.2$ km/sec; *III*, $K_1 = 8.0$ km/sec, $K_2 = 24.5$ km/sec.

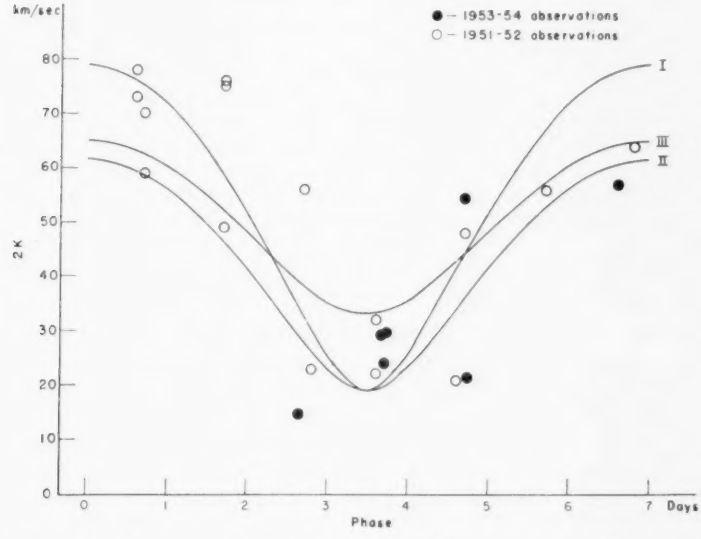

FIG. 3.—Observed and theoretical values of $2K$. *I*, $K_1 = 15.0$ km/sec, $K_2 = 24.5$ km/sec; *II*, $K_1 = 10.6$ km/sec, $K_2 = 20.2$ km/sec; *III*, $K_1 = 8.0$ km/sec, $K_2 = 24.5$ km/sec.

viously in BW Vulpeculae and σ Scorpii. But this is impossible for two reasons: (*a*) The computed maximum, uncorrected for the value of the initial epoch, is 0.816; after correction this becomes 0.808: both values fall upon the flat portion, while in BW Vulpeculae the computed maximum always *preceded* the "stillstand." (*b*) The phenomenon of double maxima and minima is pronounced only when the total range in velocity is small; in σ Scorpii the "stillstand" is most pronounced when the range is large.

We are undoubtedly concerned with another periodicity similar to those discovered by T. Walraven (1955) in AI Velorum. The present material is insufficient to examine this third period in detail. But on three nights we can estimate its value as follows: interval between two minima, October 14, 1954, 0.063 day; interval between two minima, October 21, 1954, 0.063 day; interval between two maxima, December 8, 1954, 0.067 day. We therefore suggest that there may be a period $P_3 = 0.064$ day, with an amplitude of $K_3 = 5$ km/sec.

REFERENCES

Jager, C. de. 1953, *B.A.N.*, **12**, 88.
McNamara, D. H., Struve, O., and Bertiau, S. J. 1955, *Ap. J.*, **121**, 326.
Struve, O. 1950, *Ap. J.*, **112**, 537.
Struve, O., *et al.* 1952, *Ap. J.*, **116**, 398.
Walraven, T. 1955, *B.A.N.*, **12**, 223.

THE SPECTRUM OF THE SLOW NOVA V 356 AQUILAE (1936)

DEAN B. MCLAUGHLIN
University of Michigan Observatory
Received June 9, 1955

ABSTRACT

This star was a typical slow nova of the RR Pictoris type. Numerous Lick Observatory spectrograms and several Mount Wilson Observatory plates were measured. From September to December, 1936, three absorption spectra were present: principal, −450 km/sec; diffuse enhanced (two components) −900 to −1300 km/sec; Orion, varying from −900 to −1500 km/sec. Prominent secondary maxima of light were accompanied by strengthening of the less displaced line of the diffuse enhanced absorption and disappearance of the more displaced. Orion lines weakened at light-maxima and were least displaced at or before maxima. Excitation of the emission spectrum was highest during light-minima. Emissions of [*Fe* II] were probably present in November–December. Neither *N* III absorption nor flaring *N* III emission was recorded. The nebular stage was well developed by February, 1937. The behavior in all respects resembled that of other strongly fluctuating novae. The oscillations of Orion lines are considered real, while those of the diffuse enhanced spectrum are probably illusory and due to variations of blended components.

INTRODUCTION

One marked characteristic of slow novae is the conspicuous fluctuation of brightness during the first 2 or 3 mag. of the decline of light. Secondary maxima nearly equal to the primary maximum of light are of common occurrence. Examples of this behavior were given by RR Pictoris (1925), T Aurigae (1891), DQ Herculis (1934), and V 849 Ophiuchi (1919). Striking changes in the spectrum usually accompany the light-variations. Each brightening is marked by a return to a spectrum that resembles an earlier stage of its development. Apparent oscillations of positions of the lines of the Orion and "diffuse enhanced" spectra are usually correlated with the changes of brightness and spectrum.

Nova V 356 Aquilae was typical of this class of slow novae. The present study was undertaken especially to furnish more data on the relationships between light-oscillations and changes of spectrum and velocity. The spectrum was described briefly by Wyse (1936). The author (McLaughlin 1937*a*, 1943, p. 173, 1944) has published brief accounts of a part of the spectral changes and of the apparent velocity variations that accompanied the most prominent observed secondary maximum of light.

Light-curves have been reproduced in three places (Campbell 1937; Beyer 1939; Campbell and Jacchia 1941). All these are shown on a rather small scale.

THE LIGHT-VARIATIONS

Nova V 356 Aquilae was first recognized by Nils Tamm of Bro, Sweden, on September 18, 1936 (*Harvard Anno. Card*, No. 388). Prediscovery photographs showed that it had risen rapidly from minimum, about magnitude 16.0, to 9.5 between July 17 and 19, after which it brightened more gradually for several days (Campbell 1937). Quite possibly the primary maximum of light occurred during an unobserved interval between July 31 and August 10. If so, it could have been of magnitude 7.0 or brighter. Thereafter, the brightness oscillated irregularly between magnitudes 9.0 and 7.6, until the date of discovery. From September 28 to October 3, the star brightened through 1.5 mag., reaching its brightest recorded maximum, 7.1, from which it immediately declined to 8.6 on October 8. Several additional large fluctuations and many minor ones were recorded during the next 2 months, after which the star was unobserved for several weeks near conjunction with the sun. When it was next seen, early in 1937, it was about magnitude 10.3, indicating a fairly steady decline since December. There seems to be no possibility that a very

deep minimum like that of Nova Herculis had occurred. Rather, V 356 Aquilae was of the RR Pictoris type and passed through the "transition" stage fairly smoothly. A portion of the light-curve is reproduced in Figures 1 and 2, to show the correlation with the spectral changes.

SPECTROGRAMS AND MEASUREMENTS

This study is based mainly upon a long series of spectrograms of the blue-violet region taken at the Lick Observatory with the two-prism spectrograph and the 6-inch camera on the 36-inch refractor. In the visual region several plates were obtained with the one-prism and the 16-inch camera. Dispersions are, respectively, 77 A/mm at $H\gamma$ and 120 A/mm at D. The entire series is of high quality.

Several good spectrograms were obtained at Mount Wilson with the 60-inch reflector and three-prism "ultraviolet" spectrograph with 10-inch camera, dispersion 38 A/mm at $H\gamma$. One plate of dispersion 70 A/mm was taken with the one-prism spectrograph on the 60-inch, and a film of the visual region was obtained with one prism on the 100-inch.

Three measurable plates of dispersion 40 A/mm were obtained at Ann Arbor with the 37-inch reflector and one-prism spectrograph. A very wide slit was used, and the spectra are of only fair quality.

The Mount Wilson plates were measured during a visit there in 1940. Later in the same year, through the kindness of the late Dr. Arthur B. Wyse, the writer was able to measure several Lick spectrograms to fill gaps in the Mount Wilson and Ann Arbor records for the interval September 22–October 9. Finally, during a visit to the Lick Observatory in 1951, the writer was privileged to study and measure all the long series of plates. A number of slitless spectrograms taken with the Crossley reflector and two quartz prisms were studied qualitatively but were not measured.

The complete identification of all visible spectral features was not attempted. A detailed critical examination and comparison with other novae showed that no feature previously unrecorded in normal novae was of appreciable strength. All sufficiently well-defined absorption lines and the more prominent emission-band edges were measured. Eye-estimates of intensity were recorded for most features. Radial velocities of absorption systems were obtained from selected lists of lines of undoubted identification. Means for each absorption system are given in Table 1, where most of the column headings are self-explanatory.

GENERAL ACCOUNT OF THE SPECTRUM

The first spectrograms available for this study were taken at Ann Arbor and Lick Observatory, September 22 (U.T.), during a minimum of light at magnitude 8.8. The spectrum then contained three sets of absorption lines, briefly described below. The nomenclature is that defined by the writer (McLaughlin 1942, 1943, p. 151).

1. *The principal spectrum.*—A many-lined set of sharp lines, resembling the spectrum of α Cygni, with velocity -460 km/sec.

2. *The diffuse enhanced spectrum.*—A set of wide and diffuse lines of hydrogen, *Mg* II, *Ca* II, and *Fe* II, with velocity -900 km/sec. The hydrogen lines were flanked by additional components with velocity -1130 km/sec.

3. *The Orion spectrum.*—A diffuse set of lines of *He* I, *N* II, and *O* II, with velocity -1080 km/sec.

When the nova brightened to magnitude 7.1 on October 3, the diffuse enhanced spectrum was greatly intensified, and the flanking hydrogen components disappeared. The Orion spectrum faded away entirely, except for the faint persistence of two or three lines. The principal spectrum was appreciably strengthened. With the decline to a minimum October 8, the spectrum reverted approximately to its appearance at discovery.

Later fluctuations of light were accompanied by similar changes, but, as the light declined and each succeeding maximum was lower, the absorption systems were differently affected. Thus a minimum about November 9 was accompanied by weakness of both the

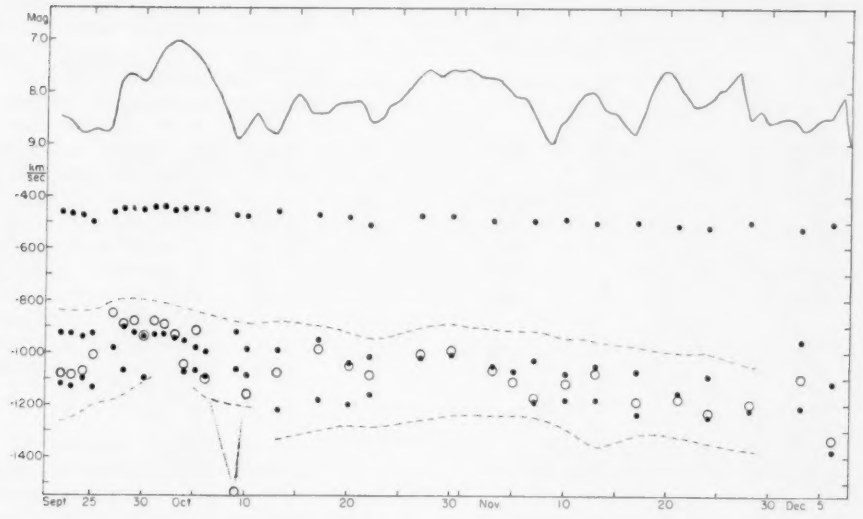

FIG. 1.—*Above*, visual light-curve of V 356 Aquilae based on observations by the A.A.V.S.O. (*Harvard Ann.*, Vol. **104**) and European observers (*A.N.*, Vols. **260** and **261**), combined by the author. *Below*, daily means of absorption velocities. *Black dots*, *upper row*, principal absorption; *lower band*, diffuse enhanced absorption (two components). *Open circles*, Orion absorption. Dashed curves represent positions of edges of wide composite absorption.

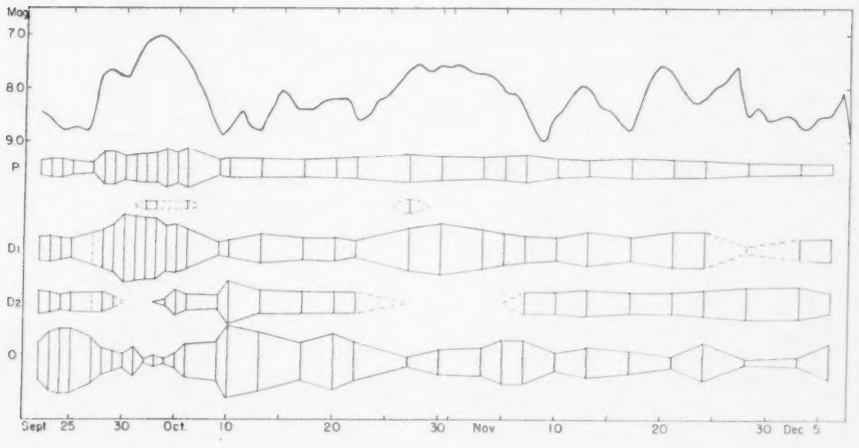

FIG. 2.—*Above*, visual light-curve. *Below*, intensity graphs for absorption systems of V 356 Aquilae. The width of each band represents the intensity of the system, based on eye-estimates of lines. *P* = principal; *D1* = inner component of diffuse enhanced system; *D2* = outer component; *O* = Orion absorption. The temporary component of small displacement is shown above *D1*.

TABLE 1

RADIAL VELOCITIES OF THE ABSORPTION SYSTEMS OF NOVA V 356 AQUILAE 1936

All velocities are negative

Date, U. T. 1936	Obs.*	Principal km/sec	Diffuse km/sec	Enhanced† km/sec	Orion km/sec	Blends; Other** km/sec	Mg II km/sec	Hydrogen Absorption Edges km/sec	km/sec
Sept. 22.13	M	458 (3)	889 (4)	1107 (2)	1056 (8)				
22.14	L	457 (7)	964 (1)	1133 (1)	1028 (7)	1037 (2)	1240	1252	835
22.20	L	464 (4)	957 (2)		1090 (8)	1036 (3)		1250	835
22.27	Lv		993 (1)		1152 (3)				
23.1	W	446 (12)	931 (5)	1146 (3)	1056 (14)			1297	816
23.14	L	498 (6)	924 (4)	1120 (2)	1108 (13)	1070 (1)			
23.19	L	465 (8)	925 (4)	1131 (2)	1092 (15)	1035 (2)		1234	851
24.15	L	466 (5)	941 (4)	1092 (3)	1071 (10)	1009 (1)			
24.20	L	480 (5)	939 (3)	1106 (2)	1077 (11)	1025 (2)			
25.22	L	499 (6)	926 (3)	1136 (2)	1009 (13)	1021 (2)		1188	843
27.27	L	463 (4)	982 (4)	bl	851 (7)			1192	801
28.15	W	442 (17)	885 (7)	1067 (2)	869 (7)		862	1199	767
28.15	L	457 (8)	919 (6)	1068 (2)	911 (6)		897	1144	788
29.1	W	452 (22)	915 (16)	1090 (3)	856 (9)		924	1125	843
29.12	L	436 (3)	933 (8)		897 (4)		908	1143	769
29.15	L	432 (8)	921 (9)		889 (5)		894	1115	804
29.22	Lv		924 (5)						
30.12	M	450 (22)	952 (14)		883 (7)		983		
30.1	Wv	453 (9)	932 (8)	1097 (2)	991 (4)				
30.14	L	457 (7)	913 (5)			967 (4)		1122	818
Oct. 1.13	L	441 (4)	921 (5)		869 (8)		918	1078	780
1.16	L	441 (6)	926 (8)		871 (7)	945 (3)	966	1111	802
1.19	Lv		911 (5)		891 (3)				
1.22	Lv		975 (6)		885 (4)				
2.12	L	440 (7)	930 (11)		894 (3)	806 K	902		
3.12	L	450 (6)	941 (12)		928 (4)	787 K	959	1087	808
3.14	L	459 (10)	943 (10)		1015 (2)	820 K	974		
3.17	Lv		943 (7)		870 (4)				
3.20	Lv		959 (6)		955 (3)				
4.12	M	447 (20)	956 (18)	1073 (2)	1044 (2)		990		
5.1	W	438 (14)	978 (15)		917 (3)		994	1116	850
5.21	L	457 (6)	986 (11)	1066 (1)	913 (5)		1005	1158	830
6.15	L	453 (12)	1023 (9)		1094 (9)	875 K	1053	1178	845‡
6.1	W	447 (20)	970 (11)	1091 (6)	1108 (5)		1065	1170	858
9.1	W	474 (4)	922 (1)	1064 (1)	1535 (5)	994 (2)			
10.15	L	477 (7)	923 (2)	1084 (6)	1174 (11)			1206	890
10.23	Lv		1048 (3)		1109 (3)				
13.12	L	460 (4)	992 (3)	1237 (2)	1091 (10)		1252	1335	872
13.18	L	454 (8)	991 (3)	1202 (2)	1060 (12)	1062 (1)		1332	868
17.11	L	468 (8)	950 (4)	1179 (2)	908 (11)	1029 (1)	1040		
17.21	Lv		bl	bl	1058 (3)	1103 (3)			
20.14	L	479 (7)	1039 (4)	1199 (3)	1049 (12)		1241	1269	916
22.13	L	508 (8)	1015 (1)	1158 (1)	1085 (9)	1091 (2)	1251	1297	946
27.11	L	472 (7)	1019 (7)		1003 (3)	806 H	1019		
30.10	L	473 (6)	1006 (10)		989 (6)		1042	1138	890
Nov. 3.11	L	490 (4)	1050 (6)		1065 (9)		1196		
5.12	Lv		1027 (6)		1077 (6)				
5.17	Lv		1114 (5)		1145 (5)				
7.13	L	492 (11)	1025 (5)	1187 (1)	1170 (9)		1265	1247	914
10.13	L	483 (7)	1078 (6)	1180 (2)	1117 (6)		1224	1285	943
13.12	L	502 (8)	1052 (1)	1178 (7)	1081 (5)		1258	1366	953
17.12	L	498 (10)	1076 (1)	1237 (1)	1189 (6)	1150 (2)	1311	1311	980
21.12	L	514 (5)	1155 (10)		1191 (4)		1308	1323	1005
24.11	L	520 (4)	1092 (1)	1247 (1)	1232 (8)		1308	1347	995
28.10	L	500 (5)		1222 (4)	1200 (1)		1166	1376	1054
Dec. 3.10	L	523 (3)	958 (3)	1214 (3)	1099 (3)		1193		
6.10	L	504 (4)	1119 (3)	1380 (3)	1336 (8)		1457		

*Observatories: L = Lick; M = Michigan; W = Mount Wilson; v = visual region.
†Diffuse enhanced absorption: bl = blend of two components.
**Other lines: K = 3933 Ca II; H = Hη and Hδ.
‡October 6.15: inner edge of Hδ at -638 km/sec, due to inner low-velocity line?

Orion and the diffuse enhanced absorptions, and a brightening a few days later revived both systems. When last observed, December 6, both the diffuse enhanced and the Orion spectra were still present and actually somewhat strengthened at a minor maximum.

During the fluctuations of brightness, emissions in the visual region showed strong changes of excitation. Lines of high excitation (*He* I, *N* II, *O* II) weakened or disappeared at light-maxima, while some low-excitation lines (e.g., *Na* I) were apparently strengthened. This variation was especially marked in the rise to the bright maximum of October 3. With each increase of brightness, the continuous spectrum was greatly intensified, and most of the weaker emissions were completely submerged by it.

So far as it was observed, this nova never developed the "flaring" *N* III emission bands though a short-lived stage of this type could have occurred during the unobserved interval from December 6, 1936, through January, 1937. The *N* III absorption lines about *Hδ*, so commonly observed in fast novae, were not seen at all. When the star was again accessible in February, 1937, the typical nebular spectrum had developed. No trace of nebular lines had been seen in December. Strong interstellar H and K lines on 28 plates yield a mean velocity of −2.7 km/sec.

THE PRINCIPAL ABSORPTION

The principal spectrum has been likened to that of α Cygni. However, the first observation was so long after the first maximum of light that this spectrum was merely a remnant. The lines of *Ti* II were stronger, relative to *Fe* II, than in α Cygni, and the spectrum resembled that of Nova Herculis in mid-March, 1935, some 80 days after light-maximum. From analogy with other novae, it can be surmised that the original composition of the principal spectrum resembled that of a supergiant star of appreciably later type than α Cygni, possibly cF0 or even cF5.

When first observed, September 22, the hydrogen lines were strong, but most others were rather weak. During the prominent maximum about October 3, the metallic lines especially were strengthened. After a general weakening with the decline from maximum, only slight fluctuations of intensity were noted. The metallic lines gradually faded, and in December only those of hydrogen and faint traces of a few *Fe* II lines remained.

The lines in the accompanying table were used for radial velocity. Each wave length is

Hydrogen	*Mg* I	*Ca* II	*Sc* II	*Ti* II		*Fe* II	*Fe* II, *Ti* II blend
Hη (3)	3838 (1)	3933 (5)	4247 (1)	3900 (2)	4308 (1−)	4233 (1+)	4549 (1½)
Hζ (3)	.....	3969 (4)	.....	3913 (2)	4315 (1−)	4924 (1)	.....
Hε (4)	.....	.....	.....	4164 (1)	4444 (1−)	5018 (1)	.....
Hδ (4)	.....	.....	.....	4172 (1)	4468 (1)	5169 (2)	.....
Hγ (3½)	.....	.....	.....	4290 (1)	4501 (1½)	5317 (1)	.....
Hβ (2)	.....	.....	.....	4294 (1)	4534 (1)	.....	.....
.....	.....	.....	.....	4300 (1)	4572 (1)	.....	.....

followed by its estimated intensity during the time when the spectrum was strongest, September 29–October 4. Radial velocities are given in the third column of Table 1, and daily means are plotted in Figure 1. There is a fairly steady trend toward greater displacement, the velocity changing from −460 to about −510 km/sec between September and December. This behavior is quite general in the principal spectra of novae. Apparent irregularities in this case are probably accidental and result from the low dispersion and small number of lines that were measurable on many plates.

THE DIFFUSE ENHANCED ABSORPTION

The spectrum defined as the diffuse enhanced absorption commonly emerges when a nova has faded about 1 mag. from maximum and reaches greatest strength at 2.0 mag.

down the decline (McLaughlin 1942, p. 434; 1943, p. 172). This system of lines in the spectrum of V 356 Aquilae reached its strongest observed development during the interval September 29–October 5, which covers the bright secondary maximum of light.

The lines in the accompanying table were measured on a number of plates. Intensities

Hydrogen	*Na* I	*Si* II	*Mg* II	*Ca* II	*O* I	*Fe* II	
$H\zeta$ (10)	5890–96 (3)	6347 (2)	4481 (4)	3933 (15)	6157 (3)	4173 (1½)	4924 (4)
$H\epsilon$ (12)	.....	6371 (1½)	.....	3968 (12)	.....	4179 (1½)	5018 (5)
$H\delta$ (20)	.....	.....	.....	.....	.....	4233 (3)	5169 (5)
$H\gamma$ (18)	.....	.....	.....	.....	.....	4416 (1)	5317 (2)
$H\beta$ (13)	.....	.....	.....	.....	.....	4549 (2)	6248 (1)
$H\alpha$ (5)	.....	.....	.....	.....	.....	4584 (2)	

are given in parentheses; these are based on eye-estimates during the interval of greatest strength. In addition to these, on one or two plates several other lines of *Fe* II were identified, as well as λ 4368 *O* I, and probably λ 5330 *Ca* I. Edges of the composite hydrogen absorption lines were measured on many of the plates. Daily means of the radial velocities are plotted in Figure 1, and trend lines are drawn to show the velocities of the edges. The changes of intensity of the two components of the diffuse enhanced spectrum are shown in Figure 2.

When the spectrum was first observed, September 22, this set of lines probably had already passed through a maximum of strength and had faded considerably as the star declined to a minimum at magnitude 8.8. The lines then present included only those of hydrogen and a few of the strongest of *Fe* II. The hydrogen lines had two nearly equal components, with velocities of −925 and −1130 km/sec. Only the less displaced ("inner") component was present at the metallic lines. In the subsequent history of the system, the more displaced ("outer") component was often strong at the hydrogen lines, but those of *Fe* II never showed more than a trace of it, though the inner components were quite strong.

With the rise to the bright maximum of October 3, the lines of *Fe* II, *Si* II, and *O* I strengthened, and H and K of *Ca* II emerged in especially great intensity. The D lines of *Na* I behaved similarly. The total intensification of the hydrogen lines was less noticeable. At the maximum, the diffuse enhanced spectrum was fully as strong as that of Nova Herculis at its greatest development. The decline to the following minimum brought merely a return to the former weakness of *Fe* II and the disappearance of *Ca* II and *Na* I. Subsequent maxima about October 27–November 3 and November 21–24 involved a return toward the appearance at full development but were less marked, as the maxima were lower.

The relative behavior of the two components of the hydrogen lines is of considerable interest. As the star brightened to the maximum of October 3, the outer component weakened, and the two components gradually approached each other. On three days, October 1–3, the outer component was probably absent, for the shortward edges of the lines had shrunk so far that it was quite certain that the observed features were not blends of the two components (see the trend-curves of absorption edges, Fig. 1). On October 4 the outer line was present but weak. By October 6 it was again strong, and the two were well resolved on the Mount Wilson plate. On October 9 they were seen resolved only at $H\gamma$, but this was definite, and the velocities are tabulated and plotted. On the following day the inner component had disappeared at the hydrogen lines but was present at *Fe* II λ 4549 and the K line. When the next spectrogram was taken, October 13, there were again two components, but their separation was double that observed on October 9. According to its velocity, the inner is identified as a continuation of the earlier inner one. The outer seems to have been a newly formed line with velocity −1220 km/sec. This

sudden replacement of a component by another of different velocity was similar to some changes shown by Nova Herculis (McLaughlin 1954, pp. 133, 139).

The two components remained near equality for several days while the nova was faint. At the broad maximum of light, October 27–November 3, the outer line again disappeared. On November 7, near a minimum, it had returned, though it was seen resolved only at $H\delta$. Thereafter, both components were probably present until the last plate was taken on December 6, though they were unresolved on November 21 and 28. The measures of the line edges are consistent with the presence of an unresolved blend of the two lines.

On October 27, when the outer line was absent, a weaker, but well-resolved, additional line appeared with velocity −800 km/sec at $H\gamma$ and $H\delta$, that is, to the longward of the more permanent line of least displacement. It is noteworthy that, at the maximum of October 3, weak components of the K line with a velocity of −800 km/sec appeared briefly. Experience with other novae suggests that the true situation was probably much more complicated than the analysis of these low-dispersion plates would indicate.

THE LINE OF IONIZED MAGNESIUM

Radial velocities of λ 4481 *Mg* II are tabulated separately in the eighth column of Table 1. For several days about the maximum of October 3 and again on October 27 and 30 (when the light was again at a maximum), the *Mg* II velocity was fairly accordant with that of the inner component of the diffuse enhanced absorption. On most other dates it departed widely from the velocity of any other measured feature. This recalls the anomalous behavior of the same line in Nova Herculis (McLaughlin 1937*b*, p. 171). The discordant line may have been present at all times, but when the star brightened to a maximum, a strong component emerged in the diffuse enhanced system and overshadowed the weaker discordant component.

THE ORION ABSORPTION

The Orion absorption spectrum normally becomes visible when a nova has declined about 2 mag. from maximum and is at greatest strength at 2.7 mag. below maximum (McLaughlin 1942, p. 434; 1943, p. 172). When V 356 Aquilae was first observed, on September 22, the Orion system was at nearly full strength. The lines listed in the accompanying table were measured on a number of plates. Numbers in parentheses follow-

He I	*C* II	*N* II		*O* II	
4026 (2)	4267 (1½)	3995 (2½)	5667 (2)	4070 (1½)	4642 (2)
4472 (3½)	.....	4601 (1)	5680 (2)	4072 (1½)	4649 (2)
4713 (1+)	.....	4614 (1½)	5686 (2)	4076 (2)	4662 (½)
5876 (4)	.....	4621 (1½)	5711 (1)	4317–20 (4)	4676 (2)
.....	.....	4631 (2½)	6482 (1)	4415–17 (5)	

ing the wave lengths are intensities based on eye-estimates on five spectrograms of the photographic region and four of the visual region that showed the system strongest.

The Orion lines remained strong for several days; but, beginning on September 27, they weakened as the star brightened. On October 3, in the photographic region only *He* I λ 4026 and λ 4472 were still easily measurable, while *N* II λλ 3995, 4621, and 4631, and *O* II λλ 4415–4417 were measured with difficulty. The lines in the visual region, however, remained fairly conspicuous. The entire system strengthened again as the star faded to the minimum of October 8–13, when the lines were fully as numerous and as strong as they had been 2 weeks earlier. Another weakening, though less extreme, accompanied the light-maximum of October 27–November 3. With fading light, the Orion

spectrum again became fairly strong on November 7, then weaker on November 10, when the star was still fainter. With a moderate brightening of the star the Orion lines again increased, but they were weaker near a higher maximum on November 21, strong at the following shallow minimum, and very weak on November 28, after the drop from a sharp maximum. They were still weak at minimum on December 3. They were greatly revived on December 6, as the star began to brighten to a pointed maximum. There the record ends. The fluctuations of strength are displayed in Figure 2.

Radial velocities of the Orion absorption are given in the sixth column of Table 1, and daily means are plotted as open circles in Figure 1. Strong oscillations are evident, and in a general way maxima of the velocity-curve (*least* negative displacements) are associated with maxima of light, while minima of velocity fall near light-minima. The best-defined maximum of velocity, a rather flat one on September 27–October 2, preceded the brightest maximum of light by about 4 days. There is no obvious relation between amplitude of light and velocity. Thus a rather small decline in light on October 20–22 produced just as great a change in velocity as did the much greater brightening of the star after October 22. The conspicuous maximum of light on November 28 seems to have had no effect upon the velocity, though the spectrum was so weakened that only one line was measurable and its identification could be questioned.

The very pronounced minimum of the velocity-curve on October 9 requires some comment. The velocity depends on four lines in the region of λ 4650 and the hazy blend λλ 4415–4417 *O* II. The lines in the λ 4650 region are spaced at crudely equal intervals, and possibilities of misidentification arise. The best alternative to the adopted interpretation gave highly discordant velocities ranging from −830 to −1160 km/sec. Fortunately, the blend at λλ 4415–4417 fixes the velocity definitely around −1500 km/sec. With this choice, the lines around λ 4650 give a range from −1515 to −1620 km/sec. This spread is greater than normal but not surprising in view of the diffuseness of the lines.

Wyse (1936) mentioned *N* III absorption lines, but I have found no evidence of them. Certainly, the strong pair λ 4097 and λ 4103 never appeared, nor should they have been expected, for the other characteristics of the spectrum indicated too early a stage of development. Wyse's description also mentions hydrogen lines in his third spectrum. At the date of the first observation, it is true, the outer component of the diffuse enhanced absorption had a velocity near that of the Orion system. The later development of the spectrum, however, showed that this was a coincidence. So far as I have been able to determine, no hydrogen component shifted with the Orion lines in their strong oscillations.

THE EMISSION SPECTRUM

At discovery, the spectrum contained emissions due to hydrogen, *Na* I, *Fe* II, *He* I, *N* II, and *O* II, as well as the forbidden lines λλ 5755 [*N* II], 5577, 6300, 6364 [*O* I], and the line of *Fe* II at λ 5990, which is often strong in the spectra of novae. Wyse mentioned *N* III, but I have been unable to confirm this. The wide band in the region of λ 4640 was due mainly to *O* II.

The hydrogen emissions were a composite of the principal and diffuse enhanced systems. The lines of *Fe* II, *Na* I, [*O* I], and [*N* II] represented mainly the principal spectrum, though the strongest lines of *Fe* II had appreciable outer wings associated with the diffuse enhanced absorption. The emissions of *He* I, *N* II, and *O* II were probably members of the Orion spectrum, but they may have had components also in the principal system.

With the rise to the bright maximum of October 3, the continuous spectrum strengthened, and most of the weaker emissions were completely submerged. The stronger ones that remained showed large changes of excitation. *Na* I strengthened appreciably, while λ 5680 *N* II, λ 5876 *He* I, and λ 5755 [*N* II] apparently weakened greatly as compared with lines of *Fe* II. The lines of [*O* I] were not much affected. The record in the visual re-

gion, where the emissions always contrasted fairly well with the continuum, is rather fragmentary, and little can be said of the behavior at later light-maxima.

In the region of λ 4650 a wide composite band was stronger than neighboring *Fe* II emissions at the minima of light and weaker than those at the maxima. These changes were observed visually by the writer, with the one-prism spectrograph at Ann Arbor.

The spectrum was so similar to that of Nova Herculis that a complete table of wave lengths and identifications would be superfluous. The identification of the composite band in the region of λ 4650, however, requires some comment. All band edges measured in the region between λ 4598 and λ 4814 are listed in Table 2, with suggested identifica-

TABLE 2

DIFFUSE EMISSIONS, λλ 4598–4814

Feature	λ	Identification*	Remarks
Violet edge†	4598	4601, 4607 *N* II	Separated from strong band, 4637–4682, by Orion absorptions, *N* II and *O* II
Red edge†	4612	Multiplet 5	
Violet edge	4637	4642 *O* II, multiplet 1	Outer edge
Violet edge	4647	4649–4651 *O* II	Strongest violet edge
Red edge	4656	Multiplet 1	Strongest red edge
Minimum	4659	4676 *O* II absorption	Orion absorption, $v \sim -1100$ km/sec
Violet edge	4662	4662 *O* II, multiplet 1	Strong; cut off by absorption, 4676 *O* II, Orion system
Red edge	4682	4676 *O* II, multiplet 1	Strong
Violet edge	4699	4713 *He* I	
Red edge	4719	4713 *He* I	
Violet edge	4775	4774–4810 *N* II	Weak and hazy; blend of 7 lines of *N* II
Red edge	4814	Multiplet 20	

* Multiplet designations from *Princeton Obs. Contr.*, No. 20

† Violet and red edges indicate, respectively, the edge of shorter and of longer wave length of emission bands.

tions. The bands λλ 4598–4612, λλ 4699–4719, and λλ 4775–4814 probably require no comments beyond the identifications and remarks in the table. All these features were hazy and represent the overlapping of two or more bands which were individually diffuse.

The wide band λλ 4637–4682 varied in appearance from plate to plate. Sometimes it was nearly continuous; on other dates it was split into two bands by a minimum about λ 4659. The stronger inner violet edge, λ 4647, was also variable, but always the very strongest part of the band extended approximately from λ 4647 to λ 4656, with variations of several angstroms. The band as a whole was quite surely due mainly to *O* II multiplet 1, which includes the lines λλ 4642, 4649, 4651, 4662, and 4676. At times the Orion absorption line λ 4676 *O* II cut the band in two at about λ 4659. There is no reason to suspect that the *N* III emissions λλ 4634, 4641, and 4642 (multiplet 2) were involved at any time during the observed interval.

Several rather narrow emission maxima were measured on one or more plates. These are listed in Table 3. All are certainly real features, but the interpretation of some is doubtful. The most probable identification is indicated. A fairly good case can be made out for the presence of positively displaced maxima due to [*Fe* II] during November and December, but the discordant shift of λ 4244 is disturbing. The appearance of [*Fe* II] emissions was logically to be expected at that time, as the stage of spectral development was approximately that of the novae RR Pictoris and DQ Herculis when the forbidden lines first emerged.

Measures of longward edges of the hydrogen emissions showed such large scatter that a tabulation of details would serve no purpose. Analysis of the measures showed a few definite features that will be summarized here.

At $H\beta$ an outer emission edge was measured at +1100 to +1300 km/sec, depending on the density of exposure. After October 8 an edge at $H\gamma$ was accordant with this. The velocity identifies it as the edge of a band associated with the outer component of the diffuse enhanced absorption. An innermost persistent edge of $H\gamma$ and $H\delta$ was measured at +450 km/sec during 2 weeks after discovery. Later it drifted to between +600 and +700 km/sec. Doubtless this edge corresponded to the principal absorption.

From September 28 to October 6 a conspicuous edge was present in the hydrogen bands between +800 and +900 km/sec. Its visibility was apparently correlated with the strong maximum of light. The velocity identifies this edge as probably associated with the inner diffuse enhanced component. It will be recalled that during that interval the

TABLE 3

NARROW EMISSION MAXIMA

λ	Identification	Dates	Remarks
4222.4	4233 *Fe* II ?	Sept. 24	Between absorptions ?
4231.7	4233 *Fe* II	Sept. 24	Maximum in 4233 band
4237.7	4233 *Fe* II	Nov. 13	v = +320 km/sec
4243.2	4244 [*Fe* II] ?	Sept. 24; Nov. 10–13	Part of [*Fe* II] emission ?
4270.4	4267 *C* II	Nov. 10–13	Blend 4266–4268 [*Fe* II] ?
4289.8	4287 [*Fe* II]	Nov. 10–13	v = +170 km/sec
4357.6	4353 [*Fe* II]	Dec. 3	v = +330 km/sec
4364.8	4359 [*Fe* II]	Dec. 3	v = +375 km/sec
4418.5	4414–4416 [*Fe* II]	Dec. 3	$v \sim$ +235 km/sec
4640.8	4639 [*Fe* II] ?	Oct. 6, 13	Part of 4642 *O* II emission? isolated by Orion absorption?
4668.0	4667 *Fe* II ?	Oct. 6	4665 [*Fe* II] ?; part of *O* II emission, 4662 ?
4699.2	4695 [*Fe* I] ?	Dec. 3	4696 *O* II, multiplet 1 ?
4710.4	4713 *He* I ?	Dec. 3	4708–4710 *O* II ? (mult. 89, 24)

inner diffuse enhanced line was very strong and the outer one disappeared for a few days. Again on October 27 and 30 an edge was measured in about the same position while the star was at another maximum of light. The outer emission wing evidently weakened simultaneously with the weakening and disappearance of the outer absorption component. This left the inner edge at +900 km/sec standing out in stronger contrast. It was submerged again when the outer edge and its associated absorption strengthened as the star faded from maximum.

THE NEBULAR SPECTRUM

In 1937 six slit spectrograms of the nova were taken at Lick Observatory and one at Mount Wilson Observatory. These showed a normal nebular nova spectrum with no unusual features. Lines of hydrogen, *He* II, *N* III, [*O* III], and [*Ne* III] were strong and lines of *He* I weaker. One panchromatic plate taken with the Crossley slitless spectrograph shows [*N* II], [*O* I], and *He* I λ 5876 still strong on March 5.

No pronounced internal structures were visible in the emission bands. Measures were made on their apparent edges on three plates. The resulting velocities were dependent on the strength of exposure. Means based on all lines and on the weaker lines are given in Table 4. These are close enough to the velocities of the principal absorption to indicate that the emissions originated in the principal shell of gas, without appreciable complica-

tion by other sources. Eye-estimates of intensity ratios of [*O* III] to hydrogen lines are given in the last two columns, including data from a Crossley slitless plate that was not measured.

CONCLUSION

The interpretation of spectral features of novae in terms of a physical-geometrical model has been discussed in several other papers (e.g., McLaughlin 1943, pp. 188 ff.; 1949, pp. 54 ff.; 1950) and will not be repeated here. Nova V 356 Aquilae showed no features that appear to require a significant modification of the interpretation. The correlations between the light-variations, spectral changes, and absorption velocities found in Nova Herculis and Nova Geminorum 1912 are reinforced by the data obtained for V 356 Aquilae. The spectral changes, with practically no exception, follow what may be called "Stratton's rule." This was stated by its originator as follows: "The spectrum varies with the magnitude. As a rough generalization it may be said that a maximum corresponds to a spectrum which is normal at an earlier stage of the star's history" (Stratton 1920, p. 65).

The apparent oscillations of position of absorption lines are in part very probably real and in part certainly illusory. With the probable exception of its emergent stages, the

TABLE 4

VELOCITIES OF EMISSION EDGES IN THE NEBULAR STAGE

DATE (U.T.) 1937	OBS.	ALL LINES (KM/SEC)		WEAKER LINES (KM/SEC)		RATIOS	
						λ 4363/$H\gamma$	λ 5007/$H\beta$
Feb. 21.55	L	−684 (9)	+748 (8)	−622 (4)	+704 (4)	1.6	0.8
May 14.45	L	−673 (12)	+712 (12)	−560 (4)	+544 (4)	2.0	1.3
June 17.4	W	−559 (9)	+674 (9)	−521 (4)	+659 (4)	2.5	2.0
Oct. 27.14	L					2.0	3.3

diffuse enhanced absorption does not really oscillate strongly with the variation of the star's light. The apparent oscillations result mainly from varying relative intensities of blended components and from the disappearance of some lines and the new emergence of others. Great caution is necessary in the interpretation of supposed changes of displacement of lines that may be composite, as those of the diffuse enhanced absorption usually are. Had V 356 Aquilae been observed with much lower dispersion, the illusion of oscillating lines would have been complete. As it was, the lines were resolved on enough plates to justify the conclusion that they were actually double on most, except when one line disappeared.

On the other hand, the oscillations of Orion absorption lines give every indication of being real. This is shown by the great range of displacement, with no suspicion of duplicity or asymmetry. Nova Aquilae 1918 (Wyse 1939, p. 110) is more conclusive on this point than V 356 Aquilae. Nova Geminorum 1912 also showed the same effect clearly. The most conclusive example is V 528 Aquilae 1945 (McLaughlin, unpublished).

It is a pleasure to express my gratitude to those who made the collections of spectrograms available and who showed me so many courtesies. These include Drs. W. H. Wright and C. D. Shane, directors of the Lick Observatory in 1940 and 1951, respectively, and Dr. Walter S. Adams, director of Mount Wilson Observatory during my visit there in 1940. Special mention should be made of the kindness of the late Dr. Arthur B. Wyse, who had been keenly interested in V 356 Aquilae. Travel expenses of both visits to

the California observatories were defrayed in part by grants from Faculty Research Funds of the Horace H. Rackham School of Graduate Studies of the University of Michigan. This aid is gratefully acknowledged.

REFERENCES

Beyer, M. 1939, *A.N.*, **268**, 345.
Campbell, L. 1937, *Pop. Astr.*, **45**, 219.
Campbell, L., and Jacchia, L. 1941, *The Story of Variable Stars* (Philadelphia: Blakiston Co.), p. 127.
McLaughlin, D. B. 1937*a*, *Pub. Amer. Astr. Soc.*, **9**, 12.
———. 1937*b*, *Pub. Michigan Obs.*, **6**, 107–214.
———. 1942, *Ap. J.*, **95**, 428–436.
———. 1943, *Pub. Michigan Obs.*, **8**, 149–194.
———. 1944, *Pub. Amer. Astr. Soc.*, **10**, 331.
———. 1949, *Pub. Michigan Obs.*, **9**, 13–71.
———. 1950, *Pop. Astr.*, **58**, 50–64.
———. 1954, *Ap. J.*, **119**, 124–140.
Stratton, F. J. M. 1920, *Ann. Solar Phys. Obs. Cambridge*, **4**, 1–71.
Wyse, A. B. 1936, *Pub. A.S.P.*, **48**, 302.
———. 1939, *Pub. Lick Obs.*, **14**, 93–215.

PHOTOMETRIC AND SPECTROSCOPIC OBSERVATIONS OF THE DOUBLE CLUSTER IN PERSEUS*

H. L. JOHNSON AND W. W. MORGAN
Lowell and Yerkes Observatories
Received July 11, 1955

ABSTRACT

Photoelectric magnitudes and colors on the (*U*, *B*, *V*) system are given for 123 stars in the neighborhood of the Double Cluster in Perseus. Spectral types on the MK system are given for 51 of the same stars. The relation between luminosity class and apparent magnitude (corrected for interstellar absorption) is illustrated.

Three-color photoelectric observations on stars in the neighborhood of the Double Cluster were made by Johnson during the autumns of 1953 and 1954. Most of the observations were made in 1953 with the 20-inch reflector of the Lowell Observatory; a few additional observations on the fainter stars were made in December, 1954, with the 82-inch reflector of the McDonald Observatory. We are indebted to Dr. W. A. Hiltner for allowing the use of his photometric equipment at the McDonald Observatory. The

TABLE 1*a*

ESTIMATED PROBABLE ERRORS OF ZERO POINTS

	V	*B*−*V*	*U*−*B*
p.e. (mag.)	±0^{m}008	±0^{m}004	±0^{m}008

TABLE 1*b*

PROBABLE ERRORS WITH RESPECT TO CLUSTER STANDARDS, FOR ONE OBSERVATION

	V	*B*−*V*	*U*−*B*
$V<10^m$	±0^{m}006	±0^{m}005	±0^{m}010
$V>10^m$	±0.012	±0.017	±0.025

Lowell observations were made with the same filters and photomultiplier that were used in the definition of the (*U*, *B*, *V*) system (Johnson and Morgan 1953); the photometric results given here are on that system.

The tie-in of the cluster standards with the (*U*, *B*, *V*) system depends upon special observations on fifteen different nights. The estimated probable errors of the zero points are listed in Table 1*a;* the probable errors of the values for the individual stars with respect to the cluster standards are given in Table 1*b*.

The spectroscopic observations are taken partly from a general program of spectroscopic parallaxes (Morgan, Code, and Whitford 1955) and partly from spectrograms

* *Contributions from the McDonald Observatory, University of Texas*, No. 261.

obtained especially for the present program; the plates were classified on the MK system by Morgan.

The catalogue of observations is given in Table 2. The columns in Table 2, *a*, are self-explanatory, with the possible exception of the last, which gives the number of photometric observations. In Table 2, *b*, the star designation is that of Oosterhoff (1937).

While the material is incomplete, some conclusions can be drawn concerning the relative positions of stars of the various luminosity classes. Figure 1 gives the location of all early-type stars for which spectral types and luminosity classification on the MK system had been determined. The apparent magnitudes (V) were corrected by $3E_{(B-V)}$ to derive V_0, the apparent visual magnitude corrected for the effects of interstellar absorption.

An inspection of Figure 1 shows that the brightest stars of the association are all later

TABLE 2

THE OBSERVATIONAL DATA

a) OUTER STARS

HD	MK	V	$B-V$	$U-B$	n
12150	.....	8.64	+0.27	−0.53	2
12856	B0 pe	8.55	+0.24	−0.77	2
12953	A1 I*a*	5.68	+0.62	−0.03	2
13051	B1 III:	8.72	+0.14	−0.72	2
13136	.....	7.76	+2.26	+2.27	2
13267	B5 I*a*	6.39	+0.33	−0.43	2
13402	B0.5 I	8.06	+0.60	−0.42	2
13476	A3 I*ab*	6.46	+0.59	+0.21	2
13621	B0.5 IV	8.11	+0.06	−0.78	3
13744	A0 I*ab*	7.60	+0.74	+0.18	2
13745	B0 III	7.88	+0.17	−0.78	3
13831	B0 IV	8.27	+0.09	−0.81	2
13866	B2 I*b*	7.52	+0.18	−0.63	2
13890	B1 III: pe	8.53	+0.19	−0.64	2
14142	.....	8.38	+2.33	+2.58	2
14322	B8 I*b*	6.79	+0.32	−0.34	Std.
14331	B0 III	8.45	+0.17	−0.76	2
14404	.....	7.83	+2.30	+2.64	2
14469	.....	7.69	+2.16	+2.24	2
14528	.....	9.26	+2.66	+2.69	2
14818	B2 I*a*	6.25	+0.31	−0.62	Std.
14826	.....	8.26	+2.30	+2.47	2
14899	B8 I*b*	7.40	+0.44	−0.11	2
14956	B2 I*a*	7.22	+0.72	−0.29	2
15316	A3 I*ab*	7.24	+0.77	+0.42	2
15497	B6 I*a*	7.03	+0.78	−0.07	2
15642	B0 IV	8.54	+0.08	−0.84	2
15690	B1.5 I*b*	8.00	+0.66	−0.27	2
16310	B1 II:	8.07	+0.66	−0.35	2
16778	A2 I*a*	7.73	+0.90	+0.34	2
17145	B8 I*a*	8.16	+0.82	−0.01	2
17378	A5 I*a*	6.26	+0.89	+0.49	2
236970	.....	8.96	+0.94	+0.20	2
236979	.....	8.20	+2.30	+2.61	2

TABLE 2 —*Continued*

b) INNER STARS

Star	MK	V	$B-V$	$U-B$	n
3	B2 I*b*	7.40	+0.24	−0.66	2
16	B1 I*ab*	6.49	+0.28	−0.65	2
49		9.08	+0.26	−0.66	2
146		9.19	+0.17	−0.67	2
230		13.68	−0.12	−0.92	2
339	B1 IV:	8.85	+0.31	−0.61	2
612	B1 II	8.41	+0.25	−0.62	2
662	B1 I*b*	8.18	+0.30	−0.59	2
717		9.28	+0.30	−0.56	2
782		9.45	+0.27	−0.55	2
800		12.25	+0.36	−0.28	2
837		14.08	+0.49	+0.16	2
843		9.32	+0.31	−0.53	2
847		9.11	+0.38	−0.52	2
864	B1 V	9.94	+0.31	−0.49	2
867		10.51	+0.62	+0.12	2
869		11.96	+0.37	−0.20	2
885		15.76	+0.75		2
899		9.25	+2.47	+2.67	3
935		14.02	+0.45	+0.01	
950	B2 V	11.29	+0.36	−0.40	2
960		13.69:	+0.43	0.00	2
974		15.43	+0.70	+0.78	2
978	B1.5 V	10.59	+0.38	−0.44	2
982		13.87	+0.43	+0.13	2
1000		13.23	+0.41	+0.02	2
1015		10.57	+0.28	−0.10	2
1040		14.50	+0.68	+0.40	3
1057	B3 I*a*	6.55	+0.47	−0.37	2
1078	B1 V	9.75	+0.34	−0.49	2
1119		12.57	+1.40	+1.23	2
1150		13.23:	+0.98	+0.48	4
1162	B2 I*a*	6.66	+0.51	−0.45	2
1166		13.12:	+0.54	−0.10	3
1181		12.65	+0.40	−0.23	3
1187	B2 IV	10.82	+0.39	−0.40	2
1189		13.90:	+0.92	+0.72	3
1202		12.12	+0.44	−0.22	3
1211		12.58	+0.60	+0.32	2
1586	B1 III	8.96	+0.32	−0.54	2
1655		7.81	+2.28	+2.47	2
1781		9.21	+0.30	−0.54	2
1818		7.97	+2.26	+2.54	2
1899	B2 II	8.53	+0.32	−0.53	2
2005		13.56	+0.41	+0.02	2

TABLE 2—*Continued*

b) INNER STARS—*Continued*

Star	MK	V	$B-V$	$U-B$	n
2088		9.45*	+0.32	−0.65	2
2133		12.21	+0.33	−0.38	2
2134		14.93	+0.95	+0.29	1
2138	B0 IV: pe	9.03	+0.50	−0.65	2
2139	B2 V	11.38	+0.27	−0.49	2
2147		14.34	+0.49	+0.14	3
2155*		15.33	+0.60	+0.22	1
2165		9.86	+0.40	−0.62	2
2167		13.36	+0.41	−0.13	2
2170		15.23	+0.64	+0.43	2
2172	O6	8.50	+0.16	−0.79	2
2178	A1 I*a*	6.38	+0.58	+0.02	2
2185	B3 V	10.92	+0.33	−0.25	2
2188		14.99	+0.71	+0.35	2
2194		13.45	+0.42	−0.13	2
2196		11.57	+0.32	−0.43	1
2200		12.67	+0.36	−0.25	2
2203		14.61	+0.50	+0.05	2
2227	B2 I*b*	8.05	+0.34	−0.55	2
2232	B2 V	11.11	+0.25	−0.54	2
2235		9.36	+0.33	−0.55	2
2241		13.58:	+0.43	+0.02	2
2246	B2 III	9.90	+0.32	−0.56	2
2250		15.10	+0.56	+0.29	2
2251	B3 V	11.56	+0.34	−0.34	2
2253		12.71:	+0.41	−0.10	2
2262		10.38	+0.44	−0.60	2
2269		13.19	+0.39	−0.19	2
2270		14.18	+0.42	+0.08	1
2284		9.66	+0.40	−0.59	2
2296		8.53	+0.30	−0.56	2
2299		9.08	+0.29	−0.57	1
2311		9.38	+0.30	−0.54	2
2330		11.42	+0.24	−0.39	1
2349		12.81	+0.36	−0.28	1
2361		8.75	+0.38	−0.51	2
2371		9.25	+0.32	−0.55	2
2417		8.31	+2.29	+2.28	2
2541	B2 II	9.15	+0.33	−0.55	2
2572		10.02	+0.34	−0.51	2
2589	A2 I*a* p?	7.44	+0.72	+0.11	2
2621	B8 I*a*	7.00	+0.62	−0.14	2
2691		8.13	+2.25	+2.45	2
2758		8.42	+2.30	+2.59	2

* 2155 double; $\Delta m \sim 0.4$ mag.

than type B1. The stars of luminosity class I*a* range from $V_0 = 3.9$ to $V_0 = 5.4$; those of class I*b* are included between $V_0 = 5.3$ and $V_0 = 6.5$.

For stars in the region of the two nuclear condensations, the earliest observed type is B0; the five stars observed of this type are of luminosity class III or IV. At spectral class B2 a fairly continuous range of luminosity is observed from I*a* at $V_0 = 4.4$ to class V at $V_0 = 9.9$. For types later than B2 the intermediate luminosity classes seem to be missing. A discussion of the present data and a comparison with earlier investigations will be made at a later time.

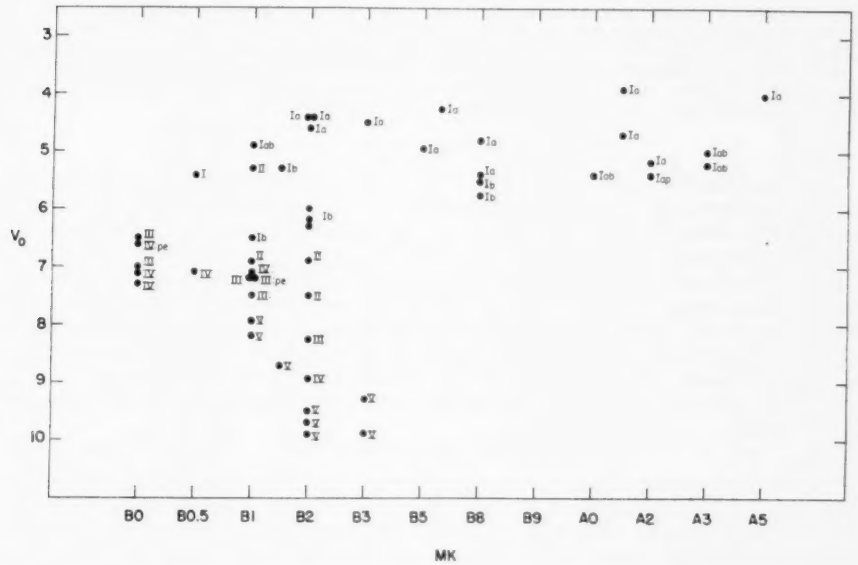

FIG. 1.—Spectral type–magnitude diagram for stars having spectral types in Table 2. The *V* magnitudes have been corrected for interstellar absorption. One star of spectral type O6 has not been plotted.

REFERENCES

Johnson, H. L., and Morgan, W. W. 1953, *Ap. J.*, **117**, 313.
Morgan, W. W., Code, A. D., and Whitford, A. E. 1955, *Astrophysical Supplement* No. 14.
Oosterhoff, P. T. 1937, *Leiden Ann.*, Vol. **17**, No. 1.

THE M-TYPE SUPERGIANTS IN h AND χ PERSEI

VICTOR M. BLANCO*
Warner and Swasey Observatory, Case Institute of Technology, Cleveland, Ohio
Received June 10, 1955

ABSTRACT

The visual and infrared magnitudes of the M-type supergiant stars near h and χ Persei clusters are discussed. Spectral classes observed during the dates of photometric observations are presented. Among the stars of luminosity class I*ab*, relationships are found between the spectral classes, the infrared absolute magnitudes, and the intrinsic $V - I$ colors. The infrared absolute magnitude for the I*ab* stars ranges from -6.4 to -7.4, depending on spectral class, while the values of M_v are close to -5.3, regardless of spectral class, the latter value being in agreement with previous estimates. A list is presented of seven M-type stars that may be new members of this group of supergiants.

INTRODUCTION

The supergiant M stars associated with the h and χ Persei clusters form the principal basis of our knowledge of the intrinsic properties of this type of star. With the development of the classification of M stars in the near infrared region of the spectrum, this group of stars has gained significance because they serve as the prototypes of a class of stars that may now be recognized at very great distances. In this study the visual and infrared luminosities, as well as the relationship between these quantities and the spectral classes, are determined for the M-type supergiants associated with the clusters. All the photometric data were collected from September 10 to October 10, 1953. Observations of the spectral classes were made twice in this period, as well as in nine other epochs from July, 1947, to November, 1954. All the observations were made with the Burrell Schmidt-type telescope.

PHOTOMETRIC DATA

Photoelectric observations were made of eleven of the thirteen M supergiants listed by Bidelman (1947). In addition, four other M-type stars were observed whose colors and magnitudes indicate probable association with the clusters. These observations have been published elsewhere (Blanco 1954). The visual magnitudes thus obtained, which have been converted to the $B-V$ system, are presented in Table 1.

In order to determine infrared magnitudes, photoelectric magnitudes and colors were obtained in the $B-V$ system for eleven early-type stars near the clusters. The magnitudes and colors were then used to compute the infrared magnitudes in accordance with a relationship given by Kron, White, and Gascoigne (1953). The resulting infrared sequence was then used to determine the magnitudes of the M stars in four Eastman IN plates taken with a Wratten 88A filter. The effective wave length of these magnitudes is estimated as 8200. The results are presented in Table 1.

THE SPECTRAL CLASSES

The classification of M stars in the infrared regions of the spectrum, although accurate to within half a subclass, does not permit the determination of luminosity classes. Supergiant early M stars, however, often show a color effect in their infrared spectra caused in part by intrinsically high color indices but mainly by interstellar absorption. Classifications following the criteria described by Nassau and van Albada (1949) were made for most of the stars listed in Table 1 at eleven different dates. In this table are given the spectral classes found during the period of photometric observations as well as the earliest and the latest classes (third, fourth, and fifth columns) found at any time for each star when observations were available. The observations show that most of the stars undergo

* Fellow of the John Simon Guggenheim Memorial Foundation.

spectral-class variations, the largest range being 2.5 spectral subclasses. The stars with the least variations are of class M0. The spectral classes and luminosity designations given by Bidelman are included in the second column.

Three of the four newly listed stars were observed in long-exposure, blue-sensitive spectrum plates. The spectra show some evidence of the strengthening of the continuum between λ 4226 and the G band as well as suppressed λ 4226, indicative of high luminosities (Keenan and Nassau 1946). From these observations, as well as from unpublished observations kindly made by Bidelman for two of these stars, the three stars have been

TABLE 1

OBSERVATIONAL DATA FOR M-TYPE SUPERGIANTS NEAR h AND χ PERSEI

STAR	SPECTRAL CLASS				V	m_{ir}	$(V-I)_{int}$	M_v	M_{ir}
	Bidelman	Sept.–Oct., 1953	Case Spectral Range						
			Earliest	Latest					
BD+58°373	.....	M0.0	M0.0	M0.0	8.5	6.3	1.5	−4.7:*	−6.2:*
HD 13136	M2 *Ib*	M1.0	M1.0	M3.5	7.6	5.6	1.5	−5.3	−6.8
BD+57°524	.....	M0.0	M0.0	M1.0	8.9	6.6	1.6:	−4.3:*	−5.9:*
K 100172†	.....	M1.0	M0.0	M1.5	9.2	6.7	1.9:	−4.0:*	−5.9:*
BU Per	M4 *Ib*	M3.5	M2.5	M4.5	9.2	6.2	2.2	−4.3	−6.5
T Per	M2 *Iab*	M1.0	M1.0	M2.5	8.3	6.0	1.4	−5.2:	−6.6:
BD+58°445	.....	M1.0	.....	.....	8.2	.....	.....	−5.0:*	.....
AD Per	M3 *Iab*	M2.0	M2.0	M3.0	7.7	5.5	1.6	−5.3	−6.9
FZ Per	M1 *Iab*	M0.5	M0.5	M2.0	8.0	5.8	1.4	−5.4	−6.8
HD 14404	M2 *Ib*	M0.5	M0.5	M2.0	7.8	5.6	1.4	−5.7:	−7.1:
SU Per	M3 *Iab*	M3.5	M3.0	M4.5	7.6	5.2	1.8	−5.4	−7.2
RS Per	M4 *Iab*	M4.5	M4.0	M5.5	8.2	5.3	2.1	−5.2	−7.3
S Per	M3 *eIa*	M4.0	M3.0	M5.0	9.0	5.6	2.7	−4.2	−6.9:
BD+56°595	M0 *Iab*	M0.5	M0.5	M1.0	8.1	6.0	1.3	−5.3	−6.6
HD 14580	M0 *Iab*	M0.0	M0.0	M0.0	8.4	6.3	1.3	−5.0	−6.3
HD 14826	M2 *Iab*	M2.5	M2.5	M3.5	.....	5.7	.....	.....	−7.0
YZ Per	M3 *Iab*	M2.5	M1.0	M3.5	.....	.....	.....	.....	.....

* Assuming the star to belong to the clusters.

† The letter "K" stands for *Catalogue of Stars of Doubtful Variability* (Kukarkin *et al.* 1951).

assigned to luminosity class *Ib*. Among these stars, BD+57°524 and K 100172 show some variability in the spectral classes. Of the other two stars, BD+58°373 was observed without variations in four epochs, while BD+58°445 was classified at one date only.

Among the stars with the more pronounced spectral variations is HD 13136, which has not previously been listed as variable. This star was observed photoelectrically on March 6, 1954, and found brighter by 1.0 visual mag. and bluer by 0.20 than on September 30, 1953. In this period the spectral class changed from M1.5 to M1.0. During the same period, S Per became fainter by 0.9 mag., while its color index increased by 0.23, the spectral class changing from M4.0 to M5.0. The relatively large changes in visual magnitude and color index, as compared with the small variations in spectral class, have been observed on other occasions also.

THE ABSOLUTE MAGNITUDES AND INTRINSIC COLORS

The amount of interstellar absorption in the direction of each of the M supergiants was determined from the colors of near-by blue stars associated with the clusters. Be-

cause of the nonuniform nature of the absorption in this region, it was not possible to determine reliable absorption estimates for some of the stars because of their separation from blue stars of known colors and distances. The absolute magnitudes and intrinsic colors of these stars are followed by colons in Table 1, where they are listed in the last three columns. In the reductions, the following data were used: spectral classes by Morgan, Whitford, and Code (1953); intrinsic colors by Morgan, Harris, and Johnson (1953); colors by Stebbins, Huffer, and Whitford (1940); and locally observed colors. Absorptions in the infrared were computed from $A_{ir} = 0.50\ A_v$, a relation derived from Whit-

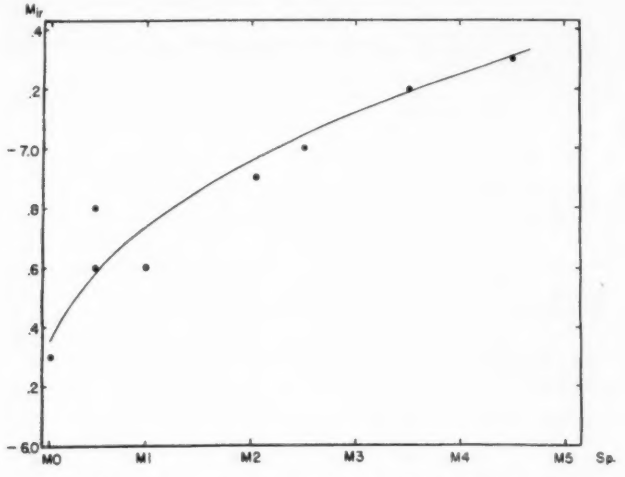

FIG. 1.—Relation between spectral class and infrared absolute magnitude

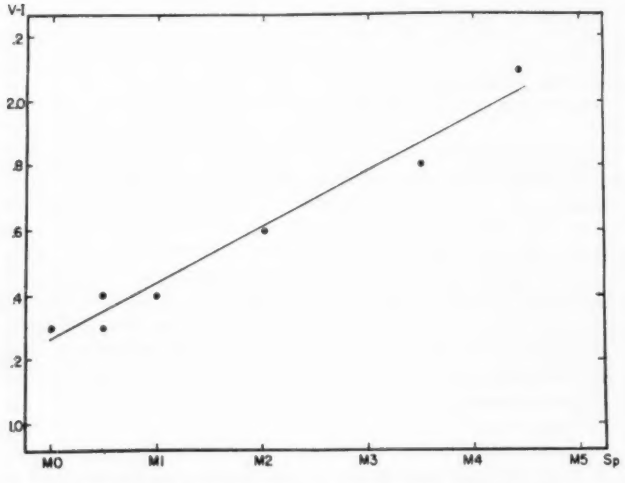

FIG. 2.—Relation between spectral class and the intrinsic $V-I$ color

ford's observations of the interstellar absorption curve. The absolute magnitudes in Table 1 are based on a corrected modulus of 11.8 as established by Morgan, Whitford, and Code (1953). The luminosities indicated are for the time of observation and not necessarily maximum luminosities.

The stars assigned by Bidelman to luminosity class I*ab*, for which absolute magnitudes were derived, have spectral classes that are correlated with the infrared absolute magnitudes and with the intrinsic $V-I$ colors, as shown in Figures 1 and 2. The small scatter shown in these figures is partly fortuitous. From the known magnitude ranges and the spectral-class variations found in this study, it appears that most of these stars were observed near mean luminosity. In general, the stars will not vary from the plotted points in Figure 1 by more than one spectral subclass, or 0.3 mag. The luminosities and intrinsic colors of stars of class I*ab* given in Table 2 were obtained from these figures. In preparing this table, the assumption was made that the designation I*ab* was appropriate during the dates of the present investigation, as indicated by the over-all agreement in spectral classes with those quoted by Bidelman.

The newly listed stars, as well as BU Per, show that for the I*b* stars the $V-I$ colors are about 0.2 mag. redder than for the I*ab* stars, while their infrared magnitudes are fainter by 0.6. Thus the mean visual luminosity is −4.5 for the I*b* group. The values of M_v found here are in good agreement with those given by Keenan and Morgan (1953).

TABLE 2

INTRINSIC COLORS AND ABSOLUTE MAGNITUDES

Spectral Class	$V-I$	M_{iv}	M_v	Spectral Class	$V-I$	M_{iv}	M_v
M0 I*ab*.....	1.3	−6.4	−5.1	M3 I*ab*.....	1.9	−7.1	−5.2
M1 I*ab*.....	1.4	−6.7	−5.3	M4 I*ab*.....	2.0	−7.3	−5.3
M2 I*ab*.....	1.6	−7.0	−5.4	M5 I*ab*.....	2.0	−7.4	−5.3

POSSIBLE NEW SUPERGIANTS NEAR h AND χ PERSEI

A study has been made of the infrared spectra of all the BD stars found within a radius of 6° of the clusters. The stars—BD+60°478, +58°490, +58°501, +57°641, +57°647, +59°580, and +59°594—were found to be of early M type and to show in their infrared spectra the wedge effect that has been found by Nassau, Blanco, and Morgan (1954) to be common in distant red supergiants. Confirmation of these stars as actual members of the h and χ Persei association must await further observations. The list is offered with the hope that other workers will observe their spectra with higher dispersions and obtain their radial velocities.

REFERENCES

Bidelman, W. P. 1947, *Ap. J.*, **105**, 492.
Blanco, V. M. 1954, *A.J.*, **59**, 396.
Keenan, P. C., and Morgan, W. W. 1951, chap. i in Hynek, *Astrophysics* (New York: McGraw-Hill Book Co.).
Keenan, P. C., and Nassau, J. J. 1946, *Ap. J.*, **104**, 458.
Kron, G. E., White, H. S., and Gascoigne, S. C. B., 1953, *Ap. J.*, **118**, 502.
Morgan, W. W., Harris, D. L., and Johnson, H. L. 1953, *Ap. J.*, **118**, 92.
Morgan, W. W., Whitford, A. E., and Code, A. D. 1953, *Ap. J.*, **118**, 318.
Nassau, J. J., and van Albada, G. B. 1949, *Ap. J.*, **109**, 391.
Nassau, J. J., Blanco, V. M., and Morgan, W. W. 1954, *Ap. J.*, **120**, 478.
Stebbins, J., Huffer, C. M., and Whitford, A. E. 1940, *Ap. J.*, **91**, 20.

PRELIMINARY NOTE ON MEASURES OF CORONAL EMISSION LINES OBSERVED AT THE TOTAL SOLAR ECLIPSE, FEBRUARY 25, 1952, BY B. LYOT AND M. K. ALY

M. K. Aly
Helwan Observatory, Egypt
Received July 1, 1954; revised June 16, 1955

ABSTRACT

The Egyptian mission for the total solar eclipse of February 25, 1952, at Khartoum undertook this present work at the suggestion of the late Bernard Lyot of Meudon, and carried it out jointly with M. K. Aly of Helwan. For this purpose, two spectrographs were designed for observing the coronal emission lines close to the sun's limb over the whole range of the spectrum from λ 6900 to λ 3100. A short account of the program is followed by a description of the plates obtained, and the wave-length measurements of all the coronal lines seen on the plates. In addition to most of the previously discovered emission lines observed at earlier eclipses, some thirteen new lines were observed at this elcipse.

I. INTRODUCTION

Our program and the equipment used have been described by the author (Aly 1952) and have also been included in the description of the general program of the Egyptian eclipse expedition (Madwar 1952). However, a brief introduction to the observational program will not be out of place here. The origin of the emission lines of the solar corona is a most important problem and deserves careful investigation. It has not yet been possible to obtain these radiations in the laboratory, but Edlén (1945) attributed their existence to forbidden transitions of very highly ionized atoms of iron, nickel, and calcium, which have lost from 9 to 14 of their electrons under extremely low pressure. The calculated wave lengths given by Edlén for these lines are generally in fairly good agreement with those in the corona of the sun.

	Red	Green	Blue	Violet	Ultra-violet
Glass	62	36	19	11	.....
Quartz	.....	.....	37	25	14

One would expect, according to Edlén's theory, based on laboratory observations of permitted transitions in the vacuum ultraviolet spark spectra, that, when comparing two coronal lines, their intensity variations all around the sun would be similar if the ionization potential of the corresponding ions is nearly the same and, in the case of very different ionization potential, the intensity variations would be different.

Such expectations have been confirmed (Lyot 1939) for the radiations in the green, red, and infrared spectra, from a number of plates obtained with a coronagraph at the Pic du Midi Observatory, not during an eclipse. These radiations can be classified into three groups, each behaving in a particular way. One group contains the red and infrared lines λ 6374 and λ 7892; the second contains the yellow line λ 5694 alone; and the third contains the green line λ 5303, together with the remaining observed lines. The lines in the blue, violet, and ultraviolet, with the exception of λ 3388, which is very strong, cannot be observed with the coronagraph outside an eclipse, as they are always blended with the strongly scattered solar light.

The program was thus arranged to obtain spectra of the inner corona, enabling us to

compare the intensity distribution of lines of wave lengths shorter than λ 5000, with some lines in the previously mentioned groups, in particular with the red line λ 6374, the yellow line λ 5694, and the green line λ 5303. The spectrographs are of reasonably high dispersion: the dispersions are shown in the preceding table (values in A/mm).

II. OBSERVATIONS OF THE ECLIPSE

We aimed at the study of the emission lines in the inner part of the solar corona. The slits of the spectrographs were designed to give circular lines all around the sun at a distance of about 1′ of arc from the solar limb. Because of an unforeseen discrepancy in letter designation of the magnitude of the eclipse as given in the *Nautical Almanac* or the *American Ephemeris* and the *Annual Report of the Bureau de Longitude*, an error was

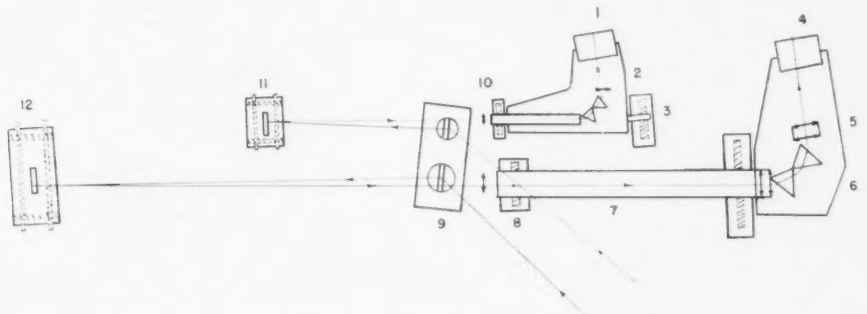

FIG. 1.—Block diagram of the equipment used: (*1*) quartz spectrograph, (*2*) calcite prism, (*3*) sliding ends, (*4*) glass spectrograph, (*5*) achromatic object, (*6*) flint prism, (*7*) collimator, (*8*) 5-cm circular slit, (*9*) coelostat, with 30-cm silvered mirror and 15-cm aluminized mirror, (*10*) 2.5-cm circular slit, (*11*) concave aluminized mirror (2.5 m, *f*-ratio 1) sliding on rails, (*12*) concave silvered mirror (5.0 m, *f*-ratio 1) sliding on rails.

introduced. The magnitude of the eclipse is given as 1.036 in the first two and as 1.018 in the French almanac. The latter value was the one we used in our calculations for the design of the instruments in Paris. Thus we found the diameter of the disk of the moon slightly greater than the designed diameter of the slits, which meant that they would be covered by the disk of the moon during the eclipse. This was discovered only the night before the eclipse, and it was too late to make any major alterations. We found it was simplest to change the position of the two correcting lenses in front of the slits by moving them farther away from the slits on their mounting. Consequently, the sun's image grew smaller, and hence light from parts farther out in the corona (about 2′ of arc) was observed. The two spectrographs are rotatable around the collimator axes, and, by turning them about 115° from the horizontal plane, the direction of the dispersion was rendered parallel to the sun's equator (see Fig. 1, which gives a block diagram of the equipment used).

III. THE PLATES

The spectrograms obtained are illustrated in Figures 2, *a*, and 3, *a*. From one exposure on each spectrograph, two spectra were obtained, one below the other, the lines in each being in the form of semicircles corresponding to each side of the sun. The middle parts of every spectral line were of 0° latitude, i.e., the equator of the sun was represented on the spectrum by the middle line along the dispersion. The widths of the spectra on the photographic plates were about 11 mm.

Four spectrograms were obtained, two for the solar corona taken during the totality and two taken the day before the eclipse (Table 1). On the glass spectrograph the exposures were made in the following order: 1, 5, 30, 90, and 10 seconds, to insure obtaining different exposures in case the beginning or end of totality was missed. A 2-second exposure was also planned to follow the 10-second one, but it was missed for lack of time at the end.

The spectra of the corona obtained with the glass spectrograph plate were excellent, especially on the western side of the sun; and they are very useful for the study of both strong and faint lines from the various exposures. On the spectrum of the other side of the sun, only strong lines are seen, with no clear traces of prominence lines. This was probably due to the exposures being interrupted by the moon's shadow covering parts of the slit. The plate was clear of any fog or defect except for my fingerprints at the red end of the 30-second exposure at the lower part of the eastern spectrum. This happened in the process of loading the plates in the hot, damp darkroom before exposures. The lightly exposed spectra will be of little use for photometry.

TABLE 1

OBSERVATIONAL MATERIAL

Plates	Spectrograph	Exposure (Seconds)	Spectra	Date
Astra III	Glass	90, 30, 10, 5, 1	Corona	Feb. 25 at 9^h15^m
Superfulger (Effet Raman)	Quartz	90, 30, 10, 5, 2, 1	Corona	Feb. 25 at 9^h15^m
Astra III	Glass	90, 10, 1 with density sheets 27, 9, 3 without density sheets	Sun	Feb. 24 at 12^h0^m
Superfulger (Effet Raman)	Quartz	90, 10, 1 with density sheets 45, 15, 5 without density sheets	Sun	Feb. 24 at 12^h45^m

On the quartz spectrograph plates, exposures were 1, 5, 30, 90, 10, and 2 seconds. There was slight general fogging due to scattered light from the quartz prisms. This was bad in early trials, but, by special shielding and backing of the prisms and other precautions, the scatter was minimized. This fogging will have to be allowed for in the microphotometric reductions. The spectra were very clear, and prominence lines were recorded as far as λ 2900. Naturally, at the short-wave limit, the lines are out of the zone of best focus. The last coronal line seen clearly on the ultraviolet side was the known line λ 3328. On this plate very thin, sharp, concentric fringes, uniform in density and at equal distances of about 3 A apart, appeared particularly prominent in the region between λ 3500 and λ 4300. These fringes are seen only on the exposures made with the quartz spectrograph. They are probably caused by the material of the prisms. However, they have no effect on the measurements, nor will they affect the photometry, as they are of about the same order of magnitude as the plate grain. Spectra of solar prominences during the eclipse were also recorded on both eclipse plates, and their positions and intensities can be studied.

Two other plates were taken with the two spectrographs the day before the eclipse at nearly the same hour as the eclipse time, for the purpose of standardization. On each plate we have three photographs of the solar spectrum of nearly the same exposure times as those of the eclipse plates, namely, 27, 9, and 3 seconds for the glass spectrograph, and 45, 15, and 5 seconds for the quartz. Three other exposures of the solar spectrum of 90, 10, and 1 second were taken on the same plates with gelatin density sheets of steps 0.0, 0.5, 1.0, and 1.5 covering one side of each slit (the other side being closed). From these

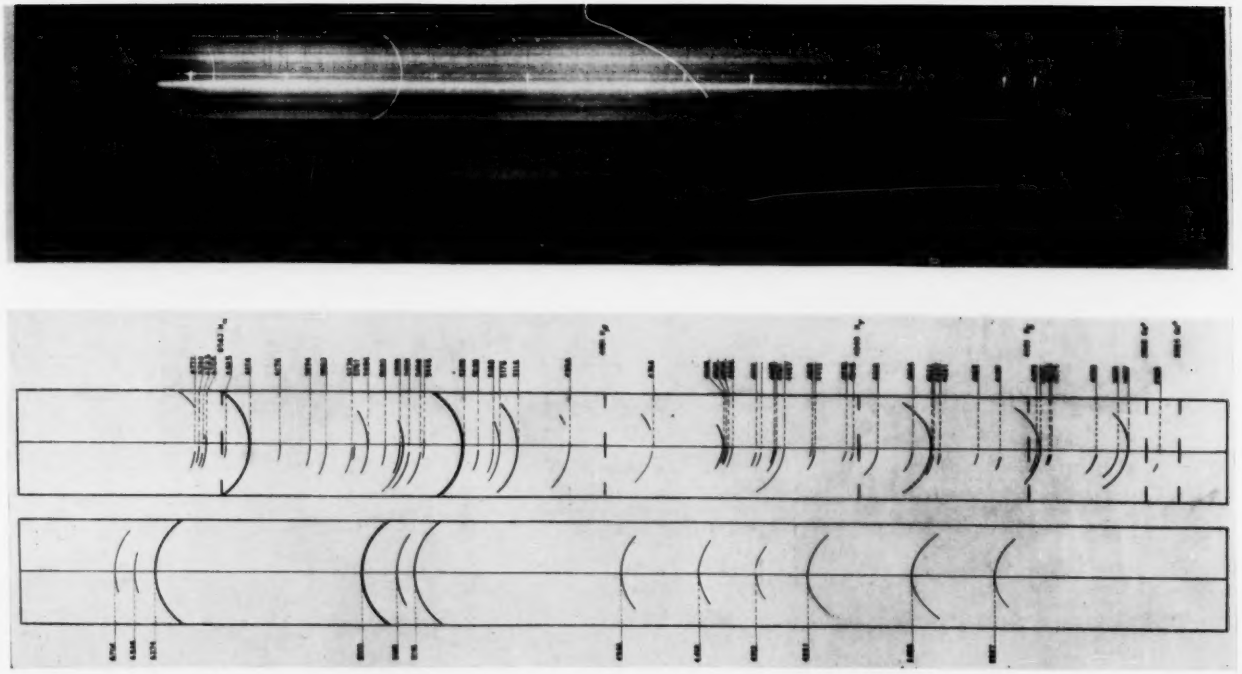

FIG. 2.—*a*, Ultraviolet spectrum of the solar corona taken with the quartz spectrograph and circular slit during the total eclipse of the sun at Khartoum on February 25, 1952. *Above:* west limb; *below:* east limb. *b*, Key to the spectrograms. The wave lengths of the principle lines are indicated.

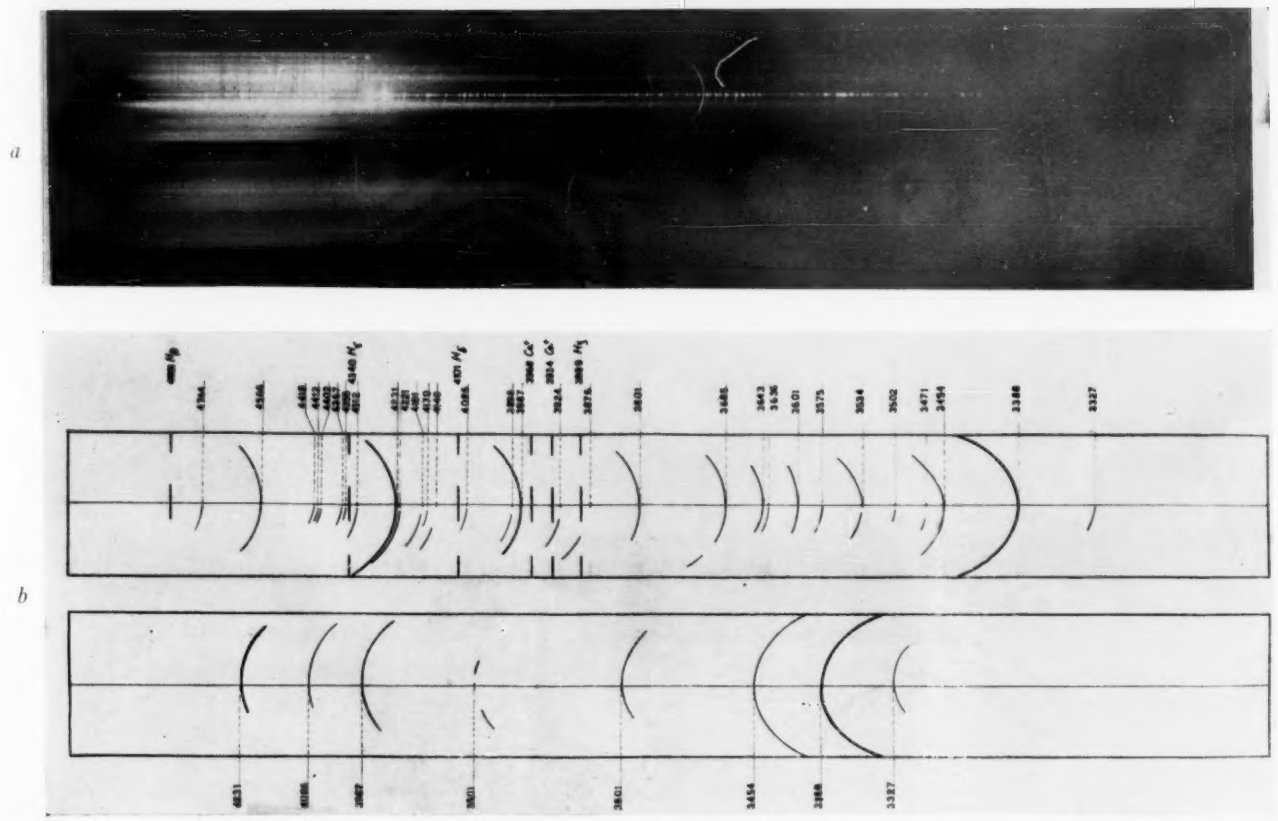

FIG. 3.—*a*, Ultraviolet spectrum of the solar corona taken with the glass spectrograph and circular slit during the total eclipse of the sun at Khartoum on February 25, 1952. *Above:* west limb; *below:* east limb. *b*, Key to the spectrograms. The wave lengths of the principle lines are indicated.

last three exposures solar lines appear with four different densities along the lines themselves. Combined measurements from these solar spectra will be used for microphotometric reductions of the eclipse plates.

IV. MEASUREMENTS

Wave lengths of all lines seen on the two spectrographs were measured to the nearest hundredth of a millimeter. Every plate was measured twice by both the late Bernard Lyot and myself on the Zeiss blink comparator at Helwan. As there are several exposures on each plate, measurements were made from every exposure, for the lines present on each. The lines appear circular, or almost so, on the plates, and their intensity distribution is different at various position angles around the sun. The very faint lines appear only in some parts of the circle, i.e., not all along the line, but all measurements have been reduced to the solar equator.

The late Bernard Lyot was concerned primarily with the presence of coronal emission lines, which are of interest in their intensity variations around the sun, and its correlation with the ionization potential. For this purpose we started soon after our return from Khartoum to measure such lines, leaving the thorough search for very faint lines until later. Unfortunately, Bernard Lyot did not live long enough to see the accordance of Edlén's theory with our observations and to complete his work.

Later, after the unfortunate death of Bernard Lyot, the author obtained good prints of the original plates enlarged six times and found more details of the spectra which were not visible on the plates. At this stage the plates were remeasured for wave-length determinations, and a thorough search for the extremely faint lines was made. This repetition showed a good number of new very faint lines on both plates and enlargements. The wave-length measurements, made by interpolation or extrapolation with close lines, gave positions accurate within 1 or 2 A. The presence of some of the extremely faint lines was confirmed by wave-length measurements given for lines observed at earlier eclipses (Mitchell 1951; Edlén 1942; Menzel 1931). Slight alterations were then necessary in the reductions made earlier by Bernard Lyot and myself.

The earlier measurements by Dr. Lyot and the author are given in Table 2. The later measurements made by the author alone are given in Table 3. This latter table contains only the lines whose reality is least doubtful, thirty-two in all; the author has recorded eighty-one additional lines which need further confirmation. The wave lengths given are taken from the western limb of the sun only. It is seen in both tables that some wave lengths measured on plates taken with the quartz spectrograph differ from those taken with the glass spectrograph by 2 or 3 A; also, differences exist between our measurements and those of previous observers listed in column 6. Such measurements are given here with reserve, to indicate that they might possibly correspond to entirely different lines. This is true only in the case of faint or extremely faint lines. Tables 2 and 3 give the measured wave lengths of all lines definitely observed in the corona as taken from the western side of the sun only.

The Balmer series and the H and K lines of ionized calcium as well as a number of metallic solar lines have served as our landmarks. These, together with some of the well-known coronal lines, were very useful in forming the correction-curves of $\Delta\lambda$. The dispersion is so small near the $H\alpha$ end of the visible spectrum and the $\Delta\lambda$-curves are so indeterminate that probable errors of about ± 3 A are present.

In general, there is very close agreement between present and previous wave-length measurements of the known lines. With the exception of lines near the long-wave end, discrepancies have not exceeded 1.0 A except in rare cases, namely, for the lines $\lambda\lambda$ 4056, 5517, 5536, 5624, and 5912, where they reached 2 or 3 A. The diagrams given in Figures 2, *b*, and 3, *b*, show with sufficient accuracy the positions of most of the observed lines on both limbs, together with their wave lengths.

V. DESCRIPTION OF TABLES 2 AND 3

Column 1 gives serial numbers.

Column 2 gives wave lengths of lines observed at this eclipse, (*a*) with the quartz spectrograph and (*b*) with the glass spectrograph. In both 2, *a* and *b*, an asterisk indicates that the lines are extremely faint and were seen only on the enlargements.

Column 3 gives a general description of the lines. The following system has been found convenient in specifying the degree of certainty as regards the presence of lines: certain (C), followed by almost certain (aC), rather certain (rC), rather doubtful (rD), doubtful (D), very doubtful (vD). For the brightness, the description: very strong (vS), followed

TABLE 2

WAVE LENGTHS OF THE CORONAL LINES (MEASURED BY LYOT AND ALY)

1	2		3		4	5	6	7
	a	*b*	*a*	*b*				
1	3326.7	.....	C, S, nE, Z	.....	α	7	3328	G, M, L, D
2	3388.0	.....	C, vS, E, B	.....	α	65	3388	G, M, L, D
3	3454.2	.....	C, vS, E	.....	α	15	3454	G, M, L, D
4	3533.5	.....	C, F, E	.....	α	12	3534	G, L, D
5	3574.7	.....	rC, eF, rE	.....	γ	....	3577	M
6	3600.9	.....	C, S, nmE	.....	α	15	3601	G, M, L, D
7	3642.8	.....	C, S, rE	.....	α	11	3643	G, L, D
8	3801.2	.....	C, S, rE	.....	α	12	3801	G, M, L, D
9	3987.7	3987.0	C, S, E	C, S, E	α	25	3987	G, M, T, L, D, Allen
10	3996.0	3998.0	rD, vF, rE	C, vF, rE	α	3	3998	L, D, Allen
11	.....	4067.4	.....	rD,vF, nmE	....	....	4063	Allen
12	4086.2	4086.0	C, S, nmE	C, S, nmE	α	10	4086	G, M, T, L, D, Allen
13	4232.1	4231.9	C, vS, E, U	C, S, E	α	35	4231	G, M, T, L, D, Allen
14	4358.2	4358.1	C, vF, nE, B	C, F, fU	α	6	4359	G, T, M, L, D
15	4412.0	4413.2	C, F, nE	C, F, rE	α	10	4412	Dunham, L, D
16	4566.1	4566.3	C, F, E	C, F, E	α	15	4567	G, M, T, L, D
17	.....	4576.5	.....	rC, eF	γ	....	New	.....
18	4587.5	4585.7	aC, vF, nmE	C, vF	α	6	4586	G, D, T
19	.....	5114.8	.....	C, S, U	α	30	5116	G, M, T, S, L, D, Allen
20	.....	5301.9	.....	C, vS, E	α	100	5303	G, M, L, S, T, D, Allen
21	.....	5446.0	.....	C, eF	α	3	5445 5444	Waldmeier L, D
22	.....	5539.5	.....	C, vF, U	α	8	5536	D, G, T, M, L, Davidson
23	.....	5693.7	.....	C, vF	α	7	5694	L, D
24	.....	6374.2	.....	C, vS, E	α	80	6374	G, M, S, T, L, D, Allen
25	.....	6702.8	.....	C, vF, nmE	α	10	6702	G, L, M, S, T, D

by strong (S), faint (F), very faint (vF), and extremely faint (eF) are given. For the general appearance: the intensities vary along the lines, and for a faint or extremely faint one it is visible only at very limited parts along its length anywhere near or far from the equator. For such descriptions it was found enough at this stage to describe the lines as: extended (E), when seen on more than half the length of the circular trace, followed by rather extended (rE), not much extended (nmE), and not extended (nE) when seen only at one particular position; for a broad line (B), a uniform line (U), and a fuzzy line (Z). The descriptions under the subcolumn *a* correspond to *a* in column 2 and those under *b* correspond to *b* in column 2.

Column 4 gives the weights (α, β, γ) obtained from our observations.

Column 5 gives the approximate intensities estimated by the eye from enlargements, taking the intensity of the lines λ 5303 as 100.

Column 6 gives wave lengths of coronal lines seen by other observers at eclipses.

Column 7 gives initials of the other observers: G, Grotrian; E, Edlén; L, Lyot; M, Menzel; S, Sekeguti; D, Dollfus; and T, Tanaka.

VI. DISCUSSION AND CONCLUSION

With our equipment we have obtained recordings of 138 coronal emission lines of all categories; 78 lines of which are graded certain, almost certain, or rather certain and weighted α, β, or γ. The rest fall under the doubtful grades. Only 37 of these have grade α, 26 of which have been observed in previous eclipses; the remaining 13 are lines not known to have been observed before. The existence of the previously observed lines is thus checked, and the intensity variations at different position angles can be studied for the strong ones. It must be mentioned that some of the faint lines previously observed have been seen here with some doubt, as shown in the tables, and some others have not been found. As for the photometric values, some 16 lines in the whole range of the observed spectrum will be of value for a study of their intensity distribution.

We have also succeeded in recording spectra in the blue and the ultraviolet which were

TABLE 3

WAVE LENGTHS OF THE CORONAL LINES AS MEASURED BY ALY

1	2		3		4	5	6	7
	a	*b*	*a*	*b*				
1	3471.0		C, eF, nmE		α	2	3461	G
2	3685.0		C, vF, rE		α	4	New	
3	3876*	3876.2	rC, eF, rE	D, eF, nmE	β			
4		4020.3		aC, eF, rE	β			
5		4037.7		rC, eF, rE	γ		4041	Allen
6		4074.0		C, eF, nE	α	1	New	
7	4140*	4138.6	aC, vF, rE	rC, eF	α	2	New	
8		4165.3		C, eF, nE	α	4	New	
9	4170*	4170*	aC, vF, rE	rD, eF	β		4170	M
10	4181.2		aC, vF, rE		β			
11	4221*	4221*	aC, vF, E	rC, eF, nE	α	3	New	
12		4256.4		C, vF, rE, B	α	2	New	
13	4312.0	4312.1	aC, vF, rE	C, vF, E, B	α	8	4311	G, D, T, S
14	4349*	4350.6	rC, eF, nE	aC, vF, rE	α	3	4349 4351	Edlén L, D
15		4363.2		aC, eF, nE	β			
16	4418*	4418*	rC, eF, nE	rC, eF, nE	β			
17		4466.9		aC, vF, B	β			
18	4484.1	4482.6	D, eF	rC, eF, rE	β			
19	4504*	4504*	aC, eF, rE	aC, eF	α	3	New	
20	4580.1	4581.8	aC, vF, nE	D, eF	α	1	New	
21	4744*	4744*	C, vF, rE	rD, vF	α	3	New	
22		4956*		C, eF, E	α	2	New	
23		5178*		aC, eF, E	β			
24		5188.5		aC, eF, nE	β			
25		5232.9		aC, eF, nE	β			
26		5558.6		C, eF	α	1	New	
27		5620.1*		aC, eF, rE	β		5624	S
28		5774*		aC, eF	β			
29		5974.3		aC, vF	β			
30		6535.4		rC, vF, E, B	γ		6534	S
31		6740*		aC, vF, rE	β	2		
32		6777*		aC, vF, rE	β		6776	M, S, T

beyond the scope of the coronagraph. The strong line λ 3388 was beautifully recorded on more than one exposure and all around the sun (60° north and 60° south of the equator). As it has been observed previously with the coronograph, it will thus serve as a very good standard for comparing the intensity distribution of other lines in this region. The only coronal line that could be studied beyond that in the short-wave region is the known line λ 3327, which appears on the western limb only at a region of 20° below the equator and on the eastern limb 25° north and 25° south.

In the blue there is a number of nicely recorded lines, most of which can be used for photometric study, namely, the known lines λλ 3454, 3601, 3801, 3987, 4086, and 4231. The three lines λλ 3987, 4086, and 4231 are recorded on both spectrograms, more clearly on the quartz. The faint new line in this region, namely, λ 3534, easily seen to about 25° north and 25° south on the western limb, can be studied photometrically. The rest of the new lines in this region appearing in the list, though seen on the spectrograms, are below the intensity desired for the microphotometric investigations. In the green, in the vicinity of the strongest line recorded in all the spectrum (λ 5303), the two lines λ 4565 and λ 5115 can be studied photometrically. In the red we have, near the very strong line λ 6374 seen all around the sun, the line λ 6703 which can possibly be studied.

In this connection it is my duty to mention with the deepest regret the untimely death of Bernard Lyot, whose loss was felt by astronomers all over the world. It has been a great honor and pleasure to work under the direction of and in collaboration with this most eminent astronomer.

The program of this work was arranged jointly during my stay in Paris and was carried out at Khartoum in a most cordial and amiable atmosphere. To Mr. H. Grenat and his staff at the Meudon Observatory for building the equipment we are also grateful. It is a particular pleasure for the author to thank Mrs. Bernard Lyot for her help in giving time signals during the eclipse. I am also indebted to the director and the staff of the Meudon Observatory for the loan of the equipment.

Finally, the author wishes to acknowledge his indebtedness to Professor M. R. Madwar for making arrangements for the whole expedition in Egypt, for his efforts in alleviating all the difficulties of carrying out such a program, and for his valuable checking and criticism. The author is also grateful to the referees of this paper who have contributed substantially to its preparation.

REFERENCES

Allen, C. W. 1947, *M.N.*, **106**, 137.
Aly, M. K. 1952, *Observatory*, **72**, 867, 68.
Edlén, B. 1942. *Zs. f. Phys.*, **22**, 62.
———. 1945. *M.N.*, **105**, 6.
Grotrian, W., and Sekeguti, R. 1937, *Nature*, **140**, 724.
Lyot, Bernard. 1939, *M.N.*, **99**, 8.
Lyot, Bernard, and Dollfus, Adouin. 1953, *C.R.*, **237**, 855.
Madwar, M. R. 1952, *Bull. Inst. d'Égypte*, Vol. **34**.
Menzel, D. H. 1931, *Lick Obs. Pub.*, Vol. **17**.
Mitchell, S. A. 1951, *Eclipses of the Sun* (New York: Columbia University Press).
Petrie, W., and Menzel, D. H. 1942, *Ap. J.*, **96**, 397.
Tanaka, T. 1937, *Proc. Phys. Math. Soc. Japan* [3], **19**, 703.
Waldmeier, M. 1951, *Zs. f. Ap.*, **29**, No. 1, 29.

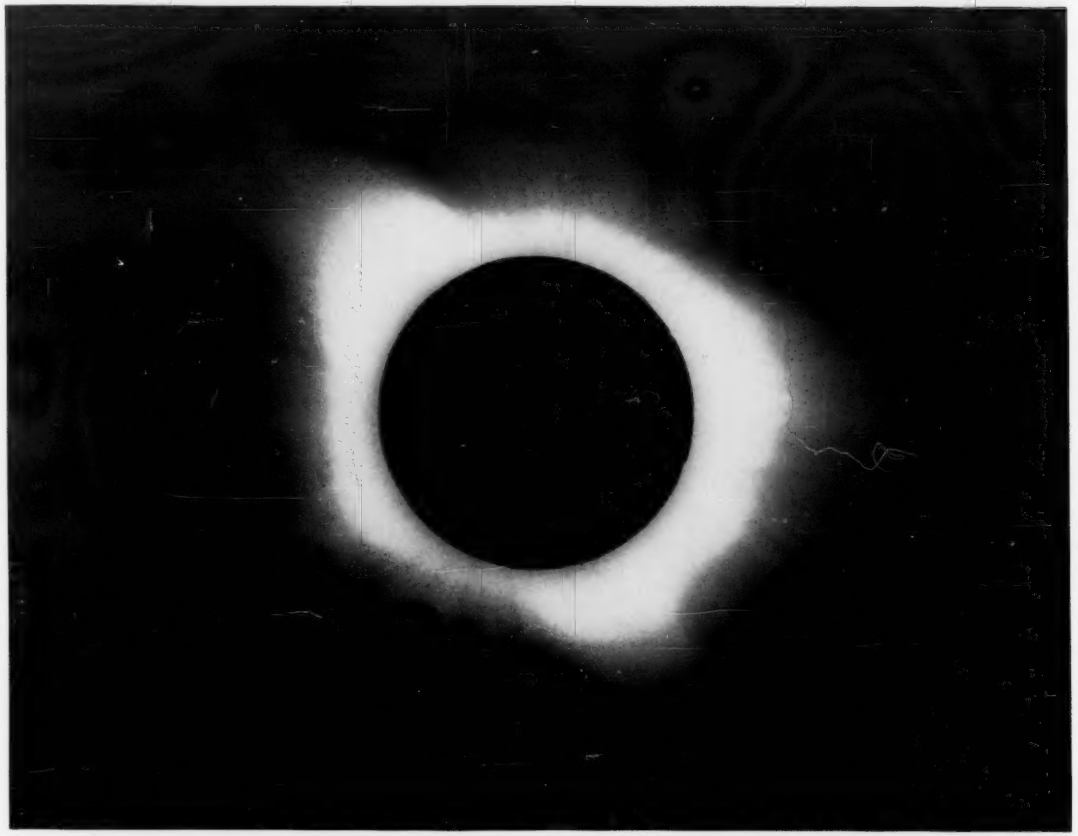

FIG. 1.—The solar eclipse of February 25, 1952, at Khartoum, Sudan, by the U.S. Naval Research Laboratory Expedition

A PHOTOMETRIC STUDY OF THE SOLAR CORONA

NANNIELOU HEPBURN*
Naval Research Laboratory, Washington, D.C.
Received June 27, 1955

ABSTRACT

Photometric measurement of the solar corona as photographed by the Naval Research Laboratory expedition to Khartoum, Sudan, on February 25, 1952, is described and related to other measurements and theoretical studies. In particular, the variation of white-light intensity with radius is compared to van de Hulst's model of the corona, and coefficients are derived for his equations which produce curves more nearly fitting the observed intensities. The removal of the *F*-corona and calculation of electron densities according to van de Hulst's model appears to give consistent results here.

These measurements extend from the solar limb out to about 2.5 solar radii from the center of the sun, so that combination of the results with those obtained by the French expedition to Khartoum (headed by Bernard Lyot) is of considerable interest. A comparison has been made between their measurement of the variation with the position angle of the red and green coronal lines near the great streamer and variations in the white-light corona. Although the center of the streamer appears to lie about 10° north of the emission-line maximum, an examination of the white-light corona near the limb ($\rho = 1.06$) shows a close correlation of white-light intensity with the emission lines.

INSTRUMENTS AND OBSERVATIONS

At the total solar eclipse of February 25, 1952, radio and optical observations were made by the Naval Research Laboratory expedition to Khartoum, Sudan (described in detail by Hulburt 1952). Eleven usable photographs of the corona (cf. Fig. 1) were obtained by Dr. John P. Hagen and Mr. David Hawkins with the Gardner camera lent by the National Bureau of Standards. The effective focal length of the camera is about 18 feet, so that the image of the moon is about 2 inches in diameter. The photographs were made on 8 × 10 Kodak panatomic-x plates with exposures ranging from 2 to 7 seconds. Although spicules remain unresolved, details such as prominences, arches, and polar rays are measurable, and on some of the plates the great northeast streamer is visible out to the edge of the plate.

A photometric scale with eight steps ranging from 88.4 to 0.012 per cent transmission was photographed on each plate, using diffused sunlight as a light-source, to determine characteristic curves. However, the plates in some cases recorded densities higher than the densest step in the scale, which was about 2.5. Therefore, exposures in daylight using an eleven-step scale were made on plates from the same box as the eclipse plates and were developed in the same way. Thus a complete characteristic curve was obtained. Each individual plate-curve was fitted to this extended curve, with an average difference between the two curves of about 2 per cent and all densities reduced to relative intensities. In every case these high densities (never so high as 4.0) were recorded within a radius of 1.1 times the solar radius from the center of the sun. Thus most of the uncertainty in the reduction to intensities lies in the measurements made very close to the limb.

The photometric measurement of the eclipse plates was carried out on a Zeiss microdensitometer in which the original electronics were replaced by a photomultiplier tube (RCA931A) followed by a Brush d.c. amplifier and recording milliameter. The spot measured on the plate was 0.2 mm wide and was therefore just above the grain size. A fine thread was stretched across each plate, to produce a sharp decrease in the record for use as a fiducial line. In order to monitor photocell sensitivity and amplifier gain, calibrations using a constant light-source behind a diffuser were carried out frequently during

* Now at Harvard College Observatory.

the measurements. An inverse-square-law calibration was also performed and showed the whole system to be linear throughout the range used. In addition, a platform slightly less than 2 inches in diameter was added to the existing plate carriage and rotated by a motor in a clockwise direction at a constant rate of about 4 minutes per rotation. The image of the sun on each plate was centered on the platform, and the whole table was set so that the light-beam was near the edge of the moon and at a known distance from the center of the sun. The platform was then allowed to go through two rotations while the recorder registered the changing density. The table was then moved to a new radius (0.2 mm larger than the first for the inner corona, where the density gradient is large), and the platform was rotated again. This procedure continued out to the edge of the plate gave a series of concentric density measurements covering the corona from the solar limb out to about 2.5 solar radii from the center on each of the eleven plates.

PROBABLE ERRORS

The errors one must consider in a measurement of this kind come from two sources—the masking of the corona as recorded on the plates by unknown amounts of scattered light and the uncertainties inherent in the photometry itself. Michard *et al.* (1954) have shown that for this eclipse the illumination of the "sky background" was by no means uniform but had isophotes parallel to the horizon, becoming a minimum near the zenith. However, the total variation across the relatively small field photographed here was less than 1 per cent, according to their estimates. Another and undoubtedly more disturbing source of scattered light lies in the camera itself, especially in the surfaces of the lenses.

The second source of error lies in the photometric measurement of the photographs. It seems likely that any errors in the measurement of densities on any one plate are rather small. The repetition of each circle around the plate and the repeated calibrations and zero checks gave results which were reproducible within 1 per cent. The densitometer system was sensitive enough to record and repeat very fine detail, especially near the edge of the moon, where the tangential speed of the plate was small. Actually, much more detailed information was obtained than could be used in this study. The conversion to relative intensities suffers from uncertainties which are difficult to assess, but it is hoped that the use of a number of plates has reduced them considerably. It is quite likely that much of the scatter appearing in the data obtained from these plates is due to errors in determining ρ, the radius of a particular run on the plate. In the first place, the slit was 0.2 mm wide, producing an uncertainty everywhere of ± 0.1 mm. The micrometer setting is accurate to ± 0.05 mm in changing from one radius to another, so that the greatest source of error lies in the centering of the plates and the determination of $\rho = 1.0$ (the solar limb). Each plate was first placed on the platform, so that the image of the moon was centered, and then the platform itself was moved to an eccentric position to make the runs concentric about the center of the sun rather than the moon. The radius of the first run was then determined by knowing the position of the moon at the time each plate was taken. This procedure makes the variation in the determination of ρ from one plate to another about ± 0.5 mm, and, since the radius of the sun on these plates is approximately 25 mm, this produces a 2 per cent error in ρ from one plate to another. The additional errors on a single plate bring the probable error in a single determination of ρ up to about 2.5 per cent.

In general, the comparison of these measurements of the corona with theoretical models and with other observations of this eclipse shows them to be consistent, despite the multiple sources of error.

ELLIPTICITY OF THE CORONA

In order to plot isophotes in the corona, a series of steps in intensity was set up, and the positions where these intensities appeared were plotted on large polar paper for each plate.

Isophotes out to about $\rho = 2.5$ (where ρ is the distance from the center of the sun measured in solar radii) are shown in Figure 2. The ellipticity of the isophotes on all the plates was measured by Ludendorff's (1928, 1934) method, in which the ellipticity $e = 3R/D - 1$, where R is the mean of the equatorial diameter of a certain isophote and the two diameters inclined at 22°.5 to the equator and D is the sum of the three corresponding polar diameters. For this eclipse near minimum phase, the mean of eleven plates gives a maximum ellipticity of 0.24 at an equatorial diameter 1.9 times the solar diameter. This is identical with Waldmeier's (1954) value for this eclipse. Since the Naval Re-

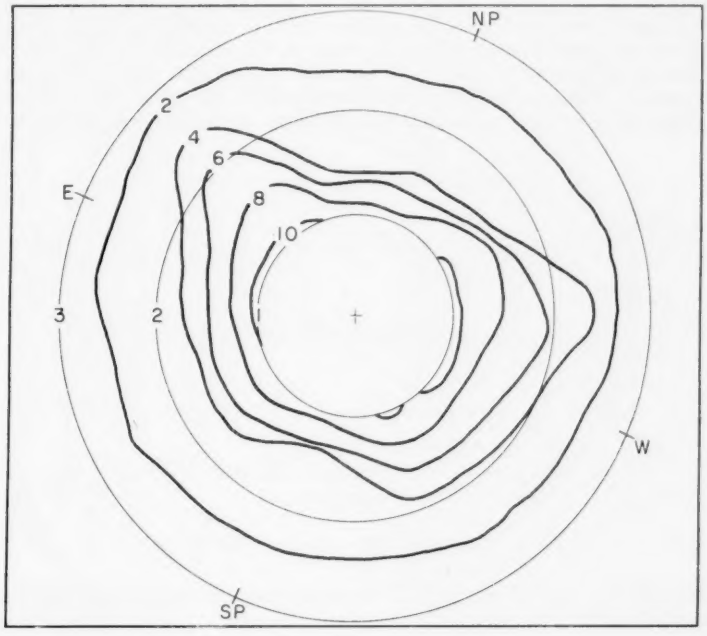

FIG. 2.—Isophotes in the solar corona. The intensity of each isophote is four times greater than the one immediately preceding. The contours used in the analysis show much greater detail than is evident here.

search Laboratory photographs do not show the outer corona, not much can be said from these measurements about the decrease in ellipticity beyond this maximum, but it is of interest to compare Waldmeier's values with those of Michard *et al.* (1954). Figure 3 shows their combined measurements of ellipticity from near the limb out to an ellipse with major axis 40 solar diameters long.

INTENSITY AS A FUNCTION OF RADIUS

A study has been made of the variation in total intensity, that is, of the combined K and F coronas, with distance from the sun. For this purpose, densities were read off the complete records along equatorial and polar radii. These were then converted to relative intensities and are designated as follows: $K_{\min} + F$ is the total light received in the equatorial region (at minimum phase); $K_{\text{pole}} + F$ is the total light in the polar regions.

These symbols are taken from van de Hulst's (1950*a*) paper, where he derives a model of the corona leading to equations describing the variation in intensity with radius. His equations are

$$K_{\min}+F=\frac{200.0}{\rho^{17}}+\frac{114.0}{\rho^{7}}+\frac{5.39}{\rho^{2.5}},$$

$$K_{\text{pole}}+F=\frac{191.0}{\rho^{17}}=\frac{27.45}{\rho^{7}}+\frac{4.99}{\rho^{2.5}},$$

where the intensity unit is 10^{-8} times the average surface brightness of the sun. These distributions agree very well with Bergstrand's (1919) measures of the 1914 eclipse, which occurred at approximately the same phase in the solar cycle as the 1952 eclipse, and with van de Hulst's own measures of the 1900 eclipse, also near minimum.

For comparison with van de Hulst's model, the scale of the relative intensities derived here was adjusted as follows: a constant was added to the intensity at a radius of 1.4 to

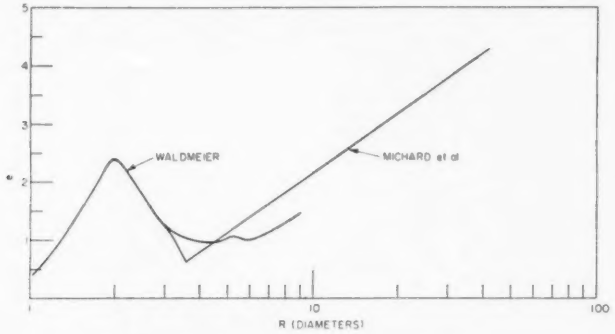

FIG. 3.—Ellipticity of the corona. $e = 3R/D - 1$

make it agree for the equatorial case, and the same constant was then added to all other NRL intensities. It will be shown that the absolute-intensity scale adopted in this way is entirely consistent with the direct absolute-intensity measurements made by the French expedition to Khartoum (Michard *et al.* 1954).

It can be seen from Figures 4*a* and 4*b* that the NRL data fail to fit van de Hulst's distributions. It was decided to derive equations using the exponents given by van de Hulst but with coefficients adjusted to bring them into closer agreement with the observations. It would certainly be desirable to obtain entirely independent functions, but the limited extent of these observations and the scatter present in the measurements made this seem impractical. The NRL equations represented in Figures 4*a* and 4*b*, then, are

$$K_{\min}+F=\frac{93.9}{\rho^{17}}+\frac{177}{\rho^{7}}+\frac{2.40}{\rho^{2.5}},$$

$$K_{\text{pole}}+F=\frac{61.2}{\rho^{17}}+\frac{58.8}{\rho^{7}}+\frac{1.81}{\rho^{2.5}}.$$

The probable error in determining ρ for a particular intensity from the polar curve is about 1 per cent, so that the coefficient of the first term would have a probable error of

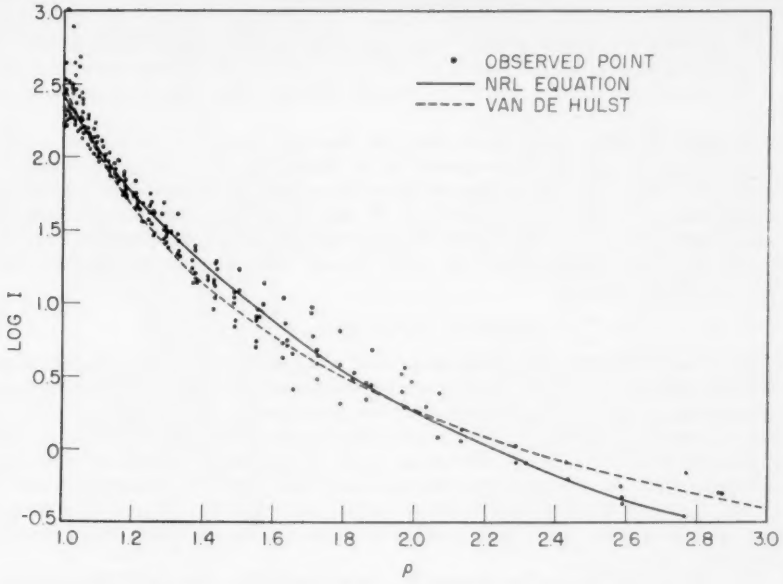

FIG. 4*a*.—Intensity as a function of radius at the equator

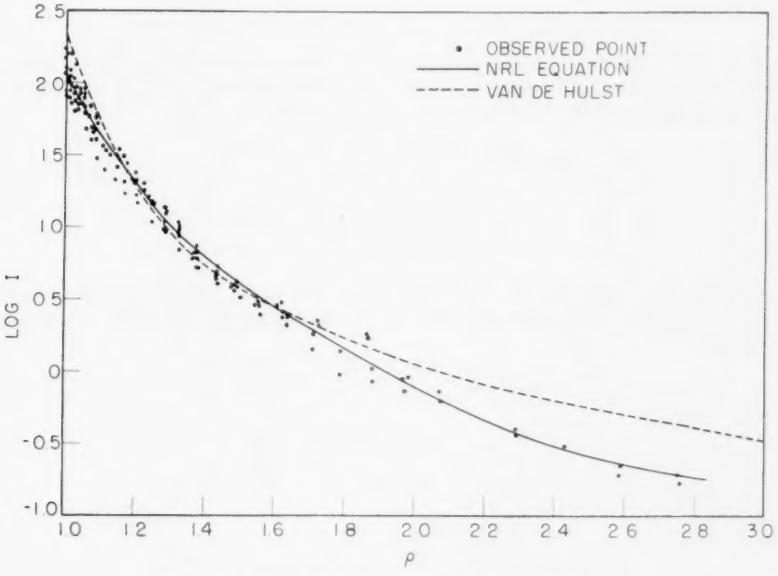

FIG. 4*b*.—Intensity as a function of radius at the pole

about 17 per cent, the second about 7 per cent, and the third about 2.5 per cent. The greater scatter in the equatorial measures, probably due in part to the streamers, which affect the east and west limbs differently, would indicate larger errors in the equatorial coefficients.

Fortunately, the NRL observations from the limb out to about $\rho = 2.5$ complete the picture obtained by the French expedition to Khartoum headed by Bernard Lyot (Michard *et al.* 1954). Their photographs show the corona (in a band 500 A wide in the red) from about $\rho = 2.5$ to more than $\rho = 10$, and their measurements are reduced to absolute intensities. Figure 5 shows the NRL intensity functions as described here, combined with the French measures of the outer corona. They present a unified picture of the corona at this eclipse.

INTENSITY IN THE STREAMERS

Values of the total intensity along solar radii were taken from the complete records at position angles of 65° and 219° corresponding to the centers of the northeast and southwest streamers, which are very striking on the photographs. Figure 6 shows the logarithm of the intensity of the $K + F$ corona in the two streamers as a function of radius, along with the derived $K_{\min} + F$. These curves point up what is obvious on most eclipse photographs—that the streamers are brighter and their gradient of intensity with distance from the sun is smaller than the surrounding coronal areas. It can also be seen that the two streamers have very similar gradients, although the northeast one is considerably brighter.

R. Michard (1954) in a very interesting paper describes this northeast streamer in detail out to 10 solar radii and finds that the ratio N_s/N_e, where N_s is the electron density in the streamer and N_e the electron density outside it at the equator, increases rapidly out to $\rho = 3.5$ or 4 and then becomes approximately constant.

ELECTRON DENSITY AS A FUNCTION OF RADIUS

Electron densities were determined for the polar and equatorial radii. For this purpose the F-corona had to be removed from the total intensity measures, and this was done in the following way. Van de Hulst's model shows

$$K_{\text{pole}} + F = \frac{191.0}{\rho^{17}} + \frac{27.45}{\rho^{7}} + \frac{4.99}{\rho^{2.5}},$$

$$F = \frac{14.86}{\rho^{7}} + \frac{4.99}{\rho^{2.5}}.$$

The coefficient of the ρ^7 term in F is 0.541 times that in $K_{\text{pole}} + F$, and the whole last term is included in F. A similar equation for F was set up for the NRL measurements at the poles:

$$K_{\text{pole}} + F = \frac{61.2}{\rho^{17}} + \frac{58.8}{\rho^{7}} + \frac{1.81}{\rho^{2.5}},$$

$$F_N = \frac{31.8}{\rho^{7}} + \frac{1.81}{\rho^{2.5}},$$

so that

$$K = \frac{61.2}{\rho^{17}} + \frac{27.0}{\rho^{7}}.$$

As a check on this doubtful method the NRL equation for F was subtracted from the NRL equation for the equator, and the coefficients were compared with van de Hulst's

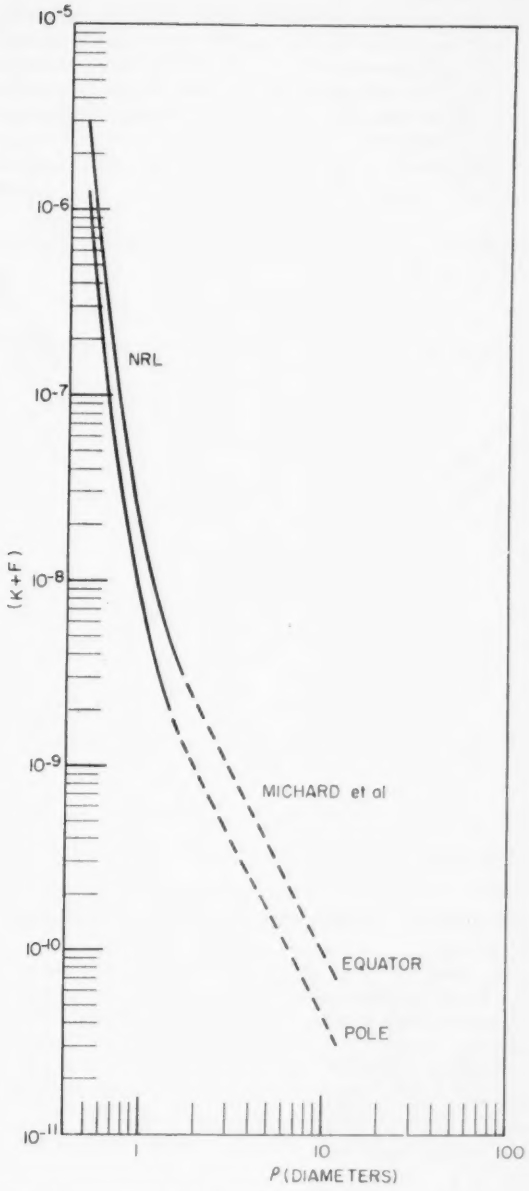

FIG. 5.—Intensity as a function of radius throughout the corona

equatorial coefficients. In the model the ratio $F/K + F$ for the ρ^{-7} term is 0.13, and in the relationship derived here it is 0.18. For the $\rho^{-2.5}$ term the model shows 0.93 for this ratio, and the NRL equation shows 0 75 It was thought that this agreement was as good as might be expected and that the polar measures should be used to determine the F-corona equation, since the values there are less affected by changes in the shape of the corona with solar cycle. This gives

$$K_{\min} = \frac{93.9}{\rho^{17}} + \frac{145}{\rho^{7}} + \frac{0.59}{\rho^{2.5}},$$

$$K_{\text{pole}} = \frac{61.2}{\rho^{17}} + \frac{27.0}{\rho^{7}}.$$

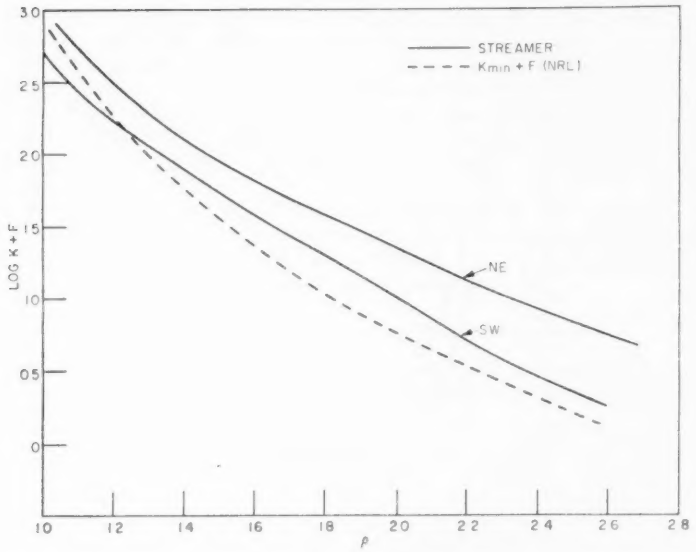

FIG. 6.—Intensity in the two streamers as compared to the background intensity

Figure 7 shows the combined $K + F$ corona for the equator at minimum phase and for the poles and the K-corona alone as well. One effect which appears here tends to confirm the correctness of the procedure in removing the F-corona. Van de Hulst finds that the ratio goes through a maximum at about $\rho = 1.4$, and, although the factor here is close to 10 rather than the 2.5 which van de Hulst finds, the removal of the F-corona shows that the ratio between the equatorial and polar K-coronas alone increases steadily outward, as would be expected from pure electron scattering. It is possible, of course, that the effect arises in both cases from using only three terms to represent the intensity function.

Further confirmation of the over-all correctness of the removal of the F-corona lies in the work of Michard *et al.* (1954). The values of K for the outer corona from their study and those for the inner corona as derived here give a smooth function for the variation with radius from $\rho = 1$ to $\rho = 10$. Since they were able to eliminate the F-corona direct-

ly by polarimetric measurements, this indicates that removing it by use of van de Hulst's model gives values for K which are consistent with observed values.

From these values of K, electron densities were determined as a function of ρ, using the relationship set up by van de Hulst. The results are shown in Figure 8. Although the polar regions were used to establish F, the equator appears to follow van de Hulst's model more closely. The large difference in density between pole and equator again points up the danger in drawing conclusions from the assumption of circular symmetry for a model corona.

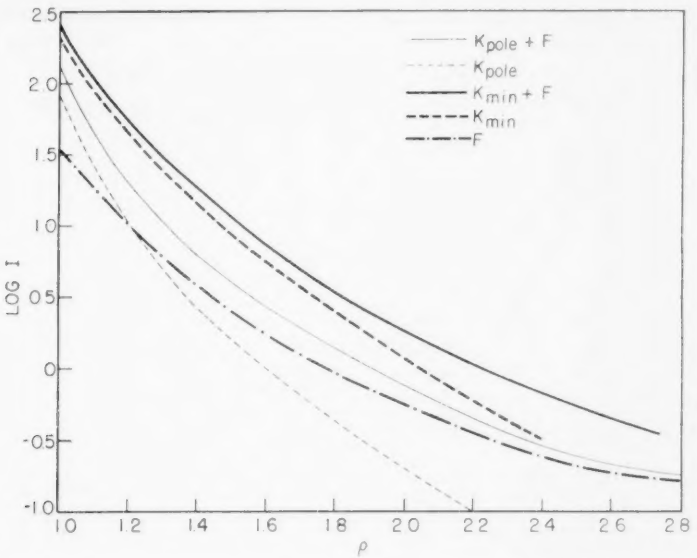

FIG. 7.—The total intensity-curves at equator and poles and the corresponding curves for the K-corona alone.

THE CORONA AS AN ATMOSPHERE OF HIGH TEMPERATURE

Assuming the corona to be an isothermal atmosphere, the temperature can be determined from the density gradient by using the equation of hydrostatic equilibrium:

$$\frac{6.89 \times 10^6}{T} = \frac{d\,(\log N_e)}{d\,(1/\rho)} + \frac{d \log T}{d\,(1/\rho)}.$$

The second term can be neglected, since the temperature gradient is small. Figure 9 shows $\log N_e$ against $1/\rho$ for the equator and poles on the NRL plates, with straight lines drawn through the points. The fact that these lines represent the data very well out to about $\rho = 2$ indicates that the isothermal model may be a good one to this height. The lines are

$$\text{Equator: } \log N_e = 4.40 + \frac{3.98}{\rho},$$

$$\text{Pole: } \log N_e = 3.22 + \frac{4.76}{\rho}.$$

These lead to temperatures of 1.73×10^6 degrees Kelvin at the equator and 1.44×10^6 degrees Kelvin at the poles. The values would be increased somewhat by the inclusion of the second term. The great northeast streamer shows the same good straight-line fit, but gives a temperature of 2.30×10^6 degrees.

ELECTRON DENSITY IN THE POLAR RAYS

The variation in intensity with radius in several polar rays was measured along with the intensity between them. An analysis was carried out similar to that shown by van

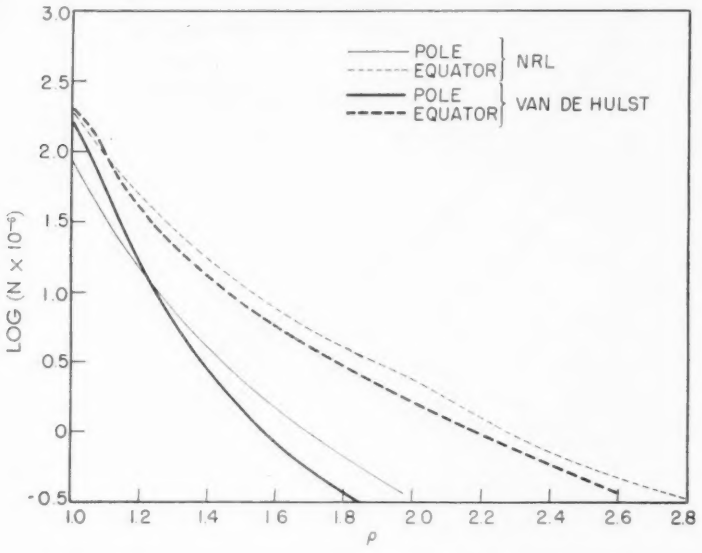

FIG. 8.—Electron density as a function of radius at the equator and pole

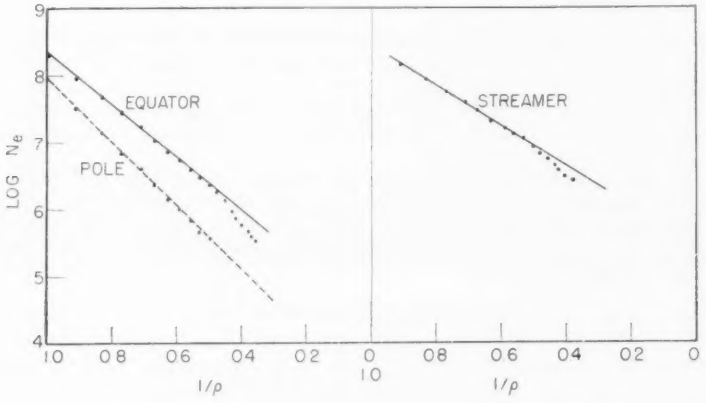

FIG. 9.—Logarithm of the electron density as a function of $1/\rho$

de Hulst (1950), with the result essentially a confirmation of his conclusion that the rays are not formed by ejection of material. Table 1 shows for one southern and two northern rays the total intensity measured in the ray ($R + B + F$), the intensity measured in an adjacent area outside the ray ($B + F$), and the intensities of the electron corona alone in the ray and in the background, using the equation derived previously to remove the F-corona. Table 2 shows the change in the various quantities between a radius of 1.04 and 1.34 in each of the rays, the average of the three, and the average of the rays measured by van de Hulst.

TABLE 1

Ray	ρ	$R+B+F$	$B+F$	F	B	R
N1	1.04	67.6	60.3	26.9	33.4	7.3
N1	1.34	7.08	6.46	4.9	1.56	0.62
N2	1.04	87.1	77.6	26.9	50.7	9.5
N2	1.34	8.91	8.51	4.9	3.61	0.40
S1	1.04	67.6	58.9	26.9	32.0	8.7
S1	1.34	6.61	5.76	4.9	0.86	0.85

TABLE 2

Quantity	Value of Quantity at 1.34 ÷ Value of Quantity at 1.04					
	Quantity	N1	N2	S1	Mean	*vdH*
Background intensity	B	0.47	0.14	0.03	0.21	0.22
Intensity of ray	R	0.08	0.04	0.10	0.07	0.09
Width of ray	w	2	2	2	2	2
Ratio of intensity	R/B	1.8	0.60	3.6	2.0	3.9
Electron density of background	N_b	0.06	0.09	0.03	0.06	0.04
Ratio of densities	$R/wB=N_r/N_b$	0.90	0.34	1.8	1.01	2.0
Electron density in ray	N_r	0.05	0.03	0.06	0.05	0.08
Total no. electrons in unit length of ray	w^2N_r	0.20	0.10	0.43	0.36	0.31

The agreement here of the average of the NRL measures and van de Hulst's average is striking, especially since the original measures were done in different ways and the plates were taken fifty-two years apart. In each case the electron density in the ray (N_r) decreases in much the same way as that outside it (N_b) between the two radii chosen. The last line in the table shows w^2N_r, the total number of electrons in unit length of the ray, which would be proportional to the ratio of the velocity at 1.04 to that at 1.34 if the particles were ejected at high velocity. The fact that w^2N_r is less than unity (0.3) indicates that the rays are not formed by ejected matter but are rather an alignment of electrons in the background.

VARIATION OF ELECTRON DENSITY WITH POSITION ANGLE

Since the electron density of the solar corona is obviously not a smoothly varying function of radius but shows complex structure varying with position angle as well, intensities were read off completely around the sun for levels in the corona at radii of 1.15, 1.38, and 3.20. Figure 10 is a plot of the density derived by van de Hulst's method from these measurements. He points out that the method is strictly applicable only near the equator and that near the poles the density should be multiplied by a factor of about

1.08, but this would not greatly change the shape of the curves. The presence of the streamers also introduces errors in the values of the electron density as determined on the assumption of cylindrical symmetry, so that these curves should probably be considered only in a general way. They show the expected increase in density near the equator and the relatively high electron densities in the inner and medium corona near the position angles of great streamers. However, the actual position angle of the great northeast streamer is displaced about 10° from the maximum in electron density in the lower corona. Von Klüber (1952) also showed that the maximum in the λ 5303 emission line did not correspond to the position of the streamer. The complex structure of the corona at a height of 100,000 km (1.15) appears to persist in considerable detail out to at least 250,000 km (1.38) but has disappeared except for the streamers in the outer corona.

Van de Hulst (1950*a*) found the electron density of the near-minimum corona in 1900

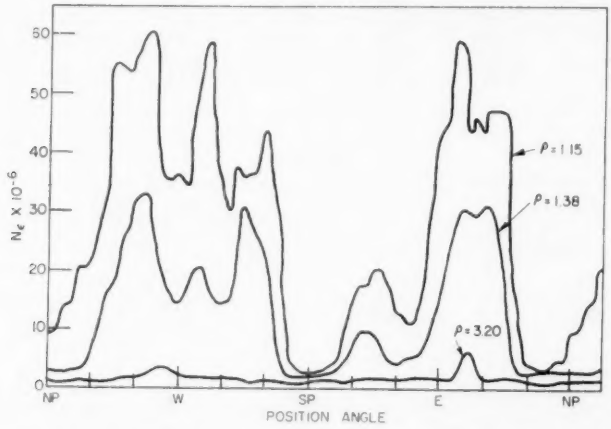

FIG. 10.—Variation of electron density with position angle at radii of 1.15, 1.38, and 3.20

at a radius of 1.15 near the poles by measuring the intensity along a line parallel to the tangent to the limb at the pole at this radius. Corrections were then applied to give values along the 1.15 circumference. A sharp dip in density was found near 70° with a peak at the poles nearly half the equatorial peak. No such dip was found in the NRL measures except in a very minor way in the northeast quadrant, which indicates that there is not always so clear a separation between high- and low-latitude contributions to the electron density as van de Hulst's measurements suggest.

An interesting comparison can be made between the intensity of the *K*-corona and the intensity of coronal emission lines. Figure 11 shows the intensity in millionths of the solar brightness for 1 A of continuous spectrum for the red (λ 6374) and green (λ 5303) coronal lines at 1′ from the eastern solar limb as measured by Michard *et al.* (1954). The values were obtained by photometric measurement of the plates which they took, using a Lyot filter. The *K*-corona intensities, also at approximately 1′ from the limb, are in units of 10^{-8} times the average surface brightness of the sun and are unaffected in shape by the removal of the *F*-corona if the latter varies monotonically with radius, as appears to be the case. The *K*-corona intensities are shown plotted at the position angles at which they were measured on the NRL plates, but the emission lines are shown shifted in angle by 3° from the published French values in a direction to decrease the angle. The fact that a much better correspondence of local bright areas appears when this is done

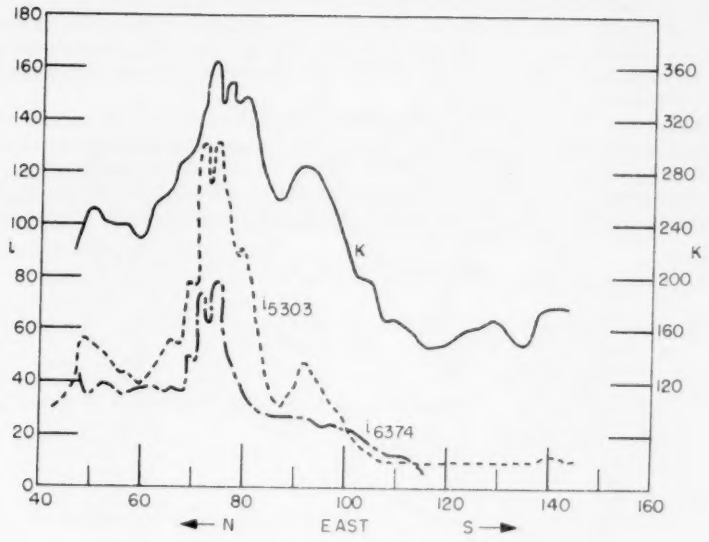

FIG. 11.—Coronal emission lines and the K-corona

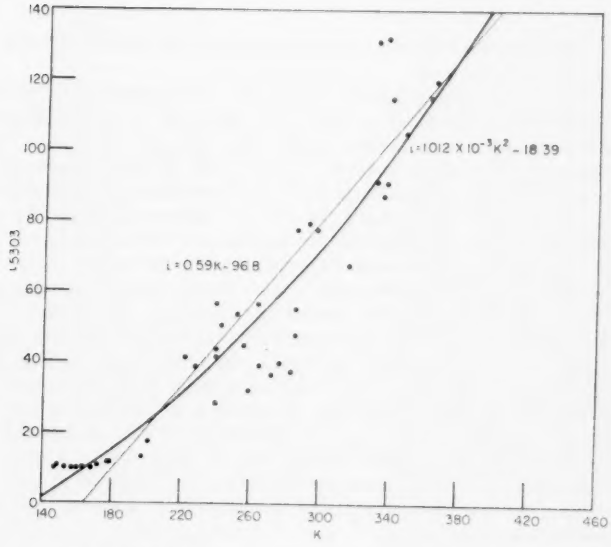

FIG. 12.—Relationship between K-corona intensity and the intensity of λ 5303

and that a real displacement of this kind would be very difficult to support physically made the adjustment seem reasonable. Also Michard *et al.* state that a displacement of 2° in position angle in their eclipse measurements brought them into better correspondence with measurements at the Pic du Midi on the same day, so that some uncertainty exists in the French position angles.

A comparison of the emission lines and the white-light corona is of special interest, since the excitation mechanism for the lines is not known theoretically and some observational evidence lies in this comparison. Excitation by collisions would lead to the emission's being proportional to N_e^2 while excitation by radiation would produce emission proportional to N_e (van de Hulst 1953). Since the intensity of the K-corona is also

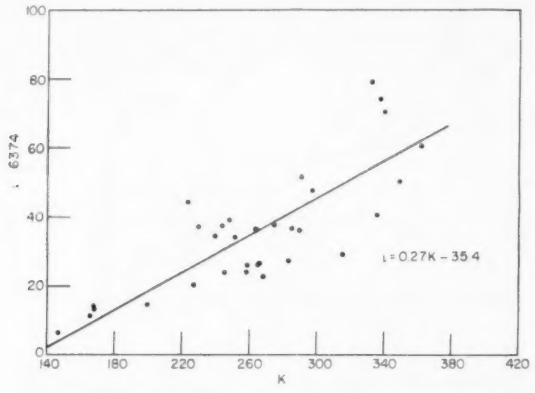

FIG. 13.—Relationship between K-corona intensity and the intensity of λ 6374

proportional to N_e, a plot of one intensity against the other should indicate whether the emission is produced by collisions or by radiation. Michard *et al.* (1954) were able to make a qualitative comparison of their emission-line measurements with Waldmeier's white-light photograph of the inner corona at the eclipse. This comparison indicates a dependence of the λ 5303 line on the square of the electron density, which is in agreement with the Woolley and Allen (1948) model, in which collisional excitation predominates for $\rho < 1.5$. Figure 12 shows a quantitative comparison for the λ 5303 line at 1′ from the limb with a least-squares line and a second-degree curve fitted to the points. The scatter is certainly large here, but the second-degree curve may fit somewhat better. Figure 13 shows a similar plot for λ 6374. Here the scatter is still greater, but no distinct curvature appears, and only a least-squares line is shown. This may indicate a difference in behavior of the *Fe* X and *Fe* XIV lines, which Michard *et al.* also point out. Shklovski (1950) finds that the λ 6374 line from $\rho = 1.2$ to 1.6 also decreases in intensity with radius like N_e rather than like N_e^2. He attributes this to changes in electron temperature with radius, which cause variation in the degree of ionization of iron, rather than to photoexcitation of the line. The relationship shown here, if truly linear, would indicate on this basis that changes occur in electron temperature with position angle also. In any case these are direct comparisons in units of the solar brightness of the two emission lines and the electron corona.

The author wishes to express her special thanks to Dr. John P. Hagen, who obtained the photographs and who suggested to her the program of measuring the plates. Thanks

are also extended to Mr. J. E. Sees, who designed the important modifications to the photometer and who gave freely of his advice and help during the extended period of the measurement, and to Mr. Fred T. Haddock for discussions which were stimulating and encouraging.

REFERENCES

Bergstrand, O. 1919, *Études sur la distribution de la lumière dans la couronne solaire*. Stockholm.
Hulburt, E. O. 1952, *Scient. Month.*, **75**, 306.
Hulst, H. C. van de. 1950*a*, *B.A.N.*, **11**, 410, 135.
———. 1950*b*, *ibid.*, p. 150.
———. 1953, in G. P. KUIPER (ed.), *The Sun* (Chicago: University of Chicago Press), p. 279.
Klüber, H. von. 1952, *Observatory*, **72**, 870.
Ludendorff, H. 1928, *Sitzungsb. preuss. Akad. Wiss. Berlin*, p. 185.
———. 1934, *ibid.*, p. 200.
Michard, R. 1954, *Ann. d'ap.*, **17**, 429.
Michard, R., Dollfus, A., Pecker, J. C., Laffineur, M., and Azambuja, M. d'. 1954, *Ann. d'ap.*, **17**, 320.
Shklovski, I. S. 1950, *Izvest. Krymsk Ap. Obs.*, **5**, 109.
———. 1951, *ibid.*, **6**, 105.
Waldmeier, M. 1954, *Zs. f. Ap.*, **33**, 4.
Woolley, R. v. d. R., and Allen, C. W. 1948, *M.N.*, **108**, 292.

A SEARCH FOR SOLAR VARIATION

R. H. Hardie and H. L. Giclas
Lowell Observatory
Received June 15, 1955

ABSTRACT

Photometric observations of Uranus and Neptune made from 1949 to 1954 are presented and discussed in relation to possible variations in the visible solar radiation. These point to the unlikelihood of any variations in excess of about 0.004 mag. during this time. The techniques which have been used to attain high accuracy are described.

The degree of constancy of the solar radiation is of considerable interest and importance in the interpretation of many solar-terrestrial and solar-planetary relationships. One of the best ways of detecting possible variations in the sun's output in the visible wave lengths was suggested by Müller (1897) and consists of making photometric observations of the planets with reference to background stars in order to avoid some of the uncertainties inherent in the delicate measures required for direct solar observations. Accordingly, he and other observers followed from time to time some of the planets and satellites in an attempt to study the constancy of the solar radiation (Stebbins 1927; Güssow 1929; Calder 1936; Campbell 1936).

In 1950 such a program was begun at the Lowell Observatory. Of the many solar-system objects which might be considered for this purpose, several have been shown to be unsuited, either because of variations in their albedo or because of irregular changes in rotational figure (i.e., Jupiter and its satellites, Saturn, the asteroids). In fact, Neptune and Uranus seem to be the only two which could be used so far as the absence of relatively short-period variations might be concerned, and even then their long-term stability is not sufficiently well known to be certain. Since their atmospheres should be quite free of condensation particles, one would not expect to find so much activity or change in albedo as in the nearer planets. They are well suited to a program of photoelectric photometry, since their image sizes are small and therefore any systematic effects caused by the different image configuration or inadequate behavior of the field lens of the photometer would be minimized. Moreover, their phase effects are small; a recent calculation by Horak and Talley (1954) predicts a maximum loss of 0.0025 mag. for Uranus and 0.0010 mag. for Neptune. The presence of satellites to these planets is not troublesome; small corrections can be applied when any have been included in the measure if the effect is of sufficient magnitude.

Initially, observations were made in the three colors: yellow, blue, and ultraviolet, but in 1953 the procedure was altered, to speed up the intercomparisons and reduce the accidental errors. Emphasis was put on observations in the blue to keep up a continuous check on the magnitude of the planets, but enough readings were made in the other two colors to have satisfactory color indices for the season. The blue seemed to represent a good compromise between a region of short wave length, where possible variations in the solar radiation are likely to be more pronounced but extinction corrections most difficult to evaluate, and a region of longer wave length, where the atmospheric extinction can be more accurately accounted for. The observations are made alternately on two stars and the planet. Readings are made for about 1 minute on each object, including the reading on the sky adjacent to each. One of the stars is taken as a comparison star, the other as a control star, which is treated in the reductions in the same way as the planet. This procedure was begun in 1953; formerly an adequate check on the comparison star was secured through observing other stars occasionally during the night; but it was

found that, to evaluate accurately the errors and the constancy of the comparison star, as complete coverage was necessary between the check stars as between the planet and its comparison.

Usually ten intercomparisons were secured each night of observation. Each of these was corrected for differential extinction, according to the following procedure. For any object producing a deflection, b, the magnitude outside the atmosphere, magnitude B', is

$$\text{mag } B' = \text{mag } b - (k_0 + k_i C_y) Q ,$$

where k_0 is the principal extinction coefficient, k_i is the color-dependent term of the extinction, C_y is the instrumental color index of the object, and Q is the air mass (essentially the secant of the zenith distance except for large zenith distance). For two objects, two such equations apply, and if they are close together in the sky, one can deduce the following expression:

$$\Delta \text{ mag } B' = \Delta \text{ mag } b - k_0 \Delta Q - k_i Q \Delta C_y ,$$

ignoring the small term involving $\Delta C_y \Delta Q$ (usually of the order of 0.0001 mag. in this work) and taking all differences in a consistent sense. The differential air mass, ΔQ, is a function of the hour angle and the distance between comparison star and planet, since this latter also varies because of the planet's motion among the stars. This quantity is conveniently computed for positions of the planet about a week apart in time and is plotted against hour angle. In this way one obtains a family of curves for chosen dates, and graphical interpolation is used for intermediate dates. A convenient formula for differential air mass, which is easily derived from the well-known expression for zenith distance, is

$$\Delta Q = (A \sin t + B \cos t + C) Q^2 ,$$

where

$$A = \Delta t \cos \phi \cos \delta , \qquad B = \Delta \delta \cos \phi \sin \delta , \qquad C = -\Delta \delta \sin \phi \cos \delta ,$$

and δ is the mean declination of the two objects, ϕ is the latitude of the observatory, and t is the hour angle, measured positively westward. Thus each measure of mag. b is corrected to become mag. B' by the application of a correction term $(-k_0 \Delta Q - k_i Q \Delta C_y)$.

After a mean value of mag. B' has been obtained from the observations of one night, another correction is applied to take into account the changing distances between the earth and the planet and between the sun and the planet. Some arbitrary distance may be chosen as standard, and in this work reduction to the mean opposition of 1950 was made as follows:

$$\Delta M = 5 (\log R_0 - \log R - \log \Delta_0 - \log \Delta) ,$$

where ΔM is the desired geometric correction in magnitudes, R is the distance of the planet from the sun, Δ is the distance of the planet from the earth, and R_0 and Δ_0 are the corresponding quantities for the 1950 mean opposition, being 19.1910 and 18.1910 a.u., respectively, for Uranus, and 30.0707 and 29.0707 a.u., respectively, for Neptune.

Another correction remains to be applied if it is desired to place the observed differences in magnitude on some arbitrary magnitude system. In this work all the measures have been converted into the blue-magnitude system defined in the U, B, V work of Johnson and Morgan (1953). If the measures are made through a filter-and-cell combination similar to the one specified for a system of magnitudes, one may find a relation between the two magnitudes of the form

$$\text{mag } B = \text{mag } B' + \alpha C_y + \beta ,$$

if one limits the range in C_y to that necessary to include the planet and star. Then, for the difference between the two objects, the following expression holds:

$$\Delta \text{ mag } B = \Delta \text{ mag } B' + \alpha \Delta C_y .$$

For each combination of filter and cell that has been used, it is necessary to determine the appropriate correction $a\Delta C_y$.

Actually, the C_y term for a planet as used in these correction formulae is not determined in the same way as for stars. Since the reflected solar spectrum is much altered, the light-distribution within any one filter band does not correspond to that of a star producing similar deflections among the filters. Therefore, the C_y term for a planet is chosen to be that of a star having similar light-distribution within a given filter. This procedure must be regarded, however, as providing only a rather crude first approximation; for a more precise determination of the appropriate relations, a detailed spectrophotometric study would be required. In the blue region Uranus and Neptune have color distributions corresponding to $B - V$ indices of about $+0.7$ and $+0.6$, respectively, and in the yellow region they correspond to about 0.0.

The results of five seasons of work are presented in Tables 1 and 2; all are reduced to the 1950 mean opposition distance and have been corrected in accordance with the foregoing data.

TABLE 1

URANUS

Year	V	B	U	Remarks
1949–1950	5.52	6.07	6.35	Filters: (U) UG 1; (B) BG 1+GG 13; (V) BG 8+GG 11; telescope: Lowell 42-inch; 931A and 1P21 cells
1950–1951	5.51	6.06	6.32	
1951–1952	5.52	6.07	6.32	
1952–1953	.....	6.090	.....	Filters and cell "UBV"; telescope: McDonald 13-inch and 82-inch
1953–1954	5.54	6.088	6.35	Filters and cell "UBV"; telescope: Lowell 20-inch

TABLE 2

NEPTUNE

Year	V	B	U	Remarks
1949–1950	7.92	8.42	8.64	Filters: (U) UG 1; (B) BG 1+GG 13; (V) BG 8+GG 11; telescope: Lowell 42-inch; 931A and 1P21 cells
1950–1951	7.88	8.39	8.62	
1951–1952	7.88	8.38	8.63	
1952–1953	7.87	8.270	8.49	Filters and cell "UBV"; telescope: Lowell 20-inch
1953–1954	7.86	8.265	8.49	

The results of the first three years have been published (Giclas 1954), but the values for V have been adjusted to allow for the color distribution within Giclas' yellow filter, as mentioned previously. For the determination of the B and U values, the $B - V$ and $U - B$ indices have been retained as published, although it may be that an improved conversion of these to more appropriate values could be found. Good agreement is, however, to be noted among the V magnitudes and $U - B$ indices for both planets and for the $B - V$ indices for Uranus. Although the manner of rendering the earlier observations homogeneous with the later ones is the best that we have devised, it should be emphasized that the homogeneity may not yet be as good as desired. Nevertheless, taking the V magnitudes at face value, the magnitude of Uranus over five years has been 5.53 ± 0.004 (p.e.), and that of Neptune has been 7.88 ± 0.007 (p.e.). No evidence for variations larger than these limits appears for this period. Moreover, the agreement within any one of the sets of observations appears to rule out any evidence for short-period

variations. This is apparent from the internal and external probable errors per night contained in Table 3, which lists these for the individual sets, together with those for the control stars of the 1953–1954 set.

The individual deviations in each series have, in general, a distribution agreeing well with that expected from the probable errors, and it seems unlikely, therefore, that there have been any variations in the solar output or in the albedos of the planets larger than these accidental deviations. No correlation is to be found between the material comprising this study and the daily solar-constant values of the Smithsonian Institution for the same periods. It has not been possible to observe unambigously any phase effect in the more precise recent series, since it has not been possible to allow completely for the effects of inhomogeneity of equipment, especially the differences among various cathodes and their influence on the color terms discussed earlier. No evidence of variation due to axial rotation of either planet has been found for any season during this interval. In the case of Uranus this is not unexpected, since the axis of rotation has been directed nearly toward the earth in this period. A representative sample of the observations for one season is shown in Figure 1; the necessity for using the same equipment for all observations is evident from the material in this diagram.

TABLE 3

MEAN PROBABLE ERRORS FOR ONE NIGHT

YEAR	URANUS		NEPTUNE	
	Internal	External	Internal	External
1949–1950				
1950–1951	0.005	0.010	0.005	0.010
1951–1952				
1952–1953	.0011	.0014	.0013	.0018
1953–1954	.0011	.0013	.0025	.0030
Control stars	0.0016	0.0020	0.0029	0.0043

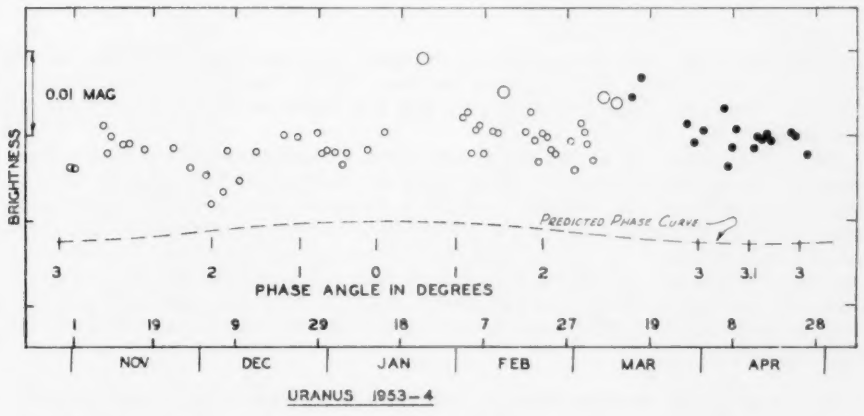
0.01 MAG
BRIGHTNESS
PREDICTED PHASE CURVE
3 2 1 0 1 2 3 3.1 3
PHASE ANGLE IN DEGREES
1 19 9 29 18 7 27 19 8 28
NOV DEC JAN FEB MAR APR
URANUS 1953–4

FIG. 1.—The brightness of Uranus as a function of date during the 1953–1954 season. The small open circles represent observations made with a 1P21; the large open circles, those made with a 6199; and the closed circles, those made with a Lallemand multiplier having also an antimony-caesium cathode.

During the last year included in these reported data, it was found that the control and comparison stars selected for Neptune were slightly variable, with amplitudes which are less than 0.01 mag., and which thus evaded detection initially. The stars are HD 118704 and 118705 and were not formerly known to be variable. The precision attained in the observations of the control star for Uranus is not so high as in the observations of the planet, although there seems to be no evidence in this study that either of the stars used for the Uranus observations was variable. This difference in precision suggests that the accuracy characteristic of this work is limited more by a scintillation phenomenon than by transparency variations, since the scintillation in the image of a planet is appreciably less than that for a star, whereas the transparency should affect each in the same way. If greater precision for stellar work were to be required, longer exposures or a larger aperture of the telescope than employed here would seem to be called for (1 minute and 20 inches, respectively). It will be noted that the errors for the 1952–1953 observations of Neptune are somewhat larger than those for Uranus in that year or the following one. This is interpreted as being due possibly to the faintness of Neptune, since from other

TABLE 4

OTHER DETERMINATIONS OF THE MAGNITUDE OF URANUS

Opposition	Observer	V
1864	Zöllner	5.52
1878	Müller	5.81
1879		5.65
1880		5.59
1881		5.58
1884		5.57
1885		5.63
1886		5.71
1888		5.70
		Mean = 5.66 ± 0.055
1927	Stebbins	5.53
1928	Güssow	5.51
1935	Calder	5.45
1936	Calder	5.44
1952	Harris, Kuiper	5.51

work with the same telescope and with a good multiplier it has been noted that for objects fainter than the eighth magnitude the shot noise at the photocathode becomes apparent, whereas for objects brighter than this it is hidden in the noise due to atmospheric conditions.

Table 4 presents some earlier determinations of the magnitude of Uranus for comparison with our data. All are reduced as nearly as possible to the V system so as to be directly comparable to the material in Table 1. However, the uncertainty in the color term which has been used to adjust the original data to this form prevents a more accurate intercomparison. Thus it is not possible to draw a general conclusion regarding the long-range stability of the solar radiation from these heterogeneous planetary observations. But one can conclude from the present work covering five years, and probably from Stebbins' results of 1927, that the sun has revealed less than 0.4 per cent variation in visible light.

This investigation has been made possible through the support and sponsorship extended by the Geophysics Research Directorate of the Air Force Cambridge Research Center. The authors are indebted to Dr. H. L. Johnson for making his 1953 data on Uranus available for discussion here, to Dr. D. L. Harris for preparation of Table 4, and

to both for many helpful discussions; to Messrs. C. L. Osterberg, C. V. Stableford, and W. C. Livingston for aid during the course of this investigation, and to Dr. Aldrich, of the Smithsonian Institution, for placing unpublished material at our disposal.

REFERENCES

Calder, W. A. 1936, *Harvard Bull.*, No. 903, p. 11.
Campbell, L. 1936, *Harvard Bull.*, No. 904, p. 32.
Giclas, H. L. 1954, *A.J.*, **59**, 128.
Güssow, M. 1929, *A.N.*, **237**, 230.
Horak, H., and Talley, R. 1954, private communication.
Johnson, H. L., and Morgan, W. W. 1953, *Ap. J.*, **117**, 313.
Müller, G. 1897, *Die Photometrie der Gestirne* (Leipzig: W. Engelmann).
Stebbins, J. 1927, *Lick Obs. Bull.*, Nos. 385 and 401.
Zöllner, J. C. F. 1865, *Photometrische Untersuchungen* (Leipzig: W. Engelmann).

ON THE SOLAR GRANULES

MAHINDER S. UBEROI
Department of Aeronautical Engineering, University of Michigan
Received February 5, 1955; revised July 6, 1955

ABSTRACT

The granule data are analyzed to show that all the characteristics of present-day measured solar brightness fluctuations (granules) are almost entirely determined by the instruments used to measure them. For example, the measured intensity and scale of the granules are not even close to the actual value. The analysis shows that the spectrum of the brightness fluctuations extends over a much wider range than that covered by any telescope thus far used to measure solar granules. The previous work on the subject is critically examined. It appears that, independent of the resolving power, some of the conclusions drawn by other investigators are open to objections.

INTRODUCTION

Even since Janssen obtained a photograph of the sun, showing random variations in brightness, there have been numerous attempts to obtain more accurate and reliable data on the intensity and scale of brightness fluctuations. However, the brightness fluctuations caused by the fluctuating density of the atmosphere of the earth introduce serious difficulties, since it is not possible to estimate their effect. It is because of this extraneous effect that estimates of the granule size vary from investigator to investigator. The "seeing" can be improved by decreasing the aperture of the telescope. For instance, the objective of the 60-foot solar telescope at Mount Wilson Observatory is usually diaphragmed down to 4 inches. Under these conditions it is necessary to investigate the effect of the telescope resolving power before we can characterize the brightness fluctuations by the intensity and size of granule or by the more sophisticated description in terms of spectrum or correlation.

In the present paper we shall investigate the effect of the telescope resolving power on the observed solar granules, and we shall assume that seeing conditions are perfect. It turns out that, when the effect of the telescope resolving power is properly considered, the entire nature of the granules is determined mostly by the resolving power of the telescope.

The situation is analogous to measurement of a wide-band electric signal through a filter of relatively narrow pass band. Within the narrow pass band the spectrum of the input can be assumed constant, and the relative magnitude of the different spectral components of output is determined entirely by the filter characteristic. The spectrum of the output is characteristic of the filter and has little resemblance to the spectrum of the input.

STATISTICAL DESCRIPTION AND EFFECT OF RESOLVING POWER

If we make a photometric traverse of the solar photograph, we find that the brightness varies quite randomly and that it is not possible to pick out any periodic variation corresponding to the apparent scale or granule size. The spectral or generalized harmonic analysis of such a randomly varying function is appropriate for a quantitative determination of the effect of the telescope resolving power on the measured brightness fluctuations. Let $B(X_1, X_2)$ be the fluctuating brightness where (X_1, X_2) specifies a point on the solar surface. Let $R(\xi_1, \xi_2)$ be the correlation of the brightness fluctuations. Then

$$R(\xi_1, \xi_2) = \lim_{L\to\infty} \frac{1}{4L^2} \int_{-L}^{L} \int_{-L}^{L} B(X_1, X_2) B(X_1 + \xi_1, X_2 + \xi_2)\, dx_1, dx_2.$$

We have assumed that $B(X_1, X_2)$ is statistically homogeneous, i.e., that the correlation $R(\xi_1, \xi_2)$ is independent of the origin of the co-ordinates X_1 and X_2. Let $P(k_1, k_2)$, where (k_1, k_2) is the wave-number vector in the Fourier transform space, be the spectral density of the brightness fluctuations. Then

$$P(k_1, k_2) = \frac{1}{4\pi^2} \iint R(\xi_1, \xi_2) \exp[i(k_1\xi_1 + k_2\xi_2)] \, d\xi_1 d\xi_2 . \tag{1}$$

The corresponding inverse relation is

$$R(\xi_1, \xi_2) = \iint P(k_1, k_2) \exp[-i(k_1\xi_1 + k_2\xi_2)] \, dk_1 dk_2 . \tag{2}$$

Let $R(r)$, $(r^2 = \xi_1^2 + \xi_2^2)$, and $G_1(k_1)$ be the one-dimensional correlation and spectrum, respectively. If we assume isotropy, i.e., $P(k_1, k_2) = P(k)$, where $k^2 = k_1^2 + k_2^2$, then it follows from equation (2) that

$$R(r) = \iint P(k) \exp[-ik_1 r] \, dk_1 dk_2 = \int_0^\infty G_1(k_1) \cos k_1 r \, dk_1 . \tag{3}$$

In this case the corresponding inverse relation is

$$G_1(k_1) = \frac{2}{\pi} \int_0^\infty R(r) \cos k_1 r \, dr , \tag{4}$$

where

$$G_1(k_1) = 4 \int_0^\infty P(k) \, dk_2 = 4 \int_{k_1}^\infty P(k) (k - k_1)^{-1/2} k \, dk . \tag{5}$$

The spectral density is given in terms of $G_1(k_1)$ by solving the foregoing integral equation (Uberoi and Kovasznay 1953),

$$P(k) = -\frac{1}{2\pi} \int_k^\infty \frac{dG_1(k_1)}{dk_1} (k_1^2 - k^2)^{-1/2} dk_1 . \tag{6}$$

Because of the finite resolving power of the instruments, each point of the solar surface is spread out on the photographic plate according to the distribution $K(x_1, x_2)$, (x_1, x_2) being, again, a position on the plate. The observed brightness fluctuation is

$$B^*(x_1, x_2) = \iint K(y_1, y_2) B(x_1 + y_1, x_2 + y_2) \, dy_1 dy_2 \qquad \left(\iint K(x_1, x_2) \, dx_1 dx_2 = 1\right), \tag{7}$$

where B is the true brightness fluctuation. Here and later the asterisk denotes a measured quantity. It can be shown (Uberoi and Kovasznay 1953) that

$$R^*(\xi_1, \xi_2) = \iint R(\xi_1 - y_1, \xi_2 - y_2) \psi(y_1, y_2) \, dy_1 dy_2 . \tag{8}$$

The expression for the observed spectrum takes the particularly simple form

$$P^*(k_1, k_2) = S(k_1, k_2 P(k_1, k_2) , \tag{9}$$

where

$$\psi(y_1, y_2) = \iint K(x_1, x_2) K(x_1 + y_1, x_2 + y_2) \, dx_1 dx_2 \tag{10}$$

and

$$S(k_1, k_2) = \iint \psi(y_1, y_2) \exp[-i(k_1 y_1 + k_2 y_2)] \, dy_1 dy_2 . \tag{11}$$

It follows that, by using these relations, we can recover any true quantity from the corresponding measured quantity, provided that none of the foregoing integrals diverge,

i.e., provided that the correction does not become inordinately large. In particular, it follows from equations (6) and (9) that

$$P(k) = -[2\pi S(k)]^{-1} \int_k^\infty \frac{dG_1^*(y)}{dy} (y^2 - k^2)^{-1/2} dy \tag{12}$$

and, from equations (5) and (12), that

$$G_1(k_1) = \int_{k_1}^\infty \frac{dG_1^*(y)}{dy} I(k_1 y)\, dy, \tag{13}$$

where

$$I(k_1, y) = \int_{k=k_1}^{k=y} S(k)(y^2 - k^2)(k^2 - k_1^2)^{-1} k\, dk. \tag{14}$$

These equations present two ways of recovering the true one-dimensional spectrum $G_1(k_1)$ from the measured one-dimensional spectrum $G_1^*(k_1)$. For a particular combination of instruments (telescope, photographic equipment, etc.) we can determine $I(k_1, y)$, once and for all, from equation (14) and then compute $G_1(k_1)$ by using equation (13). Alternatively, we can first compute the true spectral density $P(k)$ from the measured one-dimensional spectrum by using equation (12) and then calculate $G_1(k_1)$ by using equation (5). We will follow the latter procedure, since it brings out the difficulty encountered, because of the very poor resolving power, in recovering $G_1(k_1)$ from $G_1^*(k_1)$.

ANALYSIS OF THE DATA

The spectrum and the correlation of brightness fluctuations have been determined from a direct solar photograph taken with the 60-foot focal length Mount Wilson solar telescope (Uberoi 1955).[1] The objective was diaphragmed down to 4 inches, and the photograph was taken through a filter of effective wave length λ 5800. Each point on the solar surface is blurred out on the plate according to the distribution $K(r)$, which is the diffraction pattern of the telescope,

$$K(r) = (\pi r^2)^{-1} J_1^2 \frac{k_0 r}{2}; \qquad k_0 = 0.00735\ \text{km}^{-1}. \tag{15}$$

The sensitivity spectrum, $S(k)$, of the telescope is determined from equation (11):

$$\begin{aligned} S(k) &= 4(\pi)^{-2}\left[\cos^{-1}\left(\frac{k}{k_0} - \frac{k}{k_0}\right)\left\{1 - \left(\frac{k}{k_0}\right)^2\right\}^{1/2}\right]^2 \\ &= 0 \qquad \text{for} \qquad k > k_0. \end{aligned} \tag{16}$$

The wave number k_0 is the absolute cutoff of the telescope, and all harmonic component of brightness fluctuations for which $k > k_0$ are completely washed out.

The measured spectrum was approximated by a smooth function,

$$\frac{G_1^*(k_1)}{R^*(0)} = 377\left[1 + \left(\frac{k_1}{6.67 \times 10^{-3}}\right)^2\right]^{-6} + 79.7\left[1 + \left(\frac{k_1}{9.0 \times 10^{-4}}\right)^2\right]^{-6}.$$

The spectral density corresponding to the measured spectrum can be calculated by using equation (6)

$$\frac{P^*(k)}{R^*(0)} = 3.82 \times 10^4\left[1 + \left(\frac{k}{6.67 \times 10^{-3}}\right)^2\right]^{-6.5} + 6.0 \times 10^4\left[1 + \left(\frac{k}{9.0 \times 10^{-4}}\right)^2\right]^{6.5}.$$

[1] The simple technique used by the present author to measure the brightness correlation directly from the solar photograph is due to Dr. L. S. G. Kovasznay, *Heat Transfer and Fluid Mechanics Institute* (New York: American Society of Mechanical Engineers, 1949).

The true spectral density was obtained by using the relation

$$\frac{P(k)}{R^*(0)} = [S(k)]^{-1} \frac{P^*(k)}{R^*(0)}.$$

No particular importance should be attached to the functions used to approximate the measured spectrum. The true and measured spectra are shown in Figure 1. The true one-dimensional spectrum $G_1(k_1)$ is the integral of $P(k)$, and, since the area under the curve $P(k)$ cannot be determined, no reliable information can be obtained about $G_1(k_1)$.

The data obtained by Frenkiel and Schwarzschild (1955) were similarly analyzed, and

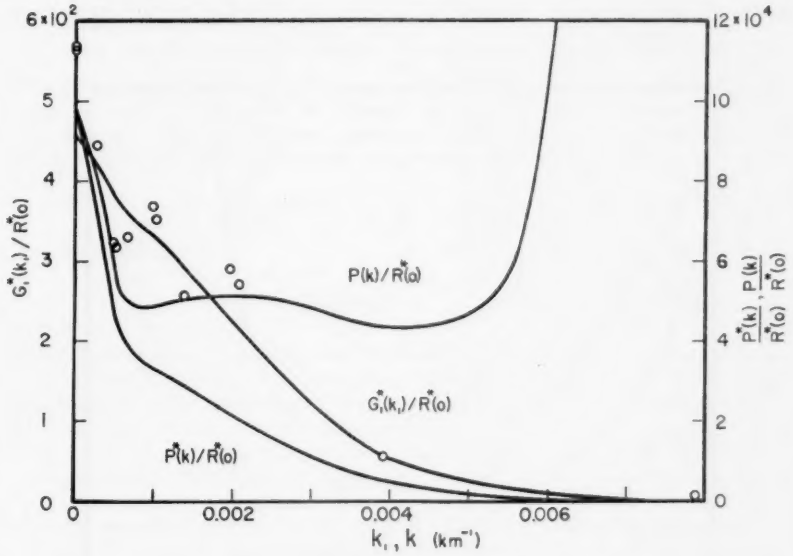

FIG. 1.—Analysis of data obtained earlier by the present author (Uberoi 1955)

the same difficulty was encountered (see Fig. 2). These data were also obtained from a Mount Wilson plate. The measured spectrum was approximated by a smooth function,

$$\frac{G_1^*(k_1)}{R^*(0)} = 72.8 \exp[-(1.825\times10^3 k_1)^2] - 53.2 \exp[5.65\times10^3 k_1)^2] + 427\left[1+\left(\frac{k_1}{5.91\times10^{-3}}\right)^2\right]^{-6}.$$

From equation (6) we have

$$\frac{P^*(k)}{R^*(0)} = 3.76\times10^4 \exp[-(1.825\times10^3 k)^2] - 8.5\times10^4 \exp[-(5.65\times10^3 k)^2] + 4.88\left[1+\left(\frac{k}{5.91\times10^{-3}}\right)^2\right]^{-6.5}$$

and

$$\frac{P(k)}{R^*(0)} = [S(k)]^{-1} \frac{P^*(k)}{R^*(0)}.$$

The $P(k)$ computed from the present author's data increases, while that computed from the Frenkiel-Schwarzschild data decreases for small k. This part of $P(k)$ is mainly determined by $R^*(r)$ for large values of r, which cannot be determined too accurately.

The accuracy of the calculated $P(k)$ is rather poor for $k > 0.005$ km^{-1}, since this part of the measured spectrum inevitably has some "noise" in it. We know from the resolving power of the telescope that $G_1^*(k_1)$ should be strictly zero beyond $k = 0.00735$ km^{-1}. A finite, though small, contribution in this region, when multiplied with a large correction factor $[S(k)]^{-1}$, makes $P(k)$ very large. Strictly speaking, the functions used to approximate $G_1^*(k_1)$ should be zero beyond $k_1 = 0.00735$ km^{-1}. However, in this region the accuracy is limited mainly by the inaccuracy of the measured $G_1^*(k_1)$.

The only thing we can assert with some confidence is that $P(k)$ is essentially constant within the effective wave-number band of the telescope. The deviations from this are too

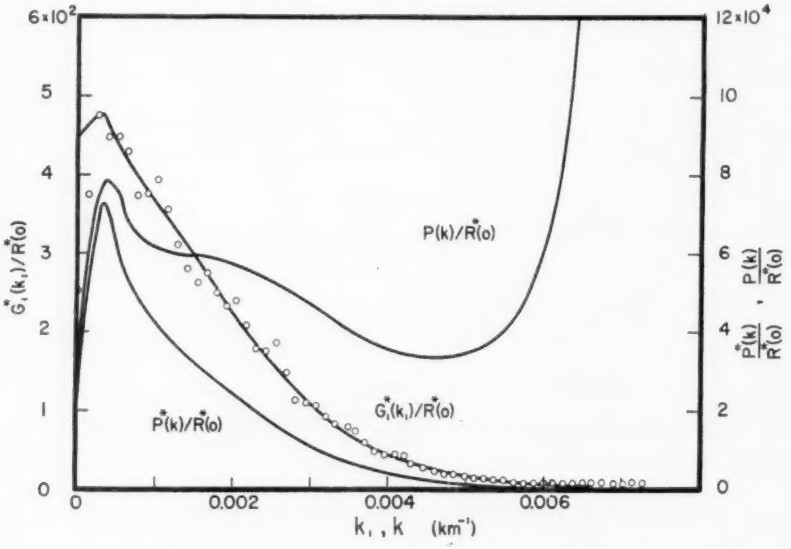

FIG. 2.—Analysis of Frenkiel-Schwarzschild data (1955)

small to be determined with any accuracy. In other words, the measured spectra of solar brightness fluctuation are almost entirely determined by the instrument used to measure them and do not give any reliable information about the actual brightness fluctuations. This conclusion appears pessimistic but is substantiated by calculating the correlation and the spectra on this basis and comparing them with the corresponding measured quantities. We denote quantities calculated on this basis by an overbar. Keeping $P(k)$ constant in equation (9), we have

$$\frac{\bar{P}(k)}{\bar{R}(0)} = \frac{S(k)}{2\pi\int_0^\infty S(k)\,k\,dk = 2.07\times 10^4\left[\cos^{-1}\left(\frac{k}{k_0}-\frac{k}{k_0}\right)\left\{1-\left(\frac{k}{k_0}\right)^2\right\}^{1/2}\right]^2} \qquad (17)$$

$$= 0 \quad \text{for} \quad k > k_0 .$$

From equation (5) we have

$$\frac{\bar{G}_1(k_1)}{\bar{R}(0)} = 8.28 \times 10^4 \int_{k_1}^{k_0} \left[\cos^{-1}\left(\frac{k}{k_0} - \frac{k}{k_0}\right)\left\{1 - \left(\frac{k}{k_0}\right)^2\right\}^{1/2}\right]^2 \frac{k\,dk}{(k^2 - k_1^2)^{1/2}} \tag{18}$$

$$= 0 \quad \text{for} \quad k_1 > k_0 .$$

Making use of the fact that $\bar{R}(r)$ and $\bar{P}(k)$ are Fourier transforms of each other, we find

$$\frac{\bar{R}(r)}{\bar{R}(0)} = \frac{\int_0^\infty S(k)\, kJ_0(kr)\, dr}{\int_0^\infty S(k)\, k\,dk} \tag{19}$$

$$= 3.3 \times 10^3 \int_0^\infty \left[\cos^{-1}\left(\frac{k}{k_0} - \frac{k}{k_0}\right)\left\{1 - \left(\frac{k}{k_0}\right)^2\right\}^{1/2}\right]^2 kJ_0(kr)\, dr .$$

Except for the normalizing factor, $\bar{P}(k)$, $\bar{G}_1(k_1)$, and $\bar{R}(r)$ are the instrument sensitivity spectral density, "one-dimensional spectrum," and "correlation," respectively. The integral for $\bar{G}_1(k_1)$ has been calculated numerically. In calculating $\bar{R}(r)$,

$$\left\{\cos^{-1}\left(\frac{k}{k_0} - \frac{k}{k_0}\right)\left[1 - \left(\frac{k}{k_0}\right)^2\right]^{1/2}\right\}^2$$

was approximated by

$$\left(\frac{\pi}{2}\right)^2 \left(1 - \frac{k}{k_0}\right)^2 \left(1 - 0.7\,\frac{k}{k_0}\right).$$

This approximation is quite good, and the final answer is given in terms of functions which are available in tables. The results are expressed in terms of the absolute cutoff k_0 of the telescope and are compared with measurements in Figures 3, 4, and 5. The curves given in these figures may be used to check the reliability of the data obtained with other telescopes. For the purposes of acceptable granule measurements, the telescope should have a narrow instrument correlation and a constant $\bar{P}(k)[\sim S(k)]$ within the wavelength band covered by the granule spectra.

We might remark that if we do not know the characteristics of an instrument or if it is too complicated to calculate them, an excellent way to calibrate the instrument is to subject it to random fluctuations covering a much wider spectral range than the pass band of the instrument. The measured correlation and spectral density give the instrument characteristics.

It is difficult to estimate the resolving power that is needed for obtaining reliable granule data. The close agreement of the measured spectrum with that of the instrument shows that we need considerable increase, probably by a factor of 10 or more, in resolving power. None of the instruments used so far to measure granules have this resolution, and it is safe to say that most granule photographs are seriously affected by poor resolution. However, the resolving power of the telescope cannot be increased without introducing the extraneous effect of poor "seeing."

The measured mean-square brightness fluctuation, $R^*(0)$, is 10.65×10^{-4} mag.^{2} (Frenkiel and Schwarzschild 1955). From Figures 1 and 2 we see that, within the effective wave-number band (0–0.00735 km^{-1}) of the telescope, $P(k)/R^*(0) \simeq 5 \times 10^4$. If we consider the brightness fluctuations only within this range, we can put a lower limit on true brightness fluctuations. Thus $R(0) > 90.5 \times 10^{-4}$ mag.^{2}. Approximating the radiation at each point by the black-body formula, we find a minimum root-mean-square temperature fluctuation of 113° K. The turbulent temperature fluctuations are probably of the order of several hundred degrees.

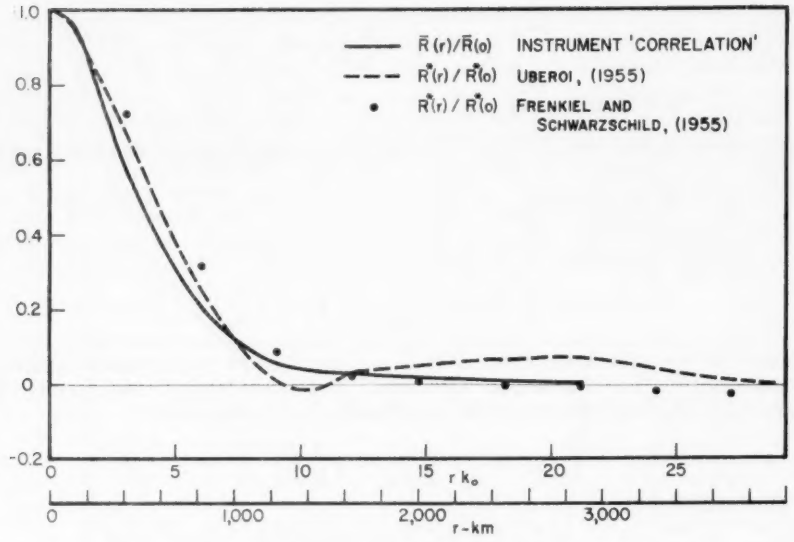

FIG. 3.—Comparison of measured correlation with that of the instrument

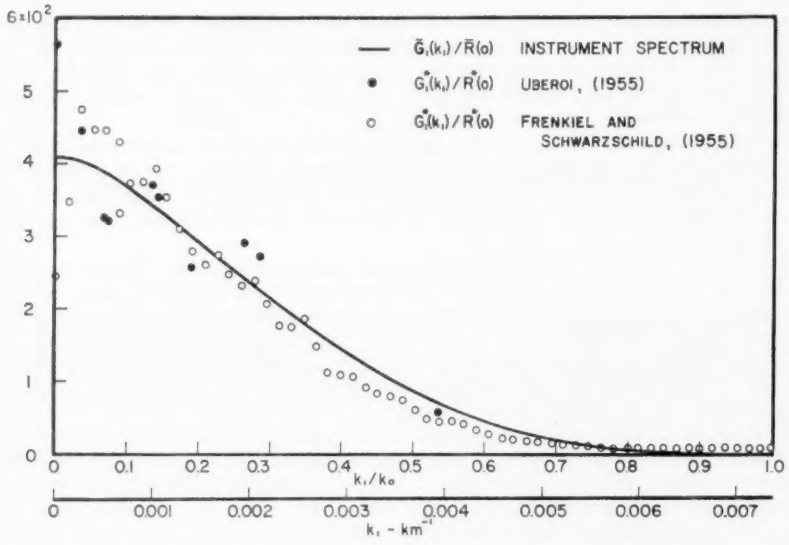

FIG. 4.—Comparison of measured spectrum with that of the instrument

The effect of different sources of error on the spectral density can be considered independently. We can first assume that the only error is due to the diffraction of the telescope aperture and that the photographic plate, etc., are perfect. This photograph is then copied on a plate of imperfect resolving power, and so on. The true spectral density is given by the relation $P(k) = [S(k)_{\text{telescope}} \cdot S(k)_{\text{photograph}}]^{-1} P^*(k)$. The consideration of the resolving power of the telescope gives the minimum correction factor, and the consideration of the resolving power of the photographic plate will make $P(k)$ increase somewhat faster beyond $k = 0.006$ km^{-1}. Under the present circumstance it does not appear that such refinements are necessary.

Frenkiel and Schwarzschild (1955) took into account the smoothing effect of telescope resolution only along the direction of the photometer tracing, i.e., according to them, $G_1(k_1) = S(k)^{-1} G_1^*(k)$, with the result that $G_1(k_1)$ thus obtained was constant from $k = 0$ to $k = 0.003$ km^{-1}. Their analysis is incorrect, since it gives no correction for $G_1^*(0)$, while actually there is a large correction for $G_1^*(0)$, since it has in it contributions of all wave lengths from ∞ to 0; the correction is so large that $G_1(0)$ cannot even be determined.[2]

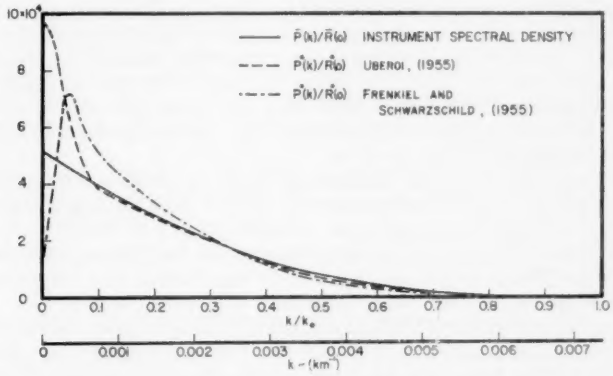

FIG. 5.—Comparison of measured spectral density with that of the instrument

SIZE AND PERIODIC STRUCTURE OF GRANULES

In view of the foregoing analysis, many of the results drawn by various investigators have to be reappraised. Even if we assume that the instruments have perfect resolving power, some previous conclusions are open to objection. One common error is that they always associate a maximum in the correlation with a periodic component in the random function. Take, for example, a one-dimensional random function whose spectrum is constant from $k = 0$ to $k = l$; its correlation is proportional to

$$\frac{\sin rl}{rl},$$

which has repetitive maxima, and the random function has no periodic component. It can be shown that when a random function does have a periodic component, its correlation becomes periodic for large distances. The spectral or generalized harmonic analysis of a randomly varying function was first developed by Schuster (1899, 1906), and he used

[2] Drs. Frenkiel and Schwarzschild have informed the present author that they have properly applied the correction for the effect of telescope resolving power in some unpublished work.

it to find hidden periodicities in the sunspot variations and other fluctuating quantities of interest. He clearly points out the distinction between line and continuous spectra and gives a procedure for finding a line (periodic component) in the presence of continuous background spectrum. Stuart and Rush (1954) assert, on the basis of a maximum in the correlation of smoothed brightness fluctuations that random brightness fluctuations have a periodic component or regular cell size of $3''$, which agrees approximately with the $1''$–$2''$ cell diameter obtained from visual observation of the direct solar photograph. The visual observation shows that the picture (random brightness) has an apparent scale which does not appear to be directly related to maxima in the correlation.

Some years ago the author took a shadowgraph of a turbulent flow field which had no regular or cellular structure, and, by proper enlargement, the shadowgraph could be made to look like a direct solar photograph (granules). Pictures of most two-dimensional random brightness fluctuations show an apparent scale, but this should not be confused with a periodic structure. For some reason, people (e.g., Wasiutynski 1946) have assumed that there should be regular cell structure in the turbulent solar atmosphere. We need hardly add that the observed scale reflects the characteristics of the telescope. From the visual observation of the solar photograph one gets the feeling that there are definite entities in the solar atmosphere which resemble rice grains. However, the detailed photometric measurements show that the brightness fluctuations are completely random; the use of the word "granules" to describe them is somewhat misleading. The word "granules" is used here because of historical precedent, and in the present paper it is synonymous with random brightness fluctuations. In a later paper the present author plans to show how the eye more or less sees definite patches or granules while, in fact, the brightness fluctuations are random.

Stuart and Rush claim that the existence of regular or periodic structure in the turbulent solar atmosphere is further supported by the fact that the brightness-velocity correlation of the smoothed fluctuations has a maximum at $r = 34{,}000$ km.[3] The position of this maximum coincides with the maximum in the brightness autocorrelation. The coincidence of the two maxima may have some significance, but, for the reasons given previously, it does not by itself point to periodic structure.

Frenkiel and Schwarzschild (1955) and Stuart and Rush (1954) used certain "smoothing" operations (running mean, etc.) on the data before computing various correlations. Frenkiel and Schwarzschild state that there remains the investigation of how the results are affected by this procedure. We might remark that the correlation and spectrum of the smoothed fluctuations can be obtained by first calculating the correlation or spectrum of the raw data and then applying the corresponding smoothing operations on the raw correlation or spectra. Smoothing or other similar operations on the raw data amount to reshaping the correlation or spectrum. This reshaping can be done by considering the smoothing operation as an instrument with finite resolution. It is desirable to give both the raw and the finished correlation or spectra so that the reader can get an idea of the reshaping.

COMPARISON OF BRIGHTNESS DATA WITH VELOCITY DATA

Frenkiel and Schwarzschild (1952) have determined the one-dimensional transverse velocity spectrum $E_2(k_1)$ for the solar atmosphere, which has a maximum at $k = 0.0043$

[3] Stuart and Rush found that when large-scale fluctuations of brightness and velocity are minimized by smoothing operations, the velocity-brightness correlation coefficient has a value of -0.68 compared with a value of -0.3 for unsmoothed fluctuations. Because of the smoothing operation, the root-mean-square velocity decreased by a factor of 2 and, assuming a similar drop in root-mean-square brightness fluctuations, we find that the velocity-brightness correlation has dropped by a factor of 2. As far as the turbulent heat transfer is concerned, it is the correlation and not the correlation coefficient that is of importance. Relatively less correlated fluctuations actually account for a large part of the convective heat transfer. However, the very poor resolving power makes all these results uncertain.

km^{-1}. Stuart and Rush (1954) found a maximum in the brightness correlation at 15,000 km, and they claimed that this confirms the maximum found in the velocity spectrum $E_2(k_1)$ at $k = 0.0004$ km^{-1}. There appears to be no justification for this claim. A maximum in a function does not show up as a maximum in its Fourier transform at the corresponding position.

When comparing the brightness data with the velocity data, we must take into account the fact that we are comparing the one-dimensional correlation or spectrum of a scalar field with the one-dimensional spectrum of one component of a random vector field. Let us for simplicity assume that both are isotropic and the velocity fluctuations incompressible. The transformations between one- and three-dimensional spectra are different for a scalar field and a vector field. If the three-dimensional spectra are similar, then corresponding one-dimensional spectra are not similar and vice versa, although

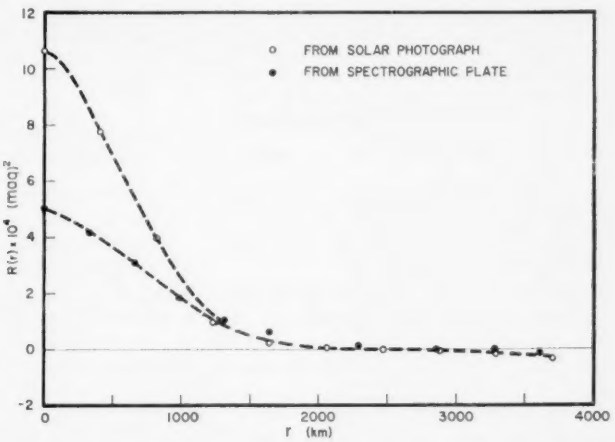

FIG. 6.—Comparison of the data obtained from the spectrographic plate with those obtained from the direct solar photograph.

there is no reason to believe that either of the situations occurs. In the absence of any sound basis for similarity, we should regard the velocity and temperature spectra as complementary data on the turbulent field.

It is possible to assess the reliability of the turbulent velocity and brightness data obtained by Richardson and Schwarzschild from the spectrographic plate. The unnormalized brightness correlation obtained from the spectrographic plate data (Uberoi 1955) is compared in Figure 6 with that obtained from the direct solar photograph (Frenkiel and Schwarzschild 1955). The fact that the correlation obtained from the spectrographic plate is lower than that obtained from the direct photograph shows that the spectrographic data are determined by the instruments to an even larger degree than are the data obtained from the direct photograph.

Just as in the case of the brightness correlation obtained from the direct solar photograph, it should be possible to predict the shapes of the autocorrelations of both the turbulent velocity and the turbulent brightness fluctuations by considering the resolution of the instruments. For this purpose we first consider the resolving power of the telescope and then the resolving power of the spectrograph both in the direction of dispersion and perpendicular to it. The velocity fluctuations measured from Doppler shift are much smaller than those determined from the curve of growth or the line profile.

Systematic analysis of the resolving power can probably account for most of the discrepancy without resort to the concept of a "secondary" maximum in the velocity spectrum. Frenkiel and Schwarzschild (1952) call the maximum in the measured $E_2(k_1)$ at $k = 0.0004$ km^{-1} "secondary" because they suspected a "primary" maximum to show up in the one-dimensional spectrum. Generally speaking, the energy in the three-dimensional spectrum at wave number k_a spills over into the one-dimensional spectrum covering the range from $k_1 = 0$ to $k_1 = k_a$. Except for a possible decrease near $k_1 = 0$ for $E_2(k_1)$, the one-dimensional spectrum will always have large energy for relatively small k_1, and in this sense one would invariably find a primary maximum in the one-dimensional spectra of all random fields.

The author is indebted to Drs. A. M. Kuethe and L. Goldberg and Mr. E. Spiegel for helpful criticism and to Drs. M. Schwarzschild and F. Frenkiel for supplying some of the granule data before its publication. The assistance of Messrs. R. Barcus, W. Williams, and J. Menkes in numerical calculation is gratefully acknowledged. The work is a part of the research program supported by the United States Office of Naval Research under contract 1224-02.

REFERENCES

Frenkiel, F., and Schwarzschild, M. 1952, *Ap. J.*, **116**, 422.
———. 1955, *ibid.*, **121**, 216.
Richardson, R. S., and Schwarzschild, M. 1950, *Ap. J.*, **111**, 351.
Schuster, A. 1899, *Cambridge Phil. Soc. Trans.*, **18**, 107.
———. 1906, *Proc. Roy. Soc. London, A*, **77**, 136.
Stuart, E. E., and Rush, J. H. 1954, *Ap. J.*, **120**, 245.
Uberoi, M. S. 1955, *Ap. J.*, **121**, 400.
Uberoi, M. S., and Kovasznay, L. S. 1953, *Quart. Appl. Math.*, **10**, 392.
Wasiutynski, J. 1946, *Astrophysica Norvegica*, **4**, 168.

EXPANDING *H* II REGION

MALCOLM P. SAVEDOFF AND JOHN GREENE
Physics Department, University of Rochester
Received March 7, 1955; revised June 2, 1955

ABSTRACT

The gas dynamic effects of star formation inside a uniform extended *H* I cloud are discussed. The temperature and pressure within the resulting *H* II region are estimated as two hundred times that in the *H* I region. It is concluded that the expanding *H* II region is surrounded by a dense *H* I region, separated from the undisturbed *H* I region by a shock front and from the *H* II region by an ionization front. This dense shell expands outward at about 14 km/sec and is perhaps two hundred times as dense as the undisturbed region. It is estimated that for $n_{H_2} \sim 0.1\ n_H$, any temperature anomaly will disappear after $2 \times 10^4\ n_H^{-1}$ years through interaction with the interstellar radiation field; thus in the analysis of the problem the *H* I region is treated as isothermal. We first obtain the motions in an isothermal gas surrounding a sphere whose surface velocity is constant. The relative motion of the ionization and shock fronts is obtained, and it is shown that the compressed shell persists, although the spherical motion is recognized as unstable. Radiation pressure is estimated to be negligible as long as the *H* II region is closed. These results need not apply to a nonuniform gas.

The high pressure within *H* II regions should produce marked effects upon the interstellar medium. J. H. Oort and L. Spitzer (1955) suggest that the intense radiation from O and B stars propels the surrounding un-ionized material outward at high speeds, producing dense high-speed clouds which are identified with the normal interstellar clouds or with the protostars. J. H. Oort (1954) estimates that this mechanism will replace the energy lost by the interstellar clouds through inelastic collisions. Further, he suggests that the dense clouds formed are sites where stars can be born in times comparable to the kinematical ages of the expanding O associations, say two million years. In this paper we shall consider the gas dynamic effects of the birth of an O star in a large, dense interstellar cloud. It appears that the "rocket" effect discussed by F. Kahn (1954) is not dominant in this case, although it is certainly important when the star lies outside the cloud. We are concerned mainly with the effects on its surroundings of the high gas pressure within the ionized region and with the ionization of the neutral material by the surplus ultraviolet photons which result from the expansion of the ionized region. In this discussion we attempt to include nonadiabatic processes and are led to consider the neutral region as approximately isothermal.

The properties of static *H* II regions are well known. The variation of the ionization within the ionized region has been obtained by B. Strömgren (1939), who found that the transition from high ionization to low ionization occurs in a very narrow shell. We shall assume that this may be idealized as a dichotomy into ionized and neutral regions. L. Spitzer and M. Savedoff (1950) have indicated that the temperature of an *H* I region is about 100° K, while that of an *H* II region is about 10,000° K. These results appear to be confirmed by recent observations. If the density of the two regions is the same, then the pressure in the *H* II region is perhaps two hundred times that in the *H* I region. In the first section we shall discuss the behavior of an *H* I region surrounding an expanding sphere forced into the *H* I region by a pressure two hundred times that of the *H* I region. Since from the calculations of Spitzer and Savedoff (1950) it appears that the temperature of an *H* I region is nearly independent of its density within the range $n_H = 1$ to $n_H = 10^6$ when there is sufficient time for the gas to reach equilibrium with the radiation field, we shall assume that the temperature of the neutral hydrogen region is constant. In the second section we shall estimate the thickness of the region in which departures from a uniform temperature are important. In the third section we shall obtain an ex-

pression for the relative positions of the H ionization front and the shock front and, in particular, shall show that the shock front, once formed, will persist. In the last section we shall discuss the approximation and the region of validity of our picture.

THE EXPANDING SPHERE

The problem of the gas motions around an expanding sphere is discussed by G. I. Taylor (1946) for the case of the wave surrounding a uniformly expanding sphere in air. In the interstellar medium the temperature is independent of the density over the relevant range. After a sufficient time the material will reach the initial temperature even after passing through a shock wave. It is this case which we shall discuss. Of the three usual equations of hydrodynamics, the energy equation is omitted from the discussion, as we are requiring the temperature throughout the gas to remain the same; otherwise, we would have to include terms representing interaction with the radiation field.

Since the equations of Taylor are singular for an isothermal gas, we will rederive the the appropriate equations. The equations of motion and conservation of matter in spherical co-ordinates are

$$\frac{\partial u}{\partial t}+u\frac{\partial u}{\partial r}=-\frac{1}{\rho}\frac{dP}{dr} \tag{1}$$

and

$$\frac{\partial \rho}{\partial t}+u\frac{\partial \rho}{\partial r}+\rho\left(\frac{\partial u}{\partial r}+\frac{2u}{r}\right)=0. \tag{2}$$

If we assume that the motion of the gas surrounding a uniformly expanding sphere is invariant in time, then we may consider the density, velocity, and pressure as functions only of $r/t = w$. We recognize w as the velocity of phenomena within the gas, while u represents the actual gas velocity. If we now introduce c, the sound velocity of an isothermal gas, into the equations and note that $P = \rho c^2$, then equations (1) and (2) may be written thus:

$$(u-w)\frac{du}{dw}=-c^2\frac{d\log\rho}{dw}, \tag{1'}$$

$$(u-w)\frac{d\log\rho}{dw}=-\left(\frac{du}{dw}+\frac{2u}{w}\right). \tag{2'}$$

These equations may be separated to yield

$$\frac{du}{dw}=-\frac{2u}{w}\left[\frac{c^2}{c^2-(u-w)^2}\right], \tag{3}$$

$$\frac{d\log\rho}{dw}=+\frac{2u}{w}\left[\frac{u-w}{c^2-(u-w)^2}\right]. \tag{4}$$

We require for rigid surfaces that the relative velocity vanish at the surface. For a uniformly expanding rigid sphere, $R = w_2 t$, and hence $u = w_2$ at the surface, where w_2 is the constant velocity of the sphere's surface. Further, there is a region for sufficiently large w which is unaware of the existence of the expanding sphere, a region where $u = 0$. Thus an actual solution of equation (3) in the w, u plane consists of a curve which connects the point $u = w_2$ with the w-axis. Several solutions are indicated schematically in Figure 1. Between the lines $u = w$ and $u = w - c$ the derivative du/dw is continuous, nonzero, and finite. Solutions which cross the line $u = w - c$ are improper, since u is then a two-valued function of w; on this locus du/dw is infinite and changes sign. This is impossible physically and is a mathematical expression of the need for a shock wave to close the solution. Unlike the problem for adiabatic gases, $\gamma > 1$, a shock wave occurs

only for w_2 greater than some critical value which could be found by numerical integration.

If we consider an isothermal shock wave, we can easily obtain the analogue of the Rankine-Hugoniot conditions by considering the conservation of matter and momentum across the boundary. Since the shock front may be considered as thin, we will confine ourselves to the case of a plane shock wave. Thus the mass flow $M = \rho(u - w_s)$ and the momentum flow $Q = P + \rho(u - w_s)^2$ are conserved across the shock. Here w_s is the shock velocity, and hence $(u - w_s)$ is the velocity of the gas relative to the shock. Again introducing $P = \rho c^2$, we obtain, from the conservation equations,

$$(u_1 - w_s)(u_0 - w_s) = c^2 , \tag{5}$$

where u_1 and u_0 are the gas velocity on either side of the shock. For our expanding spherical shock wave, $u_1 = 0$, that is, the velocity of the still gas. The velocity of the gas behind

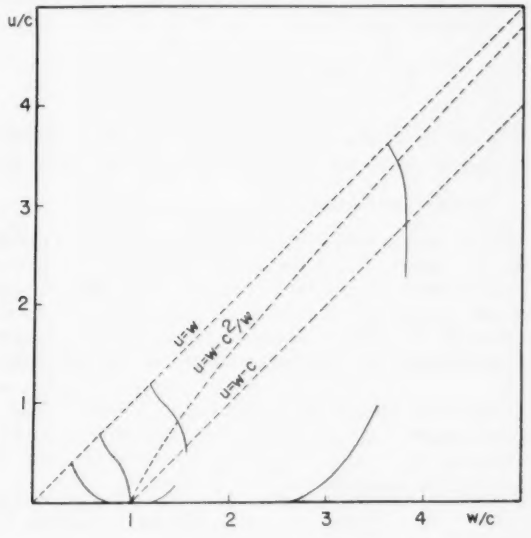

FIG. 1.—Motion of gas surrounding uniformly expanding sphere

the shock, then, is a function of c and w_s. Thus the family of expanding spherical shock waves in our similarity variables are represented by the curve

$$u_0 = w_s - \frac{c^2}{w_s} . \tag{6}$$

With a given w_2, the solution of our problem is represented by the segment of the curve defined by equation (3) bounded by the line $u = w_2$ and the curve $u = w_s - c^2 w_s^{-1}$.

For our purposes, we are interested only in solutions of this problem for $w_2 \gg c$. We note that when $u = w$ or when $u = w - c^2 w^{-1}$, $du/dw = -2$. Also the derivative du/dw is seen from equation (3) to be bounded within these limits between quite narrow limits, provided that $w_2 \gg c$; hence one may approximate the exact solutions of equation (3) by

$$u = -2w + 3w_2 . \tag{7}$$

If we then evaluate w_2 in terms of w_s, we find u as a function of w, and w_s is

$$u = -2w + 3w_s - \frac{c^2}{w_s}, \tag{7'}$$

when we substitute from equation (6). From the expression for the conservation of mass flow (M) across the shock and equation (5), we obtain the density ratio $\rho_0/\rho_1 = w_s^2/c^2$. Thus, with a pressure and density ratio of 200 between that of the surface of the sphere and that in the H I region, we expect that the shock will expand at a rate $(200)^{1/2}c$ and that the compressed region between the sphere and the shock wave will be 200 times as dense as the undisturbed region. The distance between the sphere and the shock will grow at a rate of approximately $\frac{1}{3}(c^2/w_s)$. Thus the dense material of this region has an outward velocity of 14 km/sec, and the thickness of this layer increases at a rate of nearly 0.02 km/sec when we further assume a temperature of 100° K in the H I region.

Returning, now, to equation (4), we can integrate from the sphere to the shock front by using the approximate relation (7′) between u and w. If we retain only the dominant terms for $w_s/c \gg 1$, we obtain

$$\frac{\rho}{\rho_1} = \left(\frac{w_s^2}{c^2}\right) \exp\left[\frac{1}{3}\frac{c^2}{w_s^2} - \frac{1}{18}\frac{c^4}{w_s^4} + \cdots\right]. \tag{8}$$

Here the density ratio across the shock, w_s^2/c^2, is proportional to the pressure ratio, while for the well-known adiabatic shock waves the maximum density ratio is $(\gamma + 1)/(\gamma - 1)$.

STRUCTURE OF AN ISOTHERMAL SHOCK WAVE

In the previous section we assumed that the gases compressed in the shock front cooled instantaneously. We will now evaluate the importance of the finite rate of cooling. We seek the pressure, density, and velocity behind a plane shock front in a gas which behaves adiabatically within the shock front but cools afterward according to Newton's law of cooling. Thus the usual Rankine-Hugoniot conditions for a shock wave can be applied to relate the conditions immediately behind a shock front with those immediately before the front.

From this point the further cooling of the gas can be followed. As a result of the conservation of mass and momentum, we again find that $M = \rho v$ and $Q = P + \rho v^2$ are both conserved quantities. Here v is the velocity relative to the front. Further, the conservation of energy equation per mole may be written

$$dE = -P\,dV + dH\,, \tag{9}$$

where $dE = C_V dT$, the change in the internal energy per mole, and $dV = +dv/v\rho$, and V is the specific volume. We assume that the gas cools exponentially; hence the energy either radiated or absorbed by the system is $dH = -C_V(T - T_1)dt/\tau$, where τ is recognized as the e-folding time for temperature equilibrium and T_1 is the equilibrium temperature. With these substitutions, we find

$$C_V dT = \frac{-P\,dv}{\rho v} - C_V (T - T_1)\frac{dx}{v\tau}. \tag{10}$$

If we introduce $v_1 = u_1 - w_s$ and $v_0 = u_0 - w_s$ by equation (5), with the condition that M and Q remain constant, we obtain

$$(C_P - C_V)\,T = (v_1 + v_0)\,v - v^2\,, \tag{11}$$

$$(C_P - C_V)\,(T - T_1) = (v_1 - v)\,(v - v_0)\,, \tag{12}$$

and

$$(C_P - C_V)\,dT = (v_1 + v_0 - 2v)\,dv\,. \tag{13}$$

Combining these, we obtain the differential equation

$$\frac{dx}{\tau} = \frac{\gamma(v_1 + v_0 - v) - v}{(v - v_0)(v - v_1)}\, v\, dv\,. \tag{14}$$

This can be integrated by the method of partial fractions to obtain

$$\frac{x}{\tau} = -(\gamma+1)(v - v_f) - \frac{\gamma v_1 - v_0}{v_1 - v_0}\, v_0 \log \frac{v - v_0}{v_f - v_0} - v_1 \frac{v_1 - \gamma v_0}{v_1 - v_0} \log \frac{v - v_1}{v_f - v_1}, \tag{15}$$

where v_f is the velocity immediately behind the shock front prior to any cooling effects, while $v_0 = c^2/v_1$ is the asymptotic relative velocity of the compressed material, and x is the distance behind the shock front. Thus $u_0 - w_s = v_0$.

In order to evaluate v_f in terms of v_1 and v_0, we must first note that at any point, even though the temperature changes,

$$\frac{P}{\rho} = v(v_0 + v_1 - v)\,. \tag{16}$$

TABLE 1

WIDTH OF ISOTHERMAL SHOCK WAVES IN NATURAL UNITS
(Entry Is x/τ)

P_0/P_1	$\gamma = 1.1$	$\gamma = \frac{4}{3}$	$\gamma = \frac{5}{3}$	P_0/P_1	$\gamma = 1.1$	$\gamma = \frac{4}{3}$	$\gamma = \frac{5}{3}$
4.....	1.786	2.497	3.611	200	0.921	2.685	5.432
25.....	0.906	1.665	2.842	400.....	1.136	3.596	7.423
100.....	0.813	2.102	4.101	900.....	1.560	5.225	10.921

Further, since we do not allow any time for cooling, the energy content of the material is the same on either side of the shock front, and

$$\frac{\gamma}{\gamma - 1}\frac{P}{\rho} + \tfrac{1}{2} v^2$$

is conserved. Substituting equation (16) in the expression for the conservation of the energy density, we obtain, on simplification,

$$v_f = \frac{\gamma - 1}{\gamma + 1}\, v_1 + \frac{2\gamma}{\gamma + 1}\, v_0 \tag{17}$$

Finally, τ may be estimated from Table 5 of Spitzer and Savedoff (1950) as a function of temperature and density. For the gas surrounding the Trapezium in Orion with a density of the order of 3700 hydrogen atoms/cm^3, the time for cooling is 2 years or 1000 years, depending on the H_2 concentration. Thus all the parameters in equation (15) are known. In order to avoid the logarithmic infinity corresponding to exponential cooling, we consider the gas as cold, once $v - v_0 = 0.05(v_f - v_0)$. In Table 1, representative values of x have been calculated for three values of γ. For $\gamma = \frac{5}{3}$ and a pressure ratio of 200 corresponding to a shock velocity of 14 km/sec, $x = 4.96\tau$ km/sec. By the analysis of the preceding section, the thickness of the compressed region is $\frac{1}{3}(c^2/w_s)t$, which is approximately $0.0236ct$. These distances are equal after a time 230τ. In this time the radius of the initial sphere will have increased 0.006 pc, if $\tau = 2$ years. In the absence of H_2, in the 230,000 years the region will have expanded to 3.0 pc. Compare these expansions with the present radius of the Orion Nebula of 0.5 pc. We have neglected ionization and dis-

sociation in the foregoing calculations. For smaller γ, the cooling is more rapid. For less dense regions, the cooling time is very much larger, approximately proportional to n^{-1}. The analysis of the gas wave surrounding a sphere of the first section applies only after a time greater than 230τ. The nonadiabatic spherical problem is so tedious that the isothermal approximation of that section will be used in this preliminary exploration.

FORMATION OF THE SHOCK REGION

The previous two sections have been concerned with the behavior of a neutral hydrogen region (immersed in the galactic-radiation field) which surrounds a sphere whose radius increases linearly with time. If we replace this sphere with an expanding *H* II region, several new phenomena must be considered. There may be mass flow across the interface (ionization front) between the *H* I and *H* II regions. Further, the pressure of the *H* II region is found to vary with time. Lastly, it becomes of major importance to show that the shock wave, once formed, expands at a rate exceeding that of the ionization boundary, provided that the motion of the ionization front is determined by the excess ultraviolet quanta freed by the expansion of the *H* II (ionized) region. If this is not the case, then no observable hydrodynamic effects are to be expected.

Under the assumption that the ionization is complete within the *H* II region, the total radius R is defined by

$$L = 4\pi \int_0^R r^2 n_2^2 \overline{\sigma v} \, dr \,, \tag{18}$$

or, for a uniform density in the *H* II region,

$$L = \frac{4\pi}{3} R^3 n_2^2 \overline{\sigma v} \,; \qquad \frac{dn_2}{dr} \equiv 0 \,, \tag{18'}$$

where L is the number of Lyman continuum photons per second emitted by the star; $n_2 \overline{\sigma v}$ is the recombination probability per second per electron to the Balmer or higher levels; n_2 is the proton density within the *H* II region; and R is the boundary of the *H* II region. Each recombination as defined here destroys one Lyman continuum ionizing quantum.

The total number of protons within the ionized region is

$$N = 4\pi \int_0^R n_2 r^2 \, dr \,, \tag{19}$$

or, again for uniform density,

$$N = \frac{4\pi}{3} n_2 R^3 \,; \qquad \frac{dn_2}{dr} \equiv 0 \,. \tag{19'}$$

For a slow expansion n_2 will be independent of r; and from equations (18′) and (19′) we can eliminate n_2, obtaining

$$N = \left(\frac{4\pi L}{3 \overline{\sigma v}} \right)^{1/2} R^{3/2} = \frac{4\pi}{3} n_1 R_0^{3/2} R^{3/2} \,. \tag{20}$$

Here R_0 is the radius of the *H* II region for the density of the undisturbed gas, n_1. The number of ionized atoms increases as R increases through the ionization of material between the ionization front and the shock front. If the rate of ionization of the material between the shock and ionization fronts is too fast, then the ionization front overtakes the shock front, and our entire model would have no meaning.

In what follows we shall neglect the number of photons required to ionize the neutral material initially. After the star has been shining a time $t \gg (n_2 \overline{\sigma v})^{-1}$, $L^{-1} dN/dt \ll 1$.

The growth of the H II region then is a result of the change of density alone. This excludes consideration of the rocket effect.

We have seen by equation (8) that, for $w_s \gg c$,

$$w_s = c\left(\frac{\rho_0}{\rho_1}\right)^{1/2} \sim c\left(\frac{2T_2}{T_1}\frac{n_2}{n_1}\right)^{1/2}, \tag{21}$$

where T_2 and n_2 are the temperature and density of the H II region, n_1 is the hydrogen density in the undisturbed region, and ρ_0 is the asymptotic density reached when the material has cooled to T_1 after passing through the shock. We have neglected the ex-

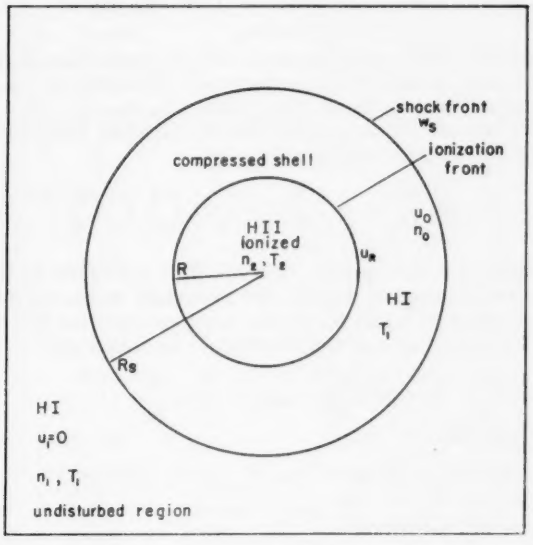

FIG. 2.—Expanding H II region

ponential term in equation (8) in the following calculations, as well as the possible pressure jump across the ionization front. For later use we note that, as the ionized region expands,

$$w_s = (2\beta)^{-1/2}\left(\frac{R_0}{R}\right)^{3/4} c\,; \qquad 2\beta = \frac{T_1}{2T_2}, \tag{22}$$

where R_0 is the radius of the H II region for $n = n_1$. In Table 3, $(2\beta)^{1/2}w_s$ is given for representative values of R/R_0.

The stability of the shock wave against encroachment of the ionization front depends on whether the shock velocity is ever greater than the ionization-front velocity and whether, once faster, it remains faster. In Figure 2 we collect the relevant notation on a diagram of the system. We obtain the pertinent velocity difference, $w_s - dR/dt$, by evaluating separately $w_s - u_R$ and $u_R - dR/dt$. The material velocity, u_R, immediately ahead of the ionization front can be found from equation (7′),

$$w_s - u_R = 2\,(w_R - w_s) + \frac{c^2}{w_s}. \tag{23}$$

The number of atoms overrun by the ionization front per second is

$$\frac{dN}{dt} = 4\pi R^2 \left(\frac{dR}{dt} - u_R\right) n_0, \tag{24}$$

where n_0 is the asymptotic density in the compressed region. Combining equations (18′) and (19′), we find

$$(4\pi R^2)^{-1} \frac{dN}{dt} = \tfrac{1}{2} n_2 \frac{dR}{dt}, \tag{25}$$

and, finally,

$$w_s - \frac{dR}{dt} = 2(w_R - w_s) + \left(w_s - \frac{n_2 dR}{2n_1 dt}\right) \frac{c^2}{w_s^2}. \tag{26}$$

We shall assume that these results obtained with the assumption of the validity of the similarity condition may be applied in the absence of this condition; that is, the transient phenomena are not of interest to us. We evaluate w_R by $w_R = R/t = w_s R/R_s$. Now w_R and dR/dt differ because dR/dt is not a similarity variable! With this substitution and noting $dR_s = w_s dt$, we obtain, from equation (26),

$$(1-\beta)\frac{dR}{dR_s} = -2\frac{R}{R_s} + 3 - 2\beta \left(\frac{R}{R_s}\right)^{3/2} \left(\frac{R_s}{R_0}\right)^{3/2}, \tag{27}$$

where we have replaced w_s by equation (22) and R_0 is the radius of the ionized region corresponding to the undisturbed density. We previously estimated $\beta \sim (400)^{-1}$.

With the initial values of R and R_s, we can integrate equation (27) and find the relative positions of the ionization and shock fronts. If we substitute

$$z = \frac{R_s}{R_0} \quad \text{and} \quad y = \frac{R}{R_s}, \tag{28}$$

then equation (27) becomes

$$(1-\beta)\, z \frac{dy}{dz} = (-3+\beta)\, y + 3 - 2\beta (zy)^{3/2}. \tag{29}$$

Since β is small, we will substitute

$$y = \Sigma \beta^n y_n \tag{30}$$

and equate powers of β. The general coefficient of β^n is

$$z(y_n' - y_{n-1}') = y_{n-1} + 3\delta_{0n} - 3y_n - 2(zy_0)^{3/2} \left[\left(1 + \Sigma \frac{y_n}{y_0} \beta^n\right)^{3/2}\right]_{n-1}, \tag{31}$$

where $[\,]_n$ is the coefficient of β^n in the power-series expansion of the quantity within the brackets. The first two solutions are

$$y_0 = 1 - C z^{-3}, \tag{32}$$

$$\begin{aligned} y_1 = z^{-3} \Big\{ & D + 2C \log \frac{z}{z_0} + \tfrac{1}{3}(z^3 - z_0^3) - \tfrac{4}{9}[(z^3 - C)^{3/2} - (z_0^3 - C)^{3/2}] \\ & + \tfrac{4}{3} C [(z^3 - C)^{1/2} - (z_0^3 - C)^{1/2}] - \tfrac{8}{3} C^{3/2} [\tan^{-1} C^{-1/2} \{ z^{3/2} + (z^3 - C)^{1/2} \} \\ & - \tan^{-1} C^{-1/2} \{ z_0^{3/2} + (z_0^3 - C)^{1/2} \}] \Big\}. \end{aligned} \tag{33}$$

The asymptotic term for large z in y_2 is $\frac{2}{9}(z^3 - z_0^3)$. If we assume that, for z_0, $1 - y_0 = \epsilon \ll 1$, then

$$y = 1 - \epsilon \frac{z_0^3}{z^3} + \beta \left\{ \frac{1}{3}\left(1 - \frac{z_0^3}{z^3}\right) - \frac{4}{9} z^{3/2}\left(1 - \frac{z_0^{9/2}}{z^{9/2}}\right) + \epsilon \left[2\frac{z_0^3}{z^3} \log \frac{z}{z_0} + 2 z^{-3/2} z_0^3 \left(1 - \frac{z_0^{3/2}}{z^{3/2}}\right)\right] + \epsilon^2 \ldots \right\} + \beta^2 \left\{ \frac{2}{9} z^3 \left(1 - \frac{z_0^6}{z^6}\right) + \ldots \right\} + \ldots \quad . \tag{34}$$

For ϵ small, therefore, the shock wave is stable. If we assume, further, that $z_0^{-1} = 1 - \epsilon$, we can expand y as a double power series in ϵ and β. The first few coefficients of $y = \Sigma\Sigma y_k^n \epsilon^n \beta^k$ will be found in Table 2.

TABLE 2

COEFFICIENTS FOR CALCULATING y
($y = \Sigma\Sigma \epsilon^n \beta^k y_k^n$)

z	y_0^1	y_1^0	y_1^1	z	y_0^1	y_1^0	y_1^1
1.1.....	−0.751	−0.096	+1.125	2.0	−0.125	−0.910	+0.755
1.2.....	− .579	− .187	+1.154	2.5.....	− .064	−1.416	+ .559
1.4.	− .364	− .362	+1.088	3.0.....	− .037	−1.972	+ .429
1.6.....	− .244	− .539	+0.974	5.0.....	−0.008	−4.635	+0.197
1.8.....	−0.171	−0.721	+0.858				

TABLE 3

FRACTIONAL MASS IN COMPRESSED SHELL

z	Relative Mass	$(2\beta)^{-1/2} w_s$	R/R_s	z	Relative Mass	$(2\beta)^{-1/2} w_s$	R/R_s
1.0.....	0.000	1.000	1.0000	1.8.....	0.587	0.643	0.9982
1.1.....	.134	0.931	0.9998	2.0.....	.648	.595	.9977
1.2.....	.240	0.872	0.9995	2.5.....	.748	.503	.9965
1.4.....	.397	0.777	0.9991	3.0.....	.809	.439	.9951
1.6.....	0.507	0.703	0.9987	5.0.....	0.912	0.299	0.9884

One may inquire as to the mass of the compressed region. Since the mass of the entire system is $\frac{4}{3}\pi R_s^3 n_1 m_H$ and that of the ionized region by equation (20) is $\frac{4}{3}\pi R_0^{3/2} R^{3/2} n_1 m_H$, the net mass is $\frac{4}{3}\pi R_s^3 (1 - y^{3/2}/z^{3/2}) n_1 m_H$. The fraction of the mass in the compressed region has been estimated in Table 3 for our typical β. The second column in Table 3 is approximately the factor by which the original shock strength has decreased. At $z = 5$ a large part of the mass of the system is already in the compressed shell. Our approximations are breaking down at this point as $w_s/c \sim 4$ for this radius.

CONCLUSIONS

A reconnaissance of the probable evolution of an *H* II region formed in a uniform interstellar medium by the radiation of a newly born supergiant O star has been made. We find that the high-pressure *H* II region will be surrounded by a dense neutral region expanding at supersonic speed into the neutral undisturbed region. This result is valid under certain conditions, which we shall now enumerate. Only for $R_0 > t_f (P_2/\rho_2)^{1/2}$ will

the shock wave form before the region has expanded considerably. This is a condition on the time scale of the rate of luminosity increase, t_f, which for the Orion nebulae implies that the O stars become fully luminous in about 70,000 years.

The omission of radiation pressure is justified, provided that the total change in radiation pressure within our model is small. If all the hydrogen resonance radiation (L_α) is absorbed on the front surface of the *H* I region,

$$\Delta P = \frac{h\nu_{L_\alpha}}{c}\frac{L}{4\pi R^2}. \tag{35}$$

We can express the ratio $\Delta P/P$ in terms of the recombination time $(n_2\,\overline{\sigma v})^{-1}$, the radius of the ionized region, and the physical constants,

$$\frac{\Delta P}{P} = Rn\,\frac{h\nu_{L_\alpha}\overline{\sigma v}}{3\,ckT_2} = 1.32\times 10^{-23}Rn\ \text{cm}^2. \tag{36}$$

It may be assumed that the *H* I region is transparent to all other radiation. For the Orion nebulae with $R = \frac{1}{2}$ parsec and $n = 3700$, we obtain $\Delta P/P \sim 0.8$. We believe that the intrinsic breadth of L produced by both large- and small-scale motions will "detune" the precise resonance envisaged here. In general, $\Delta P/P$ proves to be proportional to $(nL)^{1/3}$, so that only for more luminous sources of Lyman continuum radiation or for denser regions will radiation pressure be dominant.

It is supposed here that the ionization front reaches R_0 so rapidly that no hydrodynamic effects can be propagated into the medium, that is, that conditions are "*R* type" (see Kahn 1954). If we apply Kahn's criterion for the appearance of a shock wave and the data given previously for the Orion nebulae, we find that the shock first appears when the ionization front reaches $0.99R_0$. This calculation is not legitimate, however, as Kahn's analysis refers to expansion into a vacuum.

Thus we find that this mechanism will produce regions two hundred times denser than the initial region and that these regions will be propagated outward at speeds of the order of 14 km/sec. These shells are unstable, since we have the less dense *H* II region accelerating the denser *H* I region, and so we may expect the shell to break up into the interstellar clouds.

When the original medium is sufficiently dense, the compression of the neutral region raises the density to the point where gravitational forces can perhaps account for formation of the expanding stellar associations. Thus

$$t = (6\pi G n_1 m_H)^{1/2}\left(1 - \frac{n_1^{1/2}}{n_f^{1/2}}\right) \tag{37}$$

is the time for a medium, initially at density n_1, to collapse under its own gravitational field to a density n_f. Thus a nongravitational compression even from $n_H = 10$ to $n_H = 2000$ corresponds to a decrease of t from 7 million years to 0.5 million.

It is difficult to suppose direct observational corroboration of this model. The expansion considered is known to be unstable to perturbations (Rayleigh-Taylor instability); hence the compressed shell should break up into small fragments (Oort 1954). Even in the near-by Orion Nebula the compressed shell after $R/R_0 = 2$ is only about 1″ of arc when seen edge-on, although it should be massive enough to appear in 21-cm measures, provided that its hydrogen remains monatomic.

M. Savedoff wishes to acknowledge his indebtedness to J. H. Oort for suggesting this problem to him during his U.S. National Science Foundation postdoctoral fellowship at Leiden. The authors wish to acknowledge support of this investigation by the Office of Naval Research.

REFERENCES

Courant, R., and Friedrichs, K. O. 1948, *Supersonic Flow and Shock Waves* (New York: Interscience Publishers, Inc.). A general source for this and related problems.
Kahn, F. D. 1954, *B.A.N.*, **12**, 187.
Oort, J. H. 1954, *B.A.N.*, **12**, 177.
Oort, J. H., and Spitzer, L. 1955, *Ap. J.*, **121**, 6.
Spitzer, L., and Savedoff, M. P. 1950, *Ap. J.*, **111**, 593.
Strömgren, B. 1939, *Ap. J.*, **89**, 526.
Taylor, G. I. 1946, *Proc. R. Soc. London, A*, **186**, 273.

ON THE SOLUTION OF EQUATIONS OF TRANSFER. I*

MAX KROOK
Harvard College Observatory
Received May 18, 1955

ABSTRACT

A moment method is given for the approximate solution of transfer equations. This is used to discuss the relation between various other methods that are also based on initially approximating to the angular distribution of intensity. The procedures most frequently employed are not adapted to the boundary conditions of the problems. Definite advantages attach to the use of procedures adapted to the boundary conditions; the discrete-ordinate method, the moment method, and the method of expansion in orthogonal functions are completely equivalent.

I. INTRODUCTION

Various procedures have been devised to obtain approximate solutions of radiative-transfer equations. These may be classified into two main types according to the basic approximation concerned: type A, based on approximation to the angle dependence of the intensity, and type B, based on approximation to the depth dependence of the source function. Some procedures used in problems of nongray atmospheres combine the characteristics of both A and B.

In this paper our considerations are essentially methodological. It will therefore be sufficient to illustrate the arguments by reference to the special problem of a plane-stratified gray atmosphere in radiative equilibrium. Problems of nongray atmospheres will be treated in subsequent papers. The equation of transfer then has the form

$$\mu \frac{\partial I(\tau, \mu)}{\partial \tau} = I(\tau, \mu) - \frac{1}{2}\int_{-1}^{+1} I(\tau, \mu')\, d\mu', \tag{1}$$

where $I(\tau, \mu)$ is the integrated intensity of the radiation field at optical depth τ and in directions making the angle $\cos^{-1}\mu$ with the outward normal to the layers. Equation (1) is to be solved subject to such a typical pair of boundary conditions as

$$a) \quad I(0, \mu) = 0 \qquad (-1 \leq \mu < 0), \tag{2}$$

and

$$b) \quad \text{For any } \epsilon > 0 \text{ and for } -1 \leq \mu \leq +1,$$

$$\lim_{\tau \to \infty} \epsilon^{-\epsilon\tau} I(\tau, \mu) = 0. \tag{3}$$

With $I(\tau, \mu)$ are associated two sequences of half-range moment functions $\{\alpha_k(\tau)\}_{k=0, 1, \ldots}$ and $\{\beta_k(\tau)\}_{k=0, 1, \ldots}$, defined by

$$\alpha_k(\tau) = \frac{1}{2}\int_0^1 \mu^k I(\tau, \mu)\, d\mu, \tag{4}$$

$$\beta_k(\tau) = \frac{1}{2}\int_{-1}^0 \mu^k I(\tau, \mu)\, d\mu. \tag{5}$$

* The research reported in this paper has been supported by the Geophysics Research Directorate, Air Force Cambridge Research Center, under Contract AF19(604)-146 with Harvard University.

We also define the sequence of full-range moment functions $\{M_k(\tau)\}_{k=0,\,1,\,\ldots}$ thus:

$$M_k(\tau) \equiv \alpha_k(\tau) + \beta_k(\tau) = \frac{1}{2}\int_{-1}^{+1} \mu^k I(\tau, \mu)\, d\mu . \tag{6}$$

For $k = 0, 1, 2$, we shall sometimes use the more customary notations,

$$J(\tau) \equiv M_0(\tau), \qquad H(\tau) \equiv M_1(\tau), \qquad K(\tau) \equiv M_2(\tau). \tag{7}$$

From equations (1), (2), and (3) the well-known Milne integral equations follow directly:

$$J(\tau) = \frac{1}{2}\int_{\tau}^{\infty} J(t)\, E_1(t-\tau)\, dt + \frac{1}{2}\int_{0}^{\tau} J(t)\, E_1(\tau - t)\, dt , \tag{8}$$

$$H = \frac{1}{2}\int_{\tau}^{\infty} J(t)\, E_2(t-\tau)\, dt - \frac{1}{2}\int^{\tau} J(t)\, E_2(\tau - t)\, dt , \tag{9}$$

where

$$E_n(x) = \int_0^1 e^{-x/\mu}\mu^{n-2} d\mu \qquad (n = 1, 2, \ldots) \tag{10}$$

and $4\pi H$ is the constant net flux of radiation.

In methods of type B one assumes a special functional form for $J(t)$ in equation (9) or equation (10) and then determines the coefficients of that form by some sort of "self-consistent" calculation. Methods of type A, on the other hand, are essentially equivalent to a replacement of the exponential integrals $E_n(x)$ in equations (9) and (10) by approximate expressions in terms of finite sums. In this paper we shall be concerned only with methods of type A.

Procedures A are usually formulated in terms of the integrodifferential equation (1) rather than in terms of the integral equations (9) and (10). We shall therefore first discuss the methods on the basis of equations (1), (2), and (3). There are, however, some advantages attached to the formulation based on equations (9) and (10), and we shall discuss this in Section VII.

Boundary condition (2) introduces a fundamental distinction between outgoing directions, $(\mu > 0)$, and incoming directions, $(\mu < 0)$. Procedures that incorporate this distinction into the formalism *ab initio* will be termed "adapted to the boundary conditions" or, simply, "adapted." The various methods A used most widely in practice are not thus adapted. It is this property that masks the close relations that exist between them; certain ambiguities are associated with the use of nonadapted procedures, and these are removed in different ways in different methods. When we employ a formalism adapted to the boundary conditions, the ambiguities disappear, and the various methods A are essentially equivalent.

The discrete ordinate and spherical harmonic methods have been discussed extensively in the literature (Chandrasekhar 1950; Kourganoff 1952). As has been remarked previously, they are closely related. The relationships are clearly exhibited through the intermediacy of moment methods.

II. A MOMENT THEOREM

For computational, as well as for comparative, purposes it is convenient to introduce moment methods. These are, in a certain sense, generalizations of the Eddington approximation. When a sequence of moment equations is derived from equation (1) by integrations over angle (cf. Sec. III), the first n equations involve the $(n + 1)$ moments of orders $0, 1, \ldots, n$. To obtain a determinate set of equations for the nth approximation, we have to express the nth moment in terms of the lower moments. In addition, we have to represent boundary conditions (2) and (3) in terms of moments.

This result is achieved most cogently for our present purposes by translating the Wick-Chandrasekhar (Chandrasekhar 1950) method of discrete ordinates (W-C method) into an equivalent moment procedure. The connection is provided by a simple theorem, which we shall establish in greater generality than will be required in this paper.

Let $\{\phi_k(x)\}_{k=0,\,1,\,\ldots}$ be a sequence of polynomials (ϕ_k of degree k), mutually orthogonal with respect to a weight function $w(x)$, over the interval (a, b). In particular, let

$$\phi_n(x) = \sum_{j=0}^{n} c_j x^{n-j}, \tag{11}$$

and let x_j $(j = 1, \ldots, n)$ be the zeros of $\phi_n(x)$. A "best possible" approximation to

$$\int_a^b f(x)\, w(x)\, dx$$

by a sum of n terms is then given by (cf. Chandrasekhar 1950)

$$\int_a^b f(x)\, w(x)\, dx \simeq \sum_{j=0}^{n} A_j f(x_j), \tag{12}$$

where the A_j's $(j = 1, \ldots, n)$ are uniquely determined weight constants.

Given a function $F(x)$, we define the sequence $\{m_\alpha\}_{\alpha=0,\,1,\,\ldots}$ of moments, with

$$m_\alpha \equiv \int_a^b x^\alpha F(x)\, w(x)\, dx. \tag{13}$$

THEOREM: In the approximation of order n provided by formula (12), the moments $m_0, \ldots, m_n$ satisfy the relation

$$\sum_{j=0}^{n} c_j m_{n-j} = 0, \tag{14}$$

where $c_0, c_1, \ldots, c_n$ are the coefficients of $\phi_n(x)$ in equation (11).

Proof: From equations (12) and (13) we obtain the following set of approximate moment equations:

$$m_\alpha \simeq \sum_{j=1}^{n} x_j^\alpha [A_j F(x_j)]. \tag{15}$$

These may now be regarded as a set of $(n + 1)$ linear equations for n "unknowns" $[A_j F(x_j)]$ $(j = 1, \ldots, n)$. The condition of consistency for this set is the determinantal equation

$$\begin{vmatrix} m_0 & 1 & . & . & 1 \\ m_1 & x_1 & . & . & x_n \\ . & . & & & \\ . & . & & & \\ m_n & x_1^n & . & . & x_n^n \end{vmatrix} = 0. \tag{16}$$

But $\phi_n(x)$ is, apart from a constant factor, equal to the determinant on the left-hand side of equation (16) with $m_0, m_1, \ldots, m_n$ replaced by $1, x, \ldots, x^n$, respectively. Hence expansion of the determinant in equation (16) in terms of elements of its first column leads to equation (14).

For future reference, we note that equation (14) is exactly the relation

$$\int_a^b \phi_n(x) F(x) w(x)\, dx = 0 \tag{17}$$

expressed in terms of moments. This result already suggests an intimate connection between procedures based on expansion in terms of orthogonal functions and procedures based on moments and hence also on discrete ordinates.

Adapted methods have advantages over nonadapted ones, in that they involve much less computation and, at the same time, yield more accurate results in any particular order of approximation. However, we shall first discuss the relations between the nonadapted procedures, since they are better known and are used more frequently.

III. THE MOMENT METHOD

Multiplying equation (1) by $\frac{1}{2}\mu^k$ ($k = 0, 1, \ldots, 2n-1$), integrating with respect to μ over $(-1, +1)$, and using definitions (6), we obtain the following set of $2n$ moment equations:

$$\frac{dM_{k+1}(\tau)}{d\tau} = M_k(\tau) - \frac{[1+(-1)^n]}{2(k+1)} M_0(\tau) \qquad (k = 0, 1, \ldots, 2n-1). \tag{18}$$

The appropriate polynomial for the nth approximation is the Legendre polynomial,

$$P_{2n}(\mu) = \sum_{\alpha=0}^{n} a_\alpha \mu^{2n-2\alpha}. \tag{19}$$

Equations (18) become a determinate system when we eliminate the moment $M_{2n}(\mu)$ by means of the relation (cf. eq. [14])

$$a_0 M_{2n} + a_1 M_{2n-2} + \ldots + a_n M_0 = 0. \tag{20}$$

We again note that equation (20) is equivalent to the relation

$$\int_{-1}^{+1} P_{2n}(\mu)\, I(\tau, \mu)\, d\mu = 0. \tag{21}$$

To represent boundary condition (2) in terms of the full-range moments, we return to the discrete ordinate representation. Let μ_j ($j = \pm 1, \ldots, \pm n$) be the zeros of $P_{2n}(\mu)$, and A_j ($j = \pm 1, \ldots, \pm n$) the corresponding weight constants for the Gaussian quadrature formula. Since $I(0, \mu_j) = 0$ for $j = -1, \ldots, -n$, we have

$$M_k(0) = \sum_{j=1}^{n} \mu_j^k [A_j I(0, \mu_j)] \qquad (k = 0, 1, \ldots, 2n-1), \tag{22}$$

a set of $2n$ equations in only n "unknowns" $[A_j I(0, \mu_j)]$ ($j = 1, \ldots, n$). The consistency condition applied to the set of $(n+1)$ equations of equation (22) with $k = 0, 1, \ldots, n-1, l$ ($l \geq n$) enables us to express $M_l(0)$ ($l = n, n+1, \ldots, 2n-1$) linearly in terms of $M_0(0), \ldots, M_{n-1}(0)$. This provides the n required boundary conditions at $\tau = 0$:

$$\begin{vmatrix} M_0(0) & 1 & \cdot & \cdot & 1 \\ M_1(0) & \mu_1 & \cdot & \cdot & \mu_n \\ \cdot & \cdot & & & \cdot \\ \cdot & \cdot & & & \cdot \\ M_{n-1}(0) & \mu_1^{n-1} & \cdot & \cdot & \mu_n^{n-1} \\ M_l(0) & \mu_1^l & \cdot & \cdot & \mu_n^l \end{vmatrix} = 0 \qquad (l = n, \ldots, 2n-1). \tag{23}$$

The solution of equations (18) with (20) and (23) is now completely equivalent to the solution of the nth approximation in the W-C method. In the moment procedure, the weights A_j have dropped out of the analysis; it is not necessary to know their explicit numerical values. It follows, therefore, that the A_j's do not enter in any essential way into the W-C method. On the other hand, the numerical values of the zeros of $P_{2n}(\mu)$ are essential and specifically in connection with boundary condition (2). As we shall see later, neither the weights nor the zeros enter in any essential way into adapted methods.

IV. THE SPHERICAL HARMONIC METHOD

The natural procedure for solving equation (1) would appear to be the expansion of $I(\tau, \mu)$ in a series of functions mutually orthogonal in $(-1, +1)$, i.e., in a series of Legendre polynomials (cf. Kourganoff 1952):

$$I(\tau, \mu) = \sum_{k=0}^{\infty} I_k(\tau) P_k(\mu), \tag{24}$$

$$I_k(\tau) = \frac{(2k+1)}{2} \int_{-1}^{+1} I(\tau, \mu) P_k(\mu)\, d\mu. \tag{25}$$

Substitution of equation (24) in equation (1) and use of equation (25) and the recurrence and orthogonality relations for Legendre polynomials lead to the following sequence of equations:

$$\frac{k}{(2k-1)} \frac{dI_{k-1}}{d\tau} + \frac{(k+1)}{(2k+3)} \frac{dI_{k+1}}{d\tau} = I_k \qquad (k = 0, 1, 2, \ldots) \tag{26}$$

with $I_{-1}(\tau) \equiv 0$.

The nth simple harmonic (S-H) approximation follows when we terminate series (24) after the term with $k = 2n - 1$; i.e., we set

$$I_{2n}(\tau) \equiv 0;$$

and so, by equation (25),

$$\int_{-1}^{+1} P_{2n}(\mu)\, I(\tau, \mu)\, d\mu = 0. \tag{27}$$

This is, as mentioned previously (cf. eq. [21]), identical with relation (20) of the moment method. Let

$$P_l(\mu) = \sum_{\alpha=0} a_\alpha^{(l)} \mu^{l-2\alpha}.$$

Then

$$I_l(\tau) = (2l+1) \sum_{\alpha=0} a_\alpha^{(l)} M_{l-2\alpha}. \tag{28}$$

The substitution of equation (28) in the set (26) with $I_{2n} \equiv 0$ and $k = 0, 1, \ldots, 2n-1$ transforms the differential equations of the nth S-H approximation into the equations of the nth moment approximation.

Thus, apart from boundary conditions, the nth S-H approximation is equivalent to the nth moment approximation and so also to the nth W-C approximation. The S-H method, however, encounters a serious difficulty in the application of boundary condition (2). In the nth approximation we have, at $\tau = 0$,

$$I(0, \mu) = \sum_{k=0}^{2n-1} I_k(0) P_k(\mu) \qquad (-1 \leq \mu \leq +1). \tag{29}$$

Since $I(0, \mu) = 0$ in $(-1, 0)$, we should have to take prohibitively large values of n in equation (29) to represent adequately the destructive interference of the terms over this whole interval. Thus the S-H approximation cannot reasonably be applied in a manner consistent with the general method of orthogonal functions.

However, various prescriptions have been given to render condition (2) in a form applicable to the S-H approximation. In effect, the W-C and moment methods correspond to a particular prescription imposed on the S-H method. The W-C approximation incorporates the prescription *ab initio* into the differential equations. The S-H method separates the prescription from the differential equations; the moment approximation likewise separates the prescription from the differential equations but in a form equivalent to the W-C approximation.

These considerations show that the S-H, W-C, and moment methods are merely different versions of a single basic method which essentially involves an expansion in terms of Legendre polynomials. As such, the critical remarks associated with equation (26) apply to all of them. We may thus expect relatively large deviations from the exact solution in the neighborhood of the boundary. This is borne out by an examination of the first few W-C approximations. Even though these reproduce the exact boundary temperature, comparatively large errors occur near $\tau = 0$.

V. THE EDDINGTON APPROXIMATION

For the first moment approximation we take $n = 1$ in the equations of Section III. Then, using the customary notation (7), relations (20) and (23) reduce to

$$K(\tau) = \tfrac{1}{3} J(\tau), \tag{30}$$

$$J(0) = \sqrt{3}\, H(0). \tag{31}$$

The Eddington approximation consists of equation (30) together with a boundary condition $J(0) = 2H(0)$. Eddington motivated his approximate boundary condition by a somewhat rough physical argument. The more consistent mathematical motivation provided by the general moment method indicates that the form of equation (31) is more appropriate as the boundary condition in the Eddington approximation.

As remarked previously, boundary condition (2) imposes a fundamental distinction between outgoing directions ($\mu > 0$) and incoming directions ($\mu < 0$). Adapted methods should then be based on two sets of orthogonal polynomials:

(i) The set $\{Q_k(\mu)\}_{k=0, 1, \ldots}$ mutually orthogonal in (0, 1) with weight function identical with 1.

(ii) The set $\{R_k(\mu)\}_{k=0, 1, \ldots}$ mutually orthogonal in $(-1, 0)$ with weight function identical with 1.

Both sets are related in a simple way to the Legendre polynomials,

$$Q_k(\mu) \equiv P_k(2\mu - 1) \qquad (0 \leq \mu \leq 1), \tag{32}$$

$$R_k(\mu) \equiv P_k(2\mu + 1) \qquad (-1 \leq \mu \leq 0); \tag{33}$$

and so

$$Q_k(\mu) = (-1)^k R_k(-\mu). \tag{34}$$

In the nth approximation, Gaussian quadrature formulae for (0, 1) are based on the zeros of $Q_n(\mu)$, and for $(-1, 0)$ are based on the zeros of $R_n(\mu)$. This leads to a discrete ordinate method (Sykes 1951) adapted to the boundary conditions. In the corresponding adapted moment method we do not require knowledge of the explicit values of either the zeros of Q_n, R_n, or the associated weight factors. This results in a considerable simplification of the numerical work as compared with that of nonadapted procedures.

VI. THE ADAPTED MOMENT METHOD

Multiplying equation (1) by $\frac{1}{2}\mu^k$ $(k = 0, 1, \ldots, n-1)$, integrating successively over $(0, 1)$ and $(-1, 0)$ with respect to μ, and using definitions (4) and (5), we obtain two coupled sets of half-range moment equations:

$$\frac{d\alpha_{k+1}}{d\tau} = \alpha_k - \frac{(\alpha_0 + \beta_0)}{2(k+1)} \qquad (k = 0, 1, \ldots, n-1), \tag{35}$$

$$\frac{d\beta_{k+1}}{d\tau} = \beta_k - (-1)^k \frac{(\alpha_0 + \beta_0)}{2(k+1)} \qquad (k = 0, 1, \ldots, n-1). \tag{36}$$

To obtain a determinate set, we have to eliminate α_n and β_n from equations (35) and (36). If we write

$$Q_n(\mu) \equiv \sum_{\lambda=0}^{n} a_\lambda \mu^{n-\lambda}, \tag{37}$$

$$R_n(\mu) \equiv \sum_{\lambda=0}^{n} (-1)^\lambda a_\lambda \mu^{n-\lambda}, \tag{38}$$

the elimination is effected by means of the relations (cf. eq. [14])

$$a_0\alpha_n + a_1\alpha_{n-1} + \ldots + a_n\alpha_0 = 0 \tag{39}$$

and

$$a_0\beta_n - a_1\beta_{n-1} + \ldots + (-1)^n\beta_0 = 0. \tag{40}$$

Boundary condition (2) now translates directly into the set of conditions

$$\beta_k(0) = 0 \qquad (k = 0, 1, \ldots, n-1). \tag{41}$$

We remark again that the zeros of Q_n and R_n and their associated weight constants are not required in the calculation. The only quantities that enter are the (rational) coefficients of the polynomials $Q_n(\mu)$ and $R_n(\mu)$.

It is sometimes convenient to rewrite the equations in terms of sums M_k and differences N_k of the half-range moments:

$$\begin{aligned} M_k(\tau) &\equiv \alpha_k(\tau) + \beta_k(\tau), \\ N_k(\tau) &\equiv \alpha_k(\tau) - \beta_k(\tau). \end{aligned} \tag{42}$$

Then equations (35) and (36) lead to

$$\frac{dM_{k+1}}{d\tau} = M_k - \frac{[1 + (-1)^k]}{2(k+1)} M_0 \qquad (k = 0, 1, \ldots, n-1), \tag{43}$$

$$\frac{dN_{k+1}}{d\tau} = N_k - \frac{[1 - (-1)^k]}{2(k+1)} M_0 \qquad (k = 0, 1, \ldots, n-1); \tag{44}$$

and equations (39) and (40) give

$$a_0M_n + a_1N_{n-1} + a_2M_{n-2} + \ldots = 0, \tag{45}$$

$$a_0N_n + a_1M_{n-1} + a_2N_{n-2} + \ldots = 0; \tag{46}$$

and boundary conditions (41) take the form

$$M_k(0) = N_k(0) \qquad (k = 0, 1, \ldots, n-1). \tag{47}$$

The nth adapted approximation can also be given a completely equivalent formulation in terms of orthogonal polynomial expansions (Yvon 1952). With definitions (32) and (33), the orthogonality and recurrence relations for Legendre polynomials lead to corresponding relations for the $Q_k(\mu)$ and $R_k(\mu)$. The use of these relations, together with the substitution of

$$I(\tau, \mu) = \begin{cases} \sum_{k=0}^{n-1} q_k(\tau) Q_k(\mu) & (0 < \mu \leq 1) \\ \sum_{k=0}^{n-1} r_k(\tau) R_k(\mu) & (-1 \leq \mu < 0) \end{cases} \tag{48}$$

in equation (1), yields the system of $2n$ differential equations:

$$\frac{k}{(2k-1)} \frac{dq_{k-1}}{d\tau} - \frac{dq_k}{d\tau} + \frac{(k+1)}{(2k+3)} \frac{dq_{k+1}}{d\tau} = 2q_k - (q_0 + r_0) \cdot \delta_{k,0}, \tag{49}$$

$$\frac{k}{(2k-1)} \frac{dr_{k-1}}{d\tau} + \frac{dr_k}{d\tau} + \frac{(k+1)}{(2k+3)} \frac{dr_{k+1}}{d\tau} = 2r_k - (q_0 + r_0) \cdot \delta_{k,0}. \tag{50}$$

The boundary conditions at $\tau = 0$ are, now,

$$r_k(0) = 0 \qquad (k = 0, 1, \ldots, n-1). \tag{51}$$

The ambiguity that occurs in the S-H method and so, by implication, in all non-adapted methods has now disappeared. At the same time, the internal consistency of the adapted procedures leads to a better solution in the neighborhood of the origin; this is confirmed by examination of the first few adapted approximations.

We can now also understand the reason for the result found by Kourganoff (1952) that, in the same order of approximation, the Newton-Cotes quadrature formula gives a better representation than did the W-C solution based on the Gaussian quadrature formula. The "optimum" quadrature formula for the problem is the one based on the zeros of both $Q_n(\mu)$ and $R_n(\mu)$. The Newton-Cotes points are intermediate between those zeros and the zeros of $P_{2n}(\mu)$.

VII. INTEGRAL EQUATION PROCEDURES

Methods of type A can be formulated in terms of the integral equations (8) and (9) by approximate representation of the exponential integrals as sums of n terms.

Let μ_j $(j = 1, \ldots, n)$ be n points of subdivision of the interval (0, 1), and let A_j $(j = 1, \ldots, n)$ be associated weight constants. We introduce the approximate expressions

$$E_1(x) \simeq \sum_{j=1}^{n} A_j \frac{e^{-x/\mu_j}}{\mu_j}, \tag{52}$$

$$E_2(x) \simeq \sum_{j=1}^{n} A_j e^{-x/\mu_j}, \tag{53}$$

into equations (8) and (9), respectively, and obtain the approximated integral equations

$$2J(\tau) = \sum_{j=1}^{n} \frac{A_j}{\mu_j} \left\{ \int_{\tau}^{\infty} J(t)\, e^{-(t-\tau)/\mu_j} dt + \int_{0}^{\tau} J(t)\, e^{-(\tau-t)/\mu_j} dt \right\}, \tag{54}$$

$$2H = \sum_{j=1}^{n} A_j \left\{ \int_{\tau}^{\infty} J(t)\, e^{-(t-\tau)/\mu_j} dt - \int_{0}^{\tau} J(t)\, e^{-(\tau-t)/\mu_j} dt \right\}. \tag{55}$$

By analogy with results obtained by the differential equation procedures, we look for self-consistent solutions of equations (54) and (55) that have the form

$$J(\tau) = a + b\tau + \sum_{\alpha=1}^{N} c_\alpha e^{-\lambda_\alpha \tau}. \tag{56}$$

The index N, the exponents λ_α, and the coefficients a, b, and c_α are to be determined by the condition that the right-hand side of equation (54) or equation (55), evaluated with $J(t)$ as given by equation (56), should be identically equal to the left-hand side. From equation (55) we easily obtain, in this way, the relations

$$b \sum_{j=1}^{n} A_j \mu_j^2 = H, \tag{57}$$

which determines the constant b, and

$$\sum_{j=1}^{n} \frac{A_j \mu_j^2}{\lambda_\alpha^2 \mu_j^2 - 1} = 0 \qquad (\alpha = 1, 2, \ldots), \tag{58}$$

which determines the exponents λ_α and also implies $N = n - 1$. The n constants a, $c_1, \ldots, c_{n-1}$ are obtained by solution of the equations

$$a - \sum_{\alpha=1}^{n-1} \frac{c_\alpha}{\lambda_\alpha \mu_j - 1} = b\mu_j \qquad (j = 1, \ldots, n). \tag{59}$$

These are, of course, exactly the relations we obtain from a discrete ordinate method applied symmetrically in the intervals $(0, 1)$ and $(-1, 0)$. In the special case where the μ_j's are the zeros of $Q_n(\mu)$, relations (57), (58), and (59) may be transformed in such a way that the μ_j's and A_j's are eliminated and only the coefficients of $Q_n(\mu)$ appear explicitly.

The reason for introducing the integral equation procedure is that it enables us to exhibit and analyze the main sources of error involved in type A procedures. In such procedures one essentially approximates exponential integrals by sums of the form (52) and (53) for all x in $(0, \infty)$. The question of uniformity of such approximations therefore arises. Since $E_1(x)$ has a logarithmic singularity at $x = 0$, approximation (52) certainly breaks down in the neighborhood of $x = 0$. On the other hand, $E_2(x)$ is finite everywhere. It is represented with reasonable accuracy by sums of the form (53); the major deviations again occur near $x = 0$. The considerations of this section may be extended to provide numerical estimates of the errors involved in applications of type A procedures.

VIII. OTHER APPLICATIONS OF ADAPTED PROCEDURES

We have stressed the advantages attached to the use of adapted methods that involve approximations to the angular distribution of intensity and the essential equivalence of such methods. Similar situations occur in various branches of physics, e.g., in certain boundary-value problems for the Boltzmann equation in the kinetic theory of gases. The

relevant variable here is the component of velocity of a molecule perpendicular to the boundary, say u ($-\infty < \mu < +\infty$), and the appropriate weight factor is often of the form $e^{-\alpha u^2}$. If the boundary condition introduces a distinction between $u > 0$ and $u < 0$, we may use a half-range moment method, a half-range orthogonal polynomial method, or a discrete ordinate method. In view of our considerations in Section II, these methods are equivalent.

REFERENCES

Chandrasekhar, S. 1950, *Radiative Transfer* (Oxford: Oxford University Press).
Kourganoff, V. 1952, *Basic Methods in Transfer Problems* (Oxford: Oxford University Press).
Sykes, J. B. 1951, *M.N.*, **111**, 377.
Yvon, J. Cited by Kourganoff, 1952, p. 101 n.

NEAR THERMODYNAMIC EQUILIBRIUM. II

L. G. HENYEY AND WILLIAM GRASBERGER*
Berkeley Astronomical Department, University of California
Received July 14, 1955

ABSTRACT

The concept of near thermodynamic equilibrium, described in an earlier paper (Henyey 1946), is extended to include the effect of collisions in redistributing atoms over a broadened state. Modified expressions are derived for the absorption and emission coefficients. The question of the importance of effects arising from near thermodynamic equilibrium in the deep interior is considered. No change in the usual expression for the flux is required.

In a previous paper (Henyey 1946) the concept of near thermodynamic equilibrium was introduced and discussed in terms of purely radiative effects, that is, radiative excitation processes and radiative or natural broadening of levels. This discussion is extended here to include the influence of collisional, or pressure, broadening. The analysis is carried through, both in a general form and, with more detail, in the case when collisional effects produce a complete redistribution of the atoms in each quantum level.

I

In this paper we consider a gas which exists in a steady state under conditions which approximate those of thermodynamic equilibrium. The condition of a steady state is achieved when the number of transitions from any given state is equal to the number of traditions into that state. In this section we derive an expression for the condition of a steady state (including the collisional effects) which neglects terms higher than first-order deviation from thermodynamic equilibrium.

Let $N_{kl}(\epsilon', \epsilon'')d\epsilon' d\epsilon''$ be the number of transitions per second per gram of gas from the elements of state $(\epsilon', \epsilon' + d\epsilon')$ of the discrete state k, to the element of state $(\epsilon'', \epsilon'' + d\epsilon'')$ of the discrete state l. Let $N_{k\infty}(\epsilon', \epsilon'')d\epsilon' d\epsilon''$ designate the number of transitions to the element of state $(\epsilon'', \epsilon'' + d\epsilon'')$ in the continuum. Here $h\epsilon$ expresses the energy of a state, so that ϵ is measured in frequency units.

The condition for a steady state requires that the number of transitions per second per gram from the element of state $(\epsilon', \epsilon' + d\epsilon')$, belonging to the discrete state k, be equal to the number of transitions into the element. There is a similar condition for an element of state in the continuum. Expressing these conditions mathematically, we have, for the first condition,

$$\sum_{l(\neq k)} \int_{-\infty}^{\infty} N_{kl}(\epsilon', \epsilon'')\, d\epsilon'' + \int_{0}^{\infty} N_{k\infty}(\epsilon', \epsilon'')\, d\epsilon'' + \int_{-\infty}^{\infty} N_{kk}(\epsilon', \epsilon'')\, d\epsilon'' = \sum_{l(\neq k)} \int_{-\infty}^{\infty} N_{lk}(\epsilon'', \epsilon')\, d\epsilon'' + \int_{0}^{\infty} N_{\infty k}(\epsilon'', \epsilon')\, d\epsilon'' + \int_{-\infty}^{\infty} N_{kk}(\epsilon'', \epsilon')\, d\epsilon''. \tag{1}$$

For a discrete level, $\epsilon = 0$ is taken to be the mid-point of the level, whereas $\epsilon = 0$ in the continuum corresponds to the start of the continuum of the corresponding level. The summation is to be taken over all levels except the kth level. The last term in each side of this expression includes the effect of collisions in redistributing the atoms over the breadth of state k.

* Now at the Livermore site of the Radiation Laboratory, University of California.

For the second condition we have

$$\sum_l \int_{-\infty}^{\infty} N_{\infty l}(\epsilon', \epsilon'')\, d\epsilon'' + \int_0^{\infty} N_{\infty\infty}(\epsilon', \epsilon'')\, d\epsilon'' = \sum_l \int_{-\infty}^{\infty} N_{l\infty}(\epsilon'', \epsilon')\, d\epsilon'' + \int_0^{\infty} N_{\infty\infty}(\epsilon'', \epsilon')\, d\epsilon''. \tag{2}$$

The term $N_{\infty\infty}(\epsilon', \epsilon'')d\epsilon' d\epsilon''$ is the number of transitions per second per gram from the element of state $(\epsilon', \epsilon' + d\epsilon')$ to the element of state $(\epsilon'', \epsilon'' + d\epsilon'')$, both lying in the continuum. Here the summation is taken over all discrete levels.

Let $g_k\psi_k(\epsilon)$ be the statistical weight assigned to the element of state $(\epsilon, \epsilon + d\epsilon)$ of the discrete state k, where g_k is the total statistical weight of the state k. The definition of $\psi_k(\epsilon)$ is such that

$$\int_{-\infty}^{\infty} \psi_k(\epsilon)\, d\epsilon = 1. \tag{3}$$

Let $N_k(\epsilon)d\epsilon$ be the number of atoms per gram of gas in the element of state $(\epsilon, \epsilon + d\epsilon)$ of the discrete state k. In thermodynamic equilibrium $N_k(\epsilon)$ has the value $N_k^{(0)}(\epsilon)$, where

$$N_k^{(0)}(\epsilon) \sim g_k\psi_k(\epsilon)\, e^{-h\epsilon/kT}. \tag{4}$$

Over the narrow breadth of the state we can neglect the variation of the exponential factor. Hence, if $N_k^{(0)}$ is the total number of atoms in the state k, then

$$N_k^{(0)}(\epsilon) = N_k^{(0)}\psi_k(\epsilon). \tag{5}$$

We can represent departures from thermodynamic equilibrium by the parameters $\xi_k(\epsilon)$ and ξ_k, defined by

$$\frac{N_k(\epsilon)}{N_k^{(0)}(\epsilon)} = 1 + \xi_k(\epsilon), \tag{6}$$

$$\frac{N_k}{N_k^{(0)}} = 1 + \xi_k. \tag{7}$$

Let N_i and N_e be the number of ions, of the kind considered, and the number of free electrons per gram of gas, respectively. Let ξ_∞ describe the departure from thermodynamic equilibrium of the product N_iN_e by the following equation:

$$\frac{N_iN_e}{N_i^{(0)}N_e^{(0)}} = 1 + \xi_\infty. \tag{8}$$

The deviation of J_ν, the mean specific intensity of radiation, from the black-body intensity, B_ν, can be expressed as follows:

$$J_\nu = B_\nu(1 + \eta_\nu). \tag{9}$$

In the earlier paper the transition rates were determined for the following conditions:

a) The transitions are purely radiative, so that the influence of collisions of the first and second kinds is neglected.

b) The velocity distribution of the free electrons is Maxwellian, with a parametric temperature $T^{(e)}$.

c) Any transition probability, describing a transition from a discrete state, depends only on the state as a whole and not on the part of the state from which the transition originates.

d) Any transition probability, describing a transition into a discrete state, is proportional to the statistical weight of the element of state into which the transition passes. Let $\sigma_\nu = 2h\nu^3/c^2$, and put $\nu = |\epsilon'' - \epsilon'|$. Let

$$N_{kl}^{(0)}(\epsilon', \epsilon'') = N_{kl}^{(0)} \psi_k(\epsilon') \psi_l(\epsilon'')$$

and

$$N_{k\infty}^{(0)}(\epsilon', \epsilon'') = N_{k\infty}^{(0)}(\epsilon'') \psi_k(\epsilon') .$$

As shown in the previous paper, under the foregoing conditions we have

$$N_{kl}(\epsilon', \epsilon'') = N_{kl}^{(0)} \psi_k(\epsilon') \psi_l(\epsilon'') [1 + \xi_k(\epsilon')] [1 + \eta_\nu] \qquad (k < l) , \quad (10)$$

$$N_{lk}(\epsilon'', \epsilon') = N_{kl}^{(0)} \psi_k(\epsilon') \psi_l(\epsilon'') [1 + \xi_l(\epsilon'')] \left[1 + \frac{\eta_\nu B_\nu}{\sigma_\nu + B_\nu}\right] (k < l) , \quad (11)$$

$$N_{k\infty}(\epsilon', \epsilon'') = N_{k\infty}^{(0)}(\epsilon'') \psi_k(\epsilon') [1 + \xi_k(\epsilon')] [1 + \eta_\nu] , \quad (12)$$

$$N_{\infty k}(\epsilon'', \epsilon') = N_{k\infty}^{(0)}(\epsilon'') \psi_k(\epsilon') \frac{N_i N_e}{N_i^{(0)} N_e^{(0)}} \frac{f^{(e)}(\epsilon'')}{f^{(0)}(\epsilon'')} \frac{\sigma_\nu + J_\nu}{\sigma_\nu + B_\nu} . \quad (13)$$

Here $f^{(e)}(\epsilon)$ is the Maxwellian distribution,

$$f^{(e)}(\epsilon) = 2 \left(\frac{h^3 \epsilon}{\pi \bar{t}^3 T^{(e)3}}\right)^{1/2} e^{-h\epsilon/\bar{t}T^{(e)}} . \quad (14)$$

The function $f^{(0)}(\epsilon)$ is defined as in equation (14), expect that the electron temperature $T^{(e)}$ is replaced by the reference temperature T, which describes the excitation in a first approximation. Introducing the notation

$$\frac{N_i N_e}{N_i^{(0)} N_e^{(0)}} \frac{f^{(e)}(\epsilon)}{f^{(0)}(\epsilon)} = 1 + \xi_\infty(\epsilon) , \quad (15)$$

we can readily verify that

$$\int_0^\infty f^{(0)}(\epsilon) \xi_\infty(\epsilon) \, d\epsilon = \xi_\infty . \quad (16)$$

Using equations (9) and (15), we find that equation (13) becomes

$$N_{\infty k}(\epsilon'', \epsilon') = N_{k\infty}^{(0)}(\epsilon'') \psi_k(\epsilon') [1 + \xi_\infty(\epsilon'')] \left[1 + \frac{\eta_\nu B_\nu}{\sigma_\nu + B_\nu}\right] . \quad (17)$$

The principle of detailed balancing requires that, in thermodynamic equilibrium,

$$N_{kk}^{(0)}(\epsilon', \epsilon'') = N_{kk}^{(0)}(\epsilon'', \epsilon') . \quad (18)$$

The rate $N_{kk}(\epsilon', \epsilon'')$ is the product of $N_k(\epsilon')$, the density of available atoms for making the transition, and a factor which is independent of the actual excitation. This second factor must depend on the characteristics of the particles which induce the transitions within k. We here assume that it is insensitive to first-order deviations from strict thermodynamic equilibrium. Hence $N_{kk}(\epsilon', \epsilon'')$ differs from $N_{kk}^{(0)}(\epsilon', \epsilon'')$ only because of the excitation factor. We then have

$$N_{kk}(\epsilon', \epsilon'') = N_{kk}^{(0)}(\epsilon', \epsilon'') [1 + \xi_k(\epsilon')] . \quad (19)$$

It is convenient to use the following substitutions:

$$\begin{aligned} \xi_k(\epsilon) &= \xi_\infty + \zeta_k(\epsilon), \\ \xi_\infty(\epsilon) &= \xi_\infty + \zeta_\infty(\epsilon), \\ \xi_k &= \xi_\infty + \zeta_k. \end{aligned} \tag{20}$$

Using equations (10), (11), (12), (17), (19), and (20), we can write equation (1) in the form

$$\begin{aligned} \sum_{l(<k)} \int_{-\infty}^{\infty} N_{kl}^{(0)} \psi_k(\epsilon') \psi_l(\epsilon'') \Big\{ & \zeta_k(\epsilon') - \zeta_l(\epsilon'') \\ & - \eta_\nu \Big[\frac{\sigma_\nu}{\sigma_\nu + B_\nu} + \xi_l(\epsilon'') - \xi_k(\epsilon') \frac{B_\nu}{\sigma_\nu + B_\nu} \Big] \Big\} d\epsilon'' \\ & + \int_{-\infty}^{\infty} N_{kk}^{(0)}(\epsilon', \epsilon'') \{ \zeta_k(\epsilon') - \zeta_k(\epsilon'') \} d\epsilon'' \\ & + \sum_{l(>k)} \int_{-\infty}^{\infty} N_{kl}^{(0)} \psi_k(\epsilon') \psi_l(\epsilon'') \Big\{ \zeta_k(\epsilon') - \zeta_l(\epsilon'') \\ & + \eta_\nu \Big[\frac{\sigma_\nu}{\sigma_\nu + B_\nu} + \xi_\kappa(\epsilon') - \xi_l(\epsilon'') \frac{B_\nu}{\sigma_\nu + B_\nu} \Big] \Big\} d\epsilon'' \\ & + \int_0^{\infty} N_{k\infty}^{(0)}(\epsilon'') \psi_k(\epsilon') \Big\{ \zeta_k(\epsilon') - \zeta_\infty(\epsilon'') \\ & + \eta_\nu \Big[\frac{\sigma_\nu}{\sigma_\nu + B_\nu} + \xi_k(\epsilon') - \xi_\infty(\epsilon'') \frac{B_\nu}{\sigma_\nu + B_\nu} \Big] \Big\} d\epsilon'' = 0. \end{aligned} \tag{21}$$

Equation (21) invólves the fractional deviations from thermodynamic equilibrium in the populations of the elements of states of the various discrete states and the deviation of the mean specific intensity from the black-body intensity, η_ν. In order to solve equation (21) for the ξ's or ζ's, we need to specify the reference temperature, the density, the relative abundances of the various elements, and η_ν for all frequencies.

Since the solution in the rigorous form presents great difficulties, we now introduce the approximations appropriate for small deviations, namely, the neglect of the second-order terms formed by the product of η_ν with the various ξ's. Equation (21) now becomes

$$\begin{aligned} \sum_{l(<k)} \int_{-\infty}^{\infty} N_{kl}^{(0)} \psi_k(\epsilon') \psi_l(\epsilon'') \Big\{ & \zeta_k(\epsilon') - \zeta_l(\epsilon'') - \eta_\nu \frac{\sigma_\nu}{\sigma_\nu + B_\nu} \Big\} d\epsilon'' \\ & + \int_{-\infty}^{\infty} N_{kk}^{(0)}(\epsilon', \epsilon'') \{ \zeta_k(\epsilon') - \zeta_k(\epsilon'') \} d\epsilon'' \\ & + \sum_{l(>k)} \int_{-\infty}^{\infty} N_{kl}^{(0)} \psi_k(\epsilon') \psi_l(\epsilon'') \Big\{ \zeta_k(\epsilon') - \zeta_l(\epsilon'') + \eta_\nu \frac{\sigma_\nu}{\sigma_\nu + B_\nu} \Big\} d\epsilon'' \\ & + \int_0^{\infty} N_{k\infty}^{(0)}(\epsilon'') \psi_k(\epsilon') \Big\{ \zeta_k(\epsilon') - \zeta_\infty(\epsilon'') + \eta_\nu \frac{\sigma_\nu}{\sigma_\nu + B_\nu} \Big\} d\epsilon'' = 0. \end{aligned} \tag{22}$$

For the sake of conciseness, we introduce the mean life, $\tau_k^{(0)}$, in thermodynamic equilibrium, defined by

$$\sum_{l(\neq k)} N_{kl}^{(0)} + \int_0^{\infty} N_{k\infty}^{(0)}(\epsilon)\, d\epsilon = \frac{N_k^{(0)}}{\tau_k^{(0)}}. \tag{23}$$

Define p_{kl} and $p_{k\infty}$ by the relations

$$\begin{aligned} N_{kl}^{(0)} &= \frac{N_k^{(0)}}{\tau_k^{(0)}}\, p_{kl}\,, \\ N_{k\infty}^{(0)}(\epsilon) &= \frac{N_k^{(0)}}{\tau_k^{(0)}}\, p_{k\infty}(\epsilon)\,, \\ 0 &= p_{kk}\,. \end{aligned} \tag{24}$$

Equation (22) becomes

$$\zeta_k(\epsilon')\left[1+\frac{\tau_k^{(0)}}{N_k^{(0)}\psi_k(\epsilon')}\int_{-\infty}^{\infty} N_{kk}^{(0)}(\epsilon',\epsilon'')\,d\epsilon''\right] = \sum_l p_{kl}\zeta_l + \phi_k(\epsilon') + \frac{\tau_k^{(0)}}{N_k^{(0)}\psi_k(\epsilon')}\int_{-\infty}^{\infty} N_{kk}^{(0)}(\epsilon',\epsilon'')\,\zeta_k(\epsilon'')\,d\epsilon''\,, \tag{25}$$

where

$$\begin{aligned} \phi_k(\epsilon') = &\sum_{l(<k)} p_{kl}\int_{-\infty}^{\infty}\psi_l(\epsilon'')\frac{\eta_\nu\sigma_\nu}{\sigma_\nu+B_\nu}\,d\epsilon'' - \sum_{l(>k)} p_{kl}\int_{-\infty}^{\infty}\psi_l(\epsilon'')\frac{\eta_\nu\sigma_\nu}{\sigma_\nu+B_\nu}\,d\epsilon'' \\ &- \int_0^{\infty} p_{k\infty}(\epsilon'')\frac{\eta_\nu\sigma_\nu}{\sigma_\nu+B_\nu}\,d\epsilon'' + \int_0^{\infty} p_{k\infty}(\epsilon'')\,\zeta_\infty(\epsilon'')\,d\epsilon''\,. \end{aligned} \tag{26}$$

Multiplying equation (25) by $\psi_k(\epsilon')$ and integrating over all elements of state of the state k, we find

$$\zeta_k = \sum_l p_{kl}\zeta_l + \phi_k\,, \tag{27}$$

where we use the notation

$$\phi_k = \int_{-\infty}^{\infty}\phi_k(\epsilon')\,\psi_k(\epsilon')\,d\epsilon'\,. \tag{28}$$

Define the quantities q_{jk} by

$$\sum_k q_{jk}p_{kl} = q_{jl} - p_{jl}\,. \tag{29}$$

Then the formal solution of equation (27) is

$$\zeta_j = \phi_j + \sum_k q_{jk}\phi_k\,. \tag{30}$$

This may be verified by multiplying equation (27) by q_{jk}, summing for k, and applying equation (29). The resu't is identical with that obtained in the earlier paper and is given there in equation (53).

Let us define $\theta_k(\epsilon')$ by the relation

$$\zeta_k(\epsilon') = \zeta_k + \theta_k(\epsilon')\,. \tag{31}$$

Using equations (27) and (31), we obtain, for equation (25),

$$\theta_k(\epsilon')\left[1+\frac{\tau_k^{(0)}}{N_k^{(0)}\psi_k(\epsilon')}\int_{-\infty}^{\infty} N_{kk}^{(0)}(\epsilon',\epsilon'')\,d\epsilon''\right] = \phi_k(\epsilon') - \phi_k + \frac{\tau_k^{(0)}}{N_k^{(0)}\psi_k(\epsilon')}\int_{-\infty}^{\infty}\theta_k(\epsilon'')\,N_{kk}^{(0)}(\epsilon',\epsilon'')\,d\epsilon''\,. \tag{32}$$

It now appears that the solution of the general problem reduces to the solution of the linear integral equation (32) for the function $\theta_k(\epsilon)$. The solution will depend on the deviation of $\phi_k(\epsilon)$ from its mean value ϕ_k. This, in turn, depends on deviations from thermodynamic equilibrium values for the intensities in various lines. Examination will readily reveal that only the first two terms in the right-hand member of equation (26) contribute significantly in determining $\theta_k(\epsilon)$.

II

The determination of $\zeta_k(\epsilon)$ becomes relatively simple in the event that transitions within a state, as induced by collisions, take place very much more frequently than radiative transitions into and from the level. In this case the atom has made so many collisional transitions between radiative ones that it, in effect, forgets into what element of state it first entered. For strong collisional situations the fractional deviation from that given under the conditions of thermodynamic equilibrium of the population of a given element of state of the discrete state must be the same as the fractional deviation of the state as a whole. We call such a situation the *totally noncoherent case*. Now equation (25) becomes

$$\zeta_k(\epsilon) \equiv \zeta_k = \sum_l (\delta_{kl} + q_{kl})\, \phi_l , \tag{33}$$

where δ_{kl} is the Kronecker symbol.

Multiplying equation (26) by $\psi_k(\epsilon')$ and integrating over all elements of state of the state k, we have

$$\begin{aligned}\phi_k = \sum_{l(<k)} p_{kl} \int_0^\infty \psi_{kl}(\nu)\, \frac{\eta_\nu \sigma_\nu}{\sigma_\nu + B_\nu}\, d\nu - \sum_{l(>k)} p_{kl} \int_0^\infty \psi_{kl}(\nu)\, \frac{\eta_\nu \sigma_\nu}{\sigma_\nu + B_\nu}\, d\nu \\ - \int_{-\epsilon_k}^\infty p_{kl}(\epsilon_k + \nu)\, \frac{\eta_\nu \sigma_\nu}{\sigma_\nu + B_\nu}\, d\nu + \int_0^\infty p_{k\infty}(\epsilon)\, \zeta_\infty(\epsilon)\, d\epsilon ,\end{aligned} \tag{34}$$

where $h\epsilon_k$ is the negative energy below the limit of the kth continuum, measured to the mid-point of the kth state. The quantity $\psi_{kl}(\nu)$ is the profile of the line (kl), given by

$$\psi_{kl}(\nu) = \int_{-\infty}^\infty \psi_k(\epsilon')\, \psi_l(\epsilon' + \nu)\, d\epsilon' . \tag{35}$$

Substituting equation (34) in equation (33), we have

$$\begin{aligned}\zeta_j = \sum_{m,\, n(<m)} (\delta_{jm} + q_{jm})\, p_{mn} \int_0^\infty \psi_{mn}(\nu)\, \frac{\eta_\nu \sigma_\nu}{\sigma_\nu + B_\nu}\, d\nu \\ - \sum_{m,\, n(>m)} (\delta_{jm} + q_{jm})\, p_{mn} \int_0^\infty \psi_{mn}(\nu)\, \frac{\eta_\nu \sigma_\nu}{\sigma_\nu + B_\nu}\, d\nu \\ - \sum_m (\delta_{jm} + q_{jm}) \int_{-\epsilon_m}^\infty p_{m\infty}(\epsilon_m + \nu)\, \frac{\eta_\nu \sigma_\nu}{\sigma_\nu + B_\nu}\, d\nu \\ + \sum_m (\delta_{jm} + q_{jm}) \int_0^\infty p_{m\infty}(\epsilon)\, \zeta_\infty(\epsilon)\, d\epsilon .\end{aligned} \tag{36}$$

The equation of transfer in its most general form is as follows:

$$\frac{dI_\nu}{\rho\, ds} = -a_\nu I_\nu + j_\nu , \tag{37}$$

where a_ν and j_ν are the mass absorption and spontaneous emission coefficients. We treat the effect of stimulated emissions as a negative absorption, making a_ν the reduced absorption coefficient.

The mass emission and absorption coefficients for bound-bound, bound-free, and free-free transitions were derived in forms of general validity in the earlier paper, where reference should be made to equations (61), (62), (80), (83), (87), and (89).

Under conditions of thermodynamic equilibrium the three absorption coefficients become, respectively,

$$a^{(0)}_{kl,\,\nu} = \frac{h\nu}{4\pi B_\nu}\,\frac{\sigma_\nu}{\sigma_\nu + B_\nu}\,\psi_{kl}(\nu)\,N^{(0)}_{kl}\,,$$

$$a^{(0)}_{k,\,\nu} = \frac{h\nu}{4\pi B_\nu}\,\frac{\sigma_\nu}{\sigma_\nu + B_\nu}\,N^{(0)}_{k\infty}(\epsilon_k + \nu)\,, \tag{38}$$

$$a^{(0)}_{\epsilon,\,\nu} = \frac{h\nu}{4\pi B_\nu}\,\frac{\sigma_\nu}{\sigma_\nu + B_\nu}\,N^{(0)}(\epsilon,\,\epsilon + \nu)\,.$$

Using these, we may modify the six equations referred to in the preceding paragraph into the forms appropriate to the completely noncoherent case:

$$a_{kl,\,\nu} = a^{(0)}_{kl,\,\nu}\left[1 + \xi_\infty + \frac{\sigma_\nu + B_\nu}{\sigma_\nu}\,\zeta_k - \frac{B_\nu}{\sigma_\nu}\,\zeta_l\right]. \tag{39}$$

$$j_{kl,\,\nu} = a^{(0)}_{kl,\,\nu} B_\nu [1 + \xi_\infty + \zeta_l]\,. \tag{40}$$

$$a_{k,\,\nu} = a^{(0)}_{k,\,\nu}\left[1 + \xi_\infty + \frac{\sigma_\nu + B_\nu}{\sigma_\nu}\,\zeta_k - \frac{B_\nu}{\sigma_\nu}\,\zeta_\infty(\epsilon_k + \nu)\right]. \tag{41}$$

$$j_{k,\,\nu} = a^{(0)}_{k,\,\nu} B_\nu [1 + \xi_\infty + \zeta_\infty(\epsilon_k + \nu)]\,. \tag{42}$$

$$a_{\epsilon,\,\nu} = a^{(0)}_{\epsilon,\,\nu}\left[1 + \xi_\infty + \frac{\sigma_\nu + B_\nu}{\sigma_\nu}\,\zeta_\infty(\epsilon) - \frac{B_\nu}{\sigma_\nu}\,\zeta_\infty(\epsilon + \nu)\right]. \tag{43}$$

$$j_{\epsilon,\,\nu} = a^{(0)}_{\epsilon,\,\nu} B_\nu [1 + \xi_\infty + \zeta_\infty(\epsilon + \nu)]\,. \tag{44}$$

Using equations (24) and (38), we can write equation (36) as follows:

$$\begin{aligned}\zeta_j = \frac{4\pi}{h}\sum_{m,\,n(<m)}(\delta_{jm} + q_{jm})\frac{\tau^{(0)}_m}{N^{(0)}_m}\int_0^\infty (J_{\nu'} - B_{\nu'})\frac{a^{(0)}_{nm,\,\nu'}}{\nu'}\,d\nu' \\ - \frac{4\pi}{h}\sum_{m,\,n(>m)}(\delta_{jm} + q_{jm})\frac{\tau^{(0)}_m}{N^{(0)}_m}\int_0^\infty J_{\nu'} - B_{\nu'})\frac{a^{(0)}_{mn,\,\nu'}}{\nu'}\,d\nu' \\ - \frac{4\pi}{h}\sum_m (\delta_{jm} + q_{jm})\frac{\tau^{(0)}_m}{N^{(0)}_m}\int_{-\epsilon_m}^\infty (J_{\nu'} - B_{\nu'})\frac{a^{(0)}_{m,\,\nu'}}{\nu'}\,d\nu' \\ + \sum_m (\delta_{jm} + q_{jm})\int_0^\infty p_{m\infty}(\epsilon)\,\xi_\infty(\epsilon)\,d\epsilon\,.\end{aligned} \tag{45}$$

It can be shown that the following relations are valid:

$$\frac{N^{(0)}_k}{\tau^{(0)}_k}\,p_{kl} = \frac{N^{(0)}_l}{\tau^{(0)}_l}\,p_{lk}\,, \tag{46}$$

$$\frac{N_k^{(0)}}{\tau_k^{(0)}}\, q_{kl} = \frac{N_l^{(0)}}{\tau_l^{(0)}}\, q_{lk}. \tag{47}$$

Using the second of these relations, equation (45) becomes

$$\begin{aligned}\zeta_j = \frac{4\pi\tau_j^{(0)}}{h N_j^{(0)}}\Bigg\{ & \sum_{m,\, n(>m)} (\delta_{nj} + q_{nj} - \delta_{mj} - q_{mj}) \int_0^\infty (J_{\nu'} - B_{\nu'}) \frac{a^{(0)}_{mn,\,\nu'}}{\nu'}\, d\nu' \\ & - \sum_m (\delta_{mj} + q_{mj}) \int_{-\epsilon_m}^\infty (J_{\nu'} - B_{\nu'}) \frac{a^{(0)}_{m,\,\nu'}}{\nu'}\, d\nu' \Bigg\} \\ & + \sum_m (\delta_{jm} + q_{jm}) \int_0^\infty p_{m\infty}(\epsilon)\, \zeta_\infty(\epsilon)\, d\epsilon.\end{aligned} \tag{48}$$

Equation (40) may now be written as

$$\begin{aligned}j_{kl,\,\nu} = a^{(0)}_{kl,\,\nu} B_\nu \Bigg[& 1 + \xi_\infty \\ & + \frac{4\pi\tau_l^{(0)}}{h N_l^{(0)}}\Bigg\{ \sum_{m,\, n(>m)} (\delta_{nl} + q_{nl} - \delta_{ml} - q_{ml}) \int_0^\infty (J_{\nu'} - B_{\nu'}) \frac{a^{(0)}_{mn,\,\nu'}}{\nu'}\, d\nu' \\ & - \sum_m (\delta_{ml} + q_{ml}) \int_{-\epsilon_m}^\infty (J_{\nu'} - B_{\nu'}) \frac{a^{(0)}_{m,\,\nu'}}{\nu'}\, d\nu' \Bigg\} \\ & + \sum_m (\delta_{lm} + q_{lm}) \int_0^\infty p_{m\infty}(\epsilon)\, \zeta_\infty(\epsilon)\, d\epsilon \Bigg].\end{aligned} \tag{49}$$

Let us define the total absorption coefficient under the conditions of thermodynamic equilibrium as follows:

$$a_\nu^{(0)} = \sum_{k,\, l(>k)} a^{(0)}_{kl,\,\nu} + \sum_{j(>\bar{k})} a^{(0)}_{j,\,\nu} + \int_0^\infty a^{(0)}_{\epsilon,\,\nu}\, d\epsilon. \tag{50}$$

The state $\bar{k}$ is that whose continuum has its limit $|\epsilon_{\bar{k}}| > \nu$ while no other limit lies in the range ν to $|\epsilon_{\bar{k}}|$.

Combining equations (42), (44), and (49), we have, for the emission coefficient,

$$\begin{aligned}j_\nu = a_\nu^{(0)} B_\nu & [1 + \xi_\infty] \\ & + \sum_{k,\, l(>k)} a^{(0)}_{kl,\,\nu} B_\nu \Bigg[\frac{4\pi}{h} \frac{\tau_l^{(0)}}{N_l^{(0)}} \Bigg\{ \sum_{m,\, n(>m)} (\delta_{nl} + q_{nl} - \delta_{ml} - q_{ml}) \int_0^\infty (J_{\nu'} - B_{\nu'}) \\ & \times \frac{a^{(0)}_{mn,\,\nu'}}{\nu'}\, d\nu' - \sum_m (\delta_{ml} + q_{ml}) \int_{-\epsilon_m}^\infty (J_{\nu'} - B_{\nu'}) \frac{a^{(0)}_{m,\,\nu'}}{\nu'}\, d\nu' \Bigg\} \\ & + \sum_m (\delta_{lm} + q_{lm}) \int_0^\infty p_{m\infty}(\epsilon)\, \zeta_\infty(\epsilon)\, d\epsilon \Bigg] \\ & + \sum_{j(>\bar{k})} a_{j,\,\nu} B_\nu \zeta_\infty(\epsilon_j + \nu) + B_\nu \int_0^\infty a^{(0)}_{\epsilon,\,\nu} \zeta_\infty(\epsilon + \nu)\, d\epsilon.\end{aligned} \tag{51}$$

Equation (39) may now be written as

$$
\begin{aligned}
a_{kl,\,\nu} = a^{(0)}_{kl,\,\nu}\Bigg[1 + \xi_\infty
&+ \frac{\sigma_\nu + B_\nu}{\sigma_\nu}\frac{4\pi}{h}\frac{\tau^{(0)}_k}{N^{(0)}_k}\Bigg\{\sum_{m,\,n(>m)}(\delta_{nk} + q_{nk} - \delta_{mk} - q_{mk})\int_0^\infty (J_{\nu'} - B_{\nu'}) \\
&\times \frac{a^{(0)}_{mn,\,\nu'}}{\nu'}\,d\nu' - \sum_m (\delta_{mk} + q_{mk})\int_{-\epsilon_m}^\infty (J_{\nu'} - B_{\nu'})\frac{a^{(0)}_{m,\,\nu'}}{\nu'}\,d\nu'\Bigg\} \\
&- \frac{4\pi}{h}\frac{\tau^{(0)}_l}{N^{(0)}_l}\frac{B_\nu}{\sigma_\nu}\Bigg\{\sum_{m,\,n(>m)}(\delta_{nl} + q_{nl} - \delta_{ml} - q_{ml})\int_0^\infty (J_{\nu'} - B_{\nu'}) \\
&\times \frac{a^{(0)}_{mn,\,\nu'}}{\nu'}\,d\nu' - \sum_m (\delta_{ml} + q_{ml})\int_{-\epsilon_m}^\infty (J_{\nu'} - B_{\nu'})\frac{a^{(0)}_{m,\,\nu'}}{\nu'}\,d\nu'\Bigg\} \\
&+ \frac{\sigma_\nu + B_\nu}{\sigma_\nu}\sum_m (\delta_{km} + q_{km})\int_0^\infty p_{m\infty}(\epsilon)\,\zeta_\infty(\epsilon)\,d\epsilon \\
&- \frac{B_\nu}{\sigma_\nu}\sum_m (\delta_{lm} + q_{lm})\int_0^\infty p_{m\infty}(\epsilon)\,\zeta_\infty(\epsilon)\,d\epsilon\Bigg].
\end{aligned}
\tag{52}
$$

Equation (41) becomes

$$
\begin{aligned}
a_{k,\,\nu} = a^{(0)}_{k,\,\nu}\Bigg[1 + \xi_\infty - \frac{B_\nu}{\sigma_\nu}\zeta_\infty(\epsilon_k + \nu)
&+ \frac{\sigma_\nu + B_\nu}{\sigma_\nu}\frac{4\pi}{h}\frac{\tau^{(0)}_k}{N^{(0)}_k}\Bigg\{\sum_{m,\,n(>m)}(\delta_{nk} + q_{nk} - \delta_{mk} - q_{mk})\int_0^\infty (J_{\nu'} - B_{\nu'})\frac{a^{(0)}_{mn,\,\nu'}}{\nu'}\,d\nu' \\
&- \sum_m (\delta_{mk} + q_{mk})\int_{-\epsilon_m}^\infty (J_{\nu'} - B_{\nu'})\frac{a^{(0)}_{m,\,\nu'}}{\nu'}\,d\nu'\Bigg\} \\
&+ \frac{\sigma_\nu + B_\nu}{\sigma_\nu}\sum_m (\delta_{km} + q_{km})\int_0^\infty p_{m\infty}(\epsilon)\,\zeta_\infty(\epsilon)\,d\epsilon\Bigg].
\end{aligned}
\tag{53}
$$

Using equations (43), (52), and (53), we have, for the absorption coefficient,

$$
\begin{aligned}
a_\nu = a_\nu^{(0)}\,[1+\xi_\infty] \\
&+\sum_{k,\ l(>k)} a_{kl,\ \nu}^{(0)}\Big[\frac{\sigma_\nu+B_\nu}{\sigma_\nu}\frac{4\pi}{h}\frac{\tau_k^{(0)}}{N_k^{(0)}}\Big\{\sum_{m,\ n(>m)}(\delta_{nk}+q_{nk}-\delta_{mk}-q_{mk})\int_0^\infty (J_{\nu'}-B_{\nu'}) \\
&\times\frac{a_{mn,\ \nu'}^{(0)}}{\nu'}\,d\nu'-\sum_m(\delta_{mk}+q_{mk})\int_{-\epsilon_m}^\infty (J_{\nu'}-B_{\nu'})\frac{a_{m,\ \nu'}^{(0)}}{\nu'}\,d\nu'\Big\} \\
&-\frac{4\pi}{h}\frac{\tau_l^{(0)}}{N_l^{(0)}}\frac{B_\nu}{\sigma_\nu}\Big\{\sum_{m,\ n(>m)}(\delta_{nl}+q_{nl}-\delta_{ml}-q_{ml})\int_0^\infty (J_{\nu'}-B_{\nu'})\frac{a_{mn,\ \nu'}^{(0)}}{\nu'}\,d\nu' \\
&-\sum_m(\delta_{ml}+q_{ml})\int_{-\epsilon_m}^\infty (J_{\nu'}-B_{\nu'})\frac{a_{m,\ \nu'}^{(0)}}{\nu'}\,d\nu'\Big\} \\
&+\frac{\sigma_\nu+B_\nu}{\sigma_\nu}\sum_m(\delta_{km}+q_{km})\int_0^\infty p_{m\infty}(\epsilon)\,\zeta_\infty(\epsilon)\,d\epsilon \\
&-\frac{B_\nu}{\sigma_\nu}\sum_m(\delta_{lm}+q_{lm})\int_0^\infty p_{m\infty}(\epsilon)\,\zeta_\infty(\epsilon)\,d\epsilon\Big]+\sum_{j(>k)} a_{j,\ \nu}^{(0)}\Big[-\frac{B_\nu}{\sigma_\nu}\zeta_\infty(\epsilon_j+\nu) \\
&+\frac{\sigma_\nu+B_\nu}{\sigma_\nu}\frac{4\pi}{h}\frac{\tau_j^{(0)}}{N_j^{(0)}}\Big\{\sum_{m,\ n(>m)}(\delta_{nj}+q_{nj}-\delta_{mj}-q_{mj})\int_0^\infty (J_{\nu'}-B_{\nu'})\frac{a_{mn,\ \nu'}^{(0)}}{\nu'}\,d\nu' \\
&-\sum_m(\delta_{mj}+q_{mj})\int_{-\epsilon_m}^\infty (J_{\nu'}-B_{\nu'})\frac{a_{m,\ \nu'}^{(0)}}{\nu'}\,d\nu'\Big\} \\
&+\frac{\sigma_\nu+B_\nu}{\sigma_\nu}\sum_m(\delta_{jm}+q_{jm})\int_0^\infty p_{m\infty}(\epsilon)\,\zeta_\infty(\epsilon)\,d\epsilon\Big] \\
&+\int_0^\infty a_{\epsilon,\ \nu}^{(0)}\Big[\frac{\sigma_\nu+B_\nu}{\sigma_\nu}\zeta_\infty(\epsilon)-\frac{B_\nu}{\sigma_\nu}\zeta_\infty(\epsilon+\nu)\Big]\,d\epsilon\,.
\end{aligned}
\tag{54}
$$

The preceding complicated expressions summarize the specific form assumed by the various parameters under the conditions specified. A detailed study, using these expressions, will be reported in a forthcoming paper by W. Grasberger.

III

In the stellar interior it is sufficient to describe the radiation field in terms of first-order effects. Since near thermodynamic equilibrium appears to introduce additional first-order effects into the transfer problem beyond local thermodynamic equilibrium, it might appear that some modifications may be required in the formalism. Actually, this is not the case for the flux, as determined by the temperature gradient. This is seen readily by noting that the monochromatic flux is determined from the "Ergiebigkeit" to the first order by the expression

$$F_\nu = -\frac{4\pi}{3\,a_\nu\rho}\,\mathrm{grad}\,\frac{j_\nu}{a_\nu}+\ldots\,. \tag{55}$$

Since the term exhibited is already of order 1, any modification of a_ν from its equilibrium value, $a_\nu^{(0)}$, and any deviation of j_ν/a_ν from B_ν lead to second-order terms, which are negligible. The essential point is that near thermodynamic equilibrium effects are isotropic and hence do not affect the flux.

REFERENCES

Henyey, L. G. 1946, *Ap. J.*, **103**, 332–350.

THE EQUILIBRIUM OF MAGNETIC STARS

P. H. ROBERTS
Yerkes Observatory
Received May 16, 1955

ABSTRACT

A study is made of the mechanical equilibrium of bodies of incompressible fluid lying in a magnetic field. It is supposed that the system is symmetric about an axis. It is shown that, under certain simplifying assumptions, a series expansion can be derived for the equation of the free surface.

INTRODUCTION

The mechanical equilibrium of a star which possesses a magnetic field has been discussed by Chandrasekhar and Fermi (1953), who were the first to point out that such a star is likely to be oblate. They showed that the degree of ellipticity increased with $\mathfrak{M}/\Omega$, the ratio of the magnetic to the gravitational energy. Ferraro (1954) studied the equilibrium of an axially symmetric star in which the prevailing field lay in meridian planes containing the axis of symmetry. For the particular case in which the current density at a point distant ϖ from the axis is proportional to ϖ, he found that, to the first approximation, the surface of the star was an oblate spheroid. In this paper Ferraro's work is extended, and it is shown that a series expansion may be derived for the equation of the free surface.

FIELD EQUATIONS AND BOUNDARY CONDITIONS

The mechanical equilibrium of an incompressible fluid of density ρ acted upon by magnetic forces is governed by the equation

$$-\operatorname{grad}(p+\rho V)+j\times H=0\,, \tag{1}$$

where j is the electric current, H the magnetic field, p the hydrostatic pressure, and V the potential of nonmagnetic forces (assumed conservative). Equation (1) immediately restricts the choice of H, since it shows that

$$\operatorname{curl}(j\times H)=0\,. \tag{2}$$

Thus, a single-valued potential ψ exists for the Lorentz forces,

$$j\times H=-\operatorname{grad}\psi\,. \tag{3}$$

Equation (1) may therefore be integrated to give

$$p=p_0-\rho V-\psi\,, \tag{4}$$

where p_0 is a constant.

On the boundary S of the star, certain continuity conditions must be applied. The most stringent of these define a state of *true equilibrium*. The conditions may be relaxed to a certain extent and then define a state of *quasi-equilibrium*. These two states will now be considered separately.

i) TRUE EQUILIBRIUM

The magnetic field everywhere satisfies the divergence condition,

$$\operatorname{div} H=0\,. \tag{5}$$

Thus the normal component of $\boldsymbol{H}$ must be continuous across S. On using equation (5) and the result that

$$\text{curl } \boldsymbol{H} = 4\pi \boldsymbol{j} , \tag{6}$$

equation (1) may be expressed in the form

$$\frac{\partial T_{ij}}{\partial x_j} = 0 , \tag{7}$$

where T_{ij} is the total stress tensor, defined by

$$T_{ij} = -\left(p + \rho V + \frac{1}{8\pi} \boldsymbol{H}^2\right) \delta_{ij} + \frac{1}{4\pi} H_i H_j . \tag{8}$$

(The summation convention has been employed in eq. [7] and elsewhere in this paper.)

The force F_i acting across an element dS of S is therefore

$$F_i = T_{ij} dS_j . \tag{9}$$

In a state of true equilibrium *all* components of $\boldsymbol{F}$ must be continuous across S, since otherwise the outermost layers of the star would be subject to infinite accelerations. Equation (8) shows that, if V is continuous across S, the boundary conditions that must be satisfied in a state of true equilibrium are that $\boldsymbol{H}$ shall be continuous across S and p zero on it. If, however, $\boldsymbol{H} \cdot \boldsymbol{dS}$ is zero on S, the total pressure P, defined by

$$P = p + \frac{1}{8\pi} \boldsymbol{H}^2 , \tag{10}$$

must be zero on S. Since p may not be negative, this condition requires both p and $\boldsymbol{H}$ to be zero on S.

ii) QUASI-EQUILIBRIUM

A fluid body will be said to be in quasi-equilibrium if the field equations are satisfied in its interior and if $\boldsymbol{H} \cdot \boldsymbol{dS}$ and P are continuous across its surface. It is clear from equation (8) that, in general, such a body will not be in true equilibrium, since the tangential components of $\boldsymbol{F}$ are not necessarily continuous across S. The position may be clarified by considering the equilibrium of a star (of mean radius R, say) whose conductivity σ is large but not infinite. When the quasi-equilibrium conditions are satisfied, the outermost layer of the star will have a very high velocity. However, continuity of P will insure that the shape of the boundary will be unchanged for times comparable with the decay time $\pi\sigma R^2$ of the currents flowing in the star. This decay time is infinite if σ is infinite. It is essential that P be continuous, since otherwise the shape of the boundary will alter considerably in a time comparable to that taken by Alfvén waves in crossing the star. This time does not depend on σ, so that, even in the case of infinite σ, the star could in no sense be considered to be in equilibrium. For example, Chandrasekhar and Fermi (1953) have considered a liquid sphere with a uniform field inside and a dipole field outside and have shown, by energy arguments, that such a sphere would not be in equilibrium but would tend to become oblate. Although the approach adopted in this paper does not permit a simple evaluation of the degree of flattening, it does establish that the system cannot be in equilibrium, since P cannot be made continuous on S by any choice of p_0. Similarly, Gjellestad (1954) has examined the equilibrium of oblate spheroids in which the prevailing field is uniform. She finds that the system cannot be in equilibrium with respect to all deformations. This is also clear from the present approach, since it is easily shown that P cannot be made continuous.

AXIALLY SYMMETRIC STARS

The problem will now be specialized by supposing that the system is symmetric about an axis Oz. Further, it will be assumed that $\boldsymbol{H}$ lies entirely in meridian planes containing Oz. Set up cylinder co-ordinates (ϖ, ϕ, z). Denote by $\mathbf{1}_\phi$ the unit vector in the direction of ϕ increasing. It is clear that a stream function $U(\varpi, z)$ exists which is related to $\boldsymbol{H}$ by

$$\boldsymbol{H} = \operatorname{curl} \frac{1}{\varpi} U \mathbf{1}_\phi . \tag{11}$$

Equation (6) shows that U is related to the strength J of the current by

$$\nabla^2 \left\{ \frac{1}{\varpi} U \mathbf{1}_\phi \right\} = -4\pi J \mathbf{1}_\phi . \tag{12}$$

In a true equilibrium configuration, $d\boldsymbol{S} \cdot \operatorname{grad} U$ and U are continuous at S. Further, since $\boldsymbol{H}$ is assumed to be of internal origin, U must vanish as R^{-2} at large distances R from S. Under these circumstances, U is uniquely determined by equation (12). It is

$$\frac{1}{\varpi} U \mathbf{1}_\phi = \int \frac{J(\varpi', z')}{|\boldsymbol{r} - \boldsymbol{r}'|} \mathbf{1}_{\phi'} d\tau' , \tag{13}$$

where the integration is taken over the volume occupied by the fluid. On multiplying equation (13) scalarly by $\mathbf{1}_\phi$, it is found that

$$U(\boldsymbol{r}) = \varpi \int \frac{J(\varpi', z') \cos(\phi - \phi')\, d\tau'}{|\boldsymbol{r} - \boldsymbol{r}'|} . \tag{14}$$

Ferraro (1954) has shown that, if field (11) satisfies the equilibrium condition (2), then

$$J = -\varpi f(U) . \tag{15}$$

Thus equilibrium stream functions must satisfy the integral equation

$$U(\boldsymbol{r}) = -\varpi \int \frac{\varpi' f(U') \cos(\phi - \phi')\, d\tau'}{|\boldsymbol{r} - \boldsymbol{r}'|} . \tag{16}$$

Unfortunately, the only case in which equation (16) is tractable is the very simple one for which

$$f(U) = \kappa = \text{Constant} . \tag{17}$$

In this special case, equation (16) shows immediately that

$$U(\boldsymbol{r}) = -\kappa \varpi \int \frac{\varpi' \cos(\phi - \phi')\, d\tau'}{|\boldsymbol{r} - \boldsymbol{r}'|} . \tag{18}$$

Equation (4) shows that p is zero on S if

$$p_0 - \rho \Omega_s - \frac{\kappa}{4\pi} U_s = 0 . \tag{19}$$

On using equation (18), this condition becomes

$$\int \frac{d\tau'}{|\boldsymbol{r}_s - \boldsymbol{r}'|} + \frac{\kappa^2}{16\pi^2 \rho^2 G} \varpi_s \int \frac{\varpi' \cos(\phi_s - \phi')\, d\tau'}{|\boldsymbol{r}_s - \boldsymbol{r}'|} = \text{Constant} . \tag{20}$$

Introduce spherical polar co-ordinates (r, θ, ϕ) and suppose that the fluid boundary has the equation

$$r = R(\theta) . \tag{21}$$

On expanding the integrands occurring in equation (20), it is found that R must satisfy

$$\sum_{n=0}^{\infty} \frac{P_n(\cos\theta)}{(n+3)R^{n+1}} \int_0^{\pi} R^{n+3} P_n(\cos\theta) \sin\theta \, d\theta + \frac{\kappa^2}{16\pi^2\rho^2 G} \sum_{n=1}^{\infty} \frac{P_n^1(\cos\theta)\sin\theta}{n(n+1)(n+4)R^n} \times \int_0^{\pi} R^{n+4} P_n^1(\cos\theta) \sin^2\theta \, d\theta = \text{Constant}. \tag{22}$$

This equation appears to define a one-parameter family of surfaces. Suppose that the magnetic field is so weak that S is nearly spherical. Expand R in a series of the form

$$R = a \sum_{n=0}^{\infty} \lambda^n Q_n(\theta) \qquad [Q_1 = 1], \tag{23}$$

where λ is defined by

$$\lambda = \frac{a^2\kappa^2}{16\pi^2\rho^2 G} \tag{24}$$

and is approximately the ratio between the magnetic and the gravitational energy. To the first order in λ, R is given by

$$R = a[1 + \lambda Q_1(\theta)]. \tag{25}$$

Replacing R in equation (22) by this expression and working consistently to the first order in λ, we find that

$$-\tfrac{2}{3}Q_1 + \sum_{n=1}^{\infty} P_n(\cos\theta) \int_0^{\pi} Q_1(\theta) P_n(\cos\theta) \sin\theta \, d\theta + \tfrac{2}{15}\sin^2\theta = \text{Constant}. \tag{26}$$

This is satisfied by

$$Q_1(\theta) = -\tfrac{1}{2}\cos^2\theta. \tag{27}$$

Now, in place of expression (25), write R in the form

$$R = a[1 - \tfrac{1}{2}\lambda\cos^2\theta + \lambda^2 Q_2(\theta)], \tag{28}$$

and work consistently to the second order in λ. Equation (22) enables $Q_2(\theta)$ to be determined. In principle, this method enables Q_n to be determined, although the algebraic difficulties increase extremely rapidly with n and there seems to be no simple way of determining the general term. To the third order in λ, it is found that

$$\begin{aligned} R = a\Big[1 &+ \Big(-\tfrac{1}{2}\lambda - \frac{71}{490}\lambda^2 + \frac{56519}{2905210}\lambda^3 + \ldots\Big)\cos^2\theta \\ &+ \Big(+\frac{69}{280}\lambda^2 - \frac{11691}{4150300}\lambda^3 - \ldots\Big)\cos^4\theta \\ &+ \Big(-\frac{1007}{22000}\lambda^3 - \ldots\Big)\cos^6\theta + \ldots\Big] \end{aligned} \tag{29}$$

$$\begin{aligned} = a[1 &+ (-0.5\lambda - 0.1449\lambda^2 + 0.01945\lambda^3 + \ldots)\cos^2\theta \\ &+ (+0.2464\lambda^2 - 0.002817\lambda^3 - \ldots)\cos^4\theta \\ &+ (-0.04577\lambda^3 - \ldots)\cos^6\theta + \ldots]. \end{aligned}$$

To the first order in λ, S is an oblate spheroid of ellipticity $\frac{1}{2}\lambda$. This is exactly the result obtained by Ferraro (1954). However, it should be noted that there is no guaranty that

the series will converge for any value of λ or that expansion (25) is an asymptotic expansion for R. It is quite possible that equation (22) has no real solution and that consequently the simplifying assumption (17) will have to be abandoned.

CONCLUSION

The last section was devoted to a search for true equilibrium configurations. I have also tried to find quasi-equilibrium states in which the surfaces S are oblate spheroids (of eccentricity e, say). Here the technique is to add to solution (18) multiples of suitable solutions to Laplace's equation. If only odd harmonics are introduced, the continuity conditions for P determine the multiplicative constants uniquely, provided that both the first and third harmonics are present. On making the simplest possible assumption, namely, that *only* the first and third harmonics are needed, it is found that the multiplicative constants are complex, although their arguments tend to zero with e, so that, to the first order in e, the solution is real and is actually the one obtained by Ferraro (1954). The algebraic difficulties increase rapidly with the number of harmonics added, but it seems likely that there are no spheroidal quasi-equilibrium configurations compatible with assumption (17).

I am grateful to Dr. S. Chandrasekhar for the interest he has taken in this work. The research reported in this paper was supported in part by the Geophysics Research Directorate of the Air Force Cambridge Research Center, Air Research and Development Command, under Contract AF 19(604)-299 with the University of Chicago.

REFERENCES

Chandrasekhar, S., and Fermi, E. 1953, *Ap. J.*, **118**, 116.
Ferraro, V. C. A. 1954, *Ap. J.*, **119**, 407.
Gjellestad, G. 1954. *Ap. J.*, **119**, 14.

RADIO DETERMINATION OF THE ORBIT OF THE ETA AQUARID METEORS

D. W. R. McKinley
National Research Council, Ottawa, Canada
Received May 4, 1955

ABSTRACT

From an analysis of radio-echo data obtained on May 4–5, 1949, the mean observed velocity of the η-Aquarid meteors is determined to be 64.4 km/sec, and the corrected geocentric velocity to be 64.6 km/sec. A position at R.A. 330°, Dec. 0°, is found for the η-Aquarid radiant. With these data an orbit was computed with an eccentricity of 0.83, an inclination of 157°.8, and a period of 8.0 years. Some further remarks on the δ-Aquarid shower of July, 1949, are appended, and the observed velocity is corrected to give a geocentric velocity of 40.9 km/sec for the δ-Aquarid meteors.

In his recent book on meteor astronomy, Lovell (1954) has pointed out that there is scarcely any published information on the velocity of meteors of the η-Aquarid stream. Only two visual velocity determinations are available, and these have a very wide spread (Porter 1943). Hawkins and Miss Almond (1952) measured three η-Aquarid velocities as 63.7, 63.0, and 58.8 km/sec, using radio techniques at Jodrell Bank. In Table A5 of the radio observations reported by McKinley (1951) there is a noticeable peak in the range 60–65 km/sec during the early morning hours, which was tentatively associated with the η-Aquarid shower and which yielded a preliminary value of 64 km/sec from an inspection of the coarse data. It is the purpose of this paper to analyze the data contained in Table A5 of that report in greater detail, using additional information which was not presented before because of space limitations. The analytical methods to be employed will follow those described in a paper on the δ-Aquarid shower (McKinley 1954), to which the reader may refer for a fuller explanation of the procedures.

If we use the ephemeris of the η-Aquarid radiant given by McIntosh (1935*a*) from visual observations and convert to epoch 1949 and local co-ordinates, it follows that, if we adopt tentatively a radiant position at R.A. 336°, Dec. 0°, the radiant will rise at Ottawa at about 0130 E.S.T. and set about 1330 E.S.T. We shall therefore confine our attention to the data available between 0200 and 1200 E.S.T. on the days of May 4 and May 5, 1949. Figure 1 shows the over-all velocity distribution for this period, plotted with a class interval of 2 km/sec. A peak in the distribution is noticeable in the vicinity of 63–64 km/sec. As before, in computing a mean velocity, we arbitrarily select the spread of velocities between the points where the numbers are 25 per cent of the peak number. In this case the limits are 59 and 70 km/sec, inclusive, and the mean velocity of the 160 meteors in this interval is 64.1 km/sec. There will be some sporadic meteors in this group, of course, and we shall examine some of the methods that may be applied to purify the selection further.

SELECTION BY REMOVAL OF BACKGROUND METEORS

The appendix tables of McKinley (1951) do not contain the appropriate data from near-by dates to establish a "standard" velocity distribution, which could be subtracted from the distribution of Figure 1 to yield a purer sample. The nearest available data are for April 20–22, 1949 (Table A4), which obviously contains a number of Lyrid meteors with velocities approaching that of the η-Aquarids. Tables A3 (March 26 and 30, 1949) and A19 (March 16–18, 1950) might be used, but these periods were, respectively, 37 and 48 days prior to the η-Aquarid epoch. Similarly, the observations presented in Table A6 (June 27–29, 1949) were made 55 days after the η-Aquarid date. In addition, Table A6

shows an unusually strong peak at 0800–1000 E.S.T. in the velocity class 65 km/sec, which seems abnormal and may warrant further investigation. We conclude that it is not practical to deduce from the available data a standard distribution applicable to the May period.

SELECTION BY ECHO DURATION

The selected data in the range 59–70 km/sec may be divided into two groups, one containing those echoes with a duration greater than a given arbitrary value and the other containing shorter-duration echoes. Past experience, based on other shower observations, suggests that the longer-duration group should contain a higher proportion of shower meteors. On examining the records, however, it is found that the average echo durations in the 59–70 km/sec range of the May 4–5 period are significantly smaller than

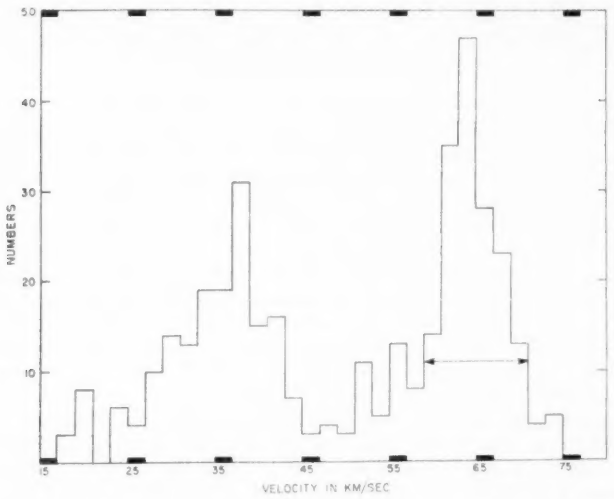

FIG. 1.—Observed velocity distribution of numbers of meteors per 2-km/sec class interval, observed between the hours of 0200 and 1200 E.S.T. on May 4 and 5, 1949. Total number, 382 meteors, in a net observing time of 15.4 hours. Arrow indicates velocity spread used in computing the mean velocity.

for the July, 1949, δ-Aquarid shower, for example. Because of its high velocity, it is probable that the average η-Aquarid meteor is observed by radio at a height of about 102 km (Millman 1954), and, owing to increased diffusion, its echo duration will be shorter than the echo of a slower meteor which is observed at a lower height (Greenhow and Neufeld 1955). In place of the arbitrary dividing line of 0.5 sec previously used for the δ-Aquarid meteors, we shall adopt a value of 0.3 sec for the η-Aquarids.

Figure 2, *A*, shows the velocity distribution for echoes less than 0.3 sec in duration; *B*, the distribution for echoes 0.3 sec and longer; and *C*, the distribution for all echoes. The data are plotted in 2-km/sec steps; e.g., the class interval, 59 km/sec, includes all meteors in the range 58.5–60.4 km/sec. However, in computing average velocities, the individual meteor velocities are taken to the nearest km/sec. For the 69 short-duration echoes, $V = 64.4$ km/sec; for the 91 long-duration echoes, $V = 63.9$ km/sec. For all echoes, $V = 64.1$ km/sec, as before, with a standard deviation of 2.9 km/sec and a probable error of the mean of ± 0.2 km/sec. The distributions do not vary significantly, and it is quite probable that the short-duration group contains many η-Aquarids. The ar-

bitrary criterion of echo duration does not appear to be particularly applicable to these observations, and therefore all echo durations will be included in the following discussion.

SELECTION BY ECHO RANGE—RADIANT DETERMINATION

The hourly-range distributions of the 160 meteors in the velocity interval 59–70 km/sec are shown in Figure 3. A preliminary breakdown into long- and short-duration echo groups failed to reveal any striking differences in the two sets of range distributions; therefore, because of the paucity of the data, all echo durations have been included. The data have been smoothed by using 2-hour averages and also by a sliding range average. This procedure tends to smooth out the minor humps in the curves at longer ranges, which might possibly be attributed to another and higher radiant, but the number of observations is too small to attach any significance to the lesser variations.

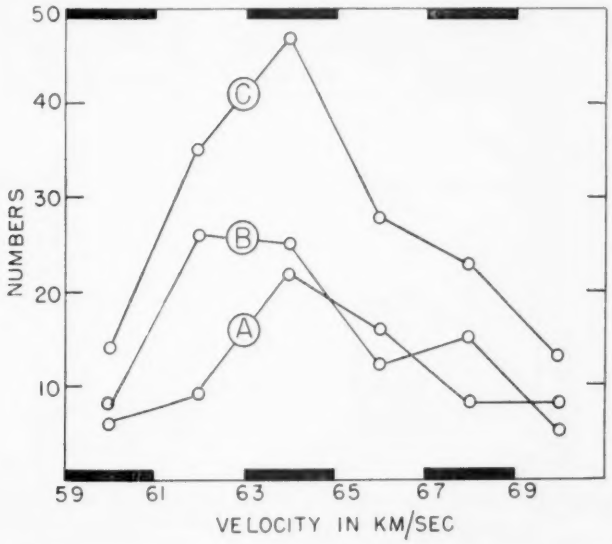

FIG. 2.—*A*, velocity distribution of echoes with durations less than 0.3 sec, 0200–1200 E.S.T. May 4–5, 1949. *B*, distribution of echoes with durations 0.3 sec and over. *C*, distribution of all echoes.

Very few observations were available for the hours 0200–0300 E.S.T. and 0700–0800 E.S.T.

The modal ranges of the graphs of Figure 3 are inserted in the formula $R_{\min} = H/\cos h$, where h is the radiant elevation and H is the mean height of the meteoric layer, which we shall take as 102 km in this case (Millman 1954*a*). The computed values of h are plotted in Figure 4 (*solid curve*). The maximum of the curve occurs at 0720 E.S.T. $\pm$20 min, and the peak elevation of the radiant is 46° $\pm$ 2°. The curve is obviously too flat, since it would fall to zero elevation at 0130 and 1330 E.S.T. if the data contained only η-Aquarid meteors. At the peak hours between 0530 and 0930 it is estimated that roughly 4 out of 5 of the selected meteors may be η-Aquarids, but the ratio of shower meteors to sporadic meteors may be as low as unity around 0300 and 1100 E.S.T. Despite this, the computed elevation of the upper transit of the radiant is not seriously affected, although the time of transit becomes more difficult to determine.

The dashed curve of Figure 4 shows the hourly rates of the selected meteors, after correcting for time lost because of film changes and equipment breakdowns. A considerable variation is evident in the rates prior to the upper transit which cannot be explained by instrumental faults. The time of the upper transit, read from the dashed curve, is 0700 E.S.T. ± 30 min, and the weighted mean of the transit time as read from both curves of Figure 4 is 0712 E.S.T. ± 17 min. The co-ordinates of the η-Aquarid radiant are therefore computed to be R.A. 330° $\pm$ 4°, Dec. 0° $\pm$ 2°. This radio determination of the

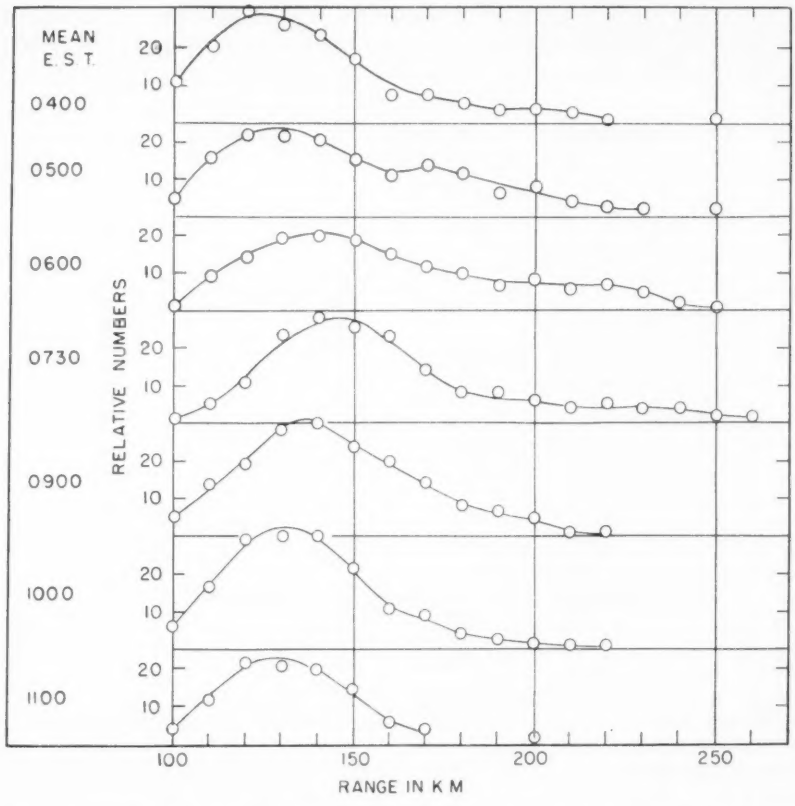

FIG. 3.—Smoothed hourly-range distributions of all echoes in the velocity range 59–70 km/sec, May 4–5, 1949. Ordinates are numbers of meteors, in relative units.

radiant may be compared with the visual determination given by McIntosh (1935*a*): there is good agreement in declination, but the Ottawa value of right ascension is 5° or 6° less than that indicated by McIntosh.

Three determinations of the radiant position have been given by the Jodrell Bank workers: R. A. 385°.5, Dec. +3°.0 (Aspinall and Hawkins 1951); R. A. 313°, Dec. −4° (Hawkins and Almond 1952); and R. A. 336°, Dec. −2° (Almond, Bullough, and Hawkins 1952). As shown in Table 1, Miss Almond has adopted a radiant at R.A. 338°, Dec. 0°, for orbital computations.

DISCUSSION OF THE η-AQUARID OBSERVATIONS

The corrected hourly-rate-curve (Fig. 4, *dashed curve*) shows a maximum rate of 7.5 meteors per hour, which is reduced to about 6 η-Aquarid radio meteors per hour after subtracting the probable sporadic background at the peak period. This rate is only 0.24 times the observed peak rate of 25 δ-Aquarid radio meteors per hour (McKinley 1954). The δ-Aquarid radiant transits at a less favorable angle of elevation, and, when allowance is made for this fact by using the radio probability function (McKinley 1951), the ratio falls to 0.12. Millman (1954*b*) suggests that the observed visual ratio of η-Aquarids to δ-Aquarids should be about 0.6, though a variation from year to year is to be expected. It is possible that the greater height of occurrence of the η-Aquarids has reduced both the durations and the numbers of the observed radio echoes, owing to increased diffusion (Greenhow and Neufeld 1955; Whipple 1955).

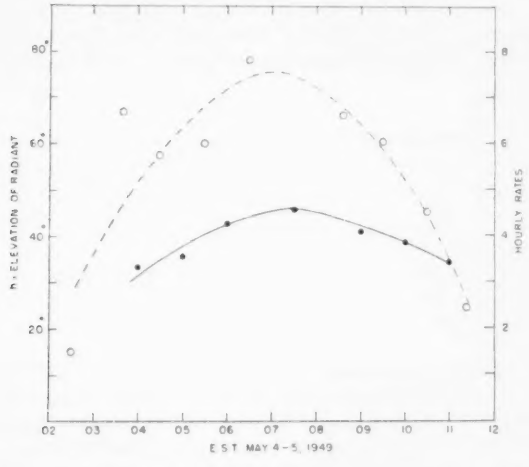

FIG. 4.—*Solid curve*, computed elevation of the η-Aquarid radiant, using data from Fig. 3. *Dashed curve*, corrected hourly rates of all meteors in the velocity range 59–70 km/sec.

The mean observed velocity of 64.1 km/sec, deduced here for the η-Aquarid shower, is subject to several corrections. In this case, where the observations are made symmetrically about the time of upper transit, the correction for diurnal motion is self-canceling, although it may cause a small spread in the observed velocities. The mean correction for the separation between the Doppler transmitter and receiver amounts to +0.3 km/sec, which revises the mean observed velocity to 64.4 km/sec. The correction for deceleration in the earth's atmosphere may be computed by several methods. Here we shall adopt the general technique outlined by Whipple (1938), but with more recent data from Jacchia (1952). The mean value of the cosine of the zenith distance of the radiant is found to be 0.551 for the observed meteors. For a mean height of 102 km we shall use the value 2.0×10^{-9} gm cm^{-3} for the density of the atmosphere. The mean mass of the particles is assumed to be 1 mg. From these data it may be computed that the no-atmosphere velocity, V_∞, is 65.6 km/sec. After applying the usual correction for the earth's attraction, it is found that the corrected geocentric velocity, V_G, is 64.6 km/sec for the η-Aquarid shower.

The mean epoch for the period of the η-Aquarid observations was taken as 2212 E.S.T., on May 4, 1949, corresponding to the longitude of the sun, $\odot\lambda = 44°.3$. With

V_G = 64.6 km/sec and the radiant position at R.A. 330°, Dec. 0°, the orbital elements of the meteor stream were computed, as shown in Table 1. The orbital elements calculated by Miss Almond of Jodrell Bank (from Lovell 1954) are also given for comparison.

The orbits in Table 1 are similar in many respects, but both have periods much shorter than that of Halley's Comet, with which the η-Aquarid shower has been conjecturally associated. Further speculation about the possibilities of such an association would be unwarranted here because of the uncertainty in the radiant position, even though it is felt that the Ottawa velocity measurement is reasonably accurate. The radiant ephemeris given by McIntosh (1935*a*) will provide a position that may be considered more probable than either of those shown in Table 1. A good photographic determination of the radiant would carry most weight, but this may be difficult to obtain because the major part of the activity occurs in daylight.

FURTHER REMARKS ON THE δ-AQUARID SHOWER

In a private communication Mr. B. A. McIntosh has suggested that our radio observations of the δ-Aquarid shower (McKinley 1954) may have been affected to some extent by meteors of the α-Piscid Australid stream (Catalogue No. 290, McIntosh 1935*b*). The

TABLE 1

ORBITAL ELEMENTS OF THE η-AQUARID SHOWER

	V_G (Km/Sec)	R.A. (Deg.)	Dec. (Deg.)	Ω (Deg.)	ω (Deg.)	i (Deg.)	q (a.u.)	e	a (a.u.)	P (Years)
Jodrell Bank. .	64.0	338	0	43.1	83.0	160.0	0.47	0.91	5.0	11.2
Ottawa.	64.6	330	0	44.3	108.5	157.8	0.70	0.83	4.0	8.0

co-ordinates he gives for the α-Piscid Australid radiant (R.A. 337°–350°, Dec. −33° to −30°) indicate that it would transit at about the same time as the δ-Aquarid radiant but that comparatively few meteors should be observed at Ottawa because of its very low declination and lesser activity. Using the relative activities for the two radiants, as catalogued by McIntosh, together with the probability function for the Ottawa radar system (McKinley 1951), we can conclude that, even at upper transit, the possible fraction of α-Piscid Australids in the total number observed could not exceed 0.2, and it would be considerably smaller over the remainder of the period. This is assuming, of course, that the mean velocity of the southern stream falls within the selected limits for the δ-Aquarids, which is an unknown factor. If an appreciable number of α-Piscid Australids were actually detected at Ottawa, the effect on the hourly-range distribution-curves would be to reduce the modal ranges slightly. Under the worst circumstances it is estimated that this could have caused an error not exceeding +1° in the declination of the δ-Aquarid radiant, i.e., our quoted value of Dec. −17° might be reduced to Dec. −16°, with the R.A. value unchanged.

Mr. McIntosh further suggests that the second radiant at R.A. 340°, Dec. 0°, given by McKinley (1954), might be correlated with a radiant at R.A. 335°, Dec. 0°, which he has named "Zeta Aquarii I" (Catalogue No. 283, McIntosh 1935*b*). It is apparent that the δ-Aquarid radiant is not the only source of shower meteors in this area of the sky during this period, although it may be the most active radiant.

In the earlier paper we did not attempt to correct the observed mean velocity of the δ-Aquarid meteors for deceleration in the atmosphere. However, for comparison with the results of other workers and for orbital calculations, it appears desirable to provide a corrected value of the geocentric velocity. The previously quoted observed velocity, 40.2

km/sec, should have been corrected for station displacement. The correction amounts to +0.1 km/sec, which revises the value of the observed velocity to 40.3 km/sec. Proceeding in the same way for the η-Aquarids, we shall adopt a mean particle mass of 1 mg., an air density of 4.5×10^{-9} gm cm^{-3} at a height of 95 km, and a mean observed value of 0.365 for the cosine of the zenith distance of the radiant. We find the no-atmosphere velocity to be $V_\infty = 42.4$ km/sec. After allowing for the earth's attraction, the corrected geocentric velocity of the δ-Aquarid meteors is determined to be $V_G = 40.9$ km/sec.

The author is indebted to Dr. Peter M. Millman for the Ottawa orbital computations in Table 1 and also for advice and assistance in the preparation of this paper.

REFERENCES

Almond, M., Bullough, K., and Hawkins, G. S. 1952, *Jodrell Bank Ann.*, **1**, 13.
Aspinall, A., and Hawkins, G. S. 1951, *M.N.*, **111**, 18.
Greenhow, J. S., and Neufeld, E. L. 1955, *J. Atm. Terr. Phys.*, **6**, 133.
Hawkins, G. S., and Almond, M. 1952, *Jodrell Bank Ann.*, **1**, 2.
Jacchia, Luigi G. 1952, *Tech. Report No. 10* (H.C.O. and Numerical Analysis Lab. M.I.T.).
Lovell, A. C. B. 1954, *Meteor Astronomy* (Oxford: Clarendon Press).
McIntosh, R. A. 1935*a*, *M.N.*, **95**, 601.
———. 1935*b*, *ibid.*, p. 709.
McKinley, D. W. R. 1951, *Ap. J.*, **113**, 225.
———. 1954. *ibid.*, **119**, 519.
Millman, Peter M. 1954*a*, *Science*, **120**, 325.
———. 1954*b*, *J.R.A.S. Canada*, **48**, 193.
Porter, J. G. 1943, *M.N.*, **103**, 134.
Whipple, Fred L. 1938, *Proc. Amer. Phil. Soc.*, **79**, 499.
———. 1955, *Ap. J.*, **121**, 241.

RECORDINGS OF THE ZODIACAL LIGHT

VICTOR H. REGENER
Department of Physics, University of New Mexico, Albuquerque
Received April 12, 1955; revised July 19, 1955

ABSTRACT

A series of 47 photoelectric recordings of the zodiacal light in the form of isophote maps has been obtained for 24 nights from March, 1953, until May, 1954. Only white light, not resolved into polarized and nonpolarized components, was used. The optical equipment consisted of an equatorially mounted reflector of 60-inch aperture with a phototube at its focus. This reflector scanned the sky automatically in the region of the zodiacal light, while values of light-intensity were recorded simultaneously on a map of the sky in equatorial co-ordinates. Such a map allowed the immediate plotting of isophotes, the convenient application of atmospheric corrections, and a rapid transfer of the data to the ecliptic co-ordinate system. During the recording period the cone of the zodiacal light shows a high degree of symmetry with respect to the ecliptic. No significant time variations of any of the measured characteristics of the zodiacal light are detected. An empirical analytic expression is given for the intensity of the zodiacal light in a limited region of the sky.

I. INTRODUCTION

The installation for the recording of the zodiacal light at Capillo Peak, New Mexico,[1] was designed for the purpose of obtaining recordings of the zodiacal light over a period of several years. Such a plan required not only that the equipment operate as automatically as possible but also that the data be recorded in such a form that they could be analyzed with reasonable speed.

The first phase of the observational program has now been concluded. It consisted of accurate mapping of zodiacal-light isophotes on as many nights as possible during a period of about one year. In particular, the position of the cone of the zodiacal light with respect to the ecliptic and time variations of the shape and the brightness of the zodiacal light were investigated. While the equipment includes provisions for recordings with color filters and for separate observations of the polarized component of the zodiacal light, only the white, natural light has been measured so far.

The technique consists of automatically scanning portions of the sky with a reflector, at whose focus a photomultiplier tube is mounted, and of recording the output of the phototube during the scanning operation in the form of a map in equatorial co-ordinates. This map allows the immediate plotting of isophotes. An optical projector with adjustable distortion is used for the superposition onto the original map of matching co-ordinate networks in the horizon and ecliptic systems; these facilitate the application of airglow and extinction corrections and the transfer of the photoelectric data to the ecliptic co-ordinate system.

Elvey and Roach (1937), Huruhata (1951), Behr and Siedentopf (1953), and Roach and collaborators (1954) also used photoelectric recording. The present work is characterized by high geometric resolution (better than 0.3 square degree) and by a large number of recordings.

II. INSTRUMENTATION[2]

The reflector is a parabolic searchlight mirror of 60 inches in diameter and 26 inches in focal length, a war-surplus item. Such a mirror is not, of course, suitable for ordinary

[1] Latitude 34°42′ N.; longitude 106°24′ W.; elevation 9200 feet.

[2] Details of this instrumentation can be found in *Scientific Report No. 2*, Contract No. AF 19(604)-181, Air Force Cambridge Research Center, June 10, 1954.

astronomical work because of the poor optical quality of its surface. For the purpose at hand, however, a large aperture is a more important feature than good optical definition of the image; the large aperture improves the signal-to-noise ratio of the phototube and permits a high scanning speed, together with a small field of view.

A circular diaphragm of 0.25 inch in diameter[3] is mounted at the focus of the mirror. Immediately behind the diaphragm is located the sensitive front surface of an RCA 5819 phototube. The effective area of the sky which is accepted through this diaphragm is 0.136 square degree.[4] This area must be used when the intensity of the zodiacal light is eventually expressed, as is customary, in terms of the number of stars of the tenth magnitude per square degree. The area of the sky from which light can reach the phototube is larger than this effective value, and it is further enlarged by the deviations of the mirror surface from a true paraboloid. It has been determined empirically that all light which is measured comes from inside a circular area which is 0°.7 in diameter ($\sim$0.3 square degree).

The reflector, in equatorial mount, is located on the highest point of South Capillo Peak. The scanning motion is electrically controlled from inside the observatory building, located 80 feet away. The remote electrical positioning system, which had been part of the original searchlight assembly, is used for this purpose.

The choice of the equatorial system of co-ordinates for the motion of the reflector leads to a number of advantages in the operation of the equipment and in the evaluation of the records. In particular, it allows a rapid reading of the recorded map in terms of both horizon co-ordinates and ecliptic co-ordinates. In addition, it is easy in the equatorial system to account for the apparent motion of the sky during the recording time.

The sky is scanned in right ascension from positions below the eastern horizon to positions below the western horizon and back, at a speed which results in one such traverse for every 55 seconds. When the turning point is reached below each of the horizons, the declination is automatically depressed by 2° before the return traverse begins. A band reaching in declination from $+42°$ to $-4°$ or, when appropriate, from $+30°$ to $-16°$ is thus covered in approximately 22 minutes.

The scanning speed is limited by the fact that the phototube circuits demand an integrating time of about 0.1 second if the signal is to be free of noise to the required degree. If the reflector moved during this integrating time through an angle larger than the effective vertex angle of the cone of acceptance ($\sim$0°.4), details of the zodiacal-light isophotes would be lost.

The complete installation is shown schematically in Figure 1. To the left is the reflector assembly. The yoke of the reflector carries a linear amplifier, which serves to reduce the output impedance of the phototube circuit before it is led over slip rings and through shielded cable into the observatory.

The upper part of Figure 1 shows the remote-control units containing the right-ascension (α) and declination (δ) control transformers which are to govern the motion of the reflector; these are designated *reflector synchro* in each case. The α-drive unit contains the drive motor for the scanning operation as well as a sidereal-time clock. When the α-drive motor is not rotating, the sidereal-time clock drives the reflector through a planetary gear, to keep its position constant in terms of right ascension. Any position of the α-drive motor shaft thus corresponds at all times to a given value of right ascension.

[3] Part of the time the diameter was 0.11 inch.

[4] This is computed from the formula $nA(360/2\pi)^2/f^2$, where A is the area of the diaphragm and f the focal length of the mirror. The numerical factor n takes account of two facts which are important when the mirror has a large aperture/focal-length ratio. First, the distance from most of the paraboloid mirror surface to the focal point is appreciably greater than f; second, much of the light enters the diaphragm at a large angle against the axis of the system. An elementary integration shows that $n = \cos^4(\alpha/2)$, where α is the angle made between the axis and the line connecting the edge of the mirror with the focal point. In the present case, $n = 0.553$.

The camera to the right of Figure 1 plots the maps. It is provided with a small objective lens of short focal length. This lens is free to travel in a plane parallel to the surface of the 5 × 5-inch film. Its position is controlled through a d.c. positioning control system[5] by the α-drive and δ-drive units. The horizontal position of the lens is determined by the lens synchro in the α-unit, and it is thus representative of the right-ascension setting of the reflector. The vertical position of the lens is similarly representative of the declination setting of the reflector. While the sky is being scanned, the lens travels in front of the film and records the information which is presented to it by the cathode-ray tube (Fig. 1).

The spot on this cathode-ray tube is controlled in position and in motion by the output from the phototube so as to produce 18 distinct, coded patterns on the oscilloscope screen. Each pattern changes into another at fixed, preselected, accurately known phototube-

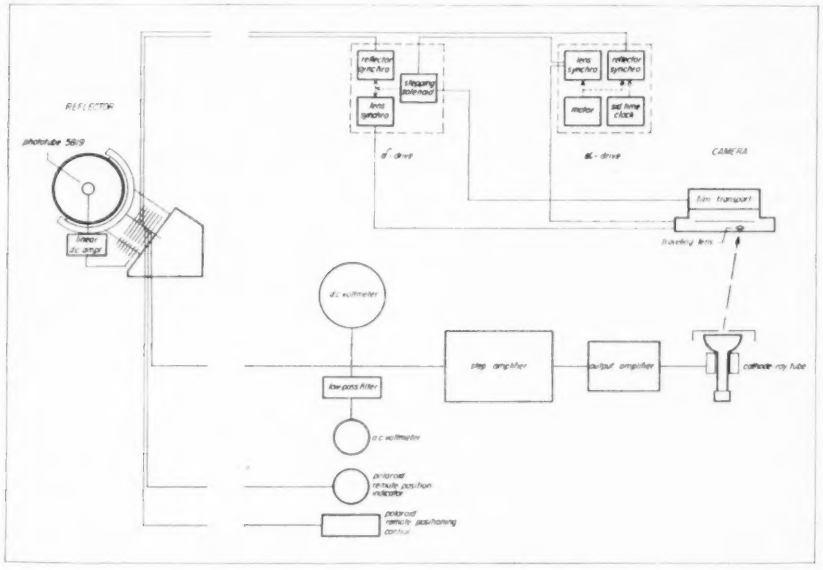

FIG. 1.—Installation for the automatic recording of zodiacal-light maps

output levels. This is accomplished by a special *step amplifier* (Fig. 1), which allows the spot of the oscilloscope tube to assume one of six possible positions, called "d.c. steps," and, for each one of these six positions, one of three possible amplitudes of audio modulation, called "a.c. steps." The traveling lens of the camera thus plots bands of three possible widths which can be located at six different levels of average displacement. Figure 2 shows, schematically, the appearance of a portion of a trace which would be obtained if the output from the phototube were continuously increasing from a low to a high value. The six thin lines are fiducial lines which allow identification of the d.c. steps. Figure 3 shows the original zodiacal-light map No. 110, taken in the morning of November 16, 1953.

The design of the step amplifier makes it possible to place the 17 phototube-output levels at which the stepping occurs within any desired range of intensity. The stepping

[5] Constructed with differential d.c. amplifiers of the vibrating-reed type (Brown Instrument Co., Philadelphia, Pa.) and with potentiometers built especially for this purpose.

method permits faster and more accurate evaluation of a map as compared with indication of a continuous type.

III. EVALUATION OF RECORDINGS[6]

Uncorrected isophotes are entered into the original maps for purposes of general orientation by simply drawing curves which connect points of corresponding pattern changes on the various traverses. The co-ordinates of these points in the horizon system and in the ecliptic system are tabulated with the aid of appropriate transparencies of co-ordinate grids which are optically projected upon an enlargement of the original map. Accurate correspondence of the scale values is achieved by means of a projector which permits continuous adjustment of the magnification in one direction. By adjusting the positions of two cylinder lenses (one positive, one negative) which are inserted between the transparency and the objective lens of the projector, the projected image may be stretched in one direction to any desired degree without defocusing. It is also possible, by rotating the transparency, to introduce a skew into the co-ordinate system. This is necessary when the horizon grid is projected, because of the 22-minute duration of the original recording.

FIG. 2.—Schematic sketch of an intensity record made by the traveling lens for a continuously increasing amount of light received by the phototube. The lens travels from left to right.

After the tabulation of the isophote positions in the two-co-ordinate systems, a preliminary background correction is subtracted from all output values. This correction is established as a function of elevation angle by drawing a graph of output values against elevation for a few vertical circles which lie as far away as possible from the ecliptic and from the galactic equator. On evening maps, the background region comes to lie in the east, on morning maps in the west. For lack of better information, it is necessary to assume that the portion of the background due to airglow is not a function of azimuth. The residual zodiacal light in the background region and the variation of the star background over the sky are considered for an especially selected series of maps after the application of the extinction correction.

The next step in the evaluation of a map consists of the application of a correction for atmospheric extinction and absorption. On the average, some 20 star-intensity readings were taken at various elevation angles during each observing night. This was originally done to obtain an empirical extinction correction as a function of elevation angle, as well as a calibration of the instrument with extra-terrestrial sources of known intensity. It turned out that these star readings were not sufficiently numerous for the first purpose. Therefore, a *molecular* correction, which essentially takes account of extinction due to Rayleigh scattering and of absorption in atmospheric ozone, is derived theoretically.

The molecular correction consists of a factor C which reduces all output readings to zenith incidence. It is applied as a matter of routine after subtraction of the preliminary background correction. If S_h is a quantity which is proportional to the theoretical response of the equipment to an extra-terrestrial source at an elevation angle h and if S_0 is the same quantity for zenith incidence, then the molecular correction factor is given by S_0/S_h as a function of the elevation angle. The quantity S_h is determined by computing

[6] Additional details of part of the procedure can be found in *Scientific Report No. 3*, Contract No. AF 19(604)-181, Air Force Cambridge Research Center, June 16, 1954.

the average theoretical response of the equipment in wave-length intervals which are 250 A wide and by adding these contributions over the whole spectrum. The zodiacal light is assumed to have a spectrum similar to that of the sun. The spectral response of the phototube is taken from an RCA publication (*Tube Handbook*), the air masses from Link (1934), the Rayleigh extinction coefficients from Wempe (1947), and the ozone masses and absorption coefficients from Paetzold (1953). The absorption in atmospheric ozone causes an increase of C by about 10 per cent at an elevation angle of 10°.

The molecular correction compensates satisfactorily for extinction on 42 out of the 47 maps, so far as one may judge from the curvature of the corrected isophotes very near the horizon, where defects of the correction are easily detected. A semiempirical dust correction is therefore applied, to account for additional extinction in dust and haze on the remaining 5 maps. It is assumed for this purpose that the dust is uniformly distributed throughout a layer, with a sharp upper boundary at the vertical distance H above the observatory. In analogy to the concept of air mass, dust masses are computed as a function of the elevation angle for several values of H, with due consideration of the earth's curvature and atmospheric refraction for Capillo Peak. These maps are then corrected through trial and error by choosing such a value of H and of the extinction coefficient for the dust as would best improve the appearance of the isophotes very near the horizon.

Of the 47 maps which are analyzed in this manner, 38 were recorded evenings on 18 nights; the dates are March 14, 1953; January 27, 29, 31, February 1, 2, 3, 4, 21, 23, 24, 28, March 27, 31, April 1, 2, 28, and May 26, 1954. Nine morning maps were recorded on 6 nights; the dates are September 14, 17, October 6, 9, and November 9, 16, 1953.

Figure 4 gives one of the maps recorded in the morning of November 16, 1953. The co-ordinate system is Cartesian in terms of ecliptic longitude and latitude, with the sun at the origin. A 5° reference grid is printed over the map in terms of elongation and position angle.[7] The isophotes are logarithmically spaced, and they are labeled with serial numbers. Isophotes with adjacent serial numbers differ in intensity by a factor of $\sqrt[4]{2}$, so that isophotes separated by four serial numbers differ by a factor of 2. This corresponds roughly to the spacing of the output values belonging to the original uncorrected isophotes. Only alternate isophotes are drawn in part of Figure 4.

The 47 maps which are analyzed to the extent described represent only a selection from a total of over 100 maps which were actually obtained. With the exception of a few maps at the beginning and at the end of the series, these selected maps have been recorded under good atmospheric conditions. Even so, the isophotes often show random distortions and asymmetries. One obtains the impression that the isophotes are likely to be more strongly distorted and displaced by variable anomalous conditions of atmospheric extinction than by natural fluctuations and irregularities in the character of the zodiacal light proper or by the lack of corrections for zodiacal light in the background region and for the inhomogeneity of the star background.

Therefore, a further selection of maps is made for the purpose of reduction to an absolute scale of intensity. This special series consists of 10 maps which are furnished, along the ecliptic, with further corrections. First, the zodiacal light in the background region, which should not have been subtracted from the output values, is restored to the data. Second, a correction is applied to take account of the difference in star background between points in the background region and points in the bright zodiacal-light region.[8]

Of these 10 maps, 3 are finally selected as suitable for an application of the same additional corrections not only on the ecliptic but also at position angles up to $\pm 20°$.[9]

As a first step, the output values, which are now provided with the preliminary back-

[7] The position angle is defined for the present purpose as a positive (negative) angle subtended at the position of the sun between the ecliptic and a point on the northern (southern) ecliptic hemisphere.

[8] These 10 maps were recorded on Oct. 9, 1953 (Nos. 97 and 98), Nov. 16, 1953 (Nos. 110 and 111), and on Jan. 27, Feb. 3, 4, 21, 23, 24, 1954 (Nos. 116, 143, 147, 156, 158, 160).

[9] These 3 maps were recorded on Feb. 3, 4, and 21, 1954 (Nos. 143, 147, 156).

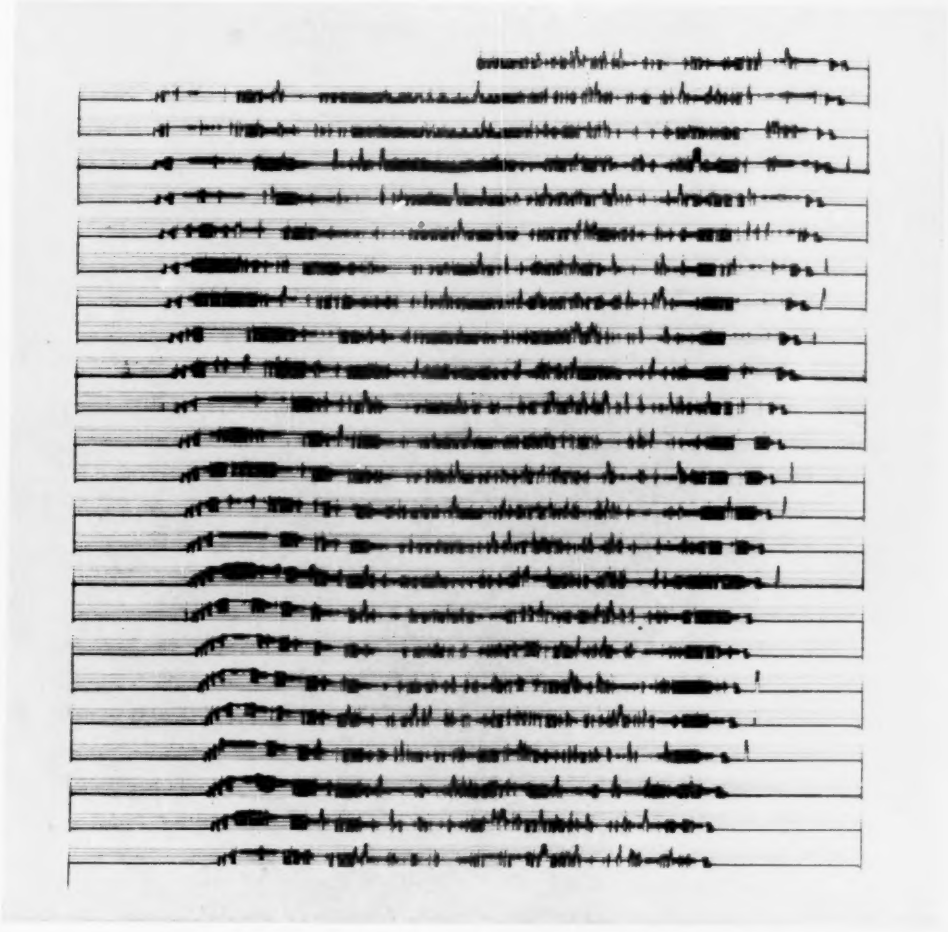

FIG. 3.—Zodiacal-light map No. 110 recorded on November 16, 1953, from 4:22 A.M. to 4:43 A.M. M.S.T. East is left, west is right, north on top. The zodiacal light is seen above the eastern horizon. The pips on the traces are due to stars. The co-ordinates are Cartesian in the equatorial system, but the scale is stretched in favor of the declination by a factor of 6. The traces for the declinations of 0°, 12°, 24°, and 36° are enhanced.

ground correction and the correction for extinction, must be converted to an absolute scale by means of the star-intensity readings mentioned above. The stars are in the range of intensity from 4.9 to 5.9 mag. (visual) and of spectral type F0–K5.[10] The reflector is first directed upon the star and then, for the purpose of subtracting the background, upon its immediate surroundings. The molecular correction C and, if appropriate, the dust correction are applied to all star readings. The color response of the instrument as determined from the total of all the star data is used to normalize the readings to spectral type G0. Finally, the value for the effective area of the sky which is seen by the reflector (Sec.

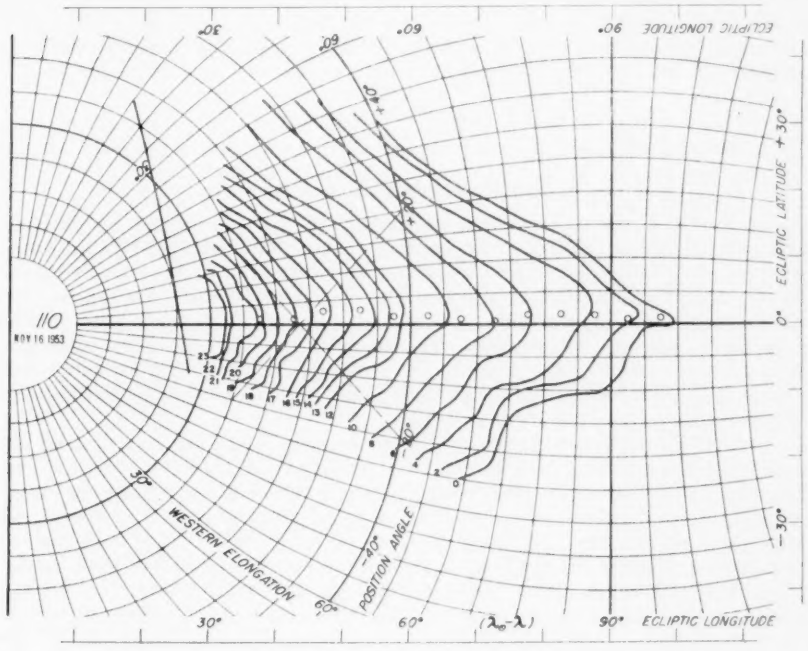

FIG. 4.—Zodiacal-light map in the ecliptic co-ordinate system as derived from map No. 110 shown in Fig. 3, corrected for background and extinction, but not yet corrected for zodiacal light in the background region and for inhomogeneity of the star background. The isophotes are numbered in arbitrary units, and their spacing is logarithmic (see text). The irregular course of isophotes Nos. 0, 2, and 4 is probably due to an anomaly of atmospheric extinction. The eastern horizon is entered as a solid line.

II) is used to convert the corrected zodiacal-light output values to read in terms of tenth-magnitude (photographic) G0 stars per square degree. This customary unit is henceforth called simply "stars."

The intensity of the zodiacal light in the background region is obtained from the composite chart published by Roach *et al.* (1954), which, in turn, is based on the photoelectric studies of Elvey and Roach (1937). It is found, however, that the intensities given in that chart must be multiplied by a factor of 0.8 if reasonable agreement between the present

[10] The star intensities are taken throughout from the *Henry Draper Catalogue*. Modern photometric data are not available for a sufficient number of stars of the prescribed characteristics. The fact that the molecular correction C is strictly valid only for a black body of 6000° does not introduce a significant error even for F0 or K5 stars.

work and that of Elvey and Roach is to be obtained at small elongations, where errors due to extraneous causes are likely to be small. This compares to a factor of 0.7, which Roach *et al.* (1954) applied to the data of Elvey and Roach for the same reason. The correction so obtained is applied as a function of elongation; it amounts to about a hundred stars, on the average.

The correction for the difference in the star background is obtained from a chart also given by Roach *et al.* (1954). Since the equipment usually resolves stars which are brighter than the seventh magnitude and since resolved stars are ignored when isophotes are drawn into the original map, the values of the Roach chart are multiplied by 0.75 before use, in addition to conversion from visual to photographic magnitude, as was done by Roach *et al.* This star-background correction usually amounts to as few as five stars or less. The combined correction for zodiacal light in the background region and for inhomogeneity of the star background is henceforth called the "final correction."

IV. RESULTS[11]

The following discussion refers, in general, only to elongations below 60°.

THE SYMMETRY WITH RESPECT TO THE ECLIPTIC

The symmetry of the zodiacal-light cone and its position in relation to the ecliptic may be judged from the 47 maps which are drawn without application of the final correction. Irregularities and asymmetries can be seen on most of these maps, but they are not persistent or peculiar enough to suggest that they originate with the zodiacal light proper. An inspection of the 38 maps taken in the evening, most of them between January 27 and May 26, 1954, shows the zodiacal light centered on the ecliptic in 32 cases and displaced to the north in 6 cases. On the 9 maps taken in the morning from September 14 to November 16, 1953, the zodiacal light appears centered in 5 cases, displaced to the south in 2 cases, and displaced to the north in 2 cases.

The map of Figure 4 shows a series of small circles near the ecliptic. Each of these circles represents, for the corresponding interval of 5° in elongation, the average position angle of all the isophotes which cross that interval or which enter and leave that interval without crossing it. This method of searching for asymmetries was applied to 9 maps taken during the period from September 17, 1953, to February 2, 1954. On 6 of these maps, the average position angle of the circles is less than 1°. Sometimes individual circles stray as much as 3° from the ecliptic, and pronounced deformations occur, such as those in Figure 4. These irregularities are, however, short-lived. They are not usually observed to persist through successive maps taken only $\frac{1}{2}$ hour apart during the same night.[12]

The high degree of symmetry with respect to the ecliptic and the small time variations of intensity which are observed here stand in contrast to earlier studies, including some of the photoelectric work (Elvey and Roach 1937; Behr and Siedentopf 1953; and Roach *et al.* 1954). It is probable that the asymmetries and the time variations of the zodiacal light which have been reported previously are essentially a result of anomalous space and time variations of atmospheric extinction and that the irregularities described in this paper are of the same origin.

TIME VARIATIONS

No systematic time variations in the intensity of the zodiacal light at an elongation of 60° on the ecliptic can be detected within any of the three periods from September 14,

[11] Details of a part of the results, including reproductions of the 47 maps (without application of the final correction) can be found in *Final Report*, Contract AF 19(604)-181, Air Force Cambridge Research Center, August 18, 1954.

[12] The cross in the map of Fig. 4 designates an area of the sky contained between elongation angles of 35° and 60° and between position angles of +20° and −20°. The total intensity of the zodiacal light coming from the northern half of this area was compared to that coming from the southern half. This analysis was carried out on a few maps; it also did not uncover systematic asymmetries of the zodiacal light.

1953, to January 31, 1954 (9 maps); from February 1 to February 4, 1954 (11 maps); and from February 21 to May 26, 1954 (14 maps), respectively. There are irregular fluctuations, but there is no trend. The root-mean-square fluctuations of the individual intensity readings amount to 11, 12, and 14 per cent within each of the three periods, respectively. Since the final correction for zodiacal light in the background region and for inhomogeneity of the star background is not applied to these maps, a part of the fluctuations may be due to this shortcoming. This is borne out by the special series of 10 maps (see Sec. III), in which the root-mean-square fluctuation of the individual 60° intensities amounts to 9 per cent before application of the final correction and to 5 per cent after its application. The fluctuations all appear random in character, and their magnitude does not seem to exceed a value which one might expect anyhow as a result of anomalies in extinction. No systematic variations in the general appearance of the isophotes can be detected.

ABSOLUTE INTENSITY

Only the last 14 maps, taken evenings between February 21 and May 26, 1954, can be reduced to an absolute-intensity scale. The star readings for the other maps are afflicted with an unknown factor due to an instrumental defect which at first was not detected. The special series of 10 selected maps (Sec. III) contains 3 maps which can be read in terms of absolute-intensity values. A measure of connection to this absolute-intensity scale is established for the other 7 maps through multiplication of the output readings by a factor which makes the average corrected reading at 60° elongation equal to the corresponding reading on the 3 absolute maps. The uncertainty introduced by this procedure is not considered substantial for the purpose of the discussions in this paper.

The selected maps furnish at 60° elongation an average value of 218 stars before final correction is applied and 326 stars after it is applied. The last value compares to 295 stars given by Roach *et al.* (1954) and to about 425 stars given by Elvey and Roach (Roach *et al.* 1954).

THE INTENSITY DISTRIBUTION ALONG THE ECLIPTIC

The fact that the zodiacal-light intensity as a function of elongation along the ecliptic can be quite naturally expressed by a power law was pointed out by Roach *et al.* (1954). These authors find $\epsilon^{-2.22}$ for this power law, where ϵ is the elongation. An analysis of the present series of 10 selected, fully corrected maps furnishes an exponent of -2.02, in fair agreement. This value is obtained by considering only elongations between 30° and 60°. Within this range, no systematic curvature can be detected on any of the 10 graphs showing intensity against elongation on logarithmic scales. Without application of the final correction, one obtains an exponent of -2.61.

THE INTENSITY DISTRIBUTION OFF THE ECLIPTIC

As discussed in Section III, 3 of the best maps are selected for the purpose of obtaining the intensity distribution off the ecliptic. These fully corrected maps furnish an average intensity of 320 stars on the ecliptic at 60° elongation and an average exponent of -2.12 for the intensity distribution along the ecliptic. The intensity distributions as a function of elongation along eight circles at the constant position angles $\pm 5°$, $\pm 10°$, $\pm 15°$, and $\pm 20°$ are also found to follow a power law quite naturally; the negative exponent increases somewhat in magnitude with increasing position angle. Within the considered region of elongation from 30° to 60° and of position angle from $-20°$ to $+20°$, the intensity distribution can be well represented by the empirical formula

$$I = I_0 \left(\frac{\epsilon}{\epsilon_0}\right)^{-(\gamma + \mu \sin^{4/3}\alpha)} .$$

The angle α is the position angle, the elongation angle ϵ_0 is equal to the sun's apparent radius of 0.°25, the intensity I_0 is equal to 3.51×10^7 stars per square degree, and the

numerical constants γ and μ have the values 2.12 and 0.43, respectively. Isophotes furnished by this function are shown in Figure 5. Some of the experimental values upon which the expression is based are entered for comparison.

CONCLUSION

Fluctuations in the shape and intensity of the zodiacal-light cone within a period of a few months appear absent at elongations up to 60°; the cone is highly symmetric and well centered upon the ecliptic. It appears appropriate to give an empirical analytic expression for the extra-terrestrial intensity of the zodiacal light between 30° and 60° elongation and at position angles up to 20°.

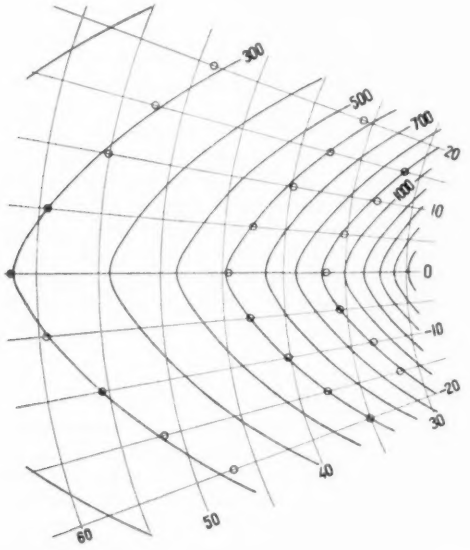

FIG. 5.—Zodiacal-light isophotes computed with the empirical analytic expression given in the text. For comparison, the locations of the intensity values 300, 600, and 900 stars per square degree are entered, as obtained, on the average, from the three fully corrected maps upon which the formula for the isophotes is based.

The intensity distribution along the ecliptic and the high degree of symmetry of the zodiacal-light cone are not in satisfactory agreement with the experimental results obtained by Behr and Siedentopf (1953). Since no polarization measurements have been made with the described equipment up to the present time, the results have no direct bearing upon the spatial distribution of electrons and dust which were derived by Behr and Siedentopf (1953) and by Elsässer (1954). The intensity function along the ecliptic as well as the absolute intensity obtained in the present paper is in good agreement with the recent work of Roach *et al.* (1954) in connection with a possible relationship between the zodiacal light and the *F*-component of the solar corona.

The author expresses his appreciation to Mr. Alan Peterson, who performed the majority of the observations and, aided by Messrs. McLane Downing, Freeman Hall, and George Kistler, many of the evaluations; to Drs. Richard Runge and Roy Thomas, who

gave valuable advice; to Messrs. Hyman Adler, James Kenney, and John McLean, who collaborated with the installation of equipment, with observations and evaluations.

This work has been supported in its initial phase by Research Corporation; since 1952 it has been made possible through support and sponsorship extended by the Geophysics Research Directorate of Air Force Cambridge Research Center under Contract No. AF 19(604)-181.

REFERENCES

Behr, A., and Siedentopf, H. 1953, *Zs. f. Ap.*, **32**, 19.
Elsässer, W. 1954, *Zs. f. Ap.*, **33**, 274.
Elvey, C. T., and Roach, F. E. 1937, *Ap. J.*, **85**, 213.
Huruhata, M. 1951, *Pub. Astr. Soc. Japan*, **2**, 156.
Link, M.F. 1934, *J. d. Obs.*, **17**, 41.
Paetzold, H.K. 1953, *A.N.*, **281**, 17.
Roach, F. E., Pettit, Helen B., Hanssen, E. Tandberg, and Davis, Dorothy N. 1954, *Ap. J.*, **119**, 253.
Tube Handbook (Harrison, N.J.: Radio Corporation of America).
Wempe, J. 1947, *A.N.*, **275**, 1.

THE HEIGHT OF THE NIGHTGLOW BY THE VAN RHIJN METHOD

F. E. ROACH*
U.S. Naval Ordnance Test Station

AND

A. B. MEINEL
Yerkes Observatory†

Received September 9, 1954; revised July 19, 1955

ABSTRACT

The several factors involved in the estimation of the location of the nightglow in the earth's upper atmosphere are discussed. These include the extinction and scattering in the lower atmosphere, the correction for the finite field of view of the photometer, and the allowance for contamination of the observations by integrated starlight and zodiacal light. The difficulty inherent in the inclusion of more than one upper-atmosphere emission by a single filter is discussed. Application is made to the evaluation of the heights of the emissions [*O* I] 5577, [*O* I] 6300, and *Na* I 5893 based on averages of photometric observations for three complete nights at Cactus Peak, California. It is found that a significant upper-atmosphere component is included by a control filter at 5300 A. Within the probable uncertainty of the extinction coefficients, upper and lower limits of the deduced heights are: 5300 (78, 43 km); 5577 (104, 62 km); 5893 (129, 108 km); 6300 (143, 116 km). The probable inclusion in the observations of a significant amount of *OH* means that the actual heights of the atomic emissions may be slightly greater than these mean heights for the composite emission.

I. INTRODUCTION

The knowledge of the height to the regions in the earth's upper atmosphere responsible for the nightglow is in a highly unsatisfactory state. Any attempt to tabulate the heights from the literature is frustrating—reports may vary between 100 and 1000 km for a single emission (Barbier 1952*a*). Since the physical conditions change by many orders of magnitude over this range of height, a theoretical inquiry into the origin of the nightglow is difficult, and the theorist may well be excused if he altogether ignores the conflicting observational results.

That the nightglow exhibits localized features has been demonstrated (Roach and Pettit 1951; Roach, Williams, and Pettit 1953*b*). However, the estimate of heights by triangulation, using methods similar to those employed in the case of the polar aurora, is difficult because of the low light-level of the nightglow, making the photography of discrete features impracticable. There has been some slight success in triangulation on nightglow patches with photoelectric photometers (Roach, Williams, and Pettit 1953*a*), but the results cannot be considered very reliable, and in one attempt the triangulation was thwarted by the dissimilar aspect of the patchy region of the nightglow as observed from the two stations (Roach, Williams, St. Amand, Pettit, and Weldon 1954). Recently a modified triangulation has been reported, in which correlations were made of *time variations* of intensity as observed from two stations (St. Amand, Pettit, Roach, and Williams 1955).

Most of the published estimates of height have utilized the fact that the nightglow systematically increases in intensity from the zenith to the horizon. If the layer responsible for the emission is at a constant height and is of uniform thickness and uniform intrinsic brightness, then the apparent increase in intensity toward the horizon is a

* Now at the Central Radio Propagation Laboratory, National Bureau of Standards, Boulder, Colorado.

† The present collaboration was the result of a visit to the Naval Ordnance Test Station by A. B. Meinel from Yerkes Observatory, University of Chicago.

function of the height, as was first shown by van Rhijn (1924). Complications arise in an actual analysis because of the extinction and scattering in the earth's lower atmosphere. A further difficulty encountered in applying the van Rhijn method is the lack of uniformity of the emission over the sky, indicating that the fundamental assumption of a uniform layer is probably violated. Thus the method is certainly not valid for *individual* sweeps from the zenith to the horizon.

We have a dilemma: The nightglow irregularities invalidate a straightforward estimate of height by the van Rhijn method and, at the same time, are not sufficiently well defined to permit triangulation. There remains the hope that the use of observations over a long interval of time may, on the average, smooth out the local patchiness of the nightglow and permit an estimate of height.

In this report we discuss, in detail, data for three nights obtained with a four-color photoelectric photometer (Roach and Pettit 1951) at Cactus Peak, California. The sky was completely surveyed by the photometer about twenty times per night in a series of eight vertical circles equally spaced in azimuth. In a single survey any particular altitude is crossed at sixteen different azimuths. Twenty surveys correspond to 320 readings at

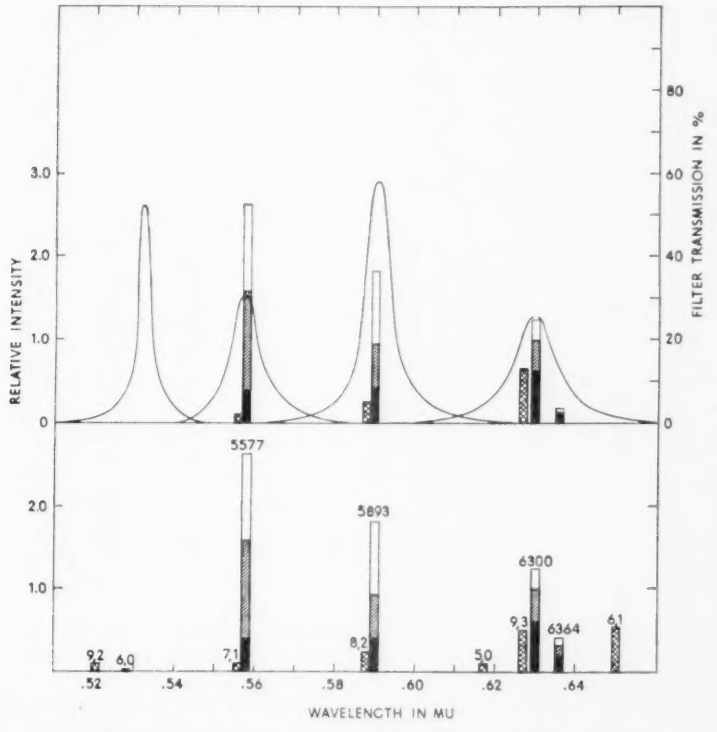

FIG. 1.—Transmission-curves of the four interference filters used in the present study (*upper plot*). In the lower plot the relative intensities of the known upper-atmosphere emissions between 5100 and 6600 A are indicated. Minimum, mean, and maximum intensities of the atomic emissions are indicated by solid, hatched, and open portions of corresponding rectangles. The position and approximate intensities of the *OH* bands (v', v'') are shown as crosshatched rectangles. In the upper plot the relative intensities are as transmitted by the filters.

each altitude, which are averaged in the present treatment. The basic strength of our procedure lies in the fact that local and sporadic irregularities are largely smoothed out in these means.

II. THE OBSERVATIONS

Four different spectral regions are isolated by interference filters, the transmission-curves of which are shown in Figure 1. We have indicated the known or predicted night-glow emissions in the region 5100–6600 A. Three prominent atomic emissions [*O* I] 5577, [*O* I] 6300 (and 6364), and *Na* I 5893 are centered near the peak transmissions of three of the filters. Several weak rotation-vibration bands of *OH* are also included by the filters.

TABLE 1

OBSERVATIONAL RESULTS

Date	z	Galvanometer Readings				Intensity (No. of 10th-Mag. G0 Vis Stars/Deg²)			
		5300	5577	5893	6300	5300	5577	5893	6300
Nov. 19–20, 1952	0	23.6	53.8	38.8	27.7	389	1137	958	643
	40	25.0	63.8	45.5	31.4	412	1347	1124	728
	50	25.7	70.6	50.0	34.2	424	1491	1235	793
	60	27.4	81.5	57.3	38.4	452	1722	1415	891
	70	29.7	98.5	66.9	44.5	490	2081	1652	1032
	75	31.1	107.8	72.6	48.0	513	2278	1793	1114
	80	31.0	115.6	76.5	50.5	512	2443	1890	1172
	85	28.8	105.3	70.4	47.9	475	2225	1739	1111
Dec. 14–15, 1952	0	20.8	21.9	29.2	26.3	343	464	721	610
	40	21.8	24.6	33.8	29.6	360	522	835	687
	50	22.4	26.5	36.2	31.8	370	562	894	738
	60	23.8	30.0	41.2	36.2	393	636	1018	840
	70	25.7	34.6	48.6	42.3	424	734	1200	981
	75	26.8	38.1	53.5	45.8	442	808	1321	1063
	80	27.3	40.5	56.6	49.0	450	859	1398	1137
	85	24.8	37.8	51.3	45.9	409	801	1267	1065
Jan. 14–15, 1953	0	18.3	24.2	29.3	24.5	302	513	727	568
	40	18.8	27.5	33.2	27.3	310	583	823	633
	50	19.4	30.1	36.4	29.6	319	638	903	687
	60	20.4	34.1	41.2	33.4	337	723	1022	775
	70	22.0	40.3	48.6	39.0	364	854	1205	905
	75	22.9	43.6	52.7	42.2	378	924	1307	979
	80	23.1	45.2	55.1	44.2	381	958	1366	1025
	85	21.0	40.7	50.2	40.9	347	863	1245	949

In Figure 1 we have indicated the approximate relative intensities by the heights of the rectangles corresponding to the different emissions. The relative intensities of the atomic emissions are based upon unpublished data obtained at Cactus Peak for the calendar year 1953. The *OH* intensities are based on the observational results of Meinel (1950) for the 8–2, 9–3, 6–1, and 5–0 bands. Meinel expressed his results relative to the intensity of [*O* I] 6300. The 9–2, 7–1, and 6–0 bands were not observed by Meinel, and their intensities have been estimated from the theoretical intensities given by Heaps and Herzberg (1952).

Figure 1 illustrates the fundamental difficulty inherent in the isolation of individual emissions by means of wide-based interference filters. All three atomic emissions have

OH bands so near that their segregation is possible only with much greater spectral resolution than we have used in the present investigation. The estimation of the degree of contamination by *OH* in any given observation is impossible, but it is apparent that it is significant in all cases, especially when the intensity of the atomic emission is exceptionally weak. The principal contaminants are the 7–1 band (near 5577), the 8–2 band (near 5893), and the 9–3 band (near 6300). Both theory and observation agree that the intensities of the *OH* bands increase in the order 7–1, 8–2, and 9–3, so that the contamination will increase in the order 5577, 5893, and 6300.

As will be seen later, there is a further serious contamination of the observations by integrated starlight and zodiacal light. Thus it is noted in the beginning that the analysis of photometric data for emission heights must necessarily proceed in a series of approximations in which the contaminations are successively reduced and eliminated.

In Table 1 we give the mean intensities for various zenith distances for the four colors and for the dates November 19–20, 1952; December 14–15, 1952; January 14–15, 1953. In Table 2 the same data are shown as intensities relative to the zenith intensity, I_z/I_0.

TABLE 2

I_z/I_0

Date	z	5300		5577		5893		6300	
		Original	Corrected	Original	Corrected	Original	Corrected	Original	Corrected
Nov. 19–20, 1952	0	1.000	1.000	1.000	1.000	1.000	1.000	1.000	1.000
	40	1.059	1.059	1.185	1.184	1.173	1.172	1.134	1.133
	50	1.089	1.089	1.312	1.310	1.289	1.287	1.235	1.233
	60	1.161	1.161	1.514	1.512	1.477	1.475	1.386	1.384
	70	1.258	1.258	1.830	1.830	1.724	1.724	1.606	1.606
	75	1.318	1.320	2.004	2.008	1.871	1.873	1.733	1.734
	80	1.313	1.316	2.148	2.160	1.971	1.978	1.823	1.828
	85	1.220	1.225	1.956	1.980	1.814	1.829	1.729	1.740
Dec. 14–15, 1952	0	1.000	1.000	1.000	1.000	1.000	1.000	1.000	1.000
	40	1.048	1.048	1.123	1.122	1.157	1.156	1.125	1.124
	50	1.077	1.077	1.210	1.208	1.239	1.237	1.209	1.207
	60	1.144	1.144	1.370	1.368	1.411	1.409	1.376	1.374
	70	1.235	1.235	1.580	1.580	1.664	1.664	1.608	1.608
	75	1.288	1.289	1.740	1.742	1.832	1.835	1.741	1.744
	80	1.312	1.315	1.849	1.856	1.938	1.946	1.863	1.871
	85	1.192	1.197	1.726	1.739	1.756	1.771	1.745	1.760
Jan. 14–15, 1953	0	1.000	1.000	1.000	1.000	1.000	1.000	1.000	1.000
	40	1.027	1.027	1.136	1.135	1.133	1.132	1.114	1.113
	50	1.057	1.057	1.244	1.242	1.242	1.242	1.208	1.206
	60	1.115	1.115	1.409	1.407	1.406	1.404	1.363	1.361
	70	1.205	1.205	1.665	1.665	1.658	1.658	1.592	1.592
	75	1.251	1.252	1.802	1.805	1.798	1.801	1.722	1.724
	80	1.262	1.266	1.868	1.876	1.880	1.888	1.804	1.811
	85	1.150	1.154	1.682	1.697	1.713	1.728	1.669	1.681
Mean	0	1.000	1.000	1.000	1.000	1.000	1.000	1.000	1.000
	40	.....	1.045	.....	1.147	.....	1.154	.....	1.123
	50	.....	1.074	.....	1.287	.....	1.255	.....	1.215
	60	.....	1.140	.....	1.429	.....	1.429	.....	1.373
	70	.....	1.233	.....	1.692	.....	1.682	.....	1.602
	75	.....	1.287	.....	1.852	.....	1.836	.....	1.734
	80	.....	1.299	.....	1.964	.....	1.937	.....	1.837
	85	.....	1.192	.....	1.805	.....	1.776	.....	1.727

The columns labeled "I_z/I_0 (Corrected)" include a correction for the finite field of view of the photometer, which will be discussed in a later section.

III. THE FUNCTION V

The basis of a height analysis by the van Rhijn method is the function

$$V = \frac{1}{\sqrt{\{1 - [R/(R+h)]^2 \sin^2 z\}}},$$

which represents the relative path length of a line through an emitting layer in the upper atmosphere at zenith distance z. Here R is the radius of the earth at the observer and h is the height of the emitting layer above the observer (see Fig. 2). In order for V to

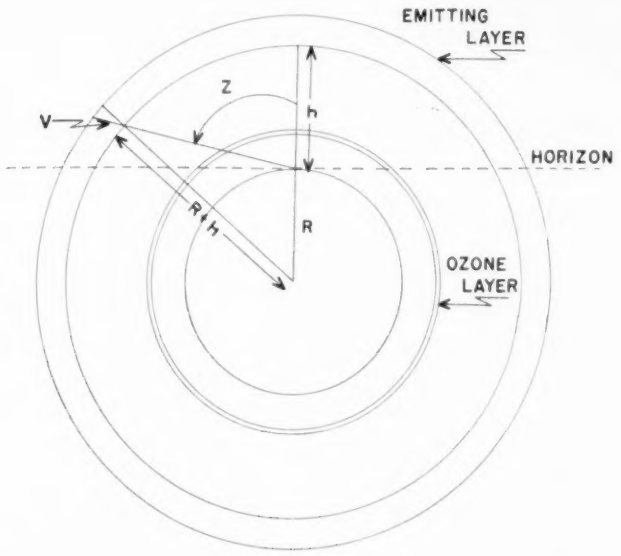

FIG. 2.—Schematic sketch of layers in the earth's upper atmosphere, illustrating apparent increase in thickness of an emitting layer with increasing zenith distance.

represent the relative *intensity* of an emission originating in such a layer, it is necessary that (*a*) there be negligible self-absorption in the layer and (*b*) the layer be at a constant height and of uniform intrinsic brightness and thickness. The fact that the second condition is probably not met forces us to resort to the use of average intensities, including a large number of individual readings. In Table 3 we give computed values of V for a number of zenith distances and for heights varying from 30 to 1000 km.

In Section II we suggest that there might be two or more upper-atmospheric components included by a single filter. It is thus of interest to examine the resultant V for various combinations of emitting layers. In general, two independent layers produce a resultant value of V corresponding to an apparent layer located between the two actual layers. The reader can easily verify that the height of the effective single layer corresponds only approximately to the weighted mean of the two layers. Examples of combinations illustrating this fact are shown in Table 4.

IV. THE EXTINCTION

In Section III we tabulated the function V, which is proportional to the intensity of the nightglow under specified conditions. Observations made at the bottom of the lower atmosphere are affected by attenuation and by scattering. The attenuation or extinction in the 5000–6500 A region has three known components: (*a*) weakening by molecular (Rayleigh) scattering in the lower atmosphere, (*b*) absorption by the Chappius band of ozone in the ozonosphere, and (*c*) absorption at discrete wave lengths by water vapor in the lower atmosphere.

In the next section we shall discuss the general problems of scattered light as applied to the nightglow. Here we are specifically concerned with the weakening of a pencil of light from a particular direction due to the molecular scattering. In order to evaluate

TABLE 3

THE FUNCTION V

z	h									
	30	50	100	150	200	250	300	350	400	1000
0	1.000	1.000	1.000	1.000	1.000	1.000	1.000	1.000	1.000	1.000
5	1.003	1.004	1.004	1.004	1.004	1.004	1.003	1.003	1.003	1.003
10	1.015	1.015	1.015	1.015	1.014	1.014	1.014	1.014	1.014	1.011
15	1.035	1.035	1.034	1.034	1.033	1.033	1.032	1.032	1.031	1.026
20	1.064	1.063	1.062	1.061	1.060	1.059	1.058	1.057	1.056	1.047
25	1.102	1.102	1.100	1.098	1.096	1.095	1.093	1.090	1.090	1.074
30	1.153	1.152	1.149	1.146	1.143	1.141	1.138	1.136	1.133	1.109
35	1.218	1.216	1.212	1.207	1.203	1.199	1.195	1.192	1.188	1.152
40	1.301	1.298	1.292	1.285	1.279	1.273	1.267	1.261	1.256	1.203
45	1.405	1.403	1.393	1.383	1.374	1.365	1.356	1.348	1.340	1.263
50	1.546	1.539	1.523	1.508	1.493	1.480	1.467	1.454	1.443	1.334
55	1.727	1.717	1.692	1.668	1.646	1.625	1.606	1.587	1.570	1.416
60	1.972	1.955	1.914	1.876	1.841	1.809	1.779	1.751	1.725	1.508
65	2.317	2.286	2.215	2.152	2.095	2.004	1.997	1.954	1.915	1.609
70	2.826	2.766	2.635	2.523	2.426	2.341	2.267	2.200	2.141	1.714
75	3.634	3.503	3.234	3.023	2.852	2.710	2.590	2.487	2.398	1.816
80	5.049	4.701	4.085	3.669	3.365	3.130	2.943	2.789	2.660	1.905
85	7.692	6.594	5.128	4.355	3.861	3.511	3.247	3.039	2.870	1.966
90	10.336	8.027	5.709	4.688	4.084	3.672	3.372	3.040	2.953	1.988

TABLE 4

EFFECTIVE HEIGHT OF TWO INDEPENDENT LAYERS

LAYER I		LAYER II		h	
h	Per Cent	h	Per Cent	Expected	Observed
100	10	300	90	280	270
	25	.....	75	250	230
	50	.....	50	200	175
100	10	200	90	190	185
	25	.....	75	175	170
	50	.....	50	150	140

this quantity, we have used the data of Table 4 in van de Hulst's treatment of atmospheric scattering (van de Hulst and Kuiper 1952).

To allow for the effect of the Chappius band of ozone on the extinction, we use the experimental results of Vigroux (1948). In Figure 3 is plotted his extinction coefficient[1] versus wave length, from which we show in Table 5 the values for the four wave lengths used by us. The ozone content at night at mid-latitudes is not well known, but it is stated by Mitra (1952) that "the average ozone content at night is greater (or at least never less) than during the day." A mean value of 0.25 cm of ozone will be assumed throughout the present study.

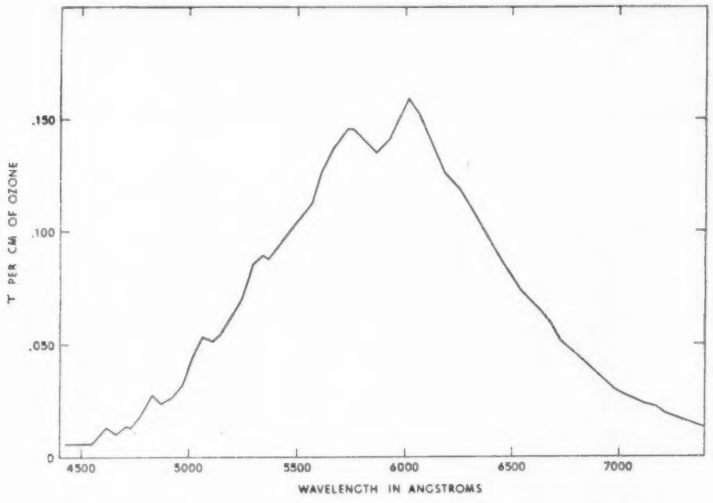

FIG. 3.—Extinction coefficient of the Chappuis band of ozone according to Vigroux (1948)

TABLE 5

EXTINCTION COEFFICIENT FOR OZONE (VIGROUX 1928)

λ	τ		λ	τ	
	For 1 Cm of Ozone	For 0.25 Cm of Ozone		For 1 Cm of Ozone	For 0.25 Cm of Ozone
5300	0.0826	0.0206	5893	0.1375	0.0344
5577	0.1142	0.0286	6300	0.1115	0.0279

In Table 6 and Figure 4 the sum of the extinction coefficient due to the ozone absorption in the Chappius band and molecular scattering are compared with the observed values at Mount Wilson (Pettit 1940). The residual is probably due to the cumulative

[1] Throughout this paper we use the extinction coefficient, τ, referred to the base e and unit air mass. Thus $I/I_0 = e^{-\tau m}$, where I is the intensity of a beam reduced from its original intensity, I_0, by passage through m air masses (one air mass corresponds to the atmosphere in the zenith at sea-level). Vigroux used a coefficient, A, given by $I/I_0 = 10^{-Am}$. Obviously, $\tau = 2.303\ A$.

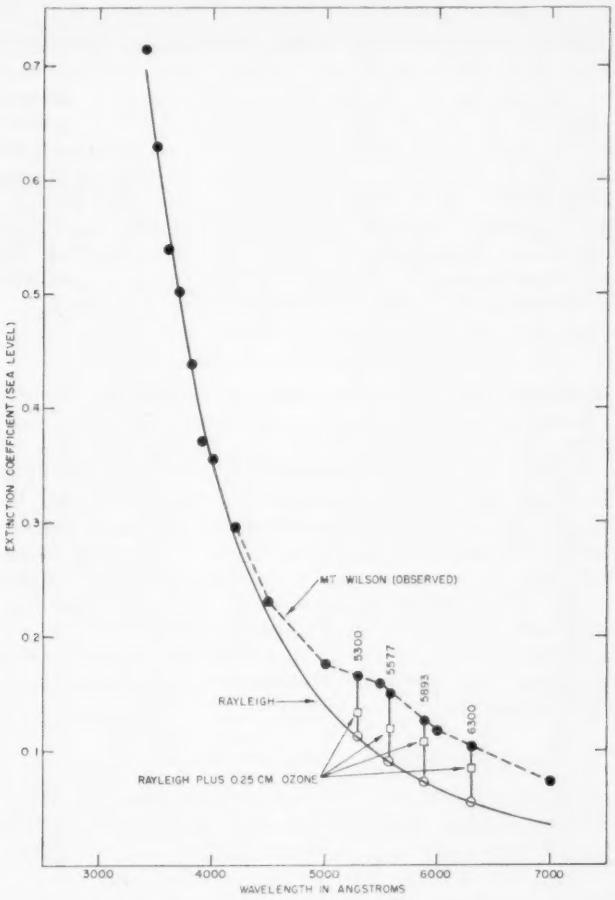

FIG. 4.—Extinction coefficients for pure air and as observed at Mount Wilson (*closed circles connected by dashed line*). The squares represent intermediate values corresponding to pure air plus 0.25 cm of ozone.

TABLE 6

EXTINCTION COEFFICIENTS
(Referred to Sea-Level)

τ	λ			
	5300	5577	5893	6300
Molecular (Rayleigh)	0.112	0.090	0.073	0.055
Ozone (0.25 cm)	.021	.029	.034	.028
Sum	.133	.119	.107	.083
Observed (Mt. W.)	.164	.150	.125	.103
Difference	0.031	0.031	0.018	0.020

absorption in wide-band photometry of such features as the numerous water-vapor bands which are actually individual monochromatic lines and a small amount of non-Rayleigh scattering particles. In photometry involving emission features the wave lengths of the emission and of individual water-vapor lines will, in general, not agree. We assume (*a*) that the values of the extinction coefficients resulting from adding the molecular and ozone (0.25 cm) components represent a *lower limit* and (*b*) that the values observed at Mount Wilson in wide-band photometry are an *upper limit*. In Section IX we actually use three values of the coefficient in parallel calculations, including, in addition to cases *a* and *b*, values corresponding to pure molecular scattering. This is done in order to obtain a plot of deduced height versus assumed extinction coefficient (Fig. 12), even though the minimum acceptable coefficient corresponds to case *a*.

V. THE SCATTERED LIGHT

The classical treatment of the scattering of light by particles of molecular dimensions is due to Rayleigh (1924). A rigorous application of the Rayleigh theory to a point source outside the earth's atmosphere (idealized as a plane-parallel atmosphere) has recently been given by Chandrasekhar (1950).[2] Integrations of Chandrasekhar's equations for discrete scattering coefficients have been tabulated by Sekera (1954) and by Sekera and Ashburn (1954). Ashburn (1953) has given tables showing the integrated intensity of the light scattered by a hemisphere illuminated by (*a*) a uniform light-source at infinity and (*b*) an emitting layer at various heights in the upper atmosphere. Reference to Figure 2 indicates that the ozone layer will weaken the radiation either from infinity or from an upper-atmosphere layer *before* the lower-atmospheric scattering is effective. We have made a correction for this ozone extinction, with results as shown in Table 7. The additional scattering due to radiation reflected back into the atmosphere by the ground has been obtained by assuming a ground albedo[3] of 0.25.

VI. CORRECTION FOR THE FINITE FIELD OF VIEW

A photometer designed specifically for the study of the nightglow usually has a field of several square degrees. The optimum field is one for which the total flux from the night sky is approximately equal to that from a first-magnitude star. The astronomical background is equivalent to about 300 tenth-magnitude visual G0 stars per square degree or to one first-magnitude star in 13 square degrees of sky. In our photometers we have included 19.6 square degrees, corresponding to a field diameter of 5°. Such a large field necessarily controls the resolution and affects the accuracy of a height determination.

The effect of the finite field on the resolution can be determined in a simple and unambiguous manner when the correction is small. To determine the effective aperture, we average the intensity over the circular field of view (see Fig. 5). Changes in intensity corresponding to linear and all odd-power terms cancel, leaving only even-power terms, of which the r^2 term is predominant. This is equivalent to saying that the curvature of intensity across the field of the photometer is adequately represented by a parabola.

[2] An excellent approximate treatment of the scattering of light in the earth's atmosphere has been given by Barbier (1944). For small τ, Barbier's analysis yields numerical values for the scattered light in close agreement with those obtained by the rigorous application of Chandrasekhar's equations (Barbier 1949; see also Barbier 1952; Mayot 1952).

[3] Appreciably higher values for the albedo should be taken if the ground is snow-covered. The albedo of the desert floor of the type surrounding our station in the absence of snow is given as 0.25 (see *Smithsonian Meteorological Tables* [6th rev. ed., 1951], Table 154, pp. 442, 443).

Simple evaluation then yields

$$\overline{r^2} = \frac{\int_0^R r^2 \, dA}{\int_0^R dA} \quad \text{or} \quad \bar{r} = \frac{R}{2}$$

for a circular field of view.

The correction, Δ, to I_z/I_0 is found by taking an interval $z - R/2$ to $z + R/2$ and finding the dip of the observed curve between these limits (see Fig. 6). The field correc-

TABLE 7

SCATTERED LIGHT*

Emission	h	z							
		0	40	50	60	70	75	80	85
5300	50	0.100	0.138	0.168	0.219	0.312	0.396	0.540	0.837
	100	.095	.130	.156	.202	.286	.365	.497	.769
	150	.091	.124	.148	.192	.272	.347	.473	.729
	200	.089	.119	.144	.184	.263	.333	.456	.707
	250	.087	.118	.140	.180	.254	.325	.442	.683
	300	.087	.115	.136	.175	.241	.316	.431	.664
	350	.085	.112	.133	.171	.241	.308	.420	.649
	400	.084	.115	.132	.169	.239	.304	.415	.639
	1000	.076	.099	.115	.147	.204	.262	.356	.550
	∞	.053	.066	.079	.099	.136	.170	.225	.331
5577	50	.080	.110	.134	.174	.250	.323	.448	.716
	100	.076	.103	.124	.161	.231	.297	.411	.658
	150	.072	.099	.120	.155	.220	.282	.391	.621
	200	.071	.095	.115	.149	.212	.271	.375	.599
	250	.071	.095	.115	.147	.210	.269	.375	.597
	300	.070	.094	.112	.144	.204	.262	.364	.580
	350	.068	.091	.110	.140	.200	.256	.354	.565
	400	.068	.090	.108	.139	.195	.251	.348	.554
	1000	.063	.080	.097	.123	.170	.220	.303	.480
	∞	.042	.054	.063	.081	.111	.138	.183	.276
5893	50	.066	.090	.109	.142	.206	.266	.371	.610
	100	.062	.084	.101	.131	.189	.244	.341	.559
	150	.060	.081	.097	.125	.180	.232	.324	.533
	200	.057	.078	.093	.121	.173	.224	.312	.515
	250	.057	.075	.091	.117	.168	.217	.304	.497
	300	.055	.073	.088	.115	.164	.211	.296	.484
	350	.055	.072	.088	.113	.161	.207	.289	.474
	400	.054	.072	.085	.110	.156	.201	.282	.462
	1000	.050	.064	.076	.097	.135	.173	.245	.398
	∞	.035	.044	.052	.066	.090	.113	.150	.231
6300	50	.053	.072	.087	.113	.167	.217	.307	.521
	100	.048	.067	.081	.104	.152	.198	.280	.473
	150	.047	.064	.077	.098	.144	.187	.264	.446
	200	.045	.061	.073	.094	.138	.178	.251	.428
	250	.045	.059	.072	.092	.133	.173	.244	.413
	300	.044	.058	.069	.090	.130	.167	.237	.401
	350	.043	.057	.068	.087	.127	.164	.232	.391
	400	.042	.055	.063	.086	.123	.161	.228	.385
	1000	.038	.049	.057	.073	.104	.136	.193	.324
	∞	0.026	0.034	0.040	0.050	0.070	0.089	0.122	0.195

* Unit = Zenith intensity outside the atmosphere (0.25 cm of ozone; albedo of ground = 0.25, for Cactus Peak; elevation = 5415 feet).

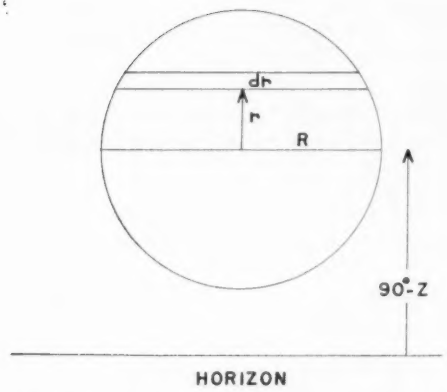

FIG. 5.—Field of view of photometer (schematic)

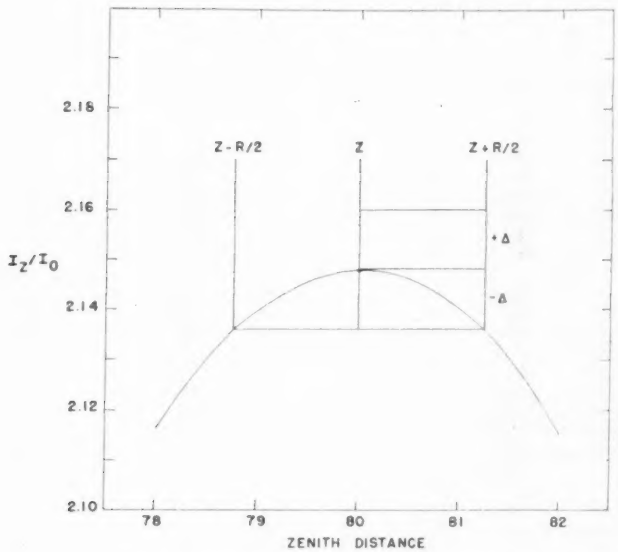

FIG. 6.—Correction, Δ, for finite field of the photometer

tion at z is *minus* the measured dip. The empirical values of Δ to apply to the original observations of Table 2 for a field of 5° diameter are shown plotted in Figure 7. These corrections have been applied to the observations in the columns headed "Corrected" in Table 2.

VII. PRELIMINARY COMPARISON OF THEORY AND OBSERVATIONS

In previous sections we have considered separately the individual elements in the analysis of the height of the nightglow. We now wish to bring the elements together. In

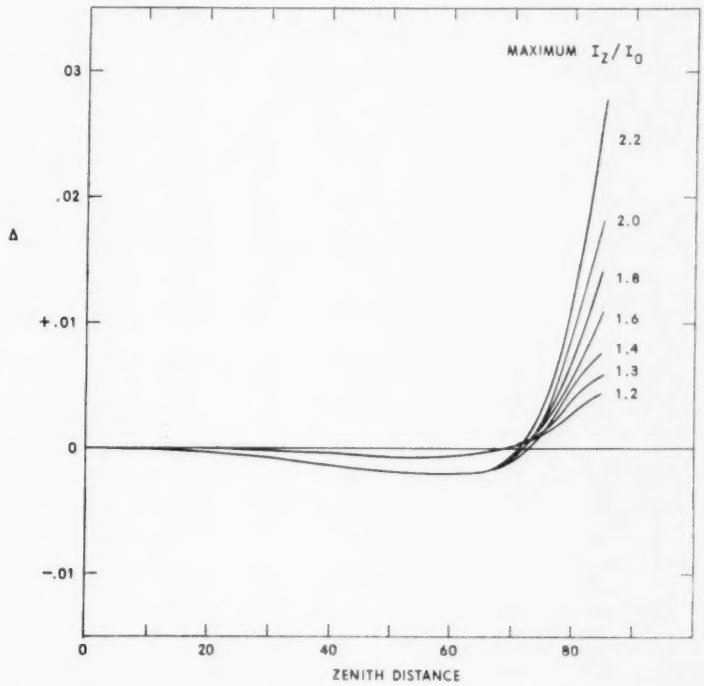

FIG. 7.—Correction, Δ, versus zenith distance for a family of curves with different values of maximum I_z/I_0. Results are based upon the empirical observations of Tables 1 and 2.

general, there are two approaches to the problem: (*a*) construct a family of theoretical curves corresponding to observations from the earth's surface, or (*b*) refer the observations to outside the scattering atmosphere for comparison with the universal curves of V against z. The two techniques are similar, in that in each case the same physical parameters enter into the analysis and the ultimate test involves a comparison of observations and theory. We show in Table 8 theoretical values of I_z/I_0 at the earth's surface (Cactus Peak) corresponding to wave lengths 5300, 5577, 5893, and 6300 for an extinction coefficient corresponding to the sum of molecular scattering and 0.25 cm of ozone. Similar tables (not reproduced here) have been prepared for assumed extinctions due to molecular scattering alone and to the observed Mount Wilson values of extinction.

In Figure 8 theoretical values of I_z/I_0 against z from Table 8 are plotted for the four wave lengths of this study. The mean corrected observed values of I_z/I_0 from Table 2 are indicated. Even a casual inspection of Figure 8 shows clearly that *the observations do not correspond to any single height of emission.* In the next two sections we show that this discrepancy is due chiefly to the contamination of the observations by radiation of astronomical origin.

TABLE 8

PREDICTED I_z/I_0 FOR CACTUS PEAK*

(Elevation = 5415 Feet)

λ	h	z							
		0	40	50	60	70	75	80	85
5300	50	1.000	1.269	1.472	1.798	2.338	2.716	3.106	2.963
	100	1.000	1.261	1.455	1.757	2.228	2.519	2.741	2.434
	150	1.000	1.254	1.439	1.723	2.140	2.370	2.499	2.153
	200	1.000	1.246	1.426	1.690	2.063	2.246	2.319	1.974
	250	1.000	1.243	1.414	1.663	1.995	2.148	2.180	1.839
	300	1.000	1.235	1.398	1.633	1.927	2.058	2.065	1.734
	350	1.000	1.229	1.387	1.610	1.881	1.985	1.972	1.655
	400	1.000	1.228	1.377	1.588	1.837	1.923	1.898	1.590
	1000	1.000	1.175	1.276	1.399	1.495	1.502	1.431	1.214
	∞	1.000	0.983	0.973	0.952	0.912	0.874	0.809	0.686
5577	50	1.000	1.270	1.476	1.807	2.364	2.773	3.213	3.141
	100	1.000	1.263	1.457	1.766	2.244	2.569	2.825	2.555
	150	1.000	1.257	1.446	1.736	2.165	2.416	2.570	2.243
	200	1.000	1.249	1.429	1.702	2.085	2.287	2.377	2.040
	250	1.000	1.244	1.418	1.673	2.017	2.185	2.237	1.908
	300	1.000	1.238	1.405	1.646	1.956	2.094	2.118	1.794
	350	1.000	1.233	1.393	1.622	1.905	2.020	2.020	1.706
	400	1.000	1.227	1.382	1.598	1.853	1.953	1.937	1.632
	1000	1.000	1.175	1.281	1.407	1.506	1.517	1.450	1.228
	∞	1.000	0.985	0.972	0.953	0.911	0.812	0.803	0.672
5893	50	1.000	1.269	1.478	1.813	2.392	2.822	3.309	3.310
	100	1.000	1.262	1.462	1.774	2.282	2.615	2.906	2.671
	150	1.000	1.256	1.446	1.739	2.188	2.452	2.633	2.333
	200	1.000	1.251	1.433	1.710	2.111	2.326	2.438	2.118
	250	1.000	1.243	1.420	1.678	2.038	2.214	2.282	1.956
	300	1.000	1.238	1.408	1.654	1.978	2.124	2.160	1.837
	350	1.000	1.231	1.396	1.638	1.922	2.045	2.056	1.742
	400	1.000	1.228	1.385	1.603	1.871	1.975	1.970	1.661
	1000	1.000	1.175	1.283	1.408	1.515	1.523	1.461	1.226
	∞	1.000	0.983	0.972	0.951	0.910	0.871	0.801	0.664
6300	50	1.000	1.278	1.491	1.844	2.470	2.959	3.568	3.814
	100	1.000	1.273	1.479	1.807	2.357	2.744	3.130	3.051
	150	1.000	1.265	1.462	1.770	2.258	2.570	2.828	2.639
	200	1.000	1.259	1.447	1.737	2.176	2.431	2.608	2.378
	250	1.000	1.251	1.434	1.707	2.100	2.313	2.436	2.186
	300	1.000	1.245	1.420	1.680	2.036	2.215	2.301	2.044
	350	1.000	1.240	1.409	1.654	1.978	2.133	2.190	1.930
	400	1.000	1.235	1.395	1.631	1.927	2.061	2.097	1.690
	1000	1.000	1.184	1.294	1.429	1.555	1.582	1.539	1.328
	∞	1.000	0.990	0.979	0.961	0.928	0.897	0.840	0.716

* Extinction = Molecular plus 0.25 cm ozone.

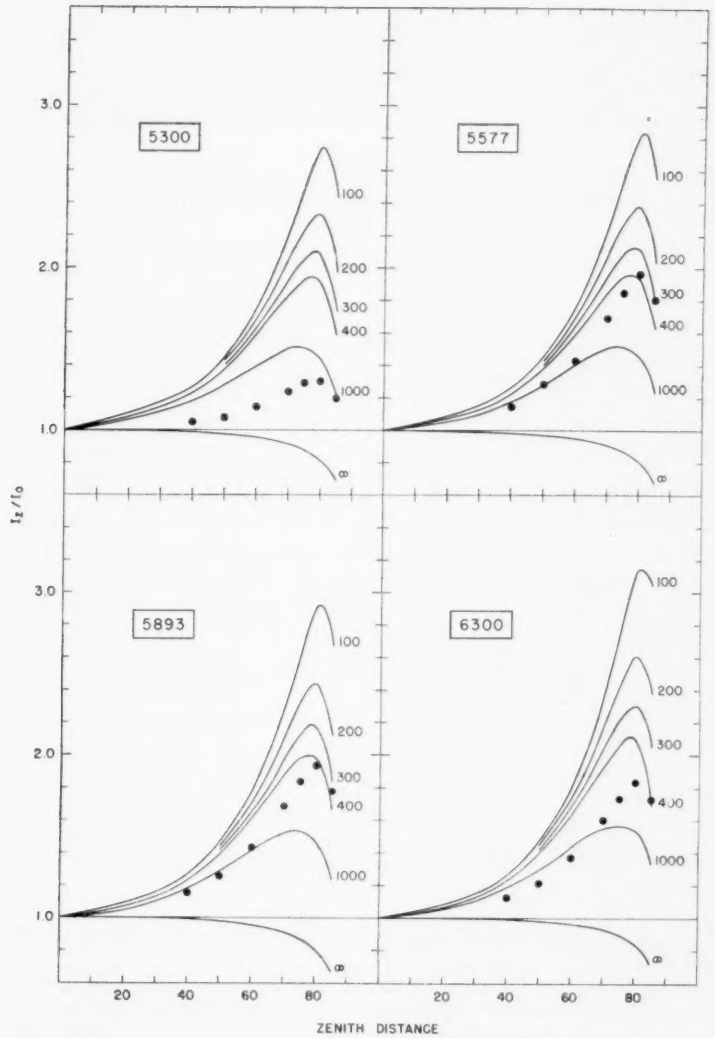

FIG. 8.—Theoretical curves I_z/I_0 against z for various values of emission height. Calculations (Table 10) were made for Cactus Peak (elevation 5415 feet). Values of extinction coefficient assumed correspond to the theoretical molecular (Rayleigh) value plus 0.25 cm of ozone. The closed circles represent the mean corrected observations from Table 2. The effect of the infinity light component is still present.

VIII. THE EXTRA-TERRESTRIAL LIGHT

The evaluation of the contamination of the observations by light of extra-terrestrial origin is a difficult problem. The principal components are the integrated starlight, the galactic light, and the zodiacal light (Elvey and Roach 1937). The first two components are concentrated toward the galactic plane, while the zodiacal light is concentrated toward the plane of the ecliptic and the longitude of the sun. In an analysis for a particular time of a given night, it is necessary to estimate the extra-terrestrial components in

TABLE 9

DATA FOR HEIGHT DETERMINATION BY TWO-COLOR METHOD
(I_{em} minus I_{5300})

Date	z	Residual			I_z/I_0			I_z/I_0 (Adjusted)		
		5577	5893	6300	5577	5893	6300	5577	5893	6300
Nov. 19–20, 1952	0	748	569	254	1.000	1.000	1.000	1.000	1.000	1.000
	40	935	712	316	1.247	1.247	1.248	1.277	1.281	1.268
	50	1067	811	369	1.423	1.424	1.459	1.471	1.477	1.507
	60	1270	963	439	1.725	1.693	1.743	1.768	1.774	1.809
	70	1591	1162	542	2.121	2.039	2.147	2.239	2.166	2.256
	75	1765	1280	601	2.357	2.247	2.376	2.494	2.397	2.516
	80	1931	1378	660	2.577	2.416	2.606	2.745	2.593	2.786
	85	1750	1264	636	2.335	2.216	2.514	2.484	2.377	2.682
Dec. 14–15, 1952	0	121	378	267	1.000	1.000	1.000	1.000	1.000	1.000
	40	162	475	327	1.338	1.261	1.226	1.262	1.302	1.251
	50	192	524	368	1.590	1.392	1.383	1.453	1.460	1.423
	60	243	625	447	2.007	1.654	1.678	1.790	1.770	1.756
	70	310	776	557	2.570	2.059	2.087	2.218	2.230	2.220
	75	366	879	621	3.028	2.327	2.322	2.568	2.556	2.492
	80	409	948	687	3.380	2.510	2.574	2.840	2.770	2.775
	85	392	858	656	3.257	2.274	2.452	2.711	2.508	2.664
Jan. 14–15, 1953	0	211	425	266	1.000	1.000	1.000	1.000	1.000	1.000
	40	273	513	323	1.289	1.207	1.214	1.261	1.263	1.255
	50	319	584	368	1.511	1.374	1.383	1.459	1.466	1.450
	60	386	685	438	1.833	1.612	1.647	1.757	1.759	1.775
	70	490	841	541	2.326	1.979	2.034	2.207	2.210	2.240
	75	546	929	601	2.588	2.186	2.259	2.450	2.459	2.500
	80	577	985	644	2.739	2.318	2.421	2.577	2.632	2.695
	85	516	898	602	2.447	2.113	2.263	2.306	2.398	2.532

a point-by-point fashion, which involves conversion from alt-azimuth to galactic and ecliptic co-ordinates.

In order to correct for the extra-terrestrial light without recourse to such a laborious procedure, we have for several years used the procedure of subtracting the 5300 reading directly from the emission reading (5577, 5893, or 6300) and treating the residual as a pure emission corresponding to the radiation under analysis (see Roach and Barbier 1950). The method suffers from uncertainty as to the relative amounts of the upper-atmospheric background emission in the control and the emission filters and from differences of extinction for wave lengths even as close as 5577 and 5300. It is very powerful, however, as a technique for the point-by-point analysis of the sky without requiring a laborious and detailed correction for the extra-terrestrial components.

The results of a treatment of the present data by the above-mentioned "two-color method" are shown in Table 9 for the three nights of observation included in Table 1.

The residuals, after subtracting out the 5300 readings, are put in terms of I_z/I_0. Any error in the absolute calibration of either of the two photometers involved in the differencing will be reflected as a systematic error in the ratio I_z/I_0 of the residual. In the column headed "Adjusted" in Table 9 we have empirically adjusted the calibrations with respect to one another so as to give an optimum fit of the observational points *at all zenith distances* with the theoretical curve corresponding to the indicated height. The method of adjustment is similar to that employed in the one-color method to find the

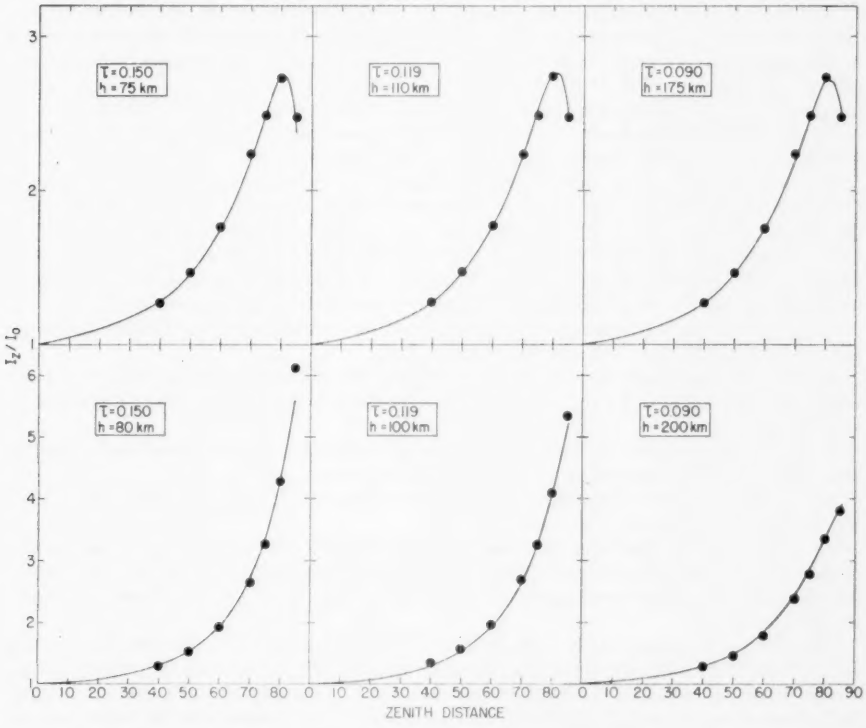

FIG. 9.—Observations (*closed circles*) for 5577 (Nov. 19–20, 1952) as a function of zenith distance after subtracting the astronomical contaminations by the two-color method (*above*) and the one-color method (*below*). The smooth lines represent theoretical solutions corresponding to the assumptions indicated in the boxes. In the upper drawings the theory refers to inside the atmosphere for comparison with the direct observations. In the lower drawings the observations have been referred to outside the atmosphere for comparison with the function V.

optimum value of the infinity contamination (see next section, especially Fig. 10) and will be discussed in detail later. In the upper curves of Figure 9 the observed values I_z/I_0 in which the background radiation has been removed by the two-color method are plotted against zenith distances, together with theoretical curves for heights indicated in the body of the figure. The discrepancy between theory and observation which was so obvious in Figure 8, where the background radiation was included in the observations, has now been removed. There can be little doubt that the extra-terrestrial light included

by our interference filters is the principal cause of disagreement between theory and observation in Figure 8.[4]

IX. DETAILED ANALYSIS OF THREE NIGHTS

In the previous section we gave a preliminary solution of the emission heights based on the use of the 5300 readings as a control. In the present section we wish to make a somewhat more general analysis, in which each color, including 5300, is treated independently.

The basis of our approach is the empirical fact that the values of I_z/I_0 as observed at the base of the atmosphere are essentially independent of height for values of z to about 40° or 50° and between heights of 50 and 300 km (the probable range of interest in the nightglow). Of equal importance is the fact that reasonable changes in the extinction and scattering coefficients also affect the numerical values of I_z/I_0 insignificantly for small zenith distances. On the other hand, the variation in I_z/I_0 with z for an infinity component departs markedly from that for the finite height components. These statements are illustrated by reference to Table 8 and Figure 8.

We now make the simplifying assumptions (*a*) that the observations include just two components, one at infinity and one at a finite height between 50 and 300 km, and (*b*) that the value of I_z/I_0 for some selected small value of z, say 40°, is the mean of the two components weighted according to their relative intensities. In this way approximate values of the fraction of the light from infinity, F_∞, and the fraction from the upper atmosphere, F_u, are obtained. The analysis now proceeds in the following steps:

a) Estimate the scattered light as a function of zenith distance from Table 7. Subtract the scattered light from the original observations.

b) Refer the residual obtained in *a* to outside the atmosphere, using the extinction coefficients of Table 6. In the first analysis presented here we use $\tau = \tau$ (Rayleigh) + τ (0.25 cm ozone).

c) Subtract the infinity light, F_∞, from the new data, which have been freed of scattered light and referred to outside the atmosphere.

d) Put the upper-atmosphere residual from *c* into units of I_z/I_0 for comparison with the theoretical values of V in Table 3.

e) The foregoing procedure necessarily depends critically on the initial observation of I_{40}/I_0. In order to give equal weight to all the other zenith distances, we make working plots of I_z/I_0 (observed) against I_z/I_0 (theoretical) for a family of heights from 50 to 400 km.

We show in Figure 10 such plots for three different values of F_∞ for the observations at 5577 on November 19–20, 1952. We note that for $F_\infty = 0.2$ and 0.5, which are included to show the effect of an erroneous choice of F_∞, the disagreement between theory and observation is severe, especially for the smaller zenith distances. In these two extreme cases the curves for 50 km are concave downward, and those for 200 km are concave upward. The curve for $h = 100$ km gives an approximately straight line.

The disagreement between theory and observation for the extreme assumptions of F_∞ (0.2 and 0.5) can be corrected by choosing an intermediate value for F_∞. In the example cited it is found that if $F_\infty = 0.343$, the values of I_z/I_0 for small values of z are now in agreement with theory, and the observed values of I_z/I_0 for $h = 100$ km are in good agreement with theoretical values of I_z/I_0 (or V) at all zenith distances. Our final choice in this example was 110 km. *We have found by repeated experimentation with curves similar to those of Figure 10 that there is always a value of the assumed height which yields a straight line in a plot of I_z/I_0 against V and that a choice of F_∞ can always be found*

[4] In an analysis of similar data, Abadie, A. Vassy, and E. Vassy (1944–1945) some time ago also noted that the direct observations cannot be interpreted as due to a single emission layer. Their interpretation assumed two emission layers in the upper atmosphere. In another paper (Paper II of this series) we rediscuss their observations in terms of a contamination by extra-terrestrial radiation.

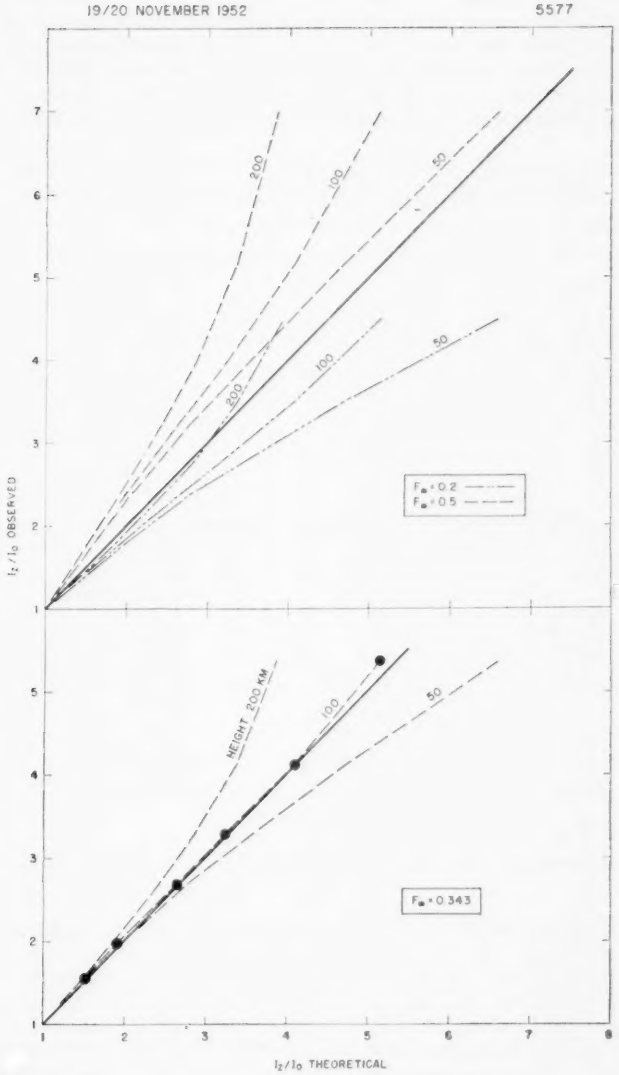

FIG. 10.—Effect of varying F_∞ on the correlation of the observed and theoretical values of I_z/I_0. Extinction coefficient (assumed) = 0.119. Observations referred to outside the atmosphere for comparison with function V.

for which this straight line has substantially a 45° slope. In the case of the two-color method (treated in Sec. VIII) the same procedure was followed to find the optimum fit between observation and theory, except that, in the second approximation, the variable parameter was the calibration of the control color with respect to the emission, rather than F_∞. We show in Figure 11 our final selections of the best solutions for 5577 for November 19–20, 1952. In the lower part of the figure the one-color method was used, and in the upper part the two-color method. A summary of the deduced heights for all cases is given in Table 10.

In order for the procedure outlined in this section to be successful, it is necessary that the observed average values of I_z/I_0 for the entire night under analysis shall correspond

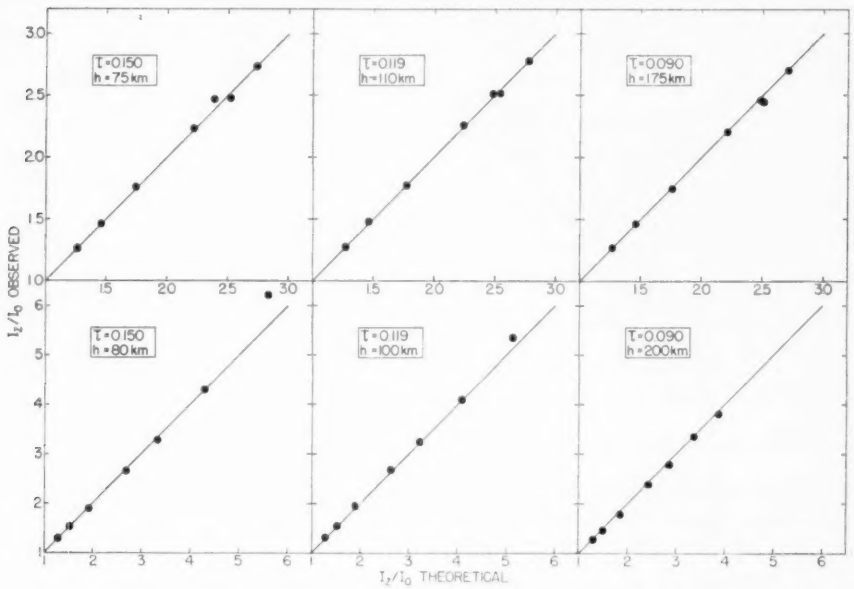

FIG. 11.—Observed versus theoretical values of I_z/I_0 for 5577 (Nov. 19–20, 1952). The same data as in Fig. 9.

to the case of a contamination, F_∞, which does not favor any zenith distances. This is certainly not true at any particular time of the night. For example, in the evening immediately after twilight and in the morning just before dawn the zodiacal light will make the intensity systematically greater near the horizon. The zodiacal light, on the average, contributes about twice as much to the contamination as the integrated starlight (see below). In November, December, and January (which include the three nights under analysis) the Milky Way is a conspicuous feature of the sky, which will give an additional asymmetry to the observations. However, the method used will reveal any systematic error in I_z/I_0 for any particular zenith distance, since an erroneous point will fall off the final 45° plots (such as those of Fig. 11). If the zenith itself is systematically affected with respect to the other observations, it is impossible to force the straight line through the origin. Thus the method includes inherent checks on the validity of the implicit assumption of uniformity of extra-terrestrial radiation over the entire sky for the averages used in the analysis.

A further test of the general correctness of our procedure is a comparison of the deduced *absolute* values of the infinity light for the different colors and the different nights, a summary of which is contained in Table 11. The mean is 320 tenth-magnitude visual G0 stars per square degree outside the atmosphere. Since the average brightness from integrated starlight is 104 tenth-magnitude visual stars per square degree (Roach and Pettit 1952), it follows that the average contribution from other nonterrestrial sources (chiefly zodiacal light) is about 216. The spread of the mean values among the three

TABLE 10

COMPILATION OF DEDUCED HEIGHTS

Emission	Extinction		Nov. 19–20, 1952		Dec. 14–15, 1952		Jan. 14–15, 1953		Mean		Comb.
	Type	Value	One-Color	Two-Color	One-Color	Two-Color	One-Color	Two-Color	One-Color	Two-Color	
5300	Mt. W.	0.164	70	...	30	.....	30	.....	43	.....	.....
	$R+O_3$	.133	100	...	60	.....	75	.....	78	.....	.....
	R	.112	150	.....	100	.....	100	.....	117	.....	.....
5577	Mt. W.	.150	80	75	30	70	50	100	53	82	68
	$R+O_3$	.119	100	110	75	90	100	150	92	117	104
	R	.090	200	175	125	150	200	200	175	175	175
5893	Mt. W.	.125	100	125	100	100	100	125	100	117	108
	$R+O_3$	.107	140	150	100	125	100	160	113	145	129
	R	.073	250	250	200	200	250	260	233	233	233
6300	Mt. W.	.103	100	110	90	125	120	150	103	128	116
	$R+O_3$	.083	150	150	100	150	150	160	133	153	143
	R	0.055	300	250	200	240	250	250	250	247	248

TABLE 11

ABSOLUTE INTENSITY OF LIGHT FROM ASTRONOMICAL SOURCES*

Date	5300	5577	5893	6300	Mean
Nov. 19–20, 1952	302	401	384	346	358
Dec. 14–15, 1952	278	256	349	349	308
Jan. 14–15, 1953	246	255	371	304	294
Mean	275	304	368	333	320

* In units of number of 10th-mag. (visual) G0 stars per square degree. Corrected to outside the atmosphere.

nights is ± 9 per cent. The spread among the four colors is ± 14 per cent, which in our judgment is a measure of the reliability of our absolute calibrations and of the method of analysis rather than an indication of a real difference in the amount of infinity light at the different wave lengths. The principal uncertainty in our absolute calibrations is the effective field of view of the sky included by the photometer. Even the use of a field lens to focus the objective on the cathode of the 1P21 photomultiplier has not given a completely uniform response over the field. In order to get a calibration approximately correct for the average of the field, we have resorted to the average stellar deflection for as many different parts of the field as possible.

The dependence of the deduced height on the numerical value of the extinction coefficient is serious. The importance of this point has recently been stressed by D. R. Bates and A. Dalgarno (1953), but limiting values were not given. To illustrate, we have determined the heights for all four colors by the methods described in the present paper for the following extinction coefficients: (*a*) Rayleigh (molecular) scattering alone, (*b*) molecular scattering plus 0.25 cm ozone, and (*c*) the Mount Wilson observed values. Case *a* is undoubtedly too small, *b* is a probable lower limit, and *c* is the probable upper limit.

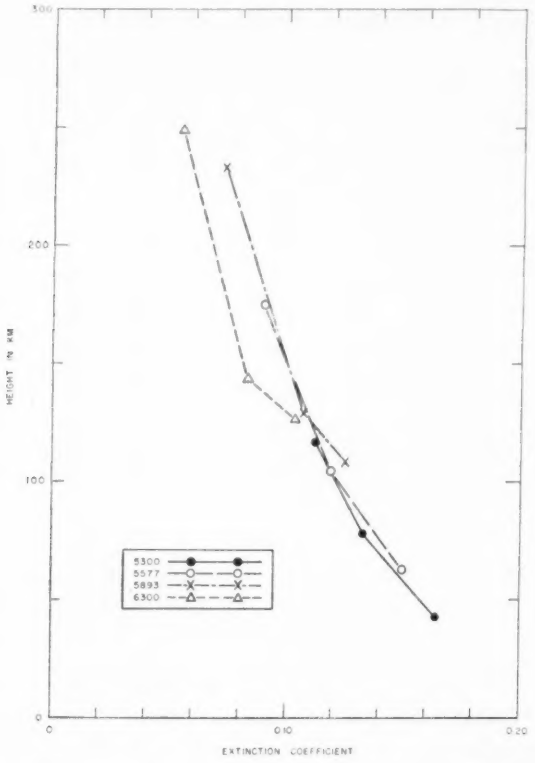

FIG. 12.—Deduced height versus assumed extinction coefficient. Results shown are the average of the one-color and two-color methods (see Table 10).

In Table 10 and Figure 12 the results are assembled for all the determinations. An uncertainty of assumed τ of 0.01 corresponds, on the average, to an uncertainty in the deduced height of about 25 km. If we assume that cases *b* and *c* represent the lower and upper limits of the extinction coefficient, the present results indicate that the heights are "boxed in" between the limits indicated in Table 12.

In a recent paper Ashburn (1953) has shown how the height depends on the assumed scattering coefficient. To illustrate this dependence, we have determined the height for 5577 for a single night, varying the assumed albedo of the ground (which is roughly equivalent to changing the scattering coefficient). The results are shown in Table 13 and

Figure 13. The deduced height is seen to double (75–150 km) when the assumed albedo varies from 0.00 to 1.00. We thus have the empirical fact that increasing the assumed scattering coefficient raises the height and increasing the assumed extinction coefficient lowers the height. Since the two coefficients are related, there is a tendency for the two errors partially to compensate.

X. ATMOSPHERIC CONTAMINATION

In the previous sections we have taken original observations at the earth's surface through filters which transmit a composite of upper-atmosphere and astronomical radiation and then, by a series of approximations, have separated the two components. The heights deduced for the atmospheric component are necessarily the effective values for

TABLE 12

DEPENDENCE OF HEIGHT ON LIMITING τ VALUES

λ	Height		λ	Height	
	Upper Limit	Lower Limit		Upper Limit	Lower Limit
5300	78	43	5893	129	108
5577	104	68	6300	143	116

TABLE 13

DEPENDENCE OF HEIGHT ON ASSUMED ALBEDO*

Assumed Albedo	Deduced Height	Assumed Albedo	Deduced Height	Assumed Albedo	Deduced Height
0.00	75	0.35	100	0.75	125
0.25	110	0.50	100	1.00	150

* 5577; Nov. 19–20, 1952; $\tau = 0.119$.

all the upper-atmosphere emissions transmitted by the filters. A general solution for the height of any single component is impossible. However, if it can be assumed that there is a principal emission through each filter with a single contaminant at a known height, then some idea of the height of the principal emission may be possible.

Referring back to Figure 1, we note the probable contamination of the three atomic emissions by *OH*. Shortly after the discovery of the *OH* bands in the nightglow, there was a generally satisfactory situation regarding their height, since the theoretical studies of Bates and Nicolet (1950), the photometric observations of Roach, Pettit, and Williams (1950), and the spectrographic studies of Meinel (1950) all agree with a height of about 70 km. More recently the situation has been clouded by newly reported heights of 150 km by Berthier (1954) and 300 km by Huruhata (1952). If *OH* is emitted in a region below 75 km, then it follows that the heights deduced for 5577, 5893, and 6300 in this investigation represent lower limits. By assuming the relative intensity of *OH* and the atomic emission in any individual case, it is possible to obtain numerical values for the height of the latter. Because of the multiplicity of possible solutions due to the uncertainty in the knowledge of the degree of *OH* contamination, it does not seem wise to pursue the matter further.

XI. CONCLUDING REMARKS

The deduction of a nightglow height by the van Rhijn method is a problem of great complexity. The basic need is a series of observations at several zenith distances over a sufficiently wide spread of conditions as to average out sporadic and local changes. If the data are for a single zenith distance, there is no control available for the estimation of the astronomical radiation included in the observations, and a multiplicity of solutions is possible. The elimination of scattered light and the correction to outside the atmosphere involve uncertainties in the appropriate coefficients. Finally, the inclusion by the filter of secondary upper-atmosphere emissions along with the primary emissions makes the problem soluble only in terms of an average height of both components. To separate

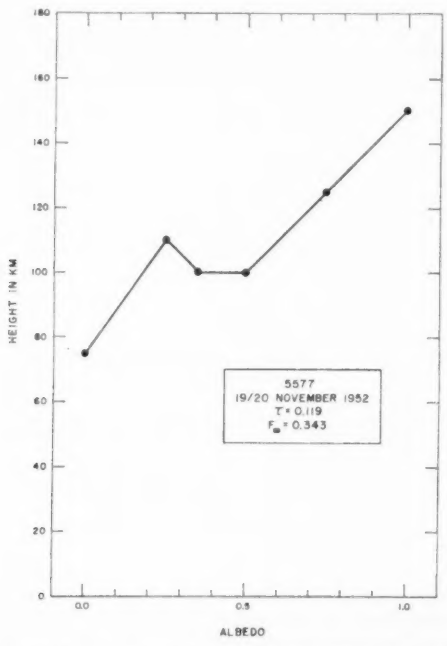

FIG. 13.—Deduced height versus assumed albedo of the ground (see Table 13)

the two and estimate independent heights for each obviously require additional observational information of one of the radiations exclusively.

With all these difficulties in the interpretation of photometric data it is little wonder that there is a wide divergence among the published heights. It is the recognition of the inherent uncertainty in the van Rhijn method that has dictated to us the necessity of recording here in a systematic fashion the several factors in the analysis.

The contamination of the readings by both the astronomical light and *OH* can be minimized in spectrographic studies with narrow slits. In a recent paper, Dufay and Tcheng Mao-Lin (1954) have reported on nightglow heights based on careful spectrographic studies. Their results are systematically higher than ours, which may be due to the contamination of our data by *OH* (see Sec. X). Even in spectroscopic studies there are inherent difficulties, notably the long exposures leading to a small number of indi-

vidual readings, the necessity of observing in only a few selected zenith distances and azimuths, and the difficulty involved in estimating the continuous background with respect to which the emission must be measured. An obvious improvement would be the use of a monochromator with photoelectric receivers, so mounted as to survey the sky in a manner similar to our photometric program. The equivalent would be the use of very narrow filters (of the order of 1 A in width) with photometric equipment.

The present paper represents conclusions reached as a result of several years of study of airglow observations at Cactus Peak, California. During this period many of our associates have contributed to our understanding of the problem both in active collaboration in published papers and in informal conversations. In particular, we wish to acknowledge our indebtedness to H. Pettit for her extensive calculations and also to E. V. Ashburn, D. R. Williams, and Pierre St. Amand.

REFERENCES

Abadie, P., Vassy, A., and Vassy, E. 1944–1945, *Ann. de géophys.*, **1**, 189.
———. 1948, *Gassiot Committee Report* (London: Physical Society).
———. 1949, *Ann. de géophys.*, **5**, 157.
Ashburn, E. V. 1953, "The Effect of Atmospheric Scattering and Ground Reflection upon the Determination of the Height of the Night Airglow," *J. Atm. and Terr. Phys.*, **5**, 83.
Barbier, Daniel. 1944, *Ann. de géophys.*, **1**, 144.
———. 1949, *ibid.*, **5**, 83.
———. 1952*a*, *Ann. d'ap.*, **15**, 247.
———. 1952*b*, *Mém. Soc. r. sci. de Liège*, **12**, 43. A complete bibliography of heights by the van Rhijn method up to 1952 is contained in this reference.
Bates, D. R., and Dalgarno, A. 1953, *J. Atm. and Terr. Phys.*, **4**, 112.
Bates, David R., and Nicolet, Marcel. 1950, *C.R.*, **230**, 1943.
Berthier, Pierre. 1954, *C.R.*, **238**, 263.
Chandrasekhar, S. 1950, *Radiative Transfer* (Oxford: Clarendon Press).
Dufay, J., and Tcheng Mao-Lin. 1954, *Ann. de géophys.*, **10**, 1.
Elvey, C. T., and Roach, F. E. 1937, *Ap. J.*, **85**, 213.
Heaps, H. S., and Herzberg, G. 1952, *Zs. f. Phys.*, **113**, 48.
Hulst, H. C. van de. 1952, *The Atmospheres of the Earth and Planets*, ed. G. P. Kuiper (rev. ed.; Chicago: University of Chicago Press).
Huruhata, Masaaki. 1952, *Rep. Ionosphere Res., Japan*, **6**, 31.
Mayot, M. 1952, *Ann. d'ap.*, **15**, 374.
Meinel, A. B. 1950, *Ap. J.*, **112**, 120.
Mitra, S. K. 1952, *The Upper Atmosphere* (2d ed.; Calcutta: Asiatic Society), p. 152.
Pettit, E. 1940, *Ap. J.*, **91**, 159.
Rayleigh, Lord. 1924, *Proc. R. Soc. London, A*, **106**, 117.
Rhijn, P. J., van. 1924, *Bull. Astr. Inst. Netherlands*, **2**, 75.
Roach, F. E., and Barbier, Daniel. 1950, *Trans. A.G.U.*, **31**, 7.
Roach, F. E., and Pettit, Helen B. 1951, *J. Geophys. Res.*, **56**, 325.
———. 1952, *Mém. Soc. r. sci. de Liège*, **12**, 13.
Roach, F. E., Pettit, Helen B., and Williams, D. R. 1950, *J. Geophys. Res.*, **55**, 183.
Roach F. E., Williams, D. R., and Pettit, Helen B. 1953*a*, *Ap. J.*, **117**, 456.
———. 1953*b*, *J. Geophys. Res.*, **58**, 73.
Roach F. E., Williams, D. R., St. Amand, P., Pettit, Helen B., and Weldon, R. G. 1954, "Simultaneous Observations of Nightglow 5577 at Two Stations," *Ann. d'ap.*, **17**, 172.
St. Amand, P., Pettit, Helen B., Roach, F. E., and Williams, D. R. 1955, *J. Atm. and Terr. Phys.*, **6**, 189.
Sekera, F., and Ashburn, E. V. 1954, *Tables Relating to Rayleigh Scattering of Light in the Atmosphere* (NavOrd Report, No. 2061) (U.S. Naval Ordnance Test Station, Inyokern).
Vigroux, Ernest. 1928, *C.R.*, **227**, 272.

NIGHTGLOW HEIGHTS: A REINTERPRETATION OF OLD DATA

F. E. ROACH*
U.S. Naval Ordnance Test Station

AND

A. B. MEINEL†
Yerkes Observatory
Received September 9, 1954‡

ABSTRACT

Observations of the nightglow by Abadie, A. Vassy, and E. Vassy in the green (5577 A) and red (6300 A + *OH*) are interpreted as due to the sum of radiation from (*a*) starlight and zodiacal light and (*b*) nightglow. The solution is in contrast with that obtained by Abadie, Vassy, and Vassy, who suggest two atmospheric emitting layers, a brighter one at 1000 km and a fainter one below 100 km.

INTRODUCTION

In an earlier paper (Roach and Meinel 1955) (Paper I) we have summarized the basic problems involved in the estimation of the height to the nightglow. In this study we propose to reinterpret observations made some years ago by Abadie, A. Vassy, and E. Vassy (1948) at the Pic du Midi. The general observing procedure used by them was similar to our own, in that they expressed the final results as mean values of I_z/I_0 for a number of zenith distances, z, and for a large number of individual observations.

In Figure 1 we reproduce the spectral transmission-curve of the filter combination used by Abadie, Vassy, and Vassy (hereafter designated "AVV") for the isolation of the oxygen 5577 line, together with the transmission-curve of an interference filter used extensively by us at Cactus Peak. In Figure 2 we show the curve for the product of the AVV filter transmission and tube sensitivity for the isolation of the red oxygen line 6300 (plus the weaker 6364). At the time of their study (1945) the *OH* bands had not been discovered. An examination of Figure 2, however, shows that the *OH* bands must have been predominant in the AVV red observations. An estimate based on the relative intensities given by Meinel (1950) indicates that the nightglow component of their red observations included about 15 per cent 6300 (plus 6364) and 85 per cent *OH*. In our own observations, quoted in Paper I, we used an interference filter giving a more nearly complete isolation of 6300, and the contamination by *OH* even in this more favorable case is significant.

The observational results of AVV are shown in Table 1 for the two colors. In Figure 3 the values of I_z/I_0 are shown plotted against z, together with some of our own observational results from Paper I.

DISCUSSION

We note the following facts from an inspection of Figure 3: (*a*) the AVV observations and ours from Paper I are in close agreement for 5577, and (*b*) in the red the AVV observations indicate significantly higher values of I_z/I_0, especially as the horizon is approached. In the AVV interpretation of their own data they noted that no single theoretical curve fitted all the observations. They reasoned that the observations repre-

* Now at the Central Radio Propagation Laboratory, National Bureau of Standards, Boulder, Colorado.

† The present collaboration was the result of a visit to the Naval Ordnance Test Station by A. B. Meinel from the Yerkes Observatory.

‡ Delayed publication on account of late revision of preceding paper.

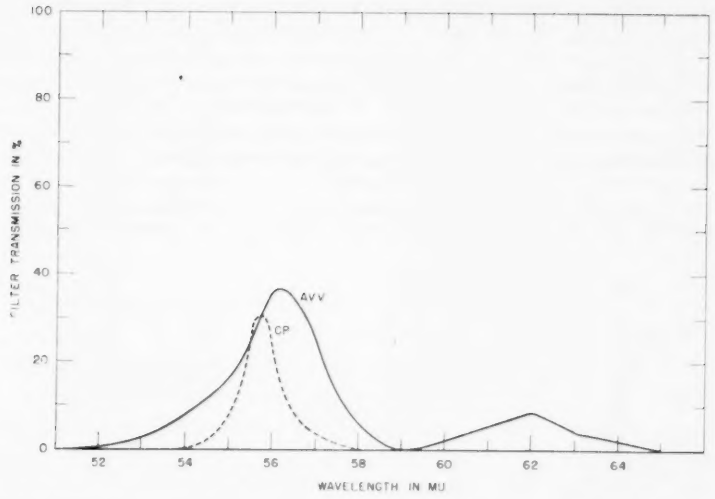

FIG. 1.— Transmission of the composite filter used by Abadie, Vassy, and Vassy (*solid line*) compared with that for an interference filter in use at Cactus Peak (*dashed line*) for isolation of nightglow 5577.

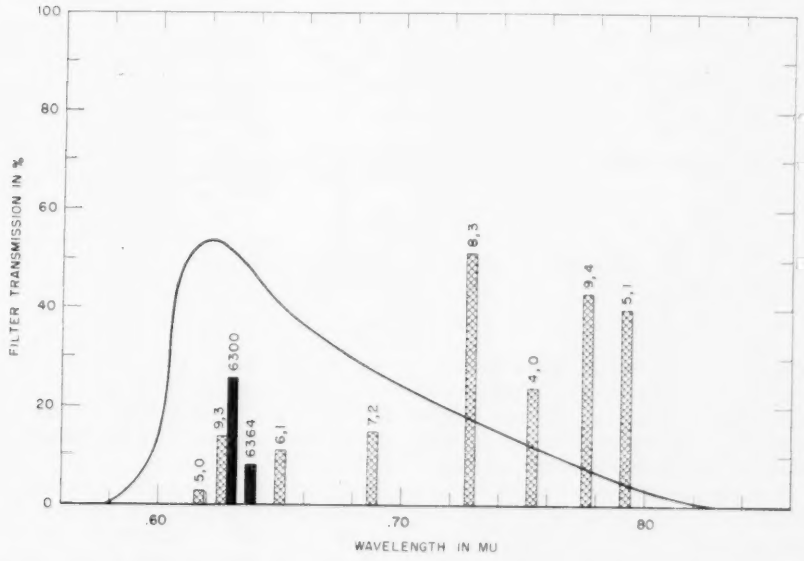

FIG. 2.—Product of filter transmission and cell sensitivity for unit used by Abadie, Vassy, and Vassy. The approximate relative intensities of [*O* I] 6300, [*O* I] 6364, and several *OH* bands as affected by the filter-cell combination are indicated by the heights of the rectangles.

sented pure upper-atmospheric emissions with no contamination from integrated starlight and zodiacal light. On this basis they found that the observations could be represented by assuming two emitting layers in the upper atmosphere, with the relative proportions of the light from each layer adjusted so as to give an optimum fit between theory and observation. In Table 2 is a summary of their solutions.

In Paper I we showed that theory and observation could be reconciled by assuming that a significant contribution of radiation from astronomical sources is transmitted by

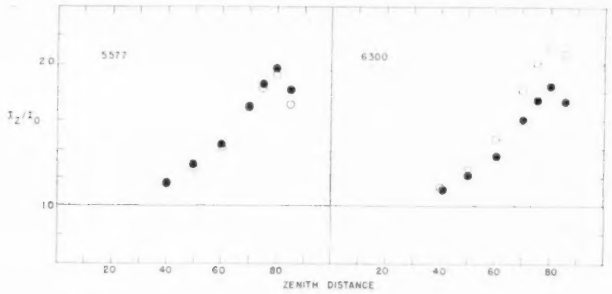

FIG. 3.—A comparison of the observational results of AVV (*open circles*) and some Cactus Peak data from Paper I (*closed circles*).

TABLE 1

OBSERVATIONS BY ABADIE, A. VASSY, AND E. VASSY

z	I_z/I_0		z	I_z/I_0	
	Red	Green		Red	Green
0°	1	1	75°	2.01	1.83
30	1.07	1.09	80	2.14	1.92
45	1.18	1.20	82°18′	2.17	1.83
60	1.48	1.41	85	2.08	1.71
65	1.64	1.55	87	1.83	.....
70	1.815	1.70			

TABLE 2

SUMMARY OF AVV SOLUTIONS

Color	Height	Rel. Int.
Red	1000	1.0
	65	0.6
Green	900–1000	1.0
	75	0.8

conventional interference filters centered on discrete emissions. The correctness of this point of view is borne out by the agreement of the absolute value for the deduced infinity light with the known intensities of integrated starlight and zodiacal light. Furthermore, the absolute intensities of the infinity light, determined independently for four different filters, are in reasonable agreement (see Table 11 of Paper I).

In Table 3 and Figure 4 we show the agreement between observation and theory for (*a*) the AVV green observations for a single atmospheric component at 130 km (60 per cent) and an infinity component (40 per cent); (*b*) the AVV red observations for an atmospheric component at a height of 150 km (65 per cent) and an infinity component (35 per cent); (*c*) the AVV green data based upon two atmospheric layers, one at 1000 km (73 per cent) and the other at 50 km (27 per cent); and (*d*) the AVV red data based on two atmospheric layers, one at 1000 km (70 per cent) and the other at 50 km (30 per cent).

So far as curve-fitting is concerned, it is apparent that our reinterpretation based on a single atmospheric layer plus astronomical contamination is superior to the AVV one based on two atmospheric layers. We feel, however, that the more conclusive argument is the fact that there is good observational evidence for the existence of the astronomical component, as brought out in Paper I.

The present paper illustrates how the excellent AVV observations can be interpreted in wholly different ways by basically different physical approaches. The AVV conclusion that there are two atmospheric emitting layers with the higher one predominant has been widely quoted in the literature, for which reason we have felt impelled to present our own analysis of two "layers," one at infinity and the other in the upper atmosphere.

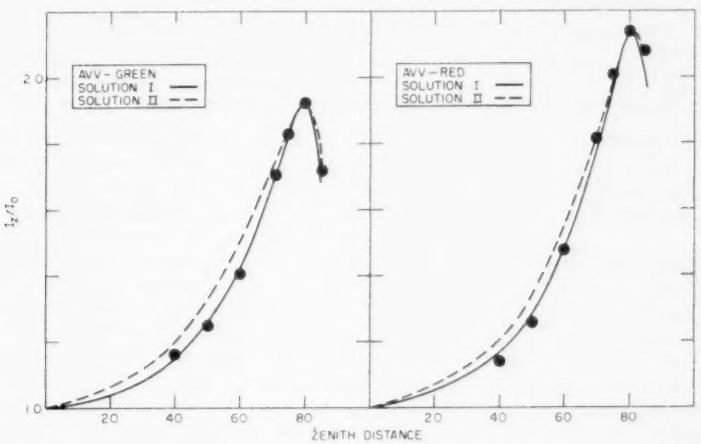

FIG. 4.—Correlation of observed and theoretical I_z/I_0 for the red and the green observations of AVV for physical assumptions indicated in the sketch. See Table 3.

TABLE 3

COMPARISON OF COMPUTED I_z/I_0 FOR SOLUTIONS I AND II

SOLUTION	I_z/I_0 (5577)			I_z/I_0 (6300)		
	Observed	I	II	Observed	I	II
h_1 (per cent)	.....	∞ (40)	1000 (73)	.....	∞ (35)	1000 (70)
h_2 (per cent)	.....	130 (60)	50 (27)	.....	150 (65)	50 (30)
Extinction	.....	0.139	0.139	.....	0.097	0.097
$z = 0$	1.00	1.00	1.00	1.00	1.00	1.00
40	1.16	1.15	1.20	1.14	1.17	1.21
50	1.25	1.26	1.33	1.26	1.29	1.35
60	1.41	1.43	1.51	1.48	1.49	1.55
70	1.70	1.68	1.73	1.815	1.79	1.83
75	1.83	1.84	1.85	2.01	1.98	1.99
80	1.92	1.92	1.92	2.14	2.13	2.14
85	1.71	1.69	1.74	2.08	1.97	2.07

A word of caution is necessary. In our solutions we used, for convenience, values of the extinction coefficient for which we had already prepared tables for Cactus Peak.[1] As brought out in Paper I, the deduced height is strongly dependent on the assumed extinction coefficient. In particular, a definitive determination of the height of *OH* (the AVV red observations) calls for a careful study of the effective extinction coefficient applicable over a wide spectral region, as shown by Roach, Pettit, and Williams (1950).

REFERENCES

Abadie, P., Vassy, A., and Vassy, E. 1944–1945, *Ann. de géophys.*, **1**, 189.
———. 1948, *Gassiot Committee Report* (London: Physical Society).
———. 1949, *Ann. de géophys.* **5**, 157.
Meinel, A. B. 1950, *Ap. J.*, **112**, 120.
Roach, F. E., and Meinel, A.B. 1954, "The Height of the Nightglow by the van Rhijn Method," *Ap. J.*, **122**, 530.
Roach, F. E., Pettit, Helen B., and Williams, D. R. 1950, *J. Geophys. Res.*, **55**, 183.

[1] Actually, in this paper we used tables computed for Cactus Peak for sea-level extinction coefficients of 0.119 for 5577 and 0.083 for 6300. Because of the greater elevation of Pic du Midi (2850 m compared with 1600 m), the corresponding sea-level coefficients in the present study are 0.139 and 0.097, respectively.

ABLATION FROM ALUMINUM ULTRASPEED PELLETS

WILLIAM C. WHITE
Michelson Laboratory, U.S. Naval Ordnance Test Station, Inyokern
China Lake, California
Received April 7, 1955; revised July 29, 1955

ABSTRACT

Velocities of droplets ablated from the surface of ultraspeed pellets have been obtained experimentally. The velocity data were analyzed to obtain the initial radii and masses of the droplets, which were 5–110 μ and 0.002–12.5 μgm, respectively. An average mass of the droplets was used to obtain the amount of material ablated in a given distance along the trajectory. The amount of mass ablated by melting was found to depend linearly on the distance the pellet had moved along its trajectory.

INTRODUCTION

There is ample spectrographic evidence (White, Rinehart, and Allen 1952) that vaporized material exists in the wake of ultraspeed pellets. Atomic lines of the metallic constituents of the pellets and the bands of the respective oxides have been observed. Evidence obtained from time-resolved spectroscopy (Allen and Mayfield 1953) indicates that some of the material is vaporized from the surface of the pellet.

In addition, a phenomenon (Rinehart, Allen, and White 1952) observed on continuously moving film photographs of ultraspeed pellets has been attributed to droplets of melted material ablated from the pellet surface. These photographs were originally used to measure the velocities (Allen, Rinehart, and White 1952) of the pellets and were obtained with a motion-picture camera in which the film was moved perpendicular to the direction of motion of the pellet. Figure 1 is a conventional photograph of an aluminum ultraspeed pellet. Figure 2 is a continuously moving film photograph in which the luminous front extending along the bottom of the picture is due to the products of explosion,[1] the luminous front extending at an angle from the bottom to the top is due to the pellet, and the short streaks extending to the left from the luminous front are due to droplets. The discussion that follows is concerned chiefly with the droplets and, consequently, ablation by melting.

PROCEDURE

Continuously moving film photographs of several pellets were analyzed to obtain positions of the droplets and their velocities directed along the trajectories of the pellets. Photographs from previous experiments (Allen, Rinehart, and White 1952) supplemented by those from additional experiments were used. The analysis was conducted with the same methods as those used in arriving at the velocities of the pellets (Allen, Rinehart, and White 1952). Figure 3 is a semilog plot of the pellet and droplet velocity against distance along the trajectory. As illustrated, the droplet-curve was extrapolated back to the pellet-curve. At the point of intersection the value of the distance along the pellet trajectory at which the droplet left the pellet is 2.65 meters, and the corresponding velocity is 4.18 km/sec. As a check, the original measurements on the photographs of the distances in the direction of motion of the pellet were plotted against those in the direction of motion of the film. Again, the droplet-curve was extrapolated back to the pellet-curve. At the point of intersection, the distance was 2.67 meters, which agrees with that obtained from the velocity versus distance plot. This procedure was followed in the analysis for each droplet.

[1] The pellet was fired by an explosive charge.

RESULTS AND DISCUSSION

The same empirical velocity-distance equation formulated for the case of pellets holds for the droplets and is represented by

$$v_d = v_{od}\, e^{-\alpha_d (s_d - s_{od})}, \tag{1}$$

where v_d is the velocity of the droplet, s_d is the distance along the pellet trajectory, v_{od} is the velocity at the distance s_{od} where the droplet leaves the surface of the pellet, and α_d is a constant and is determined from the slope of the droplet-curve such as that of Figure 3. The uncertainty in the values of α_d has been estimated to be less than 10 per

TABLE 1

THE MASSES AND RADII OF THE DROPLETS

s_{od} (Meters)	v_{od} (Km/Sec)	α_d (M^{-1})	r_{od} (μ)	m_{od} (μgm)	s_{od} (Meters)	v_{od} (Km/Sec)	α_d (M^{-1})	r_{od} (μ)	m_{od} (μgm)
0.00	3.69	4.5	35	0.4	1.92	3.11	2.6	60	2.2
0.00	3.69	2.9	55	1.3	2.11	3.41	12.3	13	0.02
0.00	3.69	1.8	88	6.8	2.13	3.79	9.5	17	0.05
0.73	3.48	10.4	15	0.03	2.13	4.29	13.9	11	0.02
0.96	3.39	1.5	107	13	2.31	3.64	2.3	68	3.1
1.17	4.26	4.3	37	0.5	2.40	2.99	3.2	50	1.2
1.38	3.98	8.5	19	0.06	2.50	3.15	6.7	24	0.1
1.43	4.32	25	6	0.002	2.54	4.19	17.5	9	0.01
1.51	3.92	9.4	17	0.05	2.65	4.18	10.2	15	0.04
1.52	3.92	3.3	47	1.1	3.02	3.20	7.9	20	0.08
1.55	3.69	8.5	18	0.06	3.04	2.81	6.0	26	0.2
1.62	3.90	2.2	72	3.7	3.04	4.11	3.4	46	1.0
1.63	3.89	19	8	0.01	3.38	3.52	29.4	5	0.002
1.88	3.82	7.6	21	0.09	3.85	2.63	13.9	11	0.02

cent. As a consequence of equation (1), the expression for the ratio of the initial presentation area to the initial mass developed for pellets (Allen, Rinehart, and White 1952) can be applied to droplets:

$$\frac{A_{od}}{m_{od}} = \frac{\alpha_d \pi}{4 \rho_a K_D}, \tag{2}$$

where A_{od} is the initial presentation area, m_{od} the initial mass, α_d the constant of equation (1), ρ_a the air density, and K_D the drag coefficient. Moreover, if it is assumed that the droplet is spherical, equation (2) becomes

$$r_{od} = \frac{3 \rho_a K_D}{\pi \alpha_d \rho_{Al}}, \tag{3}$$

where r_o is the initial droplet radius and ρ_{Al} is the density of melted aluminum.

The initial radii of the droplets were computed by using equation (3). The velocity data yield the necessary value of α_d; K_D was taken to be 0.33 (Allen, Rinehart, and White 1952); the air density as 0.0012 gm/cm^3; and the density of melted aluminum as 2.382 gm/cm^3. Table 1 lists the data according to s_o in meters, the corresponding v_{od} in km/sec, α_d in m^{-1}, the radius, r_{od}, of the droplet in microns, and the mass, in micrograms, of a sphere of melted aluminum whose radius is r_{od}. Velocities, radii, and masses were obtained for 28 droplets. Their computed radii vary from 5 to 110 μ and their masses from 0.002 to 12.5 μgm, respectively. The average radius was 32.8 μ, and the average mass was 1.28 μgm. Figure 4 is a plot of droplet radius versus velocity, v_{od}. There is no

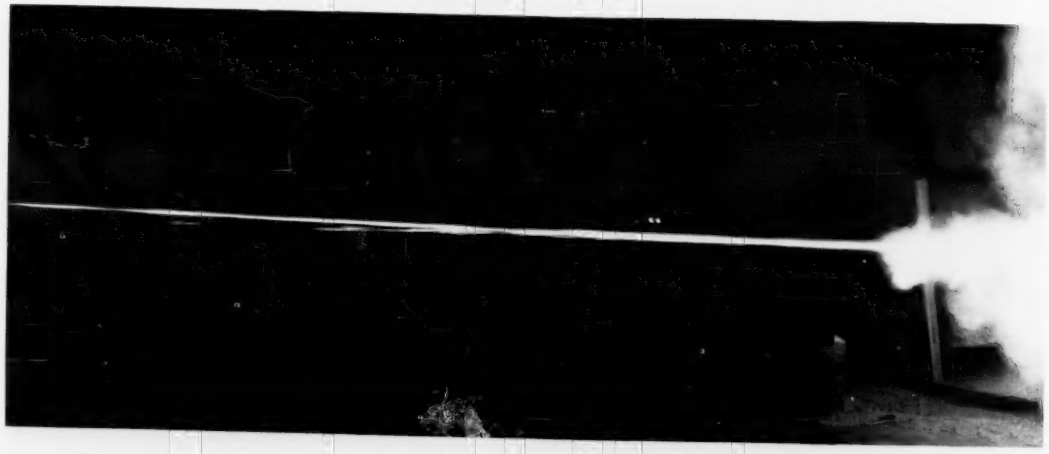

FIG. 1.—Conventional photograph of an aluminum ultraspeed pellet. The pellet moves from right to left

FIG. 2.—Continuously moving film photograph of an aluminum ultraspeed pellet. The pellet moves from bottom to top.

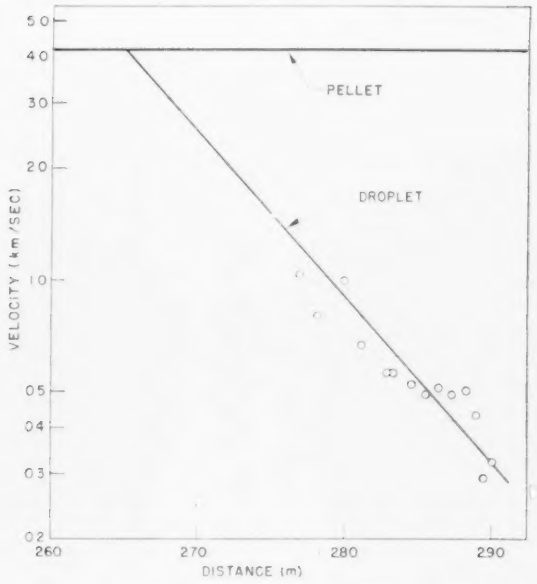

FIG. 3.—Velocity versus distance of an ultraspeed pellet and a droplet

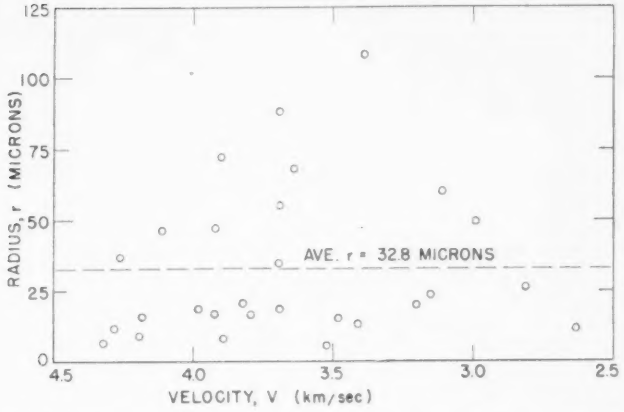

FIG. 4.—Droplet radii versus velocity at which the droplets left the pellet

TABLE 2

THE MASS ABLATED FROM A PELLET

Pellet No.	s (Meters)	N	M (μgm)	m' (μgm)	dm'/ds (μgm/Meter)
1	1.58	20	25.6	25.6	
	3.72	45	57.6	83.2	
	3.96	5	6.4	89.6	
	4.54	16	20.4	110.0	28.2
	4.73	16	20.4	130.4	
	5.36	8	10.2	140.6	
	6.02	7	9.0	149.6	
2	1.08	16	20.4	20.4	
	2.14	28	35.8	56.2	
	2.59	18	23.0	79.2	
	2.98	8	10.2	89.4	
	3.43	8	10.2	99.6	
	3.67	15	19.2	118.8	36.1
	3.75	10	12.8	131.6	
	4.20	7	9.0	140.6	
	4.70	6	7.7	148.3	
	4.99	6	7.7	156.0	
	5.28	3	3.8	159.8	
3	2.32	35	44.6	44.6	
	3.51	33	42.2	86.8	27.6
	4.78	25	32.0	118.8	
	5.25	8	10.2	129.0	
4	2.40	42	53.7	53.7	
	3.75	37	47.3	101.0	32.5
	4.96	28	35.8	136.8	
5	2.35	38	48.6	48.6	
	3.51	32	40.9	89.5	29.6
	4.49	18	23.0	112.5	
6	1.23	21	26.9	26.9	
	1.83	25	32.0	58.9	
	2.46	14	17.9	76.8	
	3.19	17	21.8	98.6	
	3.47	7	9.0	107.6	31.3
	3.95	16	20.4	128.0	
	4.65	12	15.4	143.4	
	4.99	9	11.6	155.0	
	5.29	11	14.1	169.1	
7	2.07	21	26.9	26.9	
	2.95	24	30.7	57.6	35.7
	3.38	22	28.1	85.7	
	4.64	30	38.4	114.1	
8	1.24	25	32.0	32.0	
	1.84	21	26.9	58.9	
	2.18	11	14.1	73.0	40.0
	2.61	11	14.1	87.1	
	2.92	9	11.6	98.7	
9	1.60	21	26.9	26.9	
	2.74	24	30.7	57.6	25.2
	3.60	15	19.2	76.8	
10	1.82	26	33.2	33.2	
	2.83	22	28.1	61.3	31.3
	3.35	16	20.4	81.7	

apparent correlation between droplet size and pellet velocity.

A recent publication (Smith 1954) reports the computed masses of meteor-flare fragments for three meteors. These masses were from 0.01 to 22.7 μgm. The agreement of the droplet masses with those for meteor fragments seems excellent but may be fortuitous, since meteors, at the height at which they appear, move in a highly rarefied atmosphere and have an entirely different composition in comparison with ultraspeed pellets.

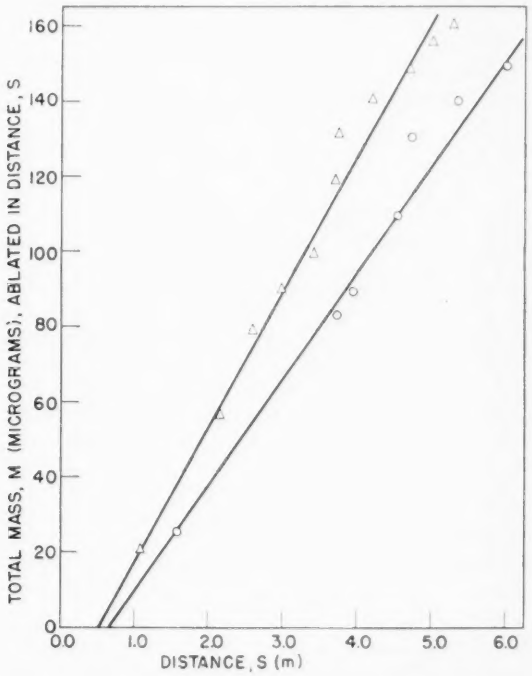

FIG. 5.—The mass ablated by melting in a given distance along the trajectory of the pellet

The amount of material ablated in a given distance interval from the pellet can be estimated by counting the number of droplet streaks in a flash. Several streak photographs were examined, and the results are presented in Table 2. The first column gives the number designation of the pellet; the second column, the distance, s, which the pellet has traveled at the end of the flash; the third column, the number, N, of the streaks in the flash or subflash; the fourth column, the mass, M, obtained by multiplying the number of streaks by the average mass of the droplets; the fifth column, the total mass, m', ablated in distance s; and the sixth column, the slope, dm'/ds, of the curve obtained by plotting m' against s.

Figure 5 is a plot of m' against s for the representative cases of pellets Nos. 1 and 2. Within the limits of the data,

$$m' = c(s - s_o), \tag{4}$$

where c is a constant and s_o is the distance at which ablation begins. The values of c for the pellets have been found to be between 25 and 40 μgm. Differentiating equation (4)

with respect to time would seem to indicate that the time rate of ablation is linearly dependent on velocity. However, the time rate of ablation for meteors is given by

$$\frac{dm}{dt} = -\frac{1}{2}\frac{\Lambda}{\zeta}\rho_a v^3 a \tag{5}$$

(Whipple 1943; Thomas and Whipple 1951), where m is the mass of the meteor, Λ the heat-transfer coefficient, ζ the heat of fusion, ρ_a the air density, v the meteor velocity, and a the meteor-projected area. If the velocity-distance relationship for pellets (Allen, Rinehart, and White 1952),

$$v = v_o e^{-cs}, \tag{6}$$

is substituted, it can be shown that, to the first approximation,

$$m' = \frac{\Lambda \rho_a A_o v_o^2}{2\zeta} e^{-2cs_o}(s - s_o). \tag{7}$$

From equations (4) and (7) a value of Λ was computed for the pellets, the average being 1.7×10^{-5}. The value of ζ that was used for aluminum is 95.4 cal/gm (Miller 1950), ρ_a is approximately 0.0012 gm/cm^3, A_o is 0.68 cm^2 (Allen, Rinehart, and White 1952), v_o is 4.6 km/sec, and the values of c are those listed in Table 2.

Free-flight values of Λ for Wood's-metal projectiles and wind-tunnel values for CO_2 pellets have been published (Thomas and Whipple 1951). The velocities which they reported were much lower than those for pellets, and the atmospheric density was varied. They reported Λ to be 1×10^{-2}, which differs by a factor of 10^3 from the value for pellets.

Several factors may account for the discrepancy between the values of Λ previously reported and those for pellets. First, the ablation from Wood's-metal projectiles is by melting, and that from CO_2 pellets is by vaporization, while the ablation for pellets is by melting and vaporization. Second, there is a difference in material. Third, only a small area of the pellet surface (such as that under the stagnation point) may be melted at any one time. Substituting 1×10^{-2} for Λ in equation (7) yields a value of approximately 200 μ for the radius of such an area. By comparison, the radius of the largest droplet is 107 μ.

SUMMARY

Velocities associated with some of the material ablated from the surface of ultraspeed pellets have been measured. The analysis of these velocities indicates that some of the material is ablated in the form of discrete particles. Sizes and masses for the particles were computed. The masses for meteor-flare fragments were compared with those for the droplets, and the agreement was excellent.

The number of droplets was counted in specific intervals along the trail of the pellet. These counts were converted to the mass ablated. The total mass ablated by melting was found to be 80–150 μgm. Experimentally, the mass lost was found to be a linear function of distance.

REFERENCES

Allen, William A., and Mayfield, Earle B. 1953, *J. Appl. Phys.*, **24**, 131.
Allen, William A., Rinehart, John S., and White, W. C. 1952, *J. Appl. Phys.*, **23**, 132.
Miller, R. R. 1950, *Liquid Metals Handbook* ("ONR Publications," NAVEXOS P-733).
Rinehart, John S., Allen, William A., and White, W. C. 1952, *J. Appl. Phys.*, **23**, 297.
Smith, Henry J. 1954, *Ap. J.*, **119**, 438.
Thomas, R. N., and Whipple, F. L. 1951, *Ap. J.*, **114**, 448.
Whipple, F. L. 1943, *Rev. Mod. Phys.*, **15**, 246.
White, W. C., Rinehart, John S., and Allen, William A. 1952, *J. Appl. Phys.*, **23**, 198.

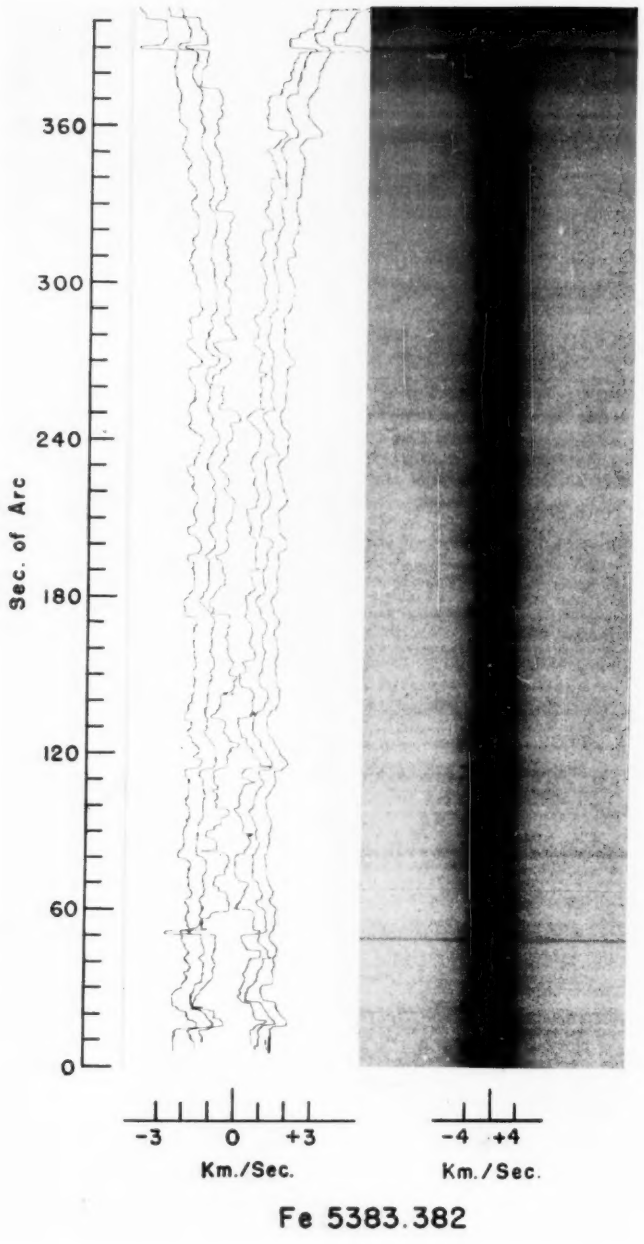

FIG. 1.—Isophotometer traces and photograph of the solar line *Fe* 5383.382 (Revised Rowland 1928)

NOTES

DOPPLER SHIFTS IN SOLAR GRANULES*

In titling this note we do not necessarily imply the existence of granules as such, but, because of the ease of discussion and widespread use in the literature, we retain the term. Shortly after the vacuum spectrograph was installed at the McGregor tower and preliminary adjustments completed, it was noticed visually that the Fraunhofer lines exhibited distortions due to Doppler shifts. Over small regions of the sun, the solar lines, in contradistinction to the atmospheric water-vapor lines, show remarkable shifts and irregularities which seem to scintillate with seeing, while, when the solar image is drifted across the first slit of the spectrograph, the line seems to wiggle and dance as various rising and falling elements are projected in turn on the slit.

Attempts to photograph the shifts have proved successful. Exposures of from 2 seconds to 1 minute have been made by using a variety of plates, and all show Doppler motions in elements corresponding to features 5″–10″ of arc size on the sun. This is comparable to the size of the granules discussed by Plaskett (1954). On days of excellent seeing, the lines, visually and on the photographs, give the appearance of having fine hairs sticking out parallel to the dispersion. Also the spectrum is streaked by the varying brightness of the granular surface. Doppler motions in elements 1′ of arc in size and larger were first photographed and analyzed by Schwarzschild and Richardson (1950). Figure 1 illustrates the fine hairs of 1″–3″ of arc size appearing in the iron line λ 5383, Rowland intensity 6. The data for this plate are: exposure: 10 sec.; film: Royal Pan film; slit width: 125 μ; dispersion: 7.92 mm/A; order: 5th; and remarks: slit radial to sun's limb.

To the left of the line is an isophotometer trace obtained with the University of Michigan isophotometer. This tracing was made with a 4× magnification along the direction of dispersion. The scanning spot was a square of effective aperture 1″ of arc by 0.012 A projected on the plate. A comparison of the displacements on the isophotometer trace with the scale indicates velocities approaching 1 km/sec from the mean. The finer structure, lost in the tracing, seems to extend to several times this value.

Figure 2 is a photograph of the atmospheric line λ 5892.4, the *Ni* line which lies between the two *Na* D lines, λ 5892.9 and λ 5895.9, with accompanying isophotometer traces. For these traces the magnification in dispersion is twice that of the photographs. An estimation of the shifts has been made for the *Ni* line by averaging constant-density contours from both sides of the line; in so doing, the variations in line width are removed. The maximum displacements are of the order of 0.5 km/sec from the mean, with a dispersion of 0.2 km/sec. This is a minimum figure both because the seeing was not the best and because the isophotometer spot integrated over 3″ of arc along the slit.

The D line shows a complex structure related to the granulation observed in spectroheliograms and first discussed by d'Azambuja (1930) and later by Unsöld (1938). The original negative shows large variations in central intensity along the line. An examination of many plates reveals that the centers of the strong lines *Na* D, *Ca* 4227, *Mg b*, etc., appear to show larger displacements than the weaker lines. However, the picture is complicated by the detailed inner structure of the cores.

It seems that all spectroscopic measurements of the physical parameters of the sun's surface may require careful revision and perhaps redefinition because of the observed

* Work was supported in part by Contract N6onr-232-5 with the Office of Naval Research.

large distortions in the spectrum lines. Doppler shifts in the 1–2-second granules and bodily displacements of the line corresponding to distances of 5″–15″ of arc along the slit have certainly influenced the determinations of solar rotation. Wave-length determinations with an interferometer in which the solar image is focused on the ring system are locally subject to error. In addition, the determination and interpretation of line profiles and magnetic-field effects will probably require a careful review. We plan further investigations of the foregoing problems and will attempt to establish variations with height by using lines of different excitation potentials and molecular bands.

ROBERT R. MCMATH
ORREN C. MOHLER
A. KEITH PIERCE

McMATH-HULBERT OBSERVATORY
UNIVERSITY OF MICHIGAN
PONTIAC, MICHIGAN

REFERENCES

Azambuja, L. d'. 1930, Thèses (Paris: Gauthier Villars et Cie), chap. ii.
Plaskett, H. H. 1954, *M.N.*, **114**, 297.
Schwarzschild, M., and Richardson, R. 1950, *Ap.J.*, **111**, 351.
Unsöld, A. 1938, *Physik der Sternatmosphären* (Berlin: Springer), § 100.

SHORT-PERIOD FLUCTUATIONS IN THE INTENSITY OF SS CYGNI

According to a report by A. H. Joy (1955), the cataclysmic variable SS Cygni is a spectroscopic binary with a period of about 6 hours. It was therefore thought desirable to make photometric observations to determine whether this system, having such a short period, might be an eclipsing variable. Consequently, SS Cygni was observed at the 40-inch Yerkes refractor with a photometer having a 1P21 photomultiplier tube; recording was by a Brown potentiometer. A Corning 3384 filter plus the spectral response of the photocell gave an effective wave length near 5500 A. The writer obtained over two thousand deflections of the variable on 14 nights during the period August 16 through September 25, 1955. The comparison stars were *b*, *a*, and *d* of those used by Parkhurst and Daniels (1900), which were found to have magnitudes of 8.57, 9.74, and 10.87, respectively, on the (*B*, *V*) system.

The period covered by the observations began 5 days after a maximum, which reached 8.6 mag. The following minimum was about 11.3 mag., which is about 0.5 mag. brighter than normal. This minimum lasted from August 21 through September 17, after which a slow rise to a new maximum began, which again reached 8.6 mag. on September 25. During the minimum the variable fluctuated markedly during the night, so that no decision as to an eclipse could be made at that time. Considerable attention was then paid to the fluctuations themselves. They were found to have amplitudes of the order of 0.2 mag., in periods often less than 10 minutes. At times a wave of 2^h–3^h period, superposed on the fluctuations and of similar amplitude, seemed indicated; but this wave did not reappear in subsequent observations. Often a flarelike increase occurred, in which the brightness rose 0.3–0.4 mag. in 10–15 minutes, followed by an irregular decrease to the former level. Typical fluctuations and an example of a flare are shown in Figure 1, *a*.

The amplitude of the fluctuations remained approximately constant in absolute units when the 3-mag. rise occurred, as is shown by Figure 1, *b* and *c*. The lengths of the arrows on the right give equal absolute amplitudes at the magnitudes referred to. Figure 1, *c*, a 6-hour run, also shows the general rise; but it is noted that no fluctuations greater than 0.01 mag. occur which could be attributed to an eclipse phenomenon.

Prior to the 40-inch run, the star was observed on August 11, 12, and 13 in the blue

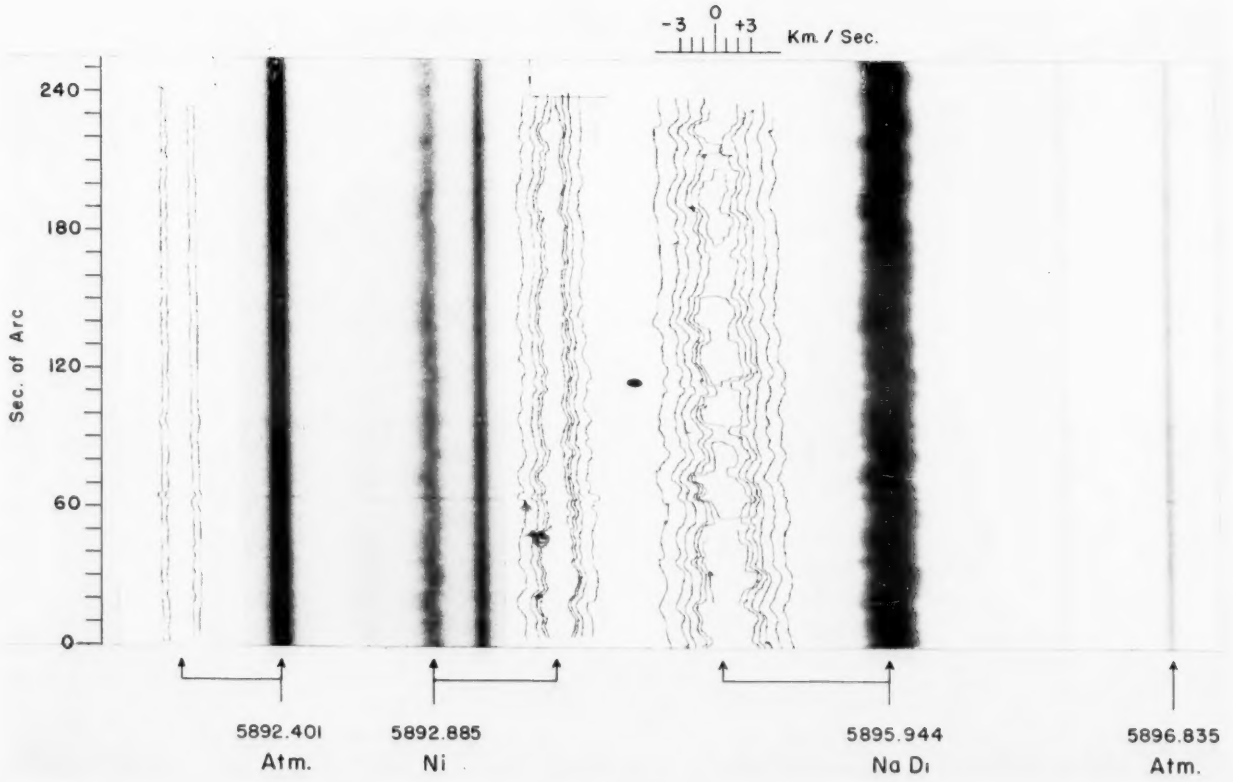

FIG. 2.—*Left:* isophotometer traces and photograph of the atmospheric line 5892.401 and the Nickel line 5892.885. *Right:* isophotometer trace and photograph of the *Na* D_1 line, 5895.944. (The approximate wave lengths are on the 1928 Revised Rowland scale.)

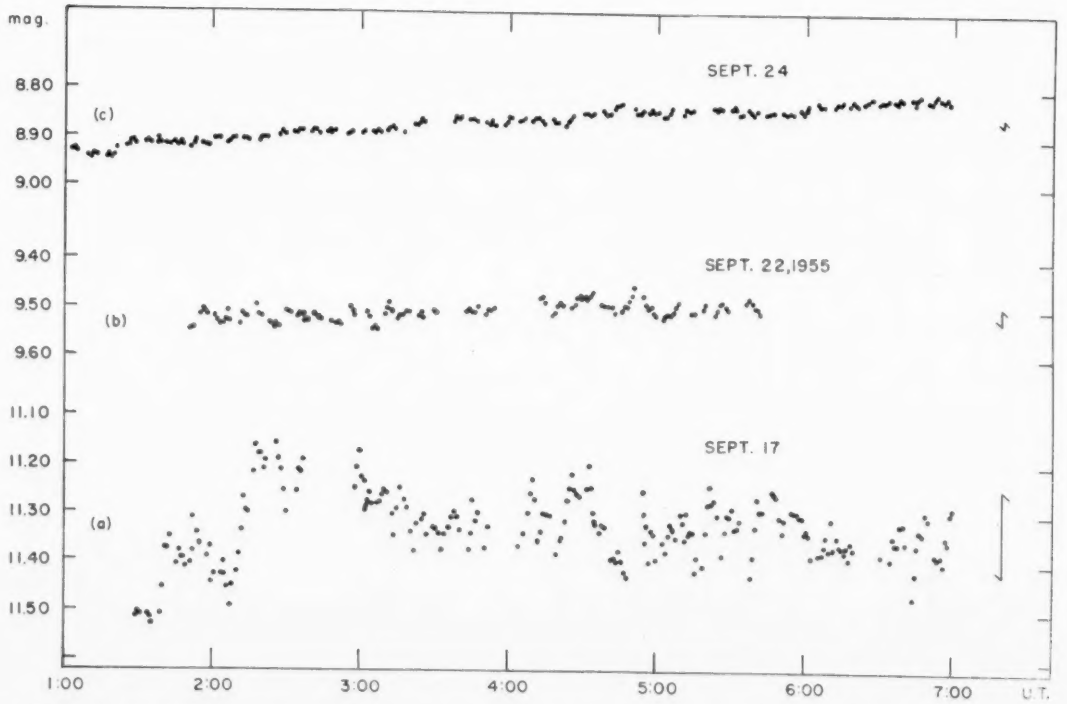

FIG. 1.—Yellow light-curves of SS Cygni on three dates. Diameter of dots is roughly equal to mean error of single observation. Time scale of diagram is insufficient to show all recorded details of fluctuations on September 17. Vertical lines near right-hand margin show equal absolute amplitudes. There is no evidence of an eclipse.

and yellow with the same photometer attached to the 12-inch Yerkes refractor. As was stated, the star was then near maximum, 8.6 mag., and the measured color corresponded to B3 (color temperature 18,000° [Hynek 1951]). During a normal minimum, the star is at 11.8 mag. and has a spectrum classified as dG5 (Elvey and Babcock 1943), which would correspond to a color temperature of 5520°. These figures indicate that there is no need to assume a change in radius as the star rises to maximum, as was done by Hinderer (1949). Hence the geometrical relations in the spectroscopic binary should remain the same at maximum and minimum; and, since no eclipse is found at maximum, none would be expected at minimum.

In Elvey and Babcock's (1943) spectroscopic observations of SS Cygni, they note that the hydrogen emission lines, which are strong at minimum, practically disappear at maximum. They state that the change in equivalent width of the lines may be explained by the increase in the continuum, amounting to 3 mag. In AE Aquarii, also classified as an SS Cygni star, Lenouvel (1954) has found short-period brightness fluctuations correlated with changes in the equivalent width of $H\alpha$. Thus it is tempting to suggest that the brightness fluctuations in SS Cygni are caused by intensity fluctuations of the emission lines, whose amplitude does *not* depend on the main 3-mag. variation of the system.

The difficulty with this explanation is the comparative paucity of emission lines in the yellow region used. $H\beta$ is on the shortward tail of the response-curve, and the D_3 helium line and $H\alpha$ are on the longward tail; these are the only strong emission lines in the region appearing on Elvey and Babcock's spectra. There is the possibility that the Paschen continuous emission contributes appreciably. Careful spectrophotometry will be needed to determine whether this explanation of the irregular variation is satisfactory.

I would like to thank Dr. G. P. Kuiper for helpful discussions.

GORDON GRANT

YERKES OBSERVATORY

REFERENCES

Elvey, C. T., and Babcock, H. W. 1943, *Ap. J.*, **97**, 412.
Hinderer, F. 1949, *A.N.*, **277**, 193.
Hynek, J. A. (ed.). 1951, *Astrophysics* (New York: McGraw-Hill Book Co., Inc.), p. 20.
Joy, A. H. 1955, private communication.
Lenouvel, F. 1954, *Ann. d'ap.*, **17**, 416.
Parkhurst, J. A., and Daniels, Z. 1900, *Ap. J.*, **12**, 259.

ABSTRACTS OF ASTROPHYSICAL JOURNAL SUPPLEMENT SERIES

Supplement No. 16, Volume 2

TOROIDAL OSCILLATIONS OF AN INCOMPRESSIBLE CONDUCTIVE FLUID SPHERE IN A DECAY FIELD

EBERHART JENSEN*
Yerkes Observatory

The decaying poloidal magnetic field in a conducting homogeneous sphere having the longest decay time is a dipole field outside the sphere. In determining this decay field, it is assumed that no material motions are taking place. In this investigation the initial state is characterized by the presence of such a decay field.

Hydromagnetic oscillations around this initial state will result if this state is subject to perturbations. If oscillations with periods short compared to the decay time are considered, the equations of the problem are much simplified, since the electrical conductivity may then be taken to be infinitely large.

We consider purely toroidal oscillations, i.e., the velocity field is expanded in toroidal functions in the sense of Elsasser. Thus the velocity has no radial component. Two cases are considered which differ in the boundary conditions. In the first case the velocity does not vanish at the boundary of the sphere; in the second case the velocity is zero on this surface. The initial magnetic field is the same in both cases, and the solutions are carried out to the same degree of approximation.

Before proceeding to the solution of the oscillation problem, certain properties of the orthogonal functions used as a base for the series expansions appearing in the solution of the perturbation equations are demonstrated. These functions are solutions of the equation governing the decaying magnetic field in a homogeneous sphere with a constant electrical conductivity. We make use of the poloidal and toroidal solutions as defined by Elsasser. These functions are derived from generating functions expressed in terms of spherical Bessel functions and Legendre polynomials. The generating functions are defined in such a way that the toroidal functions derived from them become normalized when integrated over the volume of the shpere. Expressions for the normalization constants and the corresponding integral over the squares of the poloidal functions are evaluated in the two cases with different boundary conditions considered.

After expressing the initial field in a suitable way, expressions are given for the matrix elements which later appear in our solutions. The selection rules valid with the initial field considered here are derived. A table containing numerical values of the nonvanishing matrix elements up to the fourth order for both cases of boundary conditions is given.

The equation of motion and the electromagnetic equations are linearized, and series expansions for the velocity and for the field variables are introduced. The perturbations in the magnetic field will contain a mixture of poloidal and toroidal terms. Making use of the orthogonality properties of the poloidal and toroidal functions, expressions for the various coefficients in the series expansions are found.

The final set of equations is an infinite system of ordinary linear differential equations of the second order in the coefficients in the expansion of the velocity field. These equations will admit solutions with the time-dependent factor of the form, $e^{\omega t}$, provided

* From The Institute of Theoretical Astrophysics, University of Oslo, Norway.

only that the determinant of the linear system is zero. This determinant is much reduced when the selection rules for the matrix elements are applied. It is symmetrical, and thus all characteristic values of ω^2 are real. Up to this point there is formally a complete analogy between the two cases we are considering. Since the matrix is nondiagonal, exact values of the characteristic frequencies cannot be found. In order to determine approximate eigen-values, the infinite matrix is approximated by a matrix with a finite number of terms. The first approximation is found by solving the equation resulting when only one term is retained. The second approximation is obtained when a matrix of the second order is left over, and so on. This procedure is applied up to the fourth approximation in both the cases considered.

In our first case, where the velocity is different from zero at the surface, corresponding to the case of a free boundary, the eigen-values thus found have a tendency to converge and thus give a discrete eigen-value spectrum. In the second case, however, corresponding to the case of a rigid boundary at which the velocity vanishes, the results of the numerical calculations seem to indicate a continuous range of values of the characteristic frequencies.

It appears that both positive and negative eigen-values of ω^2 are present for both cases. From the solutions given here, however, it is not possible to decide which sign the imaginary eigen-values of ω will have, whether they correspond to an exponential amplification with time or to a damping.

Finally, an application to the earth's core is made. If t
boundary, our second case should be used. Then our calu
oscillations with any period may be present.

If the surface of the highly conductive core is consid
correspond to the discontinuity of the electrical conductiv
we may apply our first case. Substituting numerical values f
of the dipole component at the surface of the fluid core,
density, we obtain 85, 96, and 189 years as the periods cor
found in our first case. These values are in the range of per
the secular variations of the terrestrial field.

THE INDEX TO
HAS BEEN REMOV
POSITION AND PL
BEGINNING OF T
THE CONVENIENC

The Second Volume in a Distinguished Series

THE EARTH AS A PLANET

The Solar System—Volume II

Edited by GERARD P. KUIPER

This is the second of four volumes designed to collect and systematize our knowledge of the solar system. Like its predecessor, *The Sun*, it is con-
ence book for the specialist and a source of general
eneral reader with some knowledge of the physical

itative articles written by internationally eminent
as a Planet is a complete and fully documented
e entire range of physics, geochemistry, oceanogra-
y as they apply to the earth in its planetary aspect.
ics treated are the rotation of the earth; the nature
the growth of continents; current systems of oceans
life-cycles of methane, carbon dioxide, oxygen, and
ion spectrum of the atmosphere; the physics and
r atmosphere; and the appearance of the earth from

Contributions by

ONES LEO GOLDBERG, SIR EDWARD BULLARD, A. B. MEINEL, BRIAN MASON, CLYDE T. HOLLIDAY, ANDRÉ DANJON, SIR HAROLD JEFFREYS, J. W. CHAMBERLAIN, H. U. SVERDRUP, M. NICOLET, G. E. HUTCHINSON

752 pages *$12.50*

The remaining two volumes in the series will consist of *Planets and Comets, Part 1, Planets and Satellites* and *Planets and Comets, Part 2, Minor Planets, Meteorites, Comets, Origin of the Solar System.*

from your bookseller or from

THE UNIVERSITY OF CHICAGO PRESS

5750 ELLIS AVENUE CHICAGO 37, ILLINOIS

O THIS VOLUME
IOVED FROM THIS
PLACED AT THE
THE FILM FOR
NCE OF READERS

only that the determinant of the linear system is zero. This determinant is much reduced when the selection rules for the matrix elements are applied. It is symmetrical, and thus all characteristic values of ω^2 are real. Up to this point there is formally a complete analogy between the two cases we are considering. Since the matrix is nondiagonal, exact values of the characteristic frequencies cannot be found. In order to determine approximate eigen-values, the infinite matrix is approximated by a matrix with a finite number of terms. The first approximation is found by solving the equation resulting when only one term is retained. The second approximation is obtained when a matrix of the second order is left over, and so on. This procedure is applied up to the fourth approximation in both the cases considered.

In our first case, where the velocity is different from zero at the surface, corresponding to the case of a free boundary, the eigen-values thus found have a tendency to converge and thus give a discrete eigen-value spectrum. In the second case, however, corresponding to the case of a rigid boundary at which the velocity vanishes, the results of the numerical calculations seem to indicate a continuous range of values of the characteristic frequencies.

It appears that both positive and negative eigen-values of ω^2 are present for both cases. From the solutions given here, however, it is not possible to decide which sign the imaginary eigen-values of ω will have, whether they correspond to an exponential amplification with time or to a damping.

Finally, an application to the earth's core is made. If the mantle is acting as a rigid boundary, our second case should be used. Then our caluclations indicate that periodic oscillations with any period may be present.

If the surface of the highly conductive core is considered to be free, which would correspond to the discontinuity of the electrical conductivity lying inside the fluid core, we may apply our first case. Substituting numerical values for the magnetic-field strength of the dipole component at the surface of the fluid core, as well as for its radius and density, we obtain 85, 96, and 189 years as the periods corresponding to the eigen-values found in our first case. These values are in the range of periods found in the spectrum of the secular variations of the terrestrial field.

The Second Volume in a Distinguished Series

THE EARTH AS A PLANET

The Solar System—Volume II

Edited by GERARD P. KUIPER

This is the second of four volumes designed to collect and systematize our knowledge of the solar system. Like its predecessor, *The Sun*, it is conceived as both a reference book for the specialist and a source of general information for the general reader with some knowledge of the physical sciences.

Consisting of authoritative articles written by internationally eminent specialists, *The Earth as a Planet* is a complete and fully documented handbook, covering the entire range of physics, geochemistry, oceanography, and biochemistry as they apply to the earth in its planetary aspect. Among the many topics treated are the rotation of the earth; the nature of the earth's interior; the growth of continents; current systems of oceans and atmospheres; the life-cycles of methane, carbon dioxide, oxygen, and nitrogen; the absorption spectrum of the atmosphere; the physics and chemistry of the upper atmosphere; and the appearance of the earth from interplanetary space.

Contributions by

SIR HAROLD SPENCER JONES
FRED L. WHIPPLE
J. TUZO WILSON
D. R. BATES
HORACE R. BYERS
LEO GOLDBERG
SIR EDWARD BULLARD
A. B. MEINEL
BRIAN MASON
CLYDE T. HOLLIDAY
ANDRÉ DANJON
SIR HAROLD JEFFREYS
J. W. CHAMBERLAIN
H. U. SVERDRUP
M. NICOLET
G. E. HUTCHINSON

752 pages *$12.50*

The remaining two volumes in the series will consist of *Planets and Comets, Part 1, Planets and Satellites* and *Planets and Comets, Part 2, Minor Planets, Meteorites, Comets, Origin of the Solar System.*

from your bookseller or from

THE UNIVERSITY OF CHICAGO PRESS
5750 ELLIS AVENUE CHICAGO 37, ILLINOIS

THE ASTROPHYSICAL JOURNAL SUPPLEMENT SERIES

These *Supplements* are intended to provide a medium for the publication of extensive investigations, such as wave-length lists of stars of special interest, photometric data, results of numerical integrations pertaining to stellar interiors, model stellar atmosphere calculations, and original memoirs.

Supplement No. 15

"Stellar Spectra in Milky Way Regions. III. A Region in Cepheus-Lacerta." S. W. McCuskey, and "Stellar Spectra and Colors in a Milky Way Region in Cassiopeia." Alice H. Farnsworth.

Dr. McCuskey presents a catalogue of spectra and photographic magnitudes to 12.3 mag. for 4222 stars in Cepheus-Lacerta, together with blue-red color indices for 1764 stars. Miss Farnsworth presents a catalogue of spectral types, photographic magnitudes to 12.4 mag. and blue-red color indices, with identification charts, for a thousand stars in Cassiopeia.

(Published August, 1955. Price, $2.00)

Supplement No. 16

"Toroidal Oscillations of an Incompressible Conductive Fluid Sphere in a Decay Field." Eberhart Jensen

Hydromagnetic oscillations of a conducting fluid sphere about an initial magnetic field is investigated. The initial field is the decay field having the longest decay time, which is a dipole field outside the sphere.

(Published October, 1955. Price, $1.75)

Supplement No. 17

"Nuclear Reactions and Element Synthesis in the Surface of Stars." W. A. Fowler, G. R. Burbidge and E. Margaret Burbidge

An attempt is made to explain the anomalous abundances of certain heavy elements observed in peculiar A stars. It is suggested that the heavy elements are synthesized from the metals by nuclear reactions such as (α, n) . . . . $(\alpha, 3$ nucleons$)$, (d, p), (d, n) and $(p, n) + (n, \gamma)$ at particle energies between 1 and 100 Mev. The charged particles are accelerated by the varying magnetic fields of these stars.

(Ready November, 1955. Price, $1.25)

An abstract of each supplement will be published in THE ASTROPHYSICAL JOURNAL. The *Supplements* will appear irregularly and may be purchased separately or by subscription. Each volume of *Supplements* will consist of approximately 500 pages.

Subscriptions

$8.00 per current volume

Canada, $8.75. Foreign, $9.50.

To members of the American Astronomical Society, $6.00 per current volume.

Price of Vol. I will be increased upon publication of Vol. II, No. 1.

Orders now accepted.

THE UNIVERSITY OF CHICAGO PRESS

5750 ELLIS AVENUE **CHICAGO 37, ILLINOIS**